2018

Dielectrophoresis at wireless bipolar electrode arrays: Applications to the marker-free selection and detection of circulating tumor cells

Min Li
Iowa State University

Dielectrophoresis at wireless bipolar electrode arrays: Applications to the marker-free selection and detection of circulating tumor cells

by

Min Li

A dissertation submitted to the graduate faculty

in partial fulfillment of the requirements for the degree of

DOCTOR OF PHILOSOPHY

Major: Chemistry

Program of Study Committee:
Robbyn K. Anand, Major Professor
Jared L. Anderson
Liang Dong
Gordon J. Miller
Emily Smith

The student author, whose presentation of the scholarship herein was approved by the program of study committee, is solely responsible for the content of this dissertation. The Graduate College will ensure this dissertation is globally accessible and will not permit alterations after a degree is conferred.

Iowa State University

Ames, Iowa

2018

TABLE OF CONTENTS

ACKNOWLEDGEMENTS

Research as a graduate student at the Chemistry department at Iowa State University has been a fulfilling experience. It would not have been possible without the patience and support of my major supervisor, Dr. Robbyn K. Anand. She has been instrumental in aiding my transition between completely unrelated research directions, and aiding in my growth from strength to strength through my graduate school experience. Her mentoring throughout my time in the Anand lab has allowed me to discover and acquire new skills, while expanding the boundaries of my knowledge.

I am extremely grateful to all my program of study committee members. Thank you for taking your time evaluating my research progress and offering valuable feedback for the projects performed in this document. I would also like to express my sincere gratitude to Prof. Gordon J. Miller for his help in my career progress since 2013, and to Prof. Liang Dong for discussing microfluidic designs and single-cell isolation research.

I would like to thank all my colleagues, collaborators and many other influential people that have helped me during my Ph.D. I am thankful to Dr. Anja Mudring, who initially introduced me to research, imparting the fundamentals and the outcomes of graduate school. Dr. Simon Steinberg was generous in his continuous support of both my research and future career plans over the last 5 years. I am also thankful to Ben Brayborn, Kevin Clark, Sungu Kim, Taejoon Kong, Anastasia Lackmann, Bryan Lampkin, Xinle Li, He Nan, Riel Opiec, Volodymyr Smetana, and Qiaochu Zhu, with whom I have had important initial discussions on developing ideas for implementation as research projects. I would also like to thank to Raghu Maligal-Ganesh, James Anderegg, Valentina Loe, Qisheng Lin, Tao Wang, Weiwei Xie and Tuo Wang for being mentors and senior researchers who provided much desired critical

input at various junctions. Karen Lowton-Dunn, Jean-Philippe Tessonnier, Mary Caruso Dailey, Krysti Knoche-Gupta, and Sara Scott thank you for your guidance during my career search. Finally, it's a great pleasure to work in Ames laboratory and Department of Chemistry that value research and team work and allot time for a researcher to develop novel ideas.

I would also sincerely like to thank all my friends, who have always been pillars of support. I would specifically like to thank Jephian Lin, Yuhui Liu, Xiaohui Tang and Ben Rayborn for your patience listening to my trials, to Jeffrey G. Bell and Martin Donakowski for your suggestions, and to Raymond Harjadi, Shu En Loew, Wshen Theh, Serafim Teknowijoyo, Michelle Yin Theng, Monica Richards, and Lan Hu for spending valuable time with me. Finally, and most importantly, I am indebted to my parents, to my partner John E. Matthiesen, my brothers and my sister, for consistently helping me develop a sense of morality, diligence and perseverance. They have been unconditionally supportive and it is their love and strength that carries me forward on all the journeys I hope to make in finding myself and being a part of communities I enjoy. Move along the upward spiral of growth, please keep it up and carry on with the truth of Henry David Thoreau's observation: "I know of no more encouraging fact that the unquestionable ability of man to elevate his life by conscious endeavor."

ABSTRACT

Metastasis is responsible for approximately 90% of cancer related deaths. The key step in metastasis is the migration of cancer cells out of the primary tumor and into bloodstream. Once reaching at a distant site, a fraction of these circulating tumor cells (CTCs) invades foreign tissues for subsequent growth of tumors. However, conventional cancer treatments ignore the metastatic process, resulting in cancer relapse. Consequently, the isolation and characterization of CTCs are crucial in understanding how cancer spread by metastasis.

The enormous value of CTCs has not been completely realized because isolation of CTCs – the first inevitable step of overall analysis, is incredibly challenging due to their extreme rarity and varied physical and biological characteristics. Thus, separation techniques that exhibit the following features are critical: (i) They must provide a pure and representative sample of CTCs; (ii) Separation of individual CTCs are mandatory considering subpopulations can be easily obscured at the bulk scale; (iii) The sorting process is continuous and high-throughput since detection of a rare phenotype or cellular response requires analysis of thousands of individual cells; (iv) Captured single-cells should be readily interfaced with assays for downstream analysis. (v) Devices need to be cost-effective, accessible, and simple in manufacturing and operation for a wide range of applications.

Microfluidic lab-on-a-chip (LOC) technologies possess micron-scale dimensions and picoliter-to- nanoliter volume handling capacities, thereby facilitating manipulation and sampling of single cells. However, they often suffer from lack of selectivity, being over- or under-selective. Selection must happen prior to the isolation step for analysis of individual cells. Further, many LOC devices have difficulty in interfacing with assays, or complexity that

hinders their applications. Thus, the development of fully integrated devices that offer simplicity in manufacturing and operation remains an important challenge.

Separation based on dielectrophoresis (DEP) exhibits less bias when compared with size- and antibody-based approaches, as it leverages the electrophysiological properties of CTCs. However, many of the current approaches to DEP suffer from low throughput and are not amenable to on-chip single-cell analysis. These limitations stem from design constraints such as the requirement that all electrodes must be connected via wire leads to the power source. Further, in DEP devices that employ insulating posts to shape the electric field, integration of these structures intended for cell capture with other features, such as chambers for on-chip analysis, is non-trivial.

The work presented in this document centers on the development of DEP devices at wireless bipolar electrode (BPE) arrays to addresses these concerns. First, DEP is employed to selectively capture and isolate CTCs in micropockets, while blood cells flow through the channels. The capture methodology used here eliminates massively screening of all cell populations one-by-one, the case in droplet separation, thus greatly increasing sorting efficiency. Further, high-fidelity single-cell capture could be readily achieved when the pocket dimensions matched to those of the cells. Second, leak channel design opens a flow circuit that enables valve-free transfer of individual isolated cells into reaction chambers, while split electrode design allows recapture and lysis of transferred cells for subsequent assay evaluation. Third, the use of arrays of wireless electrodes removes the requirement of ohmic contact to individual array elements, thus enabling device to be scalable along both x- and y- directions. This wireless electrode array not only provides a high-throughput module in cell capture, also in cell imaging and analysis. Finally, the use of ionic liquid as immiscible phase permits both

electrical lysis and fluid isolation. A key difference that distinguishes this from previous approaches is that DEP-based sorting, electrical lysis and analysis of single cells are integrated while retaining high-throughput and valve-free control. The simplicity of device manufacturing, the ease of its operation, and the potential for assay of live single cells or electric lysis for assay of cellular contents make the design broadly applicable for in-depth analysis of a variety of biological systems.

CHAPTER 1

GENERAL INTRODUCTION

1.1 Introduction

According to the Center for Disease Control and Prevention (CDC), cancer is the second most common cause of death – nearly 1 out of every 4 deaths is due to cancer. Breast cancer is the most prevalent, having over 240,000 new cases reported in 2015 in the US alone. The leading cause of mortality in cancer patients is tumor cell dissemination out of primary tumor into the blood stream (intravasation) - the first step of metastasis (**Figure 1.1**).[1] However, conventional cancer treatments target only the primary tumor and ignore the metastatic process. In fact, approximately 90% of cancer deaths result from metastasis.[1] Consequently, understanding how these tumor cells in circulation (circulating tumor cells, CTCs) spread is critical in stopping cancer.[2] Further, in comparison to open surgery, the use of CTCs as a real-time liquid biopsy is minimally invasive and more accessible (e.g., than tumors located in lung or brain).

As depicted in **Figure 1.1**, metastasis begins when tumor cells acquire the ability to detach from the primary tumor, migrate through their surrounding tissues and invade blood vessels.[3] The invasion is either passive during angiogenesis or active via biological events such as the epithelial to mesenchymal transition (EMT). After intravasation, CTCs must overcome difficulties including anoikis, shear stress and the potential for attack by the immune system to survive and spread throughout the body. After reaching a distant organ, CTCs may undergo the reverse process of EMT (MET) for further proliferation. Although only a few out of millions of dispersed CTCs might survive in circulation, they are the primary cause of cancer relapse after traditional therapeutic intervention. The ineffectiveness of primary therapeutic

strategies against these cells indicates that the patterns of response of CTCs are modified in the migrated microenviroment as compared to their ascendants in the primary tumor.[4] As a result, the detection and characterization of CTCs are crucial in interpreting how CTCs are altered during metastasis.[5]

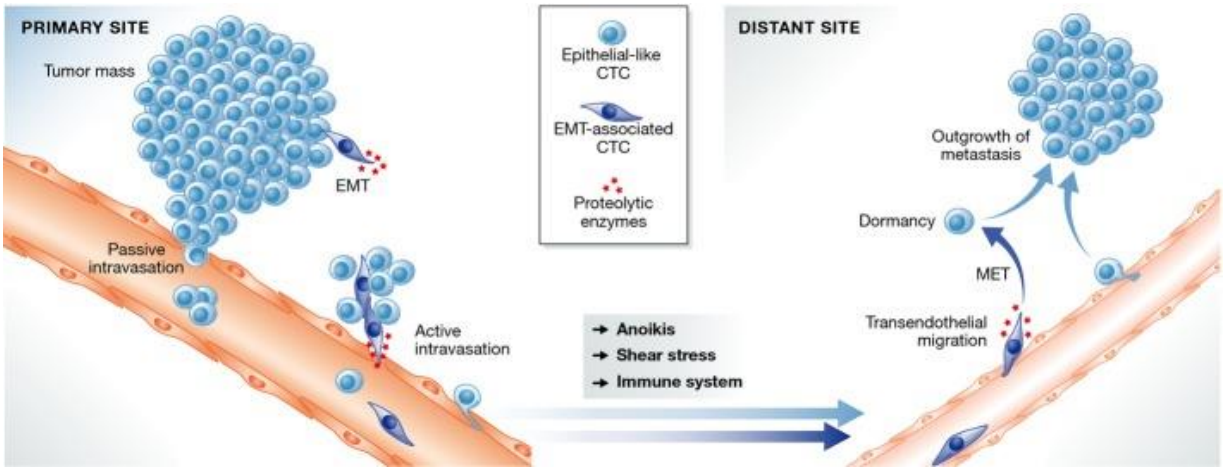

Figure 1.1. The metastatic pathway. Tumor cells first invade the bloodstream either passively or actively. Subsequently, the disseminated tumor cells (CTCs) must conquer obstacles such as anoikis, shear stress and the immune system to survive and further spread into a distant site. At a foreign organ, they may survive in a dormant state or directly grow into overt metastases. Reproduced from ref. [3].

Over the preceding decades, the critical role CTCs play in the metastatic spread of carcinomas is well-documented.[6] However, biological assays cells in ensemble yield statistical averages and can mask unique characteristics held by a minority of cells (**Figure 1.2**).[7] For example, cells that are identical in appearance may differ in the expression of a particular gene, protein, ion or signaling pathway,[8] and CTCs have been shown to exhibit significant levels of phenotypic heterogeneity even in isogenic populations.[9,10] Unexpected responses from a few single cells may have a dramatic impact on disease progress, and therefore, it is imperative to detect a rare phenotype or a cellular response, requiring analysis of individual cells.

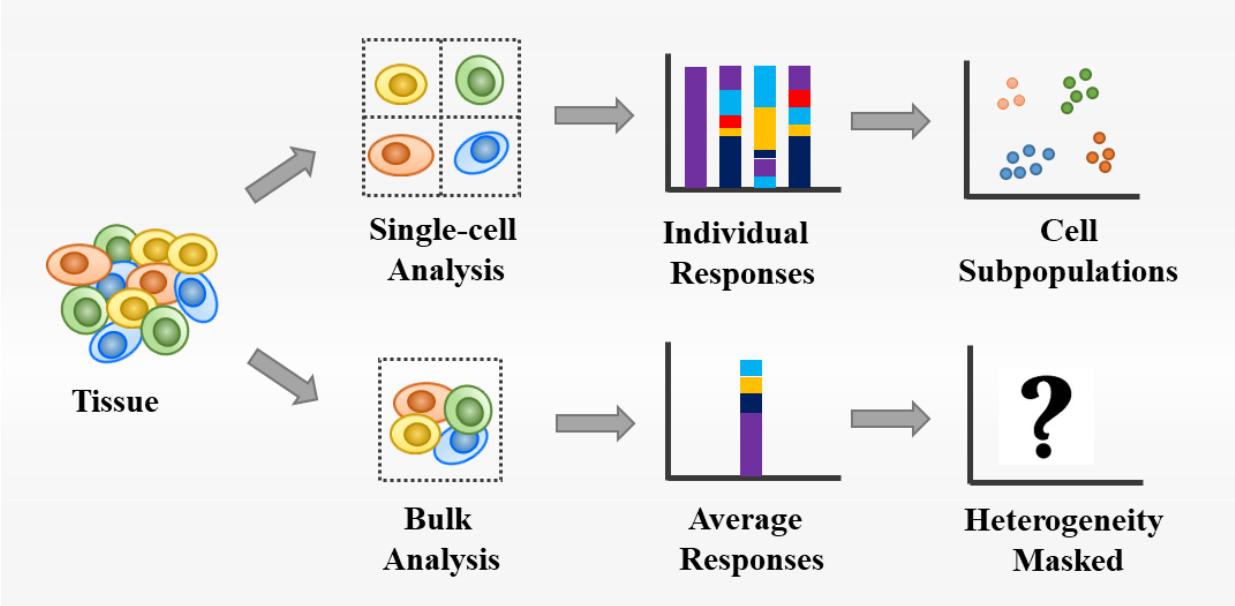

Figure 1.2. Comparison of single-cell analysis to bulk analysis. Single-cell analysis reveals differences among individual cells, whereas studies based on a large amount of samples may mask the heterogeneity and result in ambiguous data.

1.2 Single-Cell Analysis

1.2.1 Clinical Impact

Due to cellular heterogeneity, substantial interest has been elicited in technologies that allow researchers to peer into the molecular mechanisms that underlie the function of single cells.[11-13] The analysis of individual cells proves to be a 'mission critical' and impacts a broad spectrum of fundamental and applied scientific fields. For example, real-time RT-PCR opens up the possibility to differentiate whether a particular set of genes is co-expressed in the same cell or in different subpopulations.[14] Further, it becomes clear whether a change in expression is homogeneous across all cells, or only present in a subset.

In particular, CTCs have proven to be of great importance as biomarkers in cancer diagnosis, prognosis and personalized treatments.[2,15] For instance, the finding of ERBB2-positive CTCs in patients with ERBB2-negative primary tumors suggests that additional

patients could benefit from ERBB2-directed therapies.[16,17] Genomic CTC analysis reveals that metastatic colorectal cancer patients with wild-type KRAS can benefit from anti-epidermal growth factor receptor (EFGR) monoclonal antibody (mAb) treatment, while those with mutated KRAS are unresponsive to this mono-therapy.[18] Even enumeration of CTCs alone is of high value in cancer prognosis.[15,19] Thus, technical advances that enable single-cell 'omics' continues to be critical in developing effective therapeutic strategies.

1.2.2 Challenges

Despite the enormous biological and clinical value obtained, analysis of individual cells is incredibly challenging considering the following aspects. (i) A single mammalian cell has a diameter on the order of tens of microns with a volume of ~ 1 pL and weight of 3 – 4 ng.[20] These microscale dimensions necessitates delicate control of cell manipulation. (ii) Macromolecules (DNA, RNA and protein) comprise less than 25% (w/w) of cellular contents in each individual cell, which corresponds to 1 – 2 copies of a specific DNA and 8×10^9 protein molecules.[20] Thus, techniques with requisite sensitivity and reproducibility are critical for gene and protein studies. For instance, PCR is mandatory to amplify the small amount of DNA or RNA within each cell. Although PCR is a well-established technique, single-cell PCR[21,22] associated with challenges in sample handling, and further, biological interpretation is not exceptional. (iii) Each specific type of cell exists in a complex microenvironment, thus necessitating the separation and isolation of the cells of interest prior to analysis.[13] Further complicating this challenge is the seamless integration of this sample preparation with downstream evaluation.[23] These challenges impose strict technical specifications on technologies that are developed to probe the machinery of single cells.

1.3 Separation as a Primary Challenges

1.3.1 Microfluidic LOC Techniques

Lab-on-a-chip (LOC) technologies possess device components on the nano- to micrometer scale, thus offering immense opportunities in the analysis of individual cells.[24-26] Since the pioneering work in the early 1950s,[27] LOC has established itself in academia and industry as a toolbox developing robust methods and products in the life sciences. In comparison to the traditional fluorescence activated cell sorting (FACS),[28] in which one or multiple laser beams directed into a capillary tube screen a high-speed stream of cells in suspension flow as they in single file, microfluidic LOC devices offer several key advantages for the study of single cells. (i) Miniaturization of devices from conventional macro- to micro-scale. The resultant microchips dramatically reduce sample consumption and shorten the time for mass transport, while significantly increasing the interaction of the analytes of interest with embedded structures or reagents. This miniaturization is of particular importance for single-cell research since it permits cell manipulation, compartmentalization, lysis and analysis without significant dilution of target molecules. (ii) Integration of different functional units (separation, isolation, reaction, and detection) in a channel network. Thus, serial processing and analysis can be easily performed in a flow mode system, whilst retaining cells to be evaluated individually. (iii) Parallelization of sample processing for massive screening of a large group of single cells. The parallel sampling modes that LOC offers are vital to obtaining population statistics that allow a subpopulation of cells to be identified. Together with the benefits accomplished by exploring new functional materials [29,30] and microfluidic automation,[31,32] [31,32] the distinct advantages of 'all-in-one' LOC chips can be leveraged to systematically unravel single-cell biology.

1.3.2 Challenges

Although microfluidic LOC devices possess dimensions and volume handling capacities matched to single cells, the complexity of biological media and cellular microenvironments present significant challenges during cell separation. LOC methods must select a pure and representative population of interest, otherwise the overall analysis is not precise. Yet the development of a 'perfect' sorting method is incredibly difficult – it must be capable of selecting all cells of interest while never incorporating non-target cells. Further complicating sample preparation is that the separation needs to be easily interfaced with assays for analysis. This state of affairs often require multiple processing steps (e.g., trypsinization,[33] solution exchange,[34] separation/purification,[35] isolation,[36] transfer and reaction [21,37]), but doing so with minimal alteration of cells remains a challenge. Variations of cell medium such as in pH, ionic strength and temperature may result in dramatic changes in the intracellular concentrations of many species. For example, sub-second to second timescale alteration can occur for ion concentration and protein phosphorylation of a cell.[20] Retaining the biological complexities of cells during these processing steps is particularly important in performing valid and reproducible assays, especially in the case when dynamic characteristics are evaluated. In addition, the hydrophobic-hydrophilic surface nature of many macromolecules lead to adsorption of cells onto a variety of surfaces (e.g. conventional microfluidic surface, polydimethylsiloxane (PDMS) and glass).[38] Thus, preventing cell adhesion and obtaining a high recovery of target cells are another bottleneck in separation. An additional mission for single-cell analysis is that the sample preparation needs to be synchronous with detection, i.e., separation is also parallelized to retain the capacity of conducting population statistics.

Consequently, there is still a need in continued innovations developing robust separation techniques for single-cell analysis.

1.3.3 Additional Challenges Posed by CTCs

Sample preparation is further complicated by substantial difficulties associated with separation of CTCs from autochthonous blood cells.[39] In fact, considerable attentions in the LOC field have been devoted to resolving the technical problems associated with profiling CTCs.[40-42] First, CTCs are present in extremely low abundance – in 1 mL of blood, there is only about 1-3000 CTCs in a background of 10^9 red blood cells (RBCs) and 10^7 white blood cells (WBCs).[43] Thus, small sample loss during processing can be disastrous to accurately score individual CTCs. This extreme rarity imposes stringent requirements in capturing pure and representative CTCs from billions of blood cells in a timely manner.

Another pitfall in sample preparation of CTCs is their extreme heterogeneity.[44] Differences among CTCs have been reported in their biological, physical and temporal properties.[39,45] These variations can be averaged in ensemble measurements but may be highly consequential in driving a behavior (e.g., invasiveness or drug resistance) in a specific cell. To address the vast variations among CTCs, variables need to be carefully chosen to accurately discern CTCs from background cells.

1.4 Existing Sorting Techniques

Current CTC sorting techniques use one or multiple of their unique biological or physical properties to discriminate them from a large number of normal blood cells, and generally can be categorized into three approaches: (1) immunological method,[46,47] in which CTCs are isolated based on their distinct expression of surface biomarkers, (2) filtration,[48]and

stream sorting,[49] which leverage differences in size or/and deformability of CTCs, and (3) dielectrophoresis (DEP),[50] which discriminates dielectric properties. Based on the need for binding of surface markers, CTC separation can also be grouped into label-dependent (approach 1), and marker-free methods (approaches 2 and 3).

1.4.1 Immunological Approaches

Immunological approaches rely on the detection of the specific biomarkers expressed on CTCs. Epithelial markers, for example, are exclusively expressed on normal epithelial cells and in tumors derived from these tissues, thus being commonly used for the selection of CTCs from surrounding normal blood cells. Epithelial cell adhesion molecule (EpCAM)[51] – a protein marker expressed on the surface of cells with epithelial origin, is the most frequently used cell surface marker in CTC separation.[47,52,53] The key step of this immunoaffinity method is to maximize the interactions between cells and the surface-coated ligands/molecules. In fact, when an antibody is immobilized on a surface, the dissociation constant of the antibody bound to antigen increases by about 1000-fold (from 10^{-10} – 10^{-9} mol/L to ~10^{-7} mol/L),[54] due to the denaturation of protein and steric hindrance.[55] Further complicating the separation performance is non-specific capture, which leads to a trade-off between flow rate and affinity. In other words, the flow rate needs to be moderate to achieve high capture efficiency of target cells, whereas it must be fast enough to minimize attachment of irrelevant species to the capture surface. All these factors (e.g., denaturation of protein, steric hindrance and non-specific capture) must be considered in designing a robust LOC device for antibody-based sorting of CTCs.

In recent years, many microfluidic designs have been reported in the literature in an attempt to address the aforementioned needs. For instance, considering that protein

denaturation during immobilization is mainly attributed to biofouling, pretreatment of microfluidic surface using a hydrophilic material can be applied. Steric hindrance can be improved *via* surface chemistry including avidin-biotin antibody conjunction[56,57] and modification of dextran.[58] Significantly, a variety of three-dimensional (3D) surfaces have been developed to increase protein deposition and antibody-antigen interactions. Examples include the fabrication of microposts,[59] halloysite nanotubes[60] and silicon nanopillars[61] as substrate for the enhancement of local topographic interactions. Notably, the CTC-chip with antibody-coated microposts showed 10^6-fold enrichment of CTCs against leukocytes – two orders of magnitude higher than most existing technologies.[59]

Table 1.1. Summary of immunological approaches for the enrichment of CTCs.

Enrichment Method	Key in design	Reported Work	Advantages	Disadvantages
Immunological Approaches	Maximize the interactions between cells and antibodies	3D surfaces such as microposts (CTC-chip),[59] halloysite nanotubes[60] and silicon-nanopillars (SiNP)[60]	Easy-to-array High-throughput	Biomarkers on CTCs vary dramatically
	Minimize the non-specific interactions	Fluid mixings *via* grooved surfaces (HB-chip),[62] fluid-permeable surfaces,[63] and AC-EOF[64,65]		Cell detachment may damage cells

Another phenomenal advance is the use of the herringbone (HB) chip.[62] Microvortices are generated when a fluid passes the grooved surfaces,[66,67] leading to a significant increase in interactions between target CTCs and the antibody-coated chip. This passive mixing resulted in a 92% recovery rate in spiked cell samples, while only ~60% was achieved in the CTC-chip, which lacked the herringbone pattern. In parallel with the HB chip, researchers also developed fluid-permeable surfaces in which diverted streamlines were generated across the device top to bottom to facilitate cell rolling and arrest on the antibody-functionalized surface.[63] The

resultant cell rolling enabled 20-fold increase of flow rate applied, leading to a significant improvement in throughput. Similarly, AC electroosmotic flow (AC-EOF) could be employed to increase the cell-antibody collisions.[64,65] When an AC electric field is applied to a pair of asymmetric electrodes, the free charges accumulated on the larger electrode create stronger lateral forces than those on the smaller electrode, leading to a lateral flow toward the larger electrode.[68] This 'nano-shearing' effect improves analyte transport and interaction, and is tunable by the externally applied AC field. Notably, the shear force not only improves capture efficiency, but also reduces nonspecific adsorptions of blood cells.[64] The strategies demonstrated in immunological approaches provide useful paradigms for further studies centering upon CTC isolation and detection.

Despite these technical advances, a major limitation for antibody-based purification methods is that the amount of protein biomarkers expressed on CTCs varies considerably and also depends on the tumor type.[69] Metastasis relates to the epithelial to mesenchymal transition (EMT), which in turn may cause down-regulation or up-regulation of specific tumor markers.[2] EpCAM, for example, is reported to be dramatically down-regulated when CTCs undergo EMT.[70] Consequently, the use of anti-EpCAM for enrichment of CTCs can result in false-negative findings. In fact, it is reported that $EpCAM^{low}$ or $EpCAM^{-}$ CTCs were detected in the discarded samples by EpCAM based enrichment.[71] Further, the absence of EpCAM on circulating melanoma cells and other non-epithelial cancers necessitates applying additional or a cocktail of biomarkers [65,72] or negative depletion of normal cells in purification,[73] which greatly complicates sample processing. Together with the potential issue associated with cell alteration during detachment by trypsinization,[74] the development of versatile techniques for marker-free selection of CTCs becomes imperative.

1.4.2 Size-Based Approaches

Of various marker-free separation methods reported,[75] selection of CTCs by size or/and deformability have been widely developed over the last decades. CTCs are generally larger and more deformable than normal blood cells,[76] and therefore can be differentiated when passing a filter or a streamline. Correspondingly, the size-based separation can be classified into size-based filtration and streamline sorting.

Size-based filtration relies on the manipulation of flow rate and cross-sectional opening of filter microstructures. When cells pass a filter (e.g., weirs,[77] pillars,[78,79] and pores[80]), the fluid flow controls the magnitude of the force applied to deform a cell to pull it through the constriction, while the filter opening determines which size and shape of the deformed cell can be retained. For example, the Ma group developed funnel ratchets to isolate cells that differ in size and deformability.[78] Cells were first infused horizontally below the first row of funnels, followed by sorting using an oscillatory flow in the vertical direction. In other words, during forward flow, only smaller and more deformable cells squeeze through funnel constrictions, while when applying a reversed flow, those smaller cells could not pass back, resulting in isolation from larger cells (i.e., CTCs). The key advantage of this ratcheting approach is the prevention of clogging – a major concern presented in traditional filtration systems.[80] Another interesting size-based filtration approach is the positive selection of CTCs by arrays of crescent-shaped wells.[79] Each individual well has three pillars with 5 μm in between for capture of CTCs, while smaller and more deformable WBCs passed through and were removed. Considering that recovery of captured CTCs from filters may cause significant sample loss, Zheng et al. integrated electrodes with parylene membrane pores, such that cell lysis and analysis could be directly performed once CTCs were captured.[80] Although the various

filtration methods provide a convenient tool for enrichment of CTCs, the issue associated with filter saturation highlights the need of developing size-based separation that allow continuous sorting of cells.

Table 1.2. Summary of size-based approaches for the enrichment of CTCs.

Enrichment Method	Key Design Feature	Reported Work	Advantages	Disadvantages
Filtration	Prevention of clogging	Weirs,[77] funnel ratchets,[78] crescent-shaped wells[79]	Easy-to-array High-throughput Easy-to-operate	Use of deformity may cause potential cell damage Filter saturation The size of CTCs varies dramatically
	Integration of downstream analysis	Membrane microfilter device[80]		
Streamline sorting	Effect of inertial forces	DLD,[81,82] Pinched Flow Fractionation (PFF),[49] DFF[83,84]		

Size-based streamline sorting or hydrodynamic chromatography addresses the need for high-throughput isolation of cells of interest. The key step is to control fluid forces exerted on cells in such a way that cells with different sizes are focused into distinct streamlines. Since cells do not pass through any physical constrictions, potential damage caused by shear force can also be reduced. The manipulation of fluid forces can be conducted in two schemes: (1) low Reynolds number ($Re \ll 1$) regime, in which inertial forces are ignored, and (2) *Re* on the order of 1 where inertial forces play a crucial role in cell discrimination.[85] Of many low *Re* modules, the deterministic lateral displacement (DLD) method has been widely evaluated.[81,82,86] In DLD, two or more fluid streams do not mix as they pass through a channel. When the channel is embedded with a defined obstacle matrix, small particles follow the fluid flow but large particles are displaced and move along a different trajectory than the bulk fluid, allowing separation and collection at different outputs. The geometry of the obstacles governs the separation performance, and if the design is optimized, as for a reported triangular micropost array, isolation efficiencies of up to 99% for MCF-7 and 80% for MDA-MB-231

cells could be achieved.[82] Nevertheless, the requirement for high resolution in fabrication such as preparation of microposts with a tilted angle of 3.8°,[82] may limit its widespread application. Further, the output CTC fraction is highly diluted, to a greater extent than in the input blood sample, and therefore requires significant enrichment prior to downstream analysis of the cells. Consequently, simplification of device design and coupling to enrichment modules while retaining high throughput capability is needed in hydrodynamic chromatography.

Dean flow fractionation (DFF) enables the use of simple spiral microchannels for continuous particle separation.[83] DFF is operated in the regime where inertial forces are dominant in cell movement. In curved channels, a mismatch in velocity across the channel develops secondary cross-sectional flows – dean flows, which lead cells to experience an additional drag force that is orthogonal to the direction of the primary flow.[87] Under the influence of Dean drag forces (F_D), smaller cells migrate towards the outer wall, while larger cells focus along the inner wall of microchannels, leading to the formation of two distinct cell streams that can be collected at two separate outputs. Using DFF, processing 3 mL of whole blood in an hour was achieved.[84] Besides the extreme high throughput, the large channel dimensions (e.g., 500 μm (w) × 160 μm (h) × ~10 cm (l))[84] prevent cell clogging and are simple to fabricate. Further, since separation and retrieval of isolated cells are simultaneous, potential sample loss during transfer to a secondary device for subsequent characterization can be eliminated. Notably, the overall processing is simple, rapid and only requires syringe pumps to operate, which offers a robust potential platform for processing of large clinical sample volumes in a point-of-care setting.

Despite the success achieved in size-based sorting techniques, they might not be optimal for purification of CTCs. A major concern is that CTCs tend to be larger than WBCs

(12 – 15 μm), but the size can vary from 4 – 30 μm in diameter, even in cell samples from a single patient.[51] Consequently, hydrodynamic chromatography, though high throughput, may yield inadequate performance in CTC recovery from most cancer patients. Filtration allows the additional discrimination of nucleated cells *via* deformability, yet the selection of a size cutoff may easily exclude subpopulations that are critical in identifying metastasis. Within this context, the development of an alternative separation method that allows continuous sorting while conferring a higher degree of selectivity would be more relevant to CTC isolation.

1.4.3 DEP-Based Approaches

Dielectrophoresis (DEP)[88] distinguishes cells based on their size and dielectric properties. The resultant DEP force permits the attraction or repulsion of cells of interest by an external electric field. Thus, isolation by DEP does not require a labeling process. In addition, continuous sorting is readily achievable by integration of electrodes with microchannels in one device. Of particular importance, the dielectric properties that arise from the composition and morphology of cells provide a much more specific differentiator of phenotype than size alone while not being as overly selective as biomarkers such as EpCAM. Thus, collection of a pure and representative sample of CTCs can be achieved. A wide range of applications hitherto bears testimony to the robustness of DEP in that it is label-free, highly selective and effective for characterization of CTCs.[88-90]

The work presented in this document centers on the employment of DEP as a tool for highly selective marker-free isolation and detection of circulating breast tumor cells. Thus, a brief overview of DEP including the methodology, advancements of DEP techniques and associated challenges will be discussed in detail in the following section.

1.5 DEP For Highly Selective Marker-Free Selection and Detection

1.5.1 Fundamentals

1.5.1.1 What is DEP

DEP[88] is a field-induced force (F_{DEP}) exerted on a particle due to the interaction of the particle's dipole moment (P) with the spatial gradient of the electric field (∇E). As shown in **Figure 1.3**, when particles are placed in an external electric field (E), the electric field induces partial charges (δ_+ and δ_-) at the particle-medium interfaces *via* a process known as Maxwell-Wagner (MW) interfacial polarization.[91] When the external electric field is non-uniform (**Figure 1.3b**), the field gradient (∇E) results in each half of the dipole experiencing a different magnitude of electrostatic force, thereby leading to movement of the particle. In a linearly polarized sinusoidal field, the time-averaged DEP force (F_{DEP}) of a homogeneous spherical particle is given by:

$$\overrightarrow{F_{DEP}} = 2\pi r^3 \varepsilon_m Re[K(\omega)]\vec{\nabla}\left|\vec{E}\right|^2 \quad (1)$$

where Re[$K(\omega)$] is the real part of the Clausius-Mossotti (CM) factor,

$$K(\omega) = \frac{\varepsilon_p^* - \varepsilon_m^*}{\varepsilon_p^* + 2\varepsilon_m^*} \quad (2)$$

and for which r is the particle radius; ε_m is the permittivity of the medium; and ε_p^* and ε_m^* are the frequency-dependent complex permittivities of the particle and medium, respectively. Re[$K(\omega)$], which falls within a range of -0.5 to +1.0, indicates the direction and relative strength of F_{DEP} experienced by the particle. When Re[$K(\omega)$] is negative, the case when the particle is relatively less polarizable than the medium, the net F_{DEP} directs the particle in the direction of decreasing electric field strength (negative DEP, or nDEP). Accordingly, a positive value of Re[$K(\omega)$] indicates particle displacement toward higher electric field (positive DEP

or pDEP). Consequently, particles with distinct Re[$K(\omega)$] values (CM factors) are separated or transported towards pre-defined locations. Due to the high correlation of DEP response to the electrophysiological properties of cells,[92] DEP has been broadly employed in microfluidic applications in particle differentiation,[93] biopatterning,[94] and transport of selected particles to specific locations where additional processes can occur.[95]

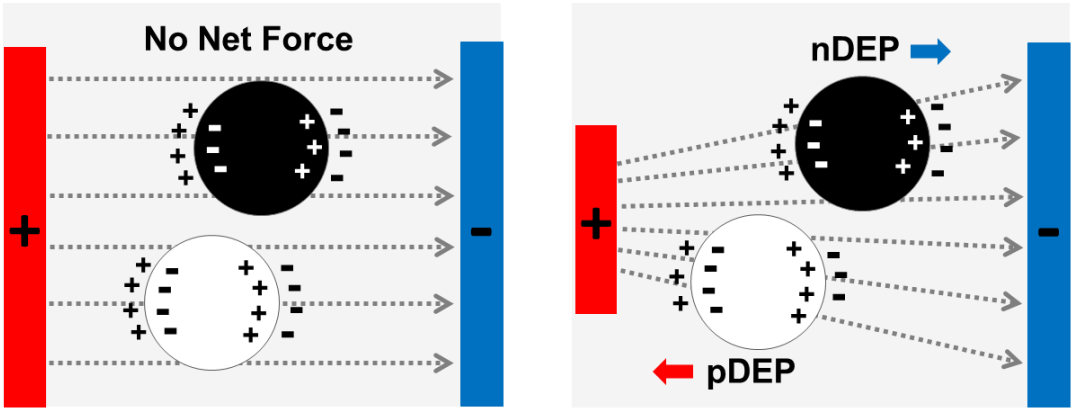

Figure 1.3. Illustration of the response of polarized particles in a uniform electric field (left) and in a non-uniform electric field (right).

1.5.1.2 Crossover Frequency

It is worth mentioning again that F_{DEP} arises from the MW polarization of dielectrics in response to an external electric field. Experimentally, the relationship between the observed DEP response and the applied electric field is regulated through the complex permittivity shown in Eq. (2) and it is defined as

$$\varepsilon^* = \varepsilon - \frac{i\sigma}{\omega} \tag{3}$$

where ε and σ are the real permittivity and conductivity of a subject (particle/medium), $i = \sqrt{-1}$ and ω is the radial frequency applied. As indicated in Eq. (3), the electrical conductivity is dominant for low-frequency polarization ($\omega \to 0, \varepsilon^* \approx -\frac{i\sigma}{\omega}$), whereas at high frequency, the polarization is dictated by permittivity ($\omega \to \infty, \varepsilon^* \approx \varepsilon$). Notably, for a specific particle-

medium system, change of frequency may lead to different ε_p^* and ε_m^* values, which in turn gives rise to different signs or magnitude of CM (Re[$K(\omega)$]). In fact, this frequency-dependent response is the key in DEP applications.

Among all the frequencies investigated, of particular importance is the crossover frequency (*cof*), in which CM equals zero and DEP response undergoes a reversal. The *cof* reflects the electrophysiological properties of biological particles, thus proving a useful tool in characterization and detection. Importantly, once *cof* is experimentally determined for two types of cell populations, isolation of cells of interest becomes feasible. For example, in neuronal physiology, 100 kHz was employed to discriminate astrocyte-biased and neuron-biased neural stem and progenitor cells (NSPCs).[92] The success in separation of NSPCs is the first step towards understanding the mechanisms that govern their fate, thereby improving the effectiveness of NSPC therapeutics. Another example is in oncology – the *cof* from nDEP to pDEP for Jurkat E6-1 T cells (a model WBC) is reported to be at the range of 110 – 190 kHz in a medium conductivity of 40 mS/m.[96] In contrast, breast CTCs exhibit pDEP at frequencies of 45 – 85 kHz in a similarly conductive medium.[97] Their distinct DEP responses for CTCs and WBCs make it possible to enrich rare CTCs from a high background of blood cells.

1.5.1.3 Effect of Medium on DEP Response

The key step in DEP sorting is to achieve pDEP and nDEP responses for two distinct cell populations. In particular, obtaining a pDEP response for targeted cells (e.g., CTCs) is the most frequently used strategy. Since the polarization dynamics of a cell are governed by the interaction of the particle with the surrounding medium, we first consider the effect of medium on DEP response.

Figure 1.4 is a plot depicting the CM factor of a mammalian cell versus electric field frequency and as a function of the medium conductivity. Clearly, the medium conductivity has a significant impact on the CM factor. In the case of a 0.1 S/m solution, the DEP response can be categorized into three stages[98,99]: (i) At low frequencies (≲100 kHz), the dominance of conductive polarization results in extensive capacitive charging of the cell membrane, thereby producing a 'shielding field' that opposes the external electric field. (ii) At intermediate frequencies (∼1 – 100 MHz), the electric field penetrates the cell membrane and into cytoplasm. Since the conductivity of the cytoplasm is higher than that of the medium in this case, the CM factor changes sign and the cell exhibits pDEP. (iii) When the applied frequency exceeds the inverse MW timescale of the membrane-cytoplasm interface (≳ 0.5 GHz), conductive polarization does not have time to occur, and the polarization is driven by permittivity differences of the cytoplasm and the medium. Thus, nDEP takes place if the cytoplasm permittivity is lower than that of the medium, leading to a second *cof*.

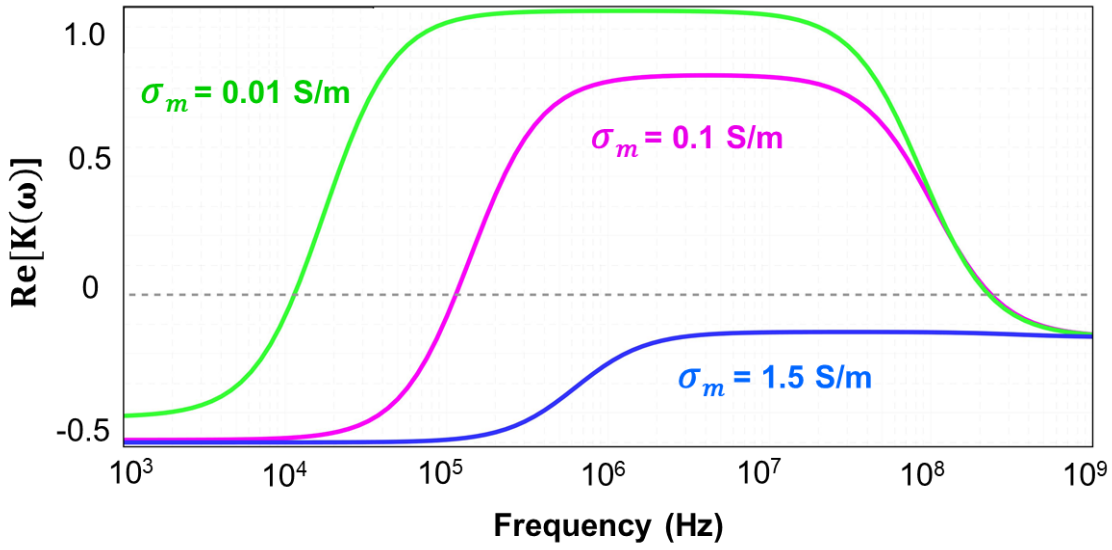

Figure 1.4. Effect of the real part of the CM factor (Re[$K(\omega)$]) of a mammalian cell as a function of frequency when changing the conductivity of the medium. Cell electrical properties are chosen from the literature[100,101] to represent MDA-MB-231 cells. The simulation used single-shell model and was done *via* MyDEP computational tool.[102]

In contrast to the 0.1 S/m solution, higher solution conductivity alters the stage (ii) and results in a dramatic increase of the first *cof*. When a medium reaches as high as 1.5 S/m, nDEP occurs across the entire frequency range.[98] Thus, in DEP processing of blood samples, the replacement of blood plasma with a low conductivity solution is entailed. The most commonly used medium consists of 8.0% sucrose and 0.3% dextrose to balance osmotic pressure, and 0.1% bovine serum albumin (BSA) to prevent non-specific absorption.

1.5.1.4 Effect of Cell Membrane on DEP Response

As mentioned above, the ability to discriminate cell types based on their dielectric properties is the key in DEP separation. Thus, in this section, the effects of cellular dielectric properties on the DEP responses are investigated. In all cases, medium conductivity with 0.1 S/m is chosen as it is most frequently used in experiments.

Figure 1.5 shows the result of a simulation of Re[$K(\omega)$] as a function of frequency obtained at several distinct values of the membrane conductivity and permittivity. As the cell membrane (**Figure 1.6a**) is largely comprised of lipids and proteins, its conductivity is extremely low (~ 10^{-6} – 10^{-7} S/m) and the relative permittivity is less than pure water (~ 3 – 20 ε_o). As shown in **Figure 1.5a**, the membrane conductivity has a great influence on the first *cof*. When the membrane conductivity increases to the order of 10^{-5} S/m (not realistic in a normal physiological system but possible during electroporation), cells only exhibit the second *cof*. Separately, variations in the membrane permittivity shift the first *cof* position. Notably, cells with larger membrane permittivity – accordingly larger membrane capacitance ($C \propto \varepsilon$), exhibit a first *cof* occurring at a lower frequency (**Figure 1.5b**). Indeed, the disparity of the membrane capacitance among cell types is reported to be the major cause for observed differences in DEP response.[92] As depicted in **Figure 1.6**, the cell membrane can be treated as a capacitor with a

resistor. Based on biophysical theory, capacitance increases when increasing the surface area ($C \propto A$), which physiologically, is achieved by the cellular process called glycosylation. It is reported that large glycoproteins are abundantly expressed on CTCs.[103] This upregulated expression of bulky glycoproteins is believed to foster metastasis by mechanically enhancing cell-surface receptor function. As a result, metastatic tumors exhibit higher membrane capacitance, shifting the first *cof* to a lower frequency, which makes it possible to choose a separation frequency (represented by the pink dashed line, **Figure 1.5**) where CTCs exhibit pDEP, while normal blood cells experience nDEP.

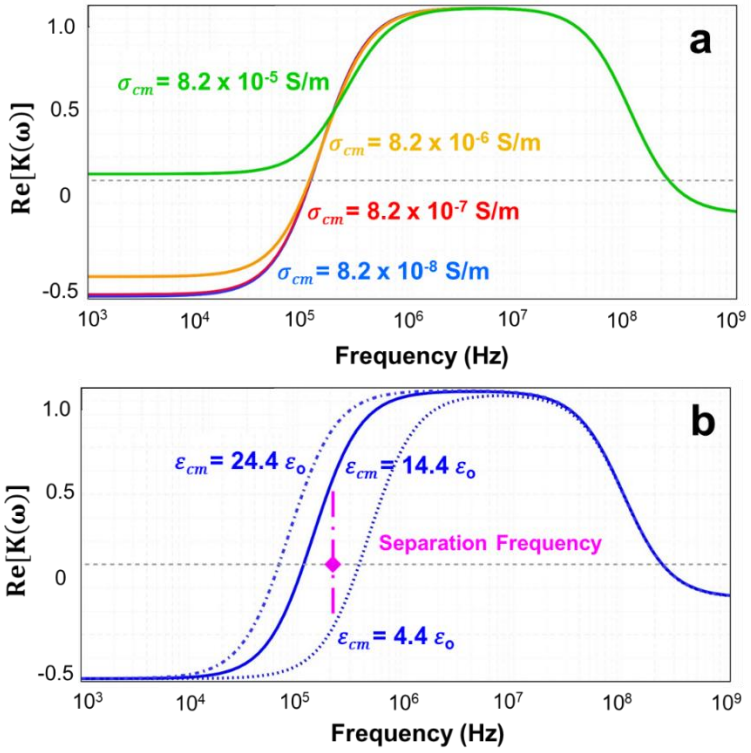

Figure 1.5. Spectrum of Re[$K(\omega)$] versus frequency when changing the membrane conductivity (a), and the membrane permittivity (b). The initial value of the membrane conductivity (8.2 x 10^{-7} S/m) and the membrane permittivity (14.4 ε_o) were derived from the membrane conductance and resistance by assuming the membrane thickness is 8 nm. Considering that metastatic tumors exhibit higher membrane capacitance (hence, higher membrane permittivity), due to the upregulated expression of glycoproteins,[103] the separation frequency is concluded assuming the spectrum with 14.4 ε_o and 4.4 ε_o represent the response of CTCs and normal blood cells, respectively. The simulation used a single-shell model and was accomplished using the MyDEP computational tool.

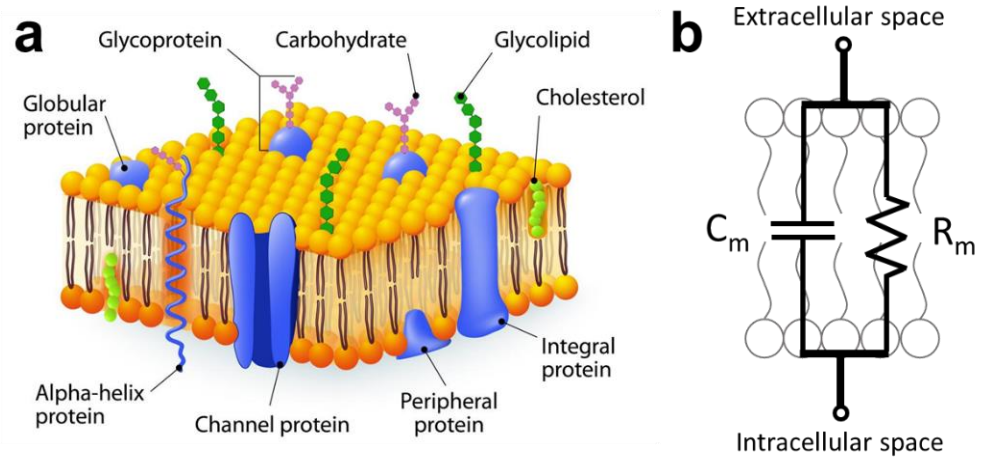

Figure 1.6. (a) The schematic depiction of a cell membrane. Image is reproduced from BiologyWise.[104] (b) The equivalent electric circuit of the cell membrane.

1.5.1.5 Effect of Cell Cytoplasm on DEP Response

The cytoplasm of a cell consists of over 75% water. The presence of ions and charged molecules results in a relatively conductive microenvironment (~ 0.1 – 1.0 S/m). Likewise, proteins and other substances inside make the relative permittivity (~ 60 ε_o) slightly lower than that of water (~ 80 ε_o). **Figure 1.7** shows the simulated Re[$K(\omega)$] as a function of frequency and over a range of values of the cytoplasm conductivity and permittivity. Clearly, the cytoplasm conductivity has a dramatic impact on the location of the second *cof*. This effect arises from the fact that over this frequency range, the electric field penetrates the cell membrane, and the conductivity of the cytoplasm dominates charging. However, this conductive polarization will not have time to occur when further increasing frequency beyond ~ 0.5 GHz, where permittivity differences of the cytoplasm and the medium govern DEP response. This loss in the dominance of conductive charging occurs at lower frequencies for a less conductive cytoplasm. Experimentally, the modification of cytoplasm conductivity and permittivity can be performed *via* transport of ions or molecules.

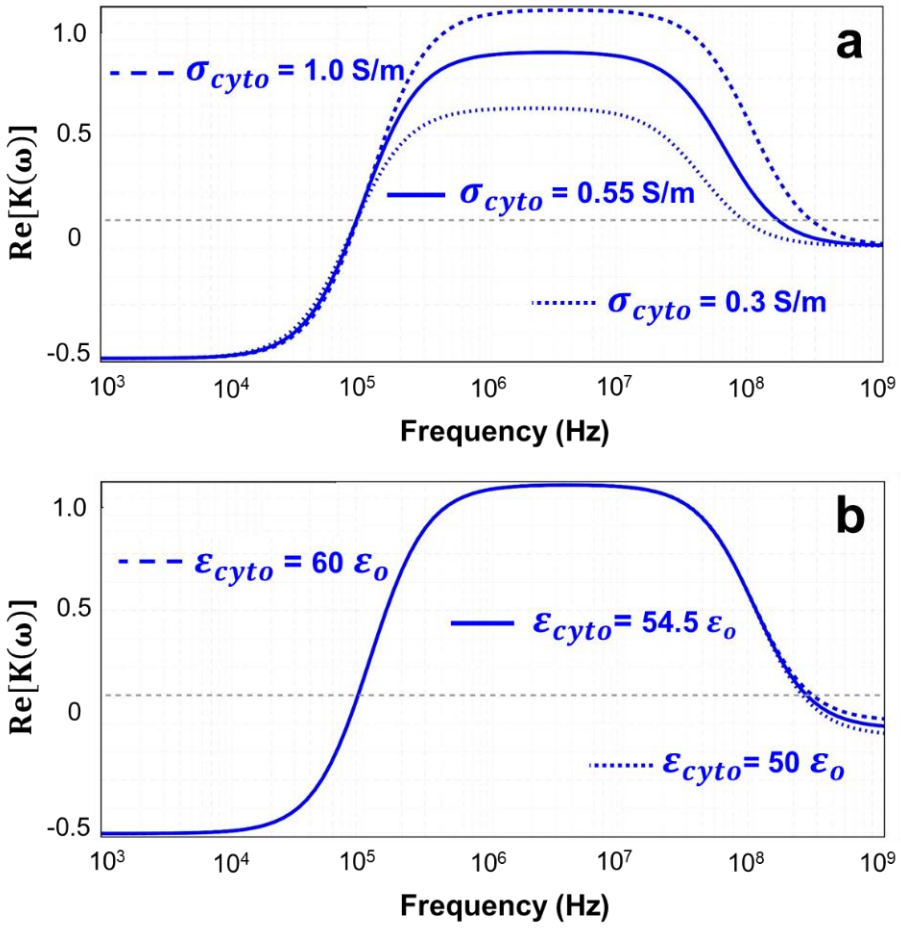

Figure 1.7. Simulation results of the Re[$K(\omega)$] versus frequency when varying the cytoplasm conductivity (a), and the membrane permittivity (b). The simulation used a single-shell model and was carried out with the MyDEP computational tool.

1.5.1.6 Effect of Cell Diameter on DEP Response

The influence of cell radius on the CM factor is shown in **Figure 1.8**. Clearly, the cell size is very sensitive to the first *cof* as it impacts the membrane conductance and capacitance. In particular, an increase of the cell size results in a shift of the first *cof* to a lower frequency. This shift reinforces the fact that the presence of the cell membrane is very crucial for the polarization of a cell at low frequency. Overall, the high correlation between cell composition and morphology and CM factor, as summarized in **Table 1.3**, demonstrates the robustness of DEP for separation of biological cells.

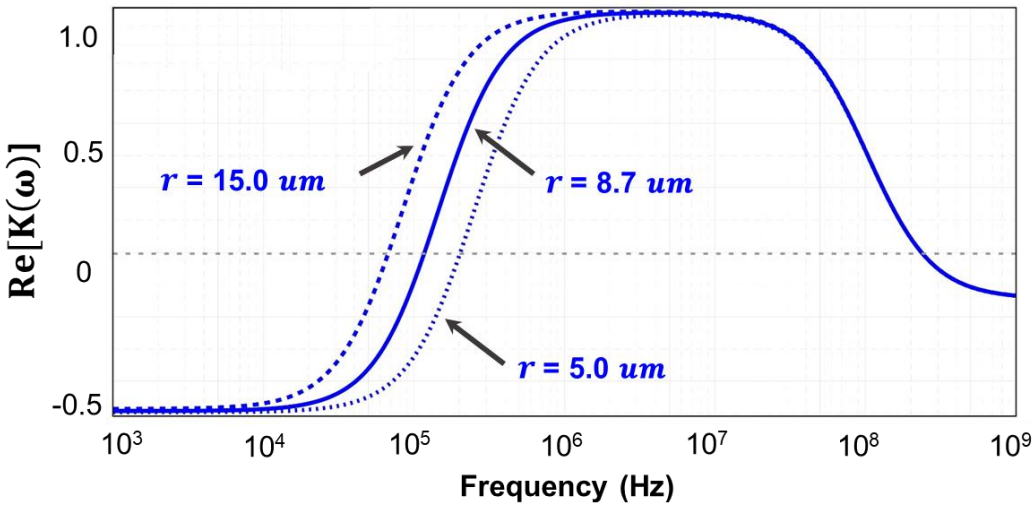

Figure 1.8. Simulation results of the Re[$K(\omega)$] versus frequency when varying the cell radius. The simulation used a single-shell model and was carried out with the MyDEP computational tool.

Table 1.3. Relative sensitivities of the DEP cof to changes of medium and cell parameters.

Parameter	Sensitivity	
	1st *cof*	2nd *cof*
Medium	High	Moderate
Cell diameter	High	None
Membrane conductivity	High	None
Membrane permittivity	High	None
Cytoplasm conductivity	None	High
Cytoplasm permittivity	None	High

1.5.2 Categories of DEP Detection Techniques

The advent of microfabrication technologies has opened up immense opportunities in DEP detection techniques.[105] Particularly, microelectrodes enable DEP trapping and transport of few or single cells, and microchannel architectures (e.g., chambers and wells) permit cell isolation for subsequent analysis. Further, extension to parallel manipulation of cells can be achieved with arrays of electrodes. A key component in the development of effective DEP detection methods is to design patterns of electric field gradient, in which cell movements can

be precisely controlled. Depending on the means by which the electric field gradients are generated, DEP separation techniques can be classified as classical or electrode-based DEP (eDEP), insulator DEP (iDEP), contactless DEP (cDEP), and optically induced DEP (oDEP) or optoelectronic tweezers (OET).

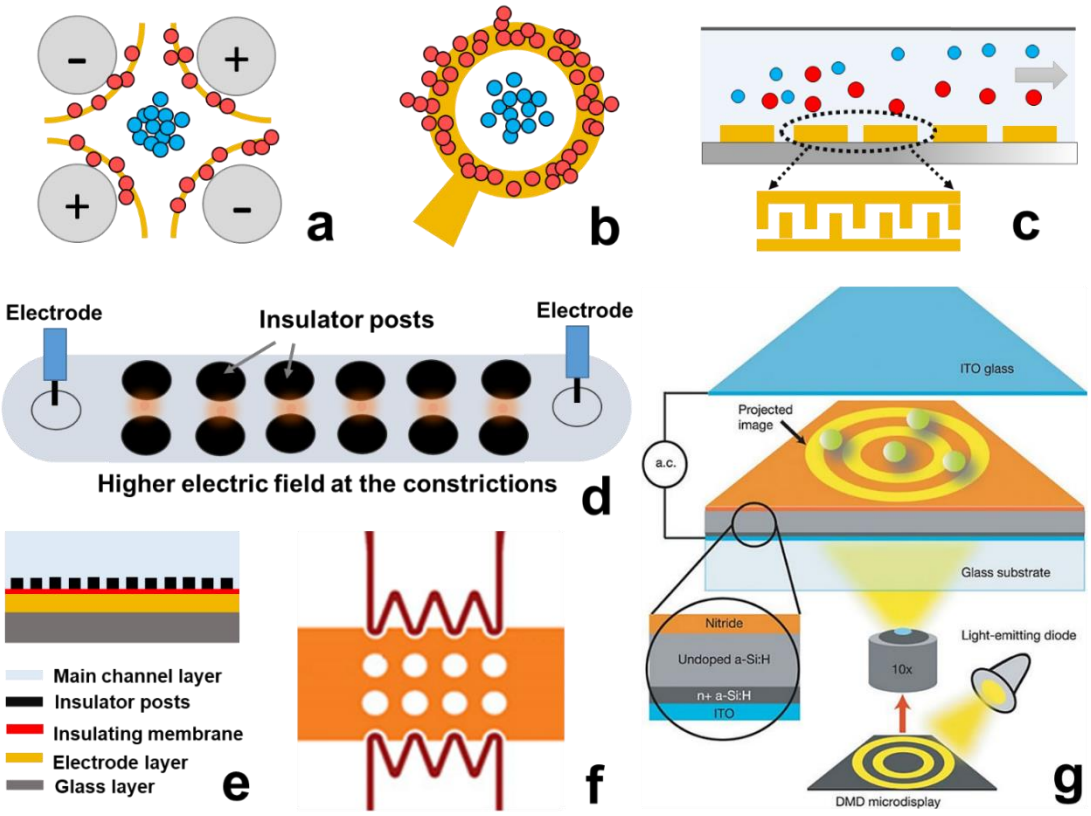

Figure 1.8. Designs of DEP detection techniques. Particles undergoing pDEP and nDEP are represented as orange and blue circles, respectively. (a) Quadrupole electrodes. (b) nDEP wells. In both designs, nDEP cells are accumulated in the center, whereas particles experiencing pDEP are attracted to electrode edges. (c) DEP field-flow fractionation (DEP-FFF) that uses interdigitated electrodes to generate the electric field. (d) iDEP in which insulator posts are employed to distort the electric field. (e) Incorporation of a thin layer membrane into design (d) to protect cells. (f) Use of liquid electrodes (red) at the side of channel walls in cDEP. Reprinted by permission from [**Wiley**]: [**Electrophoresis**] [106], (2011). (g) Schematic illustration of OET. Reprinted by permission from [**Springer Nature**]: [**Nature**] [107], (2005).

eDEP employs metal electrodes such as gold or indium tin oxide (ITO) to generate a non-uniform electric field. The field density exhibits peaks at electrode edges and dramatically

decays with distance. Over the past few decades, a variety of electrode configurations [97,108,109] have been described, indicating the versatility of eDEP in cell manipulation (**Figure 1.8a-c**). However, metal electrodes are likely to suffer from biofouling and electrolysis, which may result in electrode deactivation or dissolution. In addition, the gas bubbles generated *via* electrolysis may cause undesired change of solution composition (e.g. pH, ions) and flow rate, resulting in cell damage or chaos of cell movement. Therefore, pretreatment of metal surfaces and avoiding use of high DC need to be considered in eDEP.

In iDEP,[110] insulating microstructures (e.g., pillars or hurdles), are embedded in microchannels in such a way that the applied uniform electric field (AC or DC) can be distorted to trap or repel cells of interest (**Figure 1.8d**). A key advantage of iDEP is high-throughput sorting since microposts cross the entire channel depth, thus massive post arrays can generate localized electric field gradients across the entire chip. However, due to the long distance between driving electrodes (~10 mm), iDEP often necessitates a high voltage source that supplies on the order of kilovolts (kV).[111] The requirement for high voltage can be mitigated by repositioning the electrodes to lie in the plane above and below the post array. However, electroporation of cells may occur if they come in contact with these electrodes, especially in the case of pDEP where cells dwell at high electric field. Within this context, cDEP has been developed to address the challenges encountered in iDEP.

An important improvement in cDEP is the use of a thin insulting membrane (e.g., PDMS) that is sandwiched between the electrodes layer and the layer containing both the insulator posts and cell suspension (**Figure 1.8e**).[112] The thin membrane permits the electric field, while protecting captured cells from being directly exposed to high electric field. Using such a device, it was demonstrated that cell-size micropillars (20 μm) render cells to be trapped

individually.[112] A caveat of this approach is that the addition of the membrane further increases the voltage applied to achieve sufficient DEP force for trapping, thus limiting its widespread application. Separately, the Davalos group developed an alternative cDEP in which electrodes are placed at the channel side walls with pillars located at the center of microchannels (**Figure 1.8f**).[106] This electrode configuration dramatically decreases the gap between two driving electrodes (< 1 mm), allowing a much lower voltage, commonly at the order of tens to hundreds of volts, to be utilized. The inclusion of electrodes in side walls is achieved with 'liquid electrodes' comprised of high-conductivity solution such as phosphate-buffered saline (PBS)[106] or ionic liquid.[113] Notably, both of these strategies, which detach driving electrodes from the inlet and outlet reservoirs, confer the dual advantages of high-throughput sorting and prevention of potential cell damage.

oDEP or OET [114] incorporates a photo-conductive substrate that can be 'activated' as 'virtual electrodes' by light to induce a non-uniform electric field (**Figure 1.8g**). The distinct feature of this OET is the capability of processing a large group of individual biological particles. For example, P. Y. Chiou et al. have demonstrated parallel manipulation of 15,000 particle traps on a 1.3 x 1.0 mm^2 footprint.[107] In addition, the optical intensity needed is 100,000 times less than that used in optical tweezers, thus permitting high viability of cells.[114] In recent years, a variety of photo-generated carriers (e.g., amorphous silicon,[107] titanium oxide phthalocyanine[115] and carbon nanotubes[37]) have been reported to enhance the versatility of OET in cell manipulation. Accordingly, OET is believed to be a critical advance in applying DEP techniques to cellular characterizations.

In conclusion, the past decade has yielded significant advances in the development of various DEP techniques in preparation of biological samples. Once a specific DEP technique

is chosen, tailored patterns of microelectrodes and microchannels are of high importance for single-cell analysis. Therefore, a brief discussion of reported DEP designs will be given in the next section.

1.5.3 Advances and Challenges

In an effort to accomplish single-cell analysis, separation and individual trapping of cells of interest (e.g., CTCs) is the first inevitable step. Cell-scale pillars[112] and microwells[116] are thus designed to address this need. Another critical feature is the ability to process a large amount of cell suspension. This high-throughput capability is of great value in handling of low-abundance CTCs. However, DEP-based separation techniques often suffer from low volumetric throughput (0.01 to 1.0 mL/hr) due to the short range of DEP force (tens of microns) and design constraints such as the requirement that all electrodes must be connected *via* wire leads to the power source. Thus, numerous efforts have been made in device architecture and materials to increase DEP sorting throughput. Examples include the development of continuous flow approaches, extension of planar electrodes to 3D electrodes, and prefocusing or preenrichment of cell solutions. Detailed examples will be discussed in the section entitled 'Advances of DEP Strategies in Separation' in Chapter 3.

Once separation is achieved, the next crucial step is to isolate the captured cells in microstructures, exchange solution with analytical reagents and seal each individual compartment prior to analysis. However, many DEP strategies lack the features needed for 'on-chip' analysis, thereby requiring the transport of captured cells into a secondary device to perform 'off-chip' analysis. This single-cell selection and subsequent transfer have been automated in the DEPArray™ system.[117] In DEPArray™, an array of individually-addressable square microelectrodes are employed to generate DEP cages at electrodes having a frequency

in phase with that of a single electrode overlying the array. Under electric field control, a single cell can reside in the center of a cage. Pre-labeled cells are fluorescently imaged to identify cells of interest, which are then transported cage-to-cage and finally parked into a holding chamber for recovery. The DEPArray™ system enables processing of tens of thousands of cells, and maintains cell viability for downstream analysis. However, there are two distinct limitations to this approach. First, as described previously in immunological approaches, is that the selectivity achieved by labeling cells, especially for CTCs, may not be precise enough to obtain all subpopulations of interest. Second, the throughput is too low for many applications. These factors especially limit the application of the DEPArray™ in rare cell detection.

Integration of all steps needed for analysis into one flow system allows sample profiling to be performed directly on chip, thus avoiding any potential sample loss during transfer. To achieve such an 'assembly line,' embedded microvalves are often required to facilitate transport and isolation of individual cells in confined microstructures.[23] For instance, Jimenez-Valdes et al. incorporated PDMS-based microvalves in arrays of 16 parallel chambers (each containing 4,460 microwells, 7 pL each) for the study of neutrophil extracellular traps (NETs).[36] The PDMS-based microvalves close channel layers that containing single cells when a pressure is applied to the valve layer to collapse the thin membrane layer in between.[118] While it is relatively easy to operate and has small dead volumes, the system requires three-layer alignment, and a large number of reagent inlets and control lines to function. Another popular microvalve is the three-state valve,[119,120] which was notably employed by the Hansen group for single-cell digital polymerase chain reaction (dPCR).[21,22] To accomplish this assay, 36 inlets and outlets are needed, and delicate control is crucial for accurate measurement.[21] These

studies have significantly advanced high-throughput screening of single cells. However, the engineering complexity of these integrated cell assays and the requisite specialized control equipment makes them less amenable to widespread use in research laboratories, clinics and point-of-care (POC) settings. Consequently, the development of valve-free systems is needed to increase accessibility to on-chip analysis of single cells.

It has been reported that microwells with embedded electrodes can leverage DEP to simultaneously identify and isolate cells, followed by sealing of wells with a PDMS layer. Thus, microvalves are eliminated. In addition, microwells enables storage of reagents for on-chip analysis.[121-123] The Fujii group initiated the use of electroactive microwells (EAMs), in which single cells are actively trapped in microwells by DEP, followed by lysis *via* electroporation (EP) for subsequent analysis of the confined cell lysates.[124] Considering that DEP is a weak force (generally, decaying over tens of microns), microwells with a high-aspect ratio (wide, shallow well) were required to permit flow laminae to carry cells close to trapping electrodes. However, a small well diameter was critical to ensure single-cell capture. Thus, EAMs were further modified to create an electroactive double-well array (EdWA) to address these issues.[125] In EdWA, the bottom "trap-well" layer has cell-sized openings for individual cell confinement, while the top "reaction-well" layer has a high aspect ratio to improve capture efficiency. Although this EdWA resulted in a capture efficiency of 96 ± 3% for single PC3 cells, the geometric constraint placed on the microwells limited the reaction volumes to only tens of pL, which is far inadequate for certain assays such as single-cell RT-qPCR.[22,126,127] Clearly, there is a need to develop an alternative design that permits the assay volume to be tuned and then to be isolated fluidically, while retaining single-cell capture and high-throughput capability.

1.6 Engineered Solution: Bipolar Electrode (BPE)

1.6.1 BPE in DC Electric Field

Before discussing the possibility of using a bipolar electrode (BPE)[128] to address the aforementioned challenges, it is important to understand the fundamentals of how a BPE operates in a DC electric field.

BPE[129] refers to a conductor that lacks ohmic contact to an external power supply (is 'wireless') and that, in the presence of a DC electric field applied by external driving electrodes can facilitate coupled faradaic reactions at its ends. Notably, in contrast to a three-electrode electrochemical cell, the electric field in solution determines the potential differences between the electrode and the solution. **Figure 1.9a** is a schematic representation of a BPE in a microfluidic channel. When a DC voltage bias is applied across the microchannel, a linear potential profile develops (**Figure 1.9b**). The potential of the BPE (U_{BPE}) floats to a value intermediate to the potential of the aqueous solution (U_{tot}) in contact with its ends. Due to the potential drop in solution, the BPE is separated into two poles: the cathodic pole, where the solution potential is higher than U_{BPE}, and the anodic pole, where the solution potential is lower than U_{BPE}. The potential differences between the two poles (ΔU_{BPE}) is the driving force to couple the two faradaic reactions (**Figure 1.9c**), and can be calculated by:

$$\Delta U_{BPE} = \frac{l_{BPE}}{l_{channel}} U_{tot} \qquad (4)$$

Where l_{BPE} and $l_{channel}$ stand for the length of BPE and the microchannel, respectively. Note that at the BPE, faradaic reactions are achieved without direct electrical contact to the BPE, and this feature allows array of BPEs to be operated in one microfluidic channel.

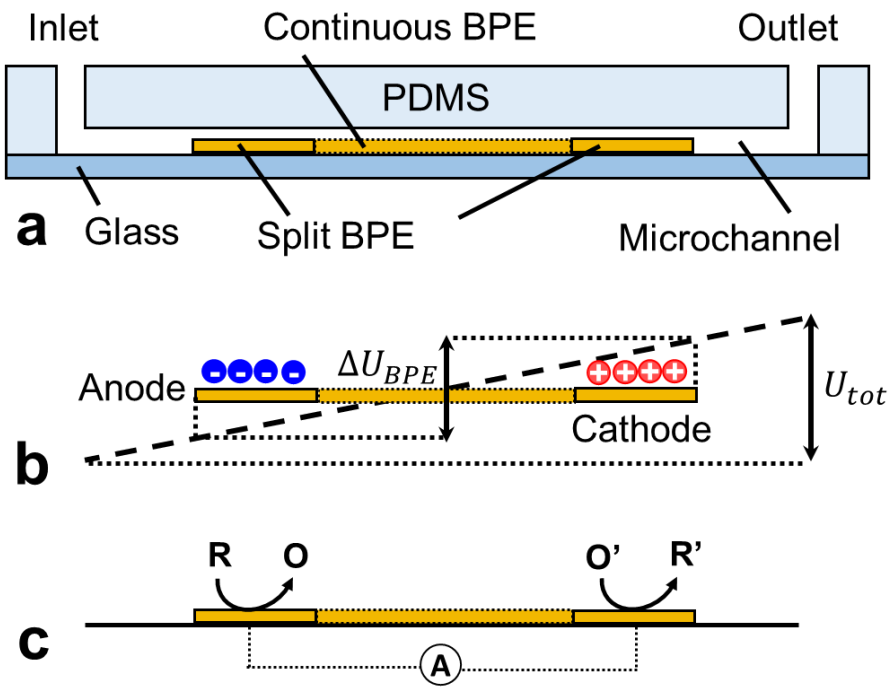

Figure 1.9. Principle of BPE operation in a DC electric field. (a) Side view schemation of the layout of a BPE in a microchannel. The BPE can be either 'split' or 'continuous' as depicted. (b) The resultant electric field profile at the BPE. (c) The associated faradaic reactions at the BPE. When 'split BPEs' are utilized, an ammeter can be connected exteriorly for *in situ* monitoring of current.

This 'wireless' technique has resulted in a broad range of electroanalytical applications such as in material preparation,[130] electrochemical sensing,[131] catalyst screening,[132,133] and electrokinetic separation and enrichment.[129] Importantly, reported works are generally based on the use of two basic BPE configurations: open and closed BPEs, depending on whether an insulator is utilized to physically separate the solution phases contacting the opposing ends of the BPE (**Figure 1.10**). As a result, the current path differs in these two BPE strategies. In a closed BPE design, the current between two half cells can only by conducted through the BPE, whereas in an open BPE system, the current path is either *via* ionic conduction in solution (i.e., through the solution resistance, R_s) or charge transfer (R_{ct}) at the BPE. Another important feature is that it is possible to connect two or more separate conductors to generate a single BPE.[134] The 'split BPE' configuration renders it possible to connect an ammeter externally so

that the current through the BPE can be measured *in situ* (**Figure 1.9**). It is this design flexibility of BPEs that has created opportunities to develop analytical strategies for sample preparation, detection, and analysis of a variety of molecules.

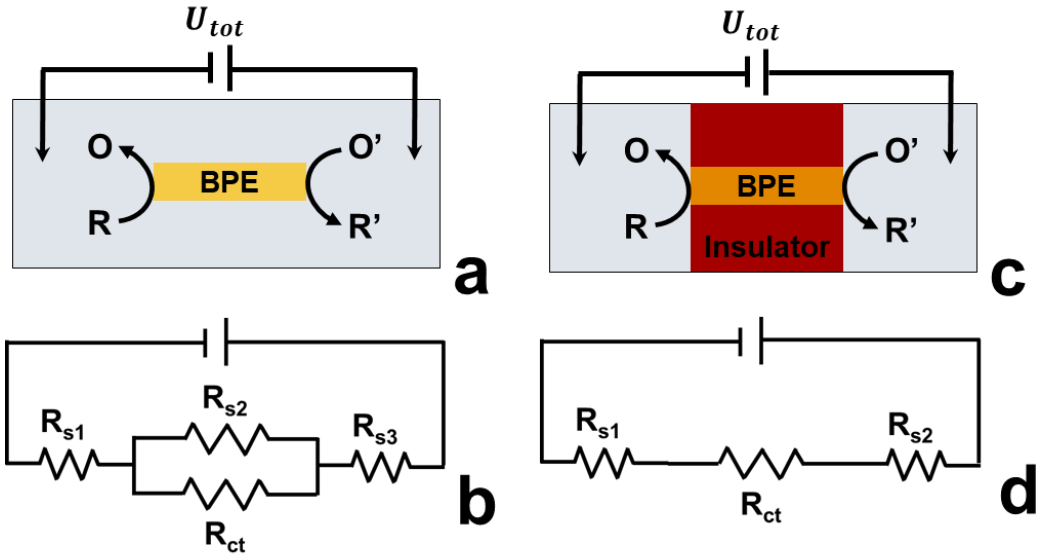

Figure 1.10. Schematic top view depiction of a BPE in a microfluidic device. Open BPE configuration (a) and the equivalent electric circuit (b). Close BPE configuration (c) and the equivalent circuit (d).

1.6.2 BPE in AC Electric Field

The utilization of BPEs permits many electrodes, in one microfluidic system, to be controlled with only two driving electrodes and a single power supply. Thus, it is possible to decouple electrodes physically to facile arraying for high-through applications. For electroanalytical applications, the prerequisite signal from a faradaic process relies on the use of a DC field to sustain charge transfer reactions. However, a DC field is not desirable for DEP for two reasons. First, faradaic reactions are not desirable for DEP applications since such reactions may damage cells and cause unexpected changes in the medium. Further, AC frequencies are required to achieve cell separation.

Note that the potential differences between the BPE and the solution drive ions to migrate, thereby forming an electrical double layer (EDL) at each end of a BPE (**Figure 1.9**). As a result, the BPE poles behave like capacitors. Now, when a BPE is placed in a DC electric field, current due to capacitive charging decays to zero. In contrast, the polarity change associated with an AC electric field leads to continuous charging-discharging, thereby 'activating' another current path through the BPE *via* capacitive charging. Consequently, it is possible to develop DEP devices to capture cells at wireless BPE arrays. This application of BPEs in an AC electric field is the core innovation of the research project. The associated theory will be discussed in details in Chapter 2, and thus is not reiterated here.

1.7 Thesis Organization

In an effort to understand tumor metastasis for developing efficacious anti-cancer therapies, MDA-MB-231 (breast adenocarcinoma) cells are chosen as model CTCs for study, and advances in techniques for the analysis of individual CTCs will be presented. The first chapter overviews literature in metastasis, single-cell analysis and associated separation approaches. The technical background of DEP is discussed in detail as it is at the center of the research project. Chapter 2 introduces the employment of BPE in DEP to achieve 'wireless' control of the AC electric field and facile arraying for high-throughput processing. Another important innovation is the incorporation of cell-scale micropockets to trap CTCs individually. Chapter 3 discusses the recent technical improvements of integrated DEP systems for 'on-chip' and 'off-chip' single-cell analysis. The microfluidic designs presented provide an insight into emerging capabilities in next-generation LOC devices. Accordingly, Chapter 4 develops an integrated DEP chip that allows marker-free selection, sequestration, lysis and analysis of individual CTCs to be performed in one microfluidic platform. Importantly, the use of a

wireless BPE array permits parallelization in processing and analysis. Chapter 5 summarizes the core advancements made in the research and their impact in both clinical and scientific fields. Finally, some remaining challenges and future potential are discussed in Chapter 6. As ion concentration polarization (ICP) is another important potential approach coupled with DEP for manipulation of biological cells, an overview of the methodology associated with the recent advances of ICP has been given in Appendix.

1.9 References

1. Dong, Y.; Skelley, A. M.; Merdek, K. D.; Sprott, K. M.; Jiang, C.; Pierceall, W. E.; Lin, J.; Stocum, M.; Carney, W. P.; Smirnov, D. A. *J. Mol. Diagn.* **2013**, *15*, 149-157.

2. Paterlini-Brechot, P.; Benali, N. L. *Cancer Lett.* **2007**, *253*, 180-204.

3. Joosse, S. A.; Gorges, T. M.; Pantel, K. *EMBO. Mol. Med.* **2015**, *7*, 1-11.

4. Liberko, M.; Kolostova, K.; Bobek, V. *Crit. Rev. Oncol. Hematol*. **2013**, *88*, 338-356.

5. Lin, E.; Cao, T.; Nagrath, S.; King, M. R. *Annu. Rev. Biomed. Eng.* **2018**, *20*, 329-352.

6. Fidler, I. J. *Nat. Rev. Cancer*. **2003**, *3*, 453-458.

7. Elowitz, M. B.; Levine, A. J.; Siggia, E. D.; Swain, P. S. *Science.* **2002**, *297*, 1183-1186.

8. Comi, T. J.; Do, T. D.; Rubakhin, S. S.; Sweedler, J. V. *J. Am. Chem. Soc.* **2017**, *139*, 3920-3929.

9. Kaern, M.; Elston, T. C.; Blake, W. J.; Collins, J. J. *Nat. Rev. Genet.* **2005**, *6*, 451-464.

10. Brock, A.; Chang, H.; Huang, S. *Nat. Rev. Genet.* **2009**, *10*, 336-342.

11. Yin, H.; Marshall, D. *Curr. Opin. Biotechnol.* **2012**, *23*, 110-119.

12. Galler, K.; Brautigam, K.; Grosse, C.; Popp, J.; Neugebauer, U. *Analyst.* **2014**, *139*, 1237-1273.

13. Hosic, S.; Murthy, S. K.; Koppes, A. N. *Anal. Chem.* **2016**, *88*, 354-380.

14. Fink, L.; Kwapiszewska, G.; Wilhelm, J.; Bohle, R. M. *Exp. Toxicol. Pathol.* **2006**, *57 Suppl 2*, 25-29.

15. Cristofanilli, M.; Budd, G. T.; Ellis, M. J.; Stopeck, A.; Matera, J.; Miller, M. C.; Reuben, J. M.; Doyle, G. V.; Allard, W. J.; Terstappen, L. W.; Hayes, D. F. *N. Engl. J. Med.* **2004**, *351*, 781-791.

16. Ignatiadis, M.; Rothe, F.; Chaboteaux, C.; Durbecq, V.; Rouas, G.; Criscitiello, C.; Metallo, J.; Kheddoumi, N.; Singhal, S. K.; Michiels, S.; Veys, I.; Rossari, J.; Larsimont, D.; Carly, B.; Pestrin, M.; Bessi, S.; Buxant, F.; Liebens, F.; Piccart, M.; Sotiriou, C. *PLoS One*. **2011**, *6*, e15624.

17. Riethdorf, S.; Muller, V.; Zhang, L.; Rau, T.; Loibl, S.; Komor, M.; Roller, M.; Huober, J.; Fehm, T.; Schrader, I.; Hilfrich, J.; Holms, F.; Tesch, H.; Eidtmann, H.; Untch, M.; von Minckwitz, G.; Pantel, K. *Clin. Cancer. Res.* **2010**, *16*, 2634-2645.

18. Bouche, O.; Beretta, G. D.; Alfonso, P. G.; Geissler, M. *Cancer. Treat. Rev.* **2010**, *36 Suppl 1*, S1-10.

19. Miller, M. C.; Doyle, G. V.; Terstappen, L. W. *J. Oncol.* **2010**, *2010*, 617421.

20. Sims, C. E.; Allbritton, N. L. *Lab Chip.* **2007**, *7*, 423-440.

21. White, A. K.; Heyries, K. A.; Doolin, C.; Vaninsberghe, M.; Hansen, C. L. *Anal. Chem.* **2013**, *85*, 7182-7190.

22. White, A. K.; VanInsberghe, M.; Petriv, O. I.; Hamidi, M.; Sikorski, D.; Marra, M. A.; Piret, J.; Aparicio, S.; Hansen, C. L. *Proc. Natl. Acad. Sci. U S A.* **2011**, *108*, 13999-14004.

23. Zare, R. N.; Kim, S. *Annu. Rev. Biomed. Eng.* **2010**, *12*, 187-201.

24. Wheeler, A. R.; Throndset, W. R.; Whelan, R. J.; Leach, A. M.; Zare, R. N.; Liao, Y. H.; Farrell, K.; Manger, I. D.; Daridon, A. *Anal. Chem.* **2003**, *75*, 3581-3586.

25. Lecault, V.; White, A. K.; Singhal, A.; Hansen, C. L. *Curr. Opin. Chem. Biol.* **2012**, *16*, 381-390.

26. Reece, A.; Xia, B.; Jiang, Z.; Noren, B.; McBride, R.; Oakey, J. *Curr. Opin. Biotechnol.* **2016**, *40*, 90-96.

27. Haeberle, S.; Zengerle, R. *Lab Chip.* **2007**, *7*, 1094-1110.

28. Herzenberg, L. A.; Parks, D.; Sahaf, B.; Perez, O.; Roederer, M.; Herzenberg, L. A. *Clin. Chem.* **2002**, *48*, 1819-1827.

29. Vitale, A.; Quaglio, M.; Marasso, S. L.; Chiodoni, A.; Cocuzza, M.; Bongiovanni, R. *Langmuir.* **2013**, *29*, 15711-15718.

30. Syed, A.; Mangano, L.; Mao, P.; Han, J.; Song, Y.-A. *Lab Chip.* **2014**, *14*, 4455-4460.

31. Melin, J.; Quake, S. R. *Annu. Rev. Biophys. Biomol. Struct.* **2007**, *36*, 213-231.

32. Au, A. K.; Bhattacharjee, N.; Horowitz, L. F.; Chang, T. C.; Folch, A. *Lab Chip.* **2015**, *15*, 1934-1941.

33. Adams, A. A.; Okagbare, P. I.; Feng, J.; Hupert, M. L.; Patterson, D.; Gottert, J.; McCarley, R. L.; Nikitopoulos, D.; Murphy, M. C.; Soper, S. A. *J. Am. Chem. Soc.* **2008**, *130*, 8633-8641.

34. Qin, Y.; Wu, L.; Schneider, T.; Yen, G. S.; Wang, J.; Xu, S.; Li, M.; Paguirigan, A. L.; Smith, J. L.; Radich, J. P.; Anand, R. K.; Chiu, D. T. *Angew. Chem. Int. Ed. Engl.* **2018**, *57*, 11378-11383.

35. Pamme, N. *Lab Chip.* **2007**, *7*, 1644-1659.

36. Jimenez-Valdes, R. J.; Rodriguez-Moncayo, R.; Cedillo-Alcantar, D. F.; Garcia-Cordero, J. L. *Anal. Chem.* **2017**, *89*, 5210-5220.

37. Huang, K. W.; Wu, Y. C.; Lee, J. A.; Chiou, P. Y. *Lab Chip.* **2013**, *13*, 3721-3727.

38. Walt, D. R. *Lab Chip*. **2014**, *14*, 3195-3200.

39. Alix-Panabieres, C.; Pantel, K. *Nat. Rev. Cancer*. **2014**, *14*, 623-631.

40. Song, Y.; Tian, T.; Shi, Y.; Liu, W.; Zou, Y.; Khajvand, T.; Wang, S.; Zhu, Z.; Yang, C. *Chem. Sci*. **2017**, *8*, 1736-1751.

41. Green, B. J.; Saberi Safaei, T.; Mepham, A.; Labib, M.; Mohamadi, R. M.; Kelley, S. O. *Angew. Chem. Int. Ed. Engl.* **2016**, *55*, 1252-1265.

42. Park, M. H.; Reategui, E.; Li, W.; Tessier, S. N.; Wong, K. H.; Jensen, A. E.; Thapar, V.; Ting, D.; Toner, M.; Stott, S. L.; Hammond, P. T. *J. Am. Chem. Soc.* **2017**, *139*, 2741-2749.

43. Jackson, J. M.; Witek, M. A.; Kamande, J. W.; Soper, S. A. *Chem. Soc. Rev.* **2017**, *46*, 4245-4280.

44. Powell, A. A.; Talasaz, A. H.; Zhang, H.; Coram, M. A.; Reddy, A.; Deng, G.; Telli, M. L.; Advani, R. H.; Carlson, R. W.; Mollick, J. A.; Sheth, S.; Kurian, A. W.; Ford, J. M.; Stockdale, F. E.; Quake, S. R.; Pease, R. F.; Mindrinos, M. N.; Bhanot, G.; Dairkee, S. H.; Davis, R. W., et al. *PLoS One*. **2012**, *7*, e33788.

45. Pantel, K.; Alix-Panabieres, C. *Trends. Mol. Med.* **2010**, *16*, 398-406.

46. Harouaka, R.; Kang, Z.; Zheng, S. Y.; Cao, L. *Pharmacol. Ther.* **2014**, *141*, 209-221.

47. Alix-Panabieres, C.; Pantel, K. *Lab Chip.* **2014**, *14*, 57-62.

48. Fan, X.; Jia, C.; Yang, J.; Li, G.; Mao, H.; Jin, Q.; Zhao, J. *Biosens. Bioelectron.* **2015**, *71*, 380-386.

49. Yamada, M.; Nakashima, M.; Seki, M. *Anal. Chem.* **2004**, *76*, 5465-5471.

50. Gascoyne, P. R.; Shim, S. *Cancers (Basel.)* **2014**, *6*, 545-579.

51. Allard, W. J.; Matera, J.; Miller, M. C.; Repollet, M.; Connelly, M. C.; Rao, C.; Tibbe, A. G.; Uhr, J. W.; Terstappen, L. W. *Clin. Cancer. Res.* **2004**, *10*, 6897-6904.

52. Hyun, K. A.; Jung, H. I. *Lab Chip.* **2014**, *14*, 45-56.

53. Riethdorf, S.; Fritsche, H.; Muller, V.; Rau, T.; Schindlbeck, C.; Rack, B.; Janni, W.; Coith, C.; Beck, K.; Janicke, F.; Jackson, S.; Gornet, T.; Cristofanilli, M.; Pantel, K. *Clin. Cancer. Res.* **2007**, *13*, 920-928.

54. Foote, J.; Eisen, H. N. *Proc. Natl. Acad. Sci. U S A.* **1995**, *92*, 1254-1256.

55. Spitznagel, T. M.; Clark, D. S. *Biotech (N Y).* **1993**, *11*, 825-829.

56. Lesch, H. P.; Kaikkonen, M. U.; Pikkarainen, J. T.; Yla-Herttuala, S. *Expert. Opin. Drug. Deliv.* **2010**, *7*, 551-564.

57. Wilchek, M.; Bayer, E. A. *Immunol. Today.* **1984**, *5*, 39-43.

58. Massia, S. P.; Stark, J.; Letbetter, D. S. *Biomater.* **2000**, *21*, 2253-2261.

59. Nagrath, S.; Sequist, L. V.; Maheswaran, S.; Bell, D. W.; Irimia, D.; Ulkus, L.; Smith, M. R.; Kwak, E. L.; Digumarthy, S.; Muzikansky, A.; Ryan, P.; Balis, U. J.; Tompkins, R. G.; Haber, D. A.; Toner, M. *Nature.* **2007**, *450*, 1235-1239.

60. Hughes, A. D.; King, M. R. *Langmuir.* **2010**, *26*, 12155-12164.

61. Wang, S.; Wang, H.; Jiao, J.; Chen, K. J.; Owens, G. E.; Kamei, K.; Sun, J.; Sherman, D. J.; Behrenbruch, C. P.; Wu, H.; Tseng, H. R. *Angew. Chem. Int. Ed.* **2009**, *48*, 8970-8973.

62. Stott, S. L.; Hsu, C. H.; Tsukrov, D. I.; Yu, M.; Miyamoto, D. T.; Waltman, B. A.; Rothenberg, S. M.; Shah, A. M.; Smas, M. E.; Korir, G. K.; Floyd, F. P., Jr.; Gilman, A. J.; Lord, J. B.; Winokur, D.; Springer, S.; Irimia, D.; Nagrath, S.; Sequist, L. V.; Lee, R. J.; Isselbacher, K. J., et al. *Proc. Natl. Acad. Sci. U S A.* **2010**, *107*, 18392-18397.

63. Mittal, S.; Wong, I. Y.; Deen, W. M.; Toner, M. *Biophys. J.* **2012**, *102*, 721-730.

64. Vaidyanathan, R.; Shiddiky, M. J.; Rauf, S.; Dray, E.; Tay, Z.; Trau, M. *Anal. Chem.* **2014**, *86*, 2042-2049.

65. Tsao, S. C.; Vaidyanathan, R.; Dey, S.; Carrascosa, L. G.; Christophi, C.; Cebon, J.; Shiddiky, M. J.; Behren, A.; Trau, M. *Sci. Rep.* **2016**, *6*, 19709.

66. Stroock, A. D.; Dertinger, S. K.; Ajdari, A.; Mezic, I.; Stone, H. A.; Whitesides, G. M. *Science.* **2002**, *295*, 647-651.

67. Stroock, A. D.; Dertinger, S. K.; Whitesides, G. M.; Ajdari, A. *Anal. Chem.* **2002**, *74*, 5306-5312.

68. Chen, J. L.; Shih, W. H.; Hsieh, W. H. *Sens. Actuators, B-Chem.* **2013**, *188*, 11-21.

69. Mikolajczyk, S. D.; Millar, L. S.; Tsinberg, P.; Coutts, S. M.; Zomorrodi, M.; Pham, T.; Bischoff, F. Z.; Pircher, T. J. *J. Oncol.* **2011**, *2011*, 252361.

70. Rao, C. G.; Chianese, D.; Doyle, G. V.; Miller, M. C.; Russell, T.; Sanders, R. A., Jr.; Terstappen, L. W. *Int. J. Oncol.* **2005**, *27*, 49-57.

71. de Wit, S.; van Dalum, G.; Lenferink, A. T.; Tibbe, A. G.; Hiltermann, T. J.; Groen, H. J.; van Rijn, C. J.; Terstappen, L. W. *Sci. Rep.* **2015**, *5*, 12270.

72. Zhao, M.; Wei, B.; Nelson, W. C.; Schiro, P. G.; Chiu, D. T. *Lab Chip.* **2015**, *15*, 3391-3396.

73. Yang, L.; Lang, J. C.; Balasubramanian, P.; Jatana, K. R.; Schuller, D.; Agrawal, A.; Zborowski, M.; Chalmers, J. J. *Biotechnol. Bioeng.* **2009**, *102*, 521-534.

74. Huang, H. L.; Hsing, H. W.; Lai, T. C.; Chen, Y. W.; Lee, T. R.; Chan, H. T.; Lyu, P. C.; Wu, C. L.; Lu, Y. C.; Lin, S. T.; Lin, C. W.; Lai, C. H.; Chang, H. T.; Chou, H. C.; Chan, H. L. *J. Biomed. Sci.* **2010**, *17*, 36.

75. Jin, C.; McFaul, S. M.; Duffy, S. P.; Deng, X.; Tavassoli, P.; Black, P. C.; Ma, H. *Lab Chip.* **2014**, *14*, 32-44.

76. Vona, G.; Sabile, A.; Louha, M.; Sitruk, V.; Romana, S.; Schutze, K.; Capron, F.; Franco, D.; Pazzagli, M.; Vekemans, M.; Lacour, B.; Brechot, C.; Paterlini-Brechot, P. *Am. J. Pathol.* **2000**, *156*, 57-63.

77. Ji, H. M.; Samper, V.; Chen, Y.; Heng, C. K.; Lim, T. M.; Yobas, L. *Biomed. Microdev.* **2008**, *10*, 251-257.

78. McFaul, S. M.; Lin, B. K.; Ma, H. *Lab Chip.* **2012**, *12*, 2369-2376.

79. Tan, S. J.; Yobas, L.; Lee, G. Y.; Ong, C. N.; Lim, C. T. *Biomed. Microdev.* **2009**, *11*, 883-892.

80. Zheng, S.; Lin, H.; Liu, J. Q.; Balic, M.; Datar, R.; Cote, R. J.; Tai, Y. C. *J. Chromatogr. A* **2007**, *1162*, 154-161.

81. Huang, L. R.; Cox, E. C.; Austin, R. H.; Sturm, J. C. *Science.* **2004**, *304*, 987-990.

82. Liu, Z.; Huang, F.; Du, J.; Shu, W.; Feng, H.; Xu, X.; Chen, Y. *Biomicrofluidics.* **2013**, *7*, 11801.

83. Bhagat, A. A. S.; Kuntaegowdanahalli, S. S.; Papautsky, I. *Lab Chip.* **2008**, *8*, 1906-1914.

84. Hou, H. W.; Warkiani, M. E.; Khoo, B. L.; Li, Z. R.; Soo, R. A.; Tan, D. S. W.; Lim, W. T.; Han, J.; Bhagat, A. A. S.; Lim, C. T. *Sci. Rep.* **2013**, *3*, 1259.

85. Di Carlo, D. *Lab Chip.* **2009**, *9*, 3038-3046.

86. Inglis, D. W.; Davis, J. A.; Austin, R. H.; Sturm, J. C. *Lab Chip.* **2006**, *6*, 655-658.

87. Di Carlo, D.; Irimia, D.; Tompkins, R. G.; Toner, M. *Proc. Natl. Acad. Sci. U S A.* **2007**, *104*, 18892-18897.

88. Gagnon, Z. R. *Electrophoresis.* **2011**, *32*, 2466-2487.

89. Chan, J. Y.; Ahmad Kayani, A. B.; Md Ali, M. A.; Kok, C. K.; Yeop Majlis, B.; Hoe, S. L. L.; Marzuki, M.; Khoo, A. S.; Ostrikov, K. K.; Ataur Rahman, M.; Sriram, S. *Biomicrofluidics.* **2018**, *12*, 011503.

90. Pethig, R. *Biomicrofluidics.* **2010**, *4*, 022811.

91. Jones, T. *Press, Cambridge* **1995**.

92. Yale, A. R.; Nourse, J. L.; Lee, K. R.; Ahmed, S. N.; Arulmoli, J.; Jiang, A. Y. L.; McDonnell, L.

P.; Botten, G. A.; Lee, A. P.; Monuki, E. S.; Demetriou, M.; Flanagan, L. A. *Stem. Cell. Rep.* **2018**, *11*, 869-882.

93. Gascoyne, P. R.; Vykoukal, J. *Electrophoresis.* **2002**, *23*, 1973-1983.

94. Nestor, B. A.; Samiei, E.; Samanipour, R.; Gupta, A.; Van den Berg, A.; Derby, M. D. D.; Wang, Z.; Nejad, H. R.; Kim, K.; Hoorfar, M. *RSC Adv.* **2016**, *6*, S7409-S7416.

95. Kim, S. H.; He, X.; Kaneda, S.; Kawada, J.; Fourmy, D.; Noji, H.; Fujii, T. *Lab Chip.* **2014**, *14*, 730-736.

96. Menachery, A.; Pethig, R. In *IEE Proc Nanobiotechnol*; IET, 2005, pp 145-149.

97. Gupta, V.; Jafferji, I.; Garza, M.; Melnikova, V. O.; Hasegawa, D. K.; Pethig, R.; Davis, D. W. *Biomicrofluidics.* **2012**, *6*, 24133.

98. Albrecht, D. R.; Underhill, G. H.; Mendelson, A.; Bhatia, S. N. *Lab Chip.* **2007**, *7*, 702-709.

99. Gagnon, Z.; Gordon, J.; Sengupta, S.; Chang, H. C. *Electrophoresis.* **2008**, *29*, 2272-2279.

100. Sancho, M.; Martinez, G.; Munoz, S.; Sebastian, J. L.; Pethig, R. *Biomicrofluidics.* **2010**, *4*, 022802.

101. Huang, C.; Liu, C.; Minne, B.; Ramirez Hernandez, J. E.; Stakenborg, T.; Lagae, L. *Appl. Phys. Lett.* **2014**, *105*, 143702.

102. BiologyWise - *https://biologywise.com/cell-membrane-structure-function*.

103. Paszek, M. J.; DuFort, C. C.; Rossier, O.; Bainer, R.; Mouw, J. K.; Godula, K.; Hudak, J. E.; Lakins, J. N.; Wijekoon, A. C.; Cassereau, L.; Rubashkin, M. G.; Magbanua, M. J.; Thorn, K. S.; Davidson, M. W.; Rugo, H. S.; Park, J. W.; Hammer, D. A.; Giannone, G.; Bertozzi, C. R.; Weaver, V. M. *Nature.* **2014**, *511*, 319-325.

104. MyDEP - *https://mydepsoftware.github.io/a_bit_of_theory/*.

105. Martinez-Duarte, R. *Electrophoresis.* **2012**, *33*, 3110-3132.

106. Henslee, E. A.; Sano, M. B.; Rojas, A. D.; Schmelz, E. M.; Davalos, R. V. *Electrophoresis.* **2011**, *32*, 2523-2529.

107. Chiou, P. Y.; Ohta, A. T.; Wu, M. C. *Nature.* **2005**, *436*, 370-372.

108. Taff, B. M.; Voldman, J. *Anal. Chem.* **2005**, *77*, 7976-7983.

109. Mittal, N.; Rosenthal, A.; Voldman, J. *Lab Chip.* **2007**, *7*, 1146-1153.

110. Lapizco-Encinas, B. H. *Electrophoresis.* **2018**.

111. Lapizco-Encinas, B. H.; Simmons, B. A.; Cummings, E. B.; Fintschenko, Y. *Anal. Chem.* **2004**, *76*, 1571-1579.

112. Cemazar, J.; Douglas, T. A.; Schmelz, E. M.; Davalos, R. V. *Biomicrofluidics*. **2016**, *10*, 014109.

113. Sun, M.; Agarwal, P.; Zhao, S.; Zhao, Y.; Lu, X.; He, X. *Anal. Chem.* **2016**, *88*, 8264-8271.

114. Wu, M. C. *Nature Photonics* **2011**, *5*, 322-324.

115. Yang, S. M.; Yu, T. M.; Huang, H. P.; Ku, M. Y.; Hsu, L.; Liu, C. H. *Opt. Lett.* **2010**, *35*, 1959-1961.

116. Lee, W. C.; Rigante, S.; Pisano, A. P.; Kuypers, F. A. *Lab Chip.* **2010**, *10*, 2952-2958.

117. Bischoff, F. Z.; Medoro, G.; Manaresi, N. *Circulating Tumor Cells: Isolation and Analysis* **2016**, 365-376.

118. Whitesides, G. M.; Ostuni, E.; Takayama, S.; Jiang, X.; Ingber, D. E. *Annu. Rev. Biomed. Eng.* **2001**, *3*, 335-373.

119. Wu, H.; Wheeler, A.; Zare, R. N. *Pro.c Natl. Acad. Sci. U S A.* **2004**, *101*, 12809-12813.

120. Marcy, Y.; Ishoey, T.; Lasken, R. S.; Stockwell, T. B.; Walenz, B. P.; Halpern, A. L.; Beeson, K. Y.; Goldberg, S. M.; Quake, S. R. *PLoS. Genet* .**2007**, *3*, 1702-1708.

121. Figueroa, X. A.; Cooksey, G. A.; Votaw, S. V.; Horowitz, L. F.; Folch, A. *Lab Chip.* **2010**, *10*, 1120-1127.

122. Rettig, J. R.; Folch, A. *Anal. Chem.* **2005**, *77*, 5628-5634.

123. Dimov, I. K.; Lu, R.; Lee, E. P.; Seita, J.; Sahoo, D.; Park, S. M.; Weissman, I. L.; Lee, L. P. *Nat. Commun.* **2014**, *5*, 3451.

124. Kim, S. H.; Yamamoto, T.; Fourmy, D.; Fujii, T. *Small.* **2011**, *7*, 3239-3247.

125. Kim, S. H.; Fujii, T. *Lab Chip.* **2016**, *16*, 2440-2449.

126. Ståhlberg, A.; Kubista, M. *Exp. Rev.Mol. Diag.* **2014**, *14*, 323-331.

127. Gong, Y.; Ogunniyi, A. O.; Love, J. C. *Lab Chip.* **2010**, *10*, 2334-2337.

128. Fosdick, S. E.; Knust, K. N.; Scida, K.; Crooks, R. M. *Angew. Chem. Int. Ed.* **2013**, *52*, 10438-10456.

129. Mavré, F. o.; Anand, R. K.; Laws, D. R.; Chow, K.-F.; Chang, B.-Y.; Crooks, J. A.; Crooks, R. M. *Anal. Chem.* **2010**, *82*, 8766-8774.

130. Loget, G.; Zigah, D.; Bouffier, L.; Sojic, N.; Kuhn, A. *Acc. Chem. Res.* **2013**, *46*, 2513-2523.

131. Bouffier, L.; Arbault, S.; Kuhn, A.; Sojic, N. *Anal. Bioanal. Chem.* **2016**, *408*, 7003-7011.

132. Fosdick, S. E.; Crooks, R. M. *J. Am. Chem. Soc.* **2012**, *134*, 863-866.

133. Fosdick, S. E.; Berglund, S. P.; Mullins, C. B.; Crooks, R. M. *Anal. Chem.* **2013**, *85*, 2493-2499.

134. Perdue, R. K.; Laws, D. R.; Hlushkou, D.; Tallarek, U.; Crooks, R. M. *Anal. Chem.* **2009**, *81*, 10149-10155.

CHAPTER 2

HIGH-THROUGHPUT SELECTIVE CAPTURE OF SINGLE CIRCULATING TUMOR CELLS BY DIELECTROPHORESIS AT A WIRELESS ELECTRODE ARRAY

A paper published in Journal of American Chemical Society

Min Li, Robbyn K. Anand*

Department of Chemistry, Iowa State University, Ames, Iowa 50011, United States

* Corresponding Author

Abstract

We demonstrate continuous high-throughput selective capture of circulating tumor cells (CTCs) by dielectrophoresis (DEP) at arrays of wireless electrodes (bipolar electrodes, BPEs). The use of BPEs removes the requirement of ohmic contact to individual array elements, thus enabling otherwise unattainable device formats. Capacitive charging of the electrical double layer (EDL) at opposing ends of each BPE allows an AC electric field to be transmitted across the entire device. Here, two such designs are described and evaluated. In the first design, BPEs interconnect parallel microchannels. Pockets extruding from either side of the microchannels volumetrically control the number of cells captured at each BPE tip and enhance trapping. High-fidelity single-cell capture was achieved when the pocket dimensions were matched to those of the cells. A second, open design allows many non-targeted cells to pass through. These devices enable high-throughput capture of rare cells and single-cell analysis.

2.1 Introduction

In this paper, we report a method for the specific dielectrophoretic (DEP) capture of single cells at an array of wireless bipolar electrodes (BPEs), yielding over 1,400 capture sites. The results of this study demonstrate the utility of BPEs to enable scalable, high-throughput DEP platforms by imparting a flexibility in device design that is unparalleled by conventional electrodes. As a cell separation and isolation tool, DEP has major advantages – it is label free, highly specific, enables single-cell capture, and can provide simple post-capture access to viable cells – yet it suffers from low throughput due to short-range electric field gradients and design constraints. This shortcoming is a major issue for research and clinical applications that require large samples to be processed. Therefore, the current study represents a significant fundamental advancement in DEP technology. Herein, we demonstrate the utility of a wireless electrode array for the isolation of circulating tumor cells (CTCs) based on their dielectric properties, and we highlight design rules for scaling and for single-cell capture.

CTCs are cells that have detached from the primary tumor and migrated into blood vessels. A fraction of these CTCs seed metastases by extravasation into the parenchyma of foreign tissues for subsequent growth of tumors. Understanding cancer spread is critical because metastasis leads to 90% of epithelial cancer-related deaths,[1] and therefore, the study of CTCs is highly valuable for the development of effective therapies. For instance, clinical studies have shown that an inverse correlation exists between patient survival and the number of CTCs that is independent of line of therapy and separately, that the reduction or elimination of CTCs after initial or adjuvant therapy prolongs survival.[2] These findings indicate that the enumeration of CTCs is relevant for diagnosis, prognosis and evaluation of drug resistance. Additionally, determination of the genetic mutations harbored by CTCs may provide guidance

for the selection of therapies and personalized treatment.[3] Given these findings, the isolation and characterization of CTCs are of paramount importance.

Despite their promise as a clinical indicator and therapeutic target, the separation of CTCs from whole blood, which is the first inevitable step of overall analysis, is challenging.[4] First, CTCs are extremely rare, such that there can be as few as 1 CTC per 10^9 erythrocytes and 10^7 leukocytes.[5] In the CellSearch system, in the standard blood volume of 7.5 mL employed, the number of CTCs detected normally ranges from a few cells to several thousand.[2,6] Second, due to the heterogeneous nature of the cell populations found in primary tumors and the changes undergone by these cells during metastatic events, the phenotypic characteristics of CTCs can vary widely. Examples include the nuclear to cytoplasmic ratios (N/C) (*the average N/C ratio of CTCs in breast cancer patients is 4.0*,[7] *while it is 1.43 in prostate cancer patients*[8]), deformability (*CTCs with large N/C ratio are less deformable and less invasive*), size (*the size of CTCs reported ranges from 4.0 μm to 30 μm, even from a single patient*[6]) and protein expression (*the abundance of biomarkers such as cytokeratin (CK) and epithelial cell adhesion molecule (EpCAM*) *vary tremendously depending on the patient, the type of cancer, and the stage of the tumor*[9]).

Despite these challenges, tremendous progress has been made to target CTCs using one or more of their unique properties to discriminate them from other cells in blood. The most prevalent isolation techniques employ immunoaffinity targeting of EpCAM, which is a membrane protein expressed exclusively by epithelial cells. For example, some prominent approaches employ antibody-based capture at microchannel walls,[10,11] or on magnetic beads (CellSearch, Veridex™, Warren, PA, USA), or sorting of immunofluorescently tagged cells.[12,13] Despite its reputation as the only FDA cleared clinical testing program, CellSearch

and other EpCAM-based approaches suffer from their incapability to capture CTCs that inherently do not express EpCAM or that have downregulated expression during acquisition of a more mobile phenotype – the epithelial to mesenchymal transition (EMT).[9] Importantly, the subpopulation of CTCs that have undergone the EMT are most likely to survive and invade, therefore determining disease outcome.[5] An evidence of the inherent limitation of immunoaffinity techniques is that cultured cancer cells with high expression of EpCAM such as MCF7 and SW620 cells (which have an average 5.0×10^5 and 1.0×10^6 EpCAM molecules/cell, respectively[2,3]), must be employed for evaluation of the assay to obtain reliable results. Mitigating with a cocktail of antibodies increases capture efficiency of CTC subpopulations,[14,15] while it is experimentally time-consuming, cost-ineffective and often requires trypsinization and high flow rate washing to release CTCs captured.[10,16]

Label-free techniques based on the physical properties of CTCs circumvent reliance on protein expression so that this capture bias may be decreased. For instance, filtration techniques integrate the microscale constrictions of weirs,[17,18] pillars,[19,20] or pores,[21-25] into cell separation so that cells with desired size and deformability can be retained. Clinical evaluation of these filtration approaches is ongoing.[26-28] However, the size distribution of CTCs overlaps with that of leukocytes, thus resulting in CTC loss or leukocyte contamination. As a further concern, clogging within filters and subsequent change in flow rate may cause shear stress and potential damage or loss of CTCs. Another label-free technique, hydrodynamic chromatography, which includes lateral displacement separation[29] and spiral channels[30] imparts cells in fluids with distinct velocities based on differences in size and deformability. Though the throughput is significantly improved relative to filtration (up to 600 mL/h),[31] enrichment becomes poorer due to the inability of these techniques to differentiate nucleated cells.[32-34]

Devices that employ dielectrophoresis (DEP)[35-37] are superior to both immunoaffinity and physical isolation techniques in that they feature antibody-independent separation and also avoid leukocyte contamination. These advantages are achieved through the integrated discrimination of both size and dielectric properties of each cell type. These dielectric properties arise from the composition and morphology of the cells and are a much more specific differentiator of phenotype than size alone while not being as overly selective as a single biomarker such as EpCAM. Therefore, separation based on DEP exhibits less selection bias when compared with size- and antibody-based approaches. For instance, Alazzam *et al.* applied DEP *via* interdigitated comb-like electrodes to achieve 96% capture efficiency of MDA-MB-231 cells (an EpCAM-negative invasive breast cancer cell line) from normal blood cells.[38] Gascoyne *et al.* reported the application of dielectrophoretic field-flow fractionation (DEP-FFF) to isolate three different kinds of tumor cells with above 90% efficiency from the nucleated cell fraction of a blood sample (the 'buffy coat').[39] Demonstrating the potential of DEP for a high degree of selectivity, Henslee *et al.* proved that late-stage breast cancer cells could be further differentiated from early and intermediate-stage CTCs.[40] Besides having low selection bias, DEP is also amenable to downstream analysis of captured cells. For example, an electroactive double-well array was fabricated to achieve single-cell DEP capture of PC3 cells, which was followed by analysis of the intracellular β-galactosidase activity.[41] Despite these advantages, when compared to filtration and hydrodynamic chromatography, which boast throughput on the order of 10-100 mL/h,[19,31,42] DEP suffers from relatively low throughput in the range of 0.01 mL/h to 1.0 mL/h.[38,40,43] Therefore, the development of high-throughput DEP devices is critical to their practical application.

Herein, we describe a high-throughput DEP device that is readily scalable along both *x*- and *y*- directions *via* the employment of a *wireless* bipolar electrode (BPE) array, and we demonstrate its utility for the separation of CTCs from blood cells using model cell lines. Significantly, the BPE array communicates an AC field across insulating barriers (channel walls) thus enabling the simultaneous capture of CTCs across parallel microchannels. Micropockets aligned to the BPE tips and embedded along the wall of each microchannel provide discrete capture sites with defined volume, thus enabling single-cell capture. Wireless electrodes are critical to the branching microchannel scheme employed. Furthermore, to exploit the capability of DEP-based techniques to retain cell viability,[38,39,44] a requirement for the downstream analysis of CTCs such as culturing and testing of drug efficacy, we demonstrate the full release of captured cells. A key point is that the ability of DEP to separate CTCs from blood has been extensively demonstrated.[39,44-47] The features that distinguish the approach reported here from existing strategies is that it is high-throughput and capable of high-fidelity single-cell capture. These features, when combined with on-chip analysis, will increase understanding of cell-to-cell heterogeneity in tumor tissue and the related clinical outcomes.

2.2 Technical Background

2.2.1 Bipolar Electrodes (BPEs) in Microfluidic Devices

A bipolar electrode (BPE)[48-50] is a conductor in an ionically conductive phase that when exposed to an external electrical field can facilitate oxidation and reduction reactions simultaneously at opposite ends. For example, a BPE can comprise a strip of metal embedded in a microfluidic channel filled with an aqueous electrolyte. When a DC electric potential is applied across the reservoirs of the microchannel, a linear potential drop is expected along the

channel length due to its high electrical resistance. This linear electric field leads to potential differences between the BPE (an equipotential object) and the solution in contact with its ends. An electrical double layer forms at each end of the BPE, and faradaic reactions occur if the potential differences at the BPE/solution interface (cathode and anode) provide sufficient overpotential to drive simultaneously the reduction and oxidation of available redox species. **Scheme 2.1a** depicts a BPE situated along the floor of a microfluidic channel. An equivalent circuit that describes this system is shown at bottom left ((b) in **Scheme 2.1**). In this microchannel, current flows between the driving electrodes either *via* ionic conduction in solution or through the BPE *via* capacitive charging or charge transfer (faradaic reactions) ((c) and (d) in **Scheme 2.1**). The solution resistance (to ionic current) is represented by R_{s1} (left of BPE), R_{s2} (above BPE), and R_{s3} (right of BPE). R_{ct} is the resistance to charge transfer reactions, whereas C_{dl1} and C_{dl2} are the double layer capacitance at each end of the BPE. This configuration has been employed most prevalently to achieve faradaic reactions (current through R_{ct}) without making direct ohmic contact to the BPEs, and many applications take advantage of the ability of BPEs to be arrayed. For example, Crooks and coworkers designed a BPE array composed of 1000 individual BPEs to facilitate faradaic reactions. They employed electrogenerated chemiluminescence (ECL) at the anode to report the activation of a sensing event at the cathode.[51] The ECL intensity profile indicated a uniform response from each BPE under the applied DC electric field. A wide range of applications[52-59] hitherto bears testimony to the fact that BPEs are effective, convenient and robust for the detection, sensing, separation and enrichment of a wide variety of analytes.

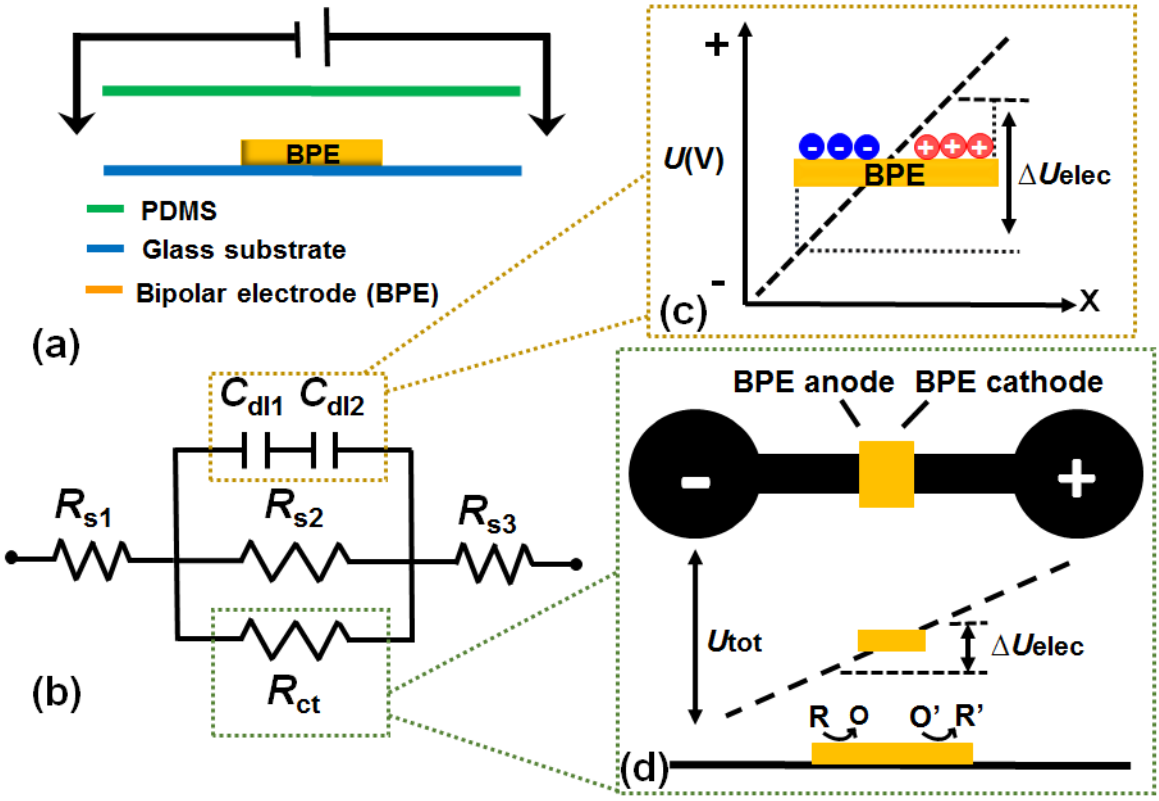

Scheme 2.1. Illustration of the functions of a BPE in a DC electric field.

However, when a sufficiently high frequency AC field is applied rather than a DC electric field, faradaic reactions do not occur (R_{ct} approaches infinity when the field frequency is greater than the rate of electron transfer from available redox species). Further, if the top of the microchannel meets the BPE, then the possibility of ionic current above the BPE is removed (R_{s2} becomes infinite). In this scenario, the continuous charging and discharging of the electrical double layer formed between each end of a BPE and the solution (C_{dl1} and C_{dl2}) becomes the primary route by which the electric field drives current between the driving electrodes.

Due to this capacitive charging, separate parallel microchannels can remain electrically interconnected by the embedded BPEs in an AC electric field. **Scheme 2.2** depicts the parallel

channel device layout (a, side view and b, top view), the corresponding equivalent circuit (c), an illustration of the location of the double layer capacitance at each BPE tip (d, side view), and a 2D simulation of the electric field distribution across a single microchannel flanked by 6 BPE tips (e, top view). Due to the equipotential quality of conductors, each BPE takes on a potential that is intermediate to the potential of the solution in contact with its ends, and then a drop in potential (electric field) is distributed across the solution in each microchannel. This electric field distribution can be readily tuned by the dimensions of the BPEs. For instance, pointed BPEs result in a maximum electric field at the BPE tip, while minimum field intensity is located at the middle of the channels (**Scheme 2.2e**). In this way, the BPEs not only transmit the AC electric field across the chip, but also shape the electric field in a desired way.

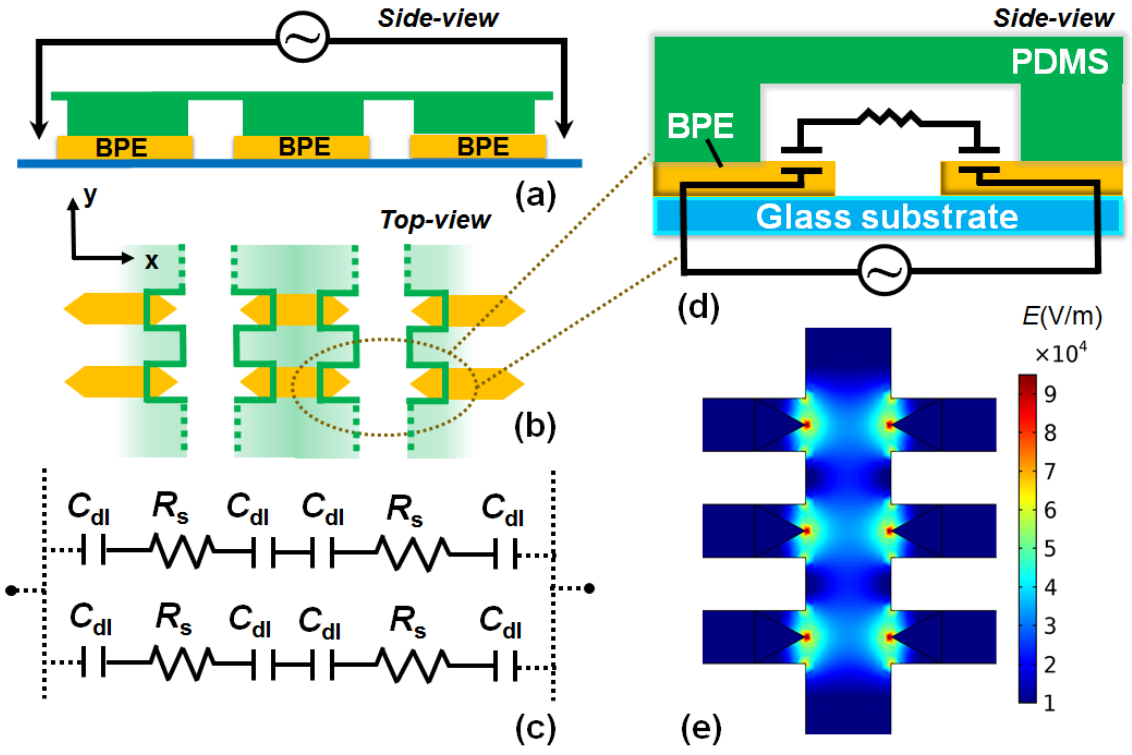

Scheme 2.2. Illustration of the BPEs in a parallel-channel device under an applied AC electric field.

2.2.2 DEP Manipulation of Cells

DEP is a field-induced force (F_{DEP}) acting on a polarizable particle when exposed to a non-uniform electric field.[60-61] The external electric field (E) induces the surface charges (bound and free charges) to accumulate at the particle-medium interface. The gradient in the electric field exerts differential force on the two opposing ends of the resulting induced electrical dipole, which in turn leads to a net dielectrophoretic force. The time-averaged DEP force experienced by a homogeneous spherical particle with radius r in a medium of permittivity ε_m is given by:

$$\overrightarrow{F_{DEP}} = 2\pi r^3 \varepsilon_m Re[K(\omega)]\vec{\nabla}\left|\vec{E}\right|^2$$

Where Re[$K(\omega)$] is the real part of Clausius-Mossotti factor,

$$K(\omega) = \frac{\varepsilon_p^* - \varepsilon_m^*}{\varepsilon_p^* + 2\varepsilon_m^*}$$

which determines the direction and relative strength of DEP force as a function of applied field frequency. Here, ε_p^* and ε_m^* are the frequency-dependent complex permittivities of the particle and medium, respectively. When Re[$K(\omega)$] is positive, the induced DEP force, displaces particles toward higher electric field (positive DEP (pDEP)), while particles move toward lower electric field when Re[$K(\omega)$] is negative (nDEP). The frequency above which cells transition from an nDEP to pDEP response is the cross-over frequency (*cof*). Importantly, the unique frequency-dependent polarization responses of biological cells allow them to be separated by DEP at a field frequency and medium conductivity where significantly disparate values of Re[$K(\omega)$] can be achieved for each. For example, for the model cell lines employed in the current study, it is reported that MDA-MB-231 (breast cancer) cells experienced pDEP at frequencies greater than 45-85 kHz in a medium with conductivity of 30 mS/m,[44] while the *cof* is 110-190 kHz for Jurkat E6-1 T cells (a model white blood cell line) in a medium with a conductivity of 40 mS/m.[62] Therefore, separation of these cell types is anticipated between 45 kHz and 110 kHz in a similar medium. An increase in medium conductivity will result in

an increase in the frequency required for separation, and eventually, in an inability of any cell type to achieve crossover to pDEP.[63] For this reason, as is common practice in DEP techniques, cells are suspended in a low conductivity isotonic medium to achieve separation.

2.3 Methods and Chemicals

2.3.1 Chemicals

The silicone elastomer and curing agent (Sylgard 184), bovine serum albumin (BSA) (biotech grade), and 0.25% Trypsin-EDTA (1X) were purchased from Fisher Scientific (Thermo Fisher Scientific, Inc., Waltham, MA). The DMEM/F12 cell culture medium, dextrose (d-glucose), sucrose, Pluronic® F-108 and 1.0 M Tris·HCl stock were obtained from Sigma-Aldrich, Inc. (St. Louis, MO). The RPMI 1640 medium was purchased from American Type Culture Collection (ATCC) (Manassas, VA). All dilutions were conducted with Type 1 water (18.2 MΩ·cm). DEP buffer was comprised of 8.0% sucrose, 0.3% dextrose, and 0.1% BSA in 1.0 mM Tris buffer (pH=8.1).

2.3.2 Cell Culture

MDA-MB-231 and Jurkat E6-1 T cells were obtained from ATCC. They were cultured in DMEM/F12 and RPMI 1640 media, respectively with 1% pen-strep and 10% fetal bovine serum supplementation at 37 ºC and 5% CO_2. All cells were subcultured every 2-3 days to maintain the concentration of cells at less than 1.0 x 10^6 cells/mL. In preparation of DEP experiments, MDA-MB-231 cells were detached from culture flask using 0.25% Trypsin-EDTA (1X), followed by pelleting by centrifugation (1100 rpm, 5 min) and resuspension in 5.0 mL Tris DEP buffer. Jurkat E6-1 T cells were directly pelleted from culture medium prior

to resuspension in DEP buffer. Pelleting and resuspension was repeated to wash cells twice in DEP buffer before DEP capture experiments.

2.3.3 DEP Experiments

All the devices were designed to operate such that the cells, suspended in DEP buffer, were flowed through and either attracted to and captured at BPE tips (pDEP) or retained in fluid flow (nDEP). Device operation was accomplished by the application of an AC voltage at coplanar driving electrodes at each side of the BPE arrays using a Tektronix AFG3011C waveform generator (Tektronix, Beaverton, OR) and Trek model 2205 amplifier (Trek, Lockport, NY). The AC frequency was maintained at 40 kHz at which MDA-MB-231 cells experienced strong pDEP, while Jurkat E6-1 T cells exhibited nDEP. Nikon eclipse T*i* inverted microscope and Nikon AZ-100 microscope (Nikon, Tokyo, Japan) were utilized to image cells to obtain fluorescence and optical images, respectively.

2.3.4 Device Dimensions

The dimensions for two device designs are described here (The complete drawings are shown in the Supporting Information). For the high-throughput parallel-channel design, 32 microchannels with each being 2.95 mm long x 200 μm wide x 25 μm tall were arranged in parallel and separated by 0.486 mm (center-to-center). Each channel had 22 pockets extruded at each side (1,408 pockets). Each pocket was 40 μm long x 40 μm wide and the edge-to-edge distance of two adjacent pockets was 80 μm. The microchannels were interconnected to a common inlet and outlet by a bifurcation (branching) scheme. A tapered channel inlet with an array of diamond-shaped pillars (100 μm x 40 μm) facilitated introduction of cells into the channels. The electrodes extend into the pockets from under the PDMS to a distance of 10 μm

from the channel. The two rows of electrodes at the ends (outermost channels) were interconnected and led to contacts for the waveform generator.

The following modifications were then made to the parallel-channel photomask design in the drawing software to create the open-channel design. Importantly, the BPE array layout was unchanged. First, groups of 8 microchannels were merged by deleting the interior channel walls. This resulted in four 3.6 mm-wide chambers interconnected with BPEs. Second, pillars with a radius of 20 μm were added at the center of each BPE to support the ceiling of these chambers. Finally, the bifurcated channels were edited to connect each chamber to inlet and outlet reservoirs. Consequently, the separation area of the open- channel design doubled compared to the parallel-channel design in the same device footprint.

2.4 Results and Discussion

The traditional electrodes[38,44,64,65] widely employed in DEP limit the extension and flexibility of device design because the electrodes have to be connected *via* wire leads to the power source. For example, the bifurcated channels employed in the current study would intersect electrodes, leading to unwanted cell capture and clogging in the inlet channels. Our results demonstrate the capability of a BPE array to enable *wireless* control of the distribution of an AC electric field while alleviating design constraints.

2.4.1 DEP characterization of Two Model Cell Lines

To test the ability of our BPE array-based device to separate CTCs from other cells in the blood, two model cell lines were employed. The DEP responses of MDA-MB-231 (breast cancer cells) and Jurkat T-cells (white blood cells) were characterized using quadrupole electrodes as follows to determine an AC electric field frequency at which the two cell types

could be separated. The conductivity of the DEP buffer used in the present work was 6.2 mS/m. The quadrupole electrode design was guided by simulation of the resulting electric field using COMSOL simulation software (Multiphysics 5.2a, COMSOL, Inc., Burlington, MA) (**Figure 2.1a**). The design was found to provide a sufficient electric field gradient to allow nDEP and pDEP responses of the cells to be distinguished. Cells undergoing nDEP move to the center of the quadrupole design at which the electric field is at a minimum. In contrast, a pDEP response is characterized by cells moving to the electrode edges, where the electric field is strongest. To determine the response of each model cell line, 100 µL of the cell sample (1×10^6 cells/mL in DEP buffer) were applied to the quadrupole electrodes, and the frequency of the AC voltage (10.0 Vpp) applied between opposing electrode pairs was swept from 1 kHz to 100 kHz (further experimental details are available in the **Supporting Information** in **Figure 2.5**). Based on the results shown in **Figure 2.1**, 40 kHz was chosen for separation as MDA cells experienced strong pDEP and Jurkat cells underwent an nDEP response.

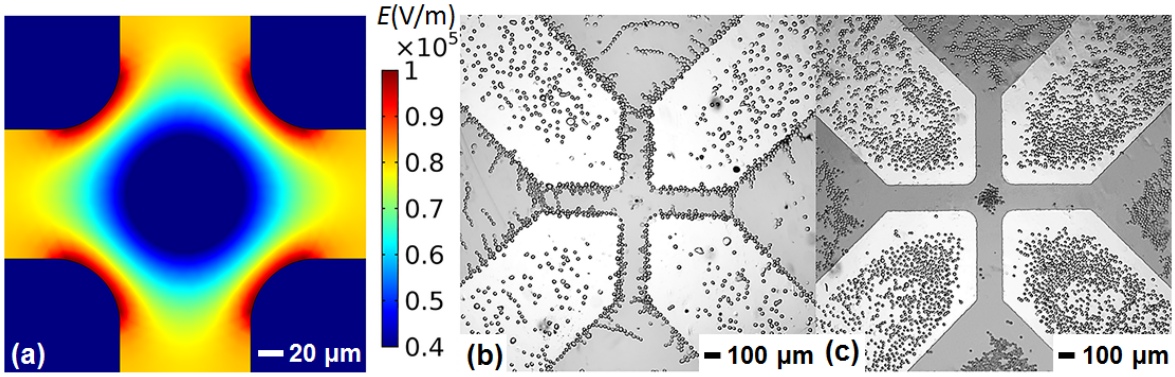

Figure 2.1. Determination of the separation frequency using quadrupole electrodes. (a) Results of the simulation of the electric field (*E* (V/m)) in the center of the quadrupole design. The center region exhibits a local minimum electric field, and the maximum field is located along the electrode edges; (b) pDEP of MDA-MB-231 cells at 40 kHz; (c) nDEP of Jurkat E6-T cells at 40 kHz.

2.4.2 Simulation of the Electric Field in the BPE Array-Based DEP Devices

Two designs that employ BPEs to shape the AC electric field were fabricated and investigated. In both designs, cells experiencing pDEP were expected to be trapped at the electric field maxima around the BPE tips, while cells undergoing nDEP remain in fluid flow. The influence of the device dimensionality in terms of the shape, arrangement and tip position of the BPEs on the electric field were simulated and optimized using the finite element method (COMSOL Multiphysics 5.2a) (details of the simulation and optimization process are available in the **Supporting Information**). The distribution of the electric field and the DEP force along a line trace intersecting the central axis of the BPEs in the two optimized devices are shown in **Figure 2.2**. In the simulation, the dimensions (e.g., channel width, pocket size and BPE tip position and shape) matched those of devices employed in the experiments. The spatially and time-averaged electric field ($E_{avg,rms}$) was 13.7 kV/m, and 6.0 kV/m for the parallel-channel and open-channel design, respectively. These values correspond to an applied voltage of 248 Vpp, which was employed in experiments. **Figures 2.2a and** 2.**2b** show the resulting electric field distribution in each design, and **Figures 2.2c and 2.2d** are plots of the electric field strength along cut-lines bisecting a row of BPEs. The maximum electric field strength is located at the BPE tips and is approximately 38 kV/m, and 34 kV/m for the parallel-channel and open-channel design, respectively. **Figures 2.2e and 2.2f** show an estimate of the pDEP force experienced by a 12.0 μm-radius cell as a result of this electric field (Re[$K(\omega)$] = 1.0). We can make several conclusions based on these data. First, we can conclude that the DEP force exerted by this electric field is sufficient for cell trapping. A force of 5.0 to 15 pN is sufficient to overcome drag force experienced by an MDA cell trapped in fluid flowing past at linear velocities in the range employed in the experiments reported here. Importantly, pDEP

forces greater than this threshold extend up to 50 µm from each BPE tip (inset of **Figure 2.2e**, BPE tip located at 446 µm). This result is significant because it indicates that channels wider than 100 µm will experience a decrease in capture efficiency as channel width increases.

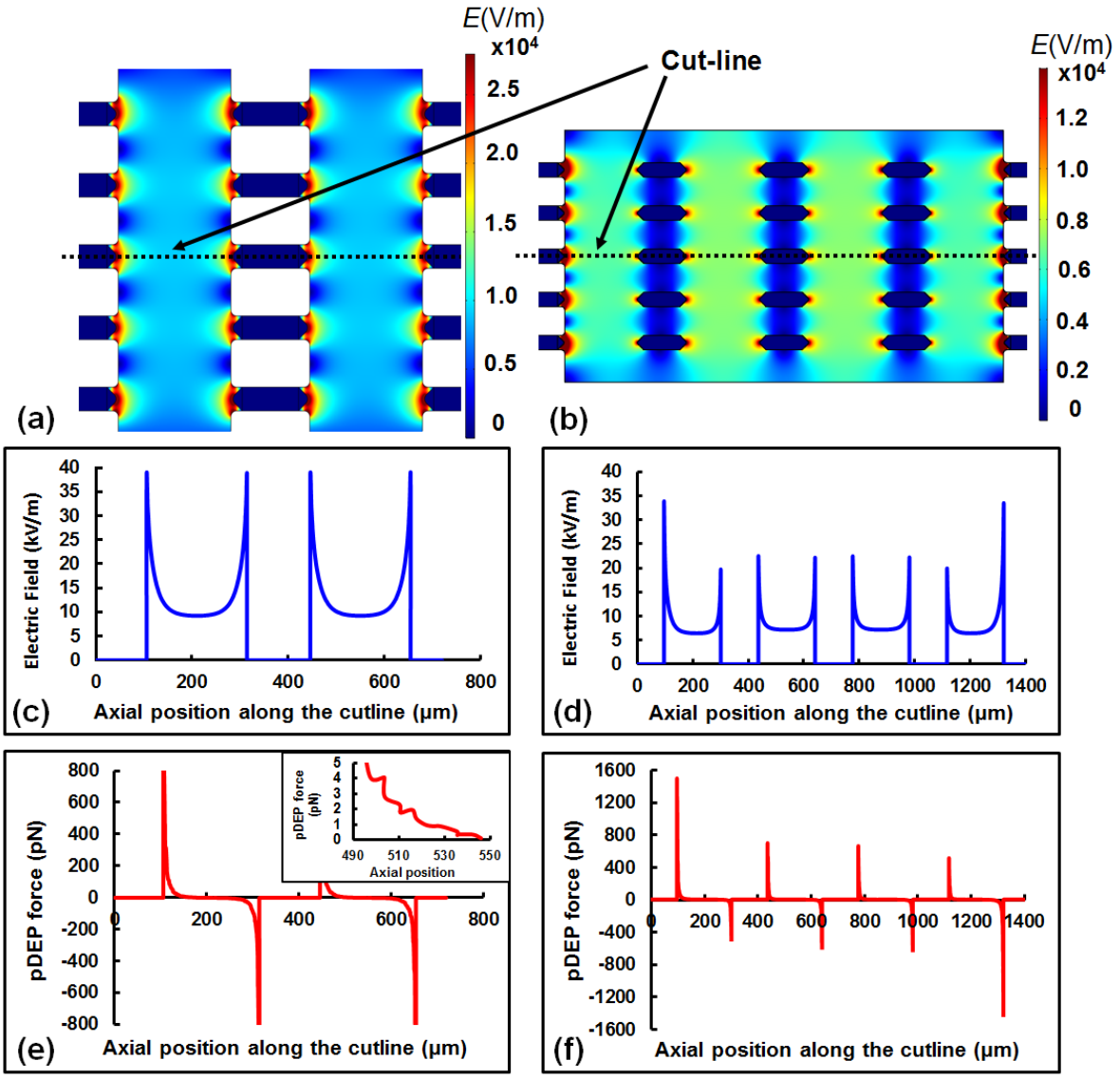

Figure 2.2. Numerical simulation of the electric field strength (a-d) and DEP force (e, f) in the parallel-channel design (a, c, e) and open-channel design (b, d, f). Inset of (e), detail of the DEP force at distances greater than 54 µm from the BPE tip (x = 446 µm).

Second, the results in **Figure 2.2** demonstrate the impact of increasing the radius of curvature of the BPE tips on the electric field distribution. In comparison to the fully pointed

tips shown in **Scheme 2.2**, these rounded tips distribute the strongest region of the electric field over a broader area, thereby preventing the damage to cells that may be incurred by an overly focused electric field. Next, we can compare the features of the electric field in the two device designs. Considering the electric field distribution in the open-channel design (**Figure 2.2**, right side), the field strength around the junctions between the large open chambers (34 kV/m) is 35% higher than that toward the middle of the chambers (22 kV/m). Thus, more cells were expected to be trapped around the junctions. In contrast, the electric field profile is uniformly distributed across the parallel channels, therefore a uniform distribution of trapped cells can be expected. Finally, as an added design feature, in the parallel-channel device, a 10 μm gap was introduced between the tip and the micropocket opening to prevent captured cells from being pulled away by the flowing DEP buffer. Therefore, while the open-channel design enables higher sample throughput, the parallel-channel design offers more uniform field distribution, more robust capture, and control over the number of cells captured at each BPE tip as defined by the micropocket geometry.

2.4.3 DEP Separation of Cells at an Array of Wireless Electrodes

The separation performance of the wireless electrode (BPE) array in the parallel-channel and open-channel was studied using Jurkat E6-1 T and MDA-MB-231 as model white blood cells (WBCs) and CTCs, respectively. First, a Pluronic-treated device was rinsed with DEP buffer for 15 min. Second, an AC signal (248 Vpp, 40 kHz) was applied at the driving electrodes. Under these conditions, the average electric field strength ($E_{avg,rms}$) in the trapping channels (between BPEs) was 13.7 kV/m, and 6.0 kV/m for the parallel-channel and open-channel devices, respectively. The solution in the inlet reservoir was then replaced with the cell sample in DEP buffer, and a height differential was established between the inlet and outlet

reservoirs to achieve a desired fluid flow in the trapping channels. Optical images showing the response of the MDA-MB-231 cells in the two designs are shown in **Figures 2.3a-2.3c**. The images obtained in **Figure 2.3a** was taken after the cells were allowed to be trapped under an average linear flow velocity of 80 μm/s in the parallel-channel device for approximately 5 min. Complete release of cells was achieved by turning off the AC field and gradually increasing the flow rate. Likewise, **Figure 2.3b** shows the result of an experiment performed under the same conditions in the open-channel device with the exception that the average linear flow velocity was 20 μm/s. This decreased flow rate was required in the absence of micropockets to obtain reliable cell capture. In both cases, the successful capture of the MDA cells is significant because it demonstrates the operation of a DEP device with a wireless BPE array. More specifically, the results show that the capacitive charging of the EDL at the BPE tips transmits the AC field across the device and provides sufficient electric field gradients to exert DEP trapping force.

In addition, it was observed that some of the MDA cells trapped in the open-channel design were washed away when the linear flow velocity was increased from 20 μm/s to 50 μm/s (**Figure 2.3c**). This feature can be exploited to control the maximum number of cells captured at each BPE tip. According to the simulations shown in **Figures 2.2c and 2.2e**, the DEP force in the parallel-channel design is about 2-fold higher than that in the open-channel design, while the flow rate tolerated by trapped cells was about 4-fold higher. Therefore, though the total separation channel width is doubled in the open-channel design, the limitation on accessible flow rates eventually results in an overall decrease in throughput. On the other hand, full release of the captured cells was easier to achieve in the absence of pockets. These

results are significant because they demonstrate that micropockets provide secure capture, while open chambers simplify recovery and downstream analysis.

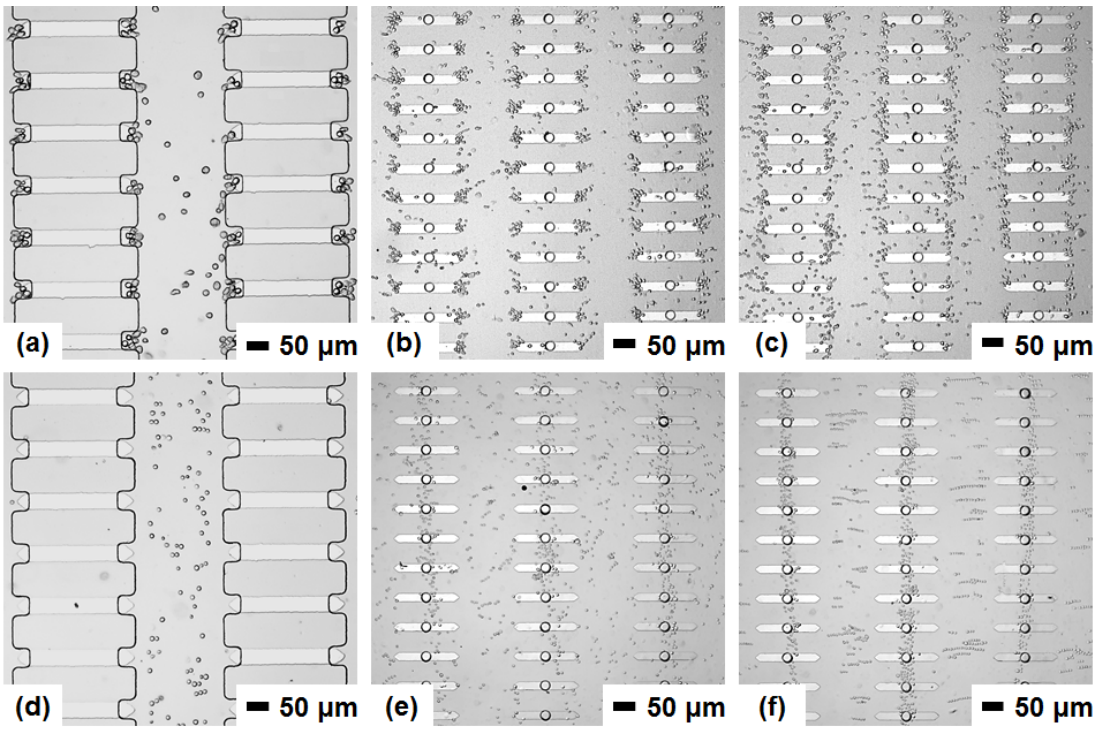

Figure 2.3. Optical micrograph of DEP responses of MDA-MB-231 and Jurkat E6-1 T cells at 40 kHz in the two device designs. (a) The pDEP response of MDA-MB-231 cells in the parallel-channel design (the applied electric field is 13.7 kV/m, the frequency is 40 kHz and the linear flow velocity is 80 µm/s); (b) and (c) The pDEP response of MDA-MB-231 cells in the open-channel design in an electric field of 6.0 kV/m and 40 kHz and a linear flow velocity at 20 µm/s for (b), and at 50 µm/s for (c). (d) The nDEP response of Jurkat E6-1 T cells in the parallel-channel design under the same electric field and linear flow rate conditions employed in (a); (e) and (f) the nDEP response of Jurkat E6-1 T cells in the open-channel design when (e) 10.9 kV/m and (f) 13.3 kV/m was applied, respectively.

Under similar conditions, the Jurkat E6-1 T cells underwent an nDEP response in which they were repelled from the BPE tips and formed 'pearl chains' (**Figures 2.3d-2.3f**). **Figure 2.3d** is an optical image of the cells flowing through the parallel-channel device under an applied voltage of 248 Vpp. **Figures 2.3e and 2.3f** show the response of Jurkat cells in the open-channel device at an applied voltage of 444 Vpp and 543 Vpp, respectively. These higher field strengths were employed to more clearly demonstrate the weak nDEP response. This

weak nDEP response of the Jurkat cells is expected because the maximum nDEP force occurs when Re[$K(\omega)$] = -0.5, while it can reach +1.0 for pDEP. We can draw two primary conclusions from these results. First, at 40 kHz, Jurkat cells remained in flow, and therefore, the clear discrimination of the DEP responses for the two types of cells at 40 kHz indicated that the frequency is sufficient for separation. Second, for the open-channel design, Jurkat cells could be repelled to either of two regions of the chambers with a low electric field – directly above the center line of the BPEs or along the midline between BPEs. This feature is favorable for separation of CTCs from blood because it provides more paths for the large number of blood cells to pass through.

2.4.4 Scaling Strategies

An important advancement afforded by BPEs is the facile scaling of DEP-based devices. When BPEs are arranged in an open-channel design, an applied voltage at the chamber walls results in a linear potential drop along the width of the chamber. The potential difference between the opposite ends of the BPEs (ΔU_{elec}) can then be estimated by:

$$\Delta U_{elec} = \frac{l_{elec}}{n_{ch} w_{ch}} U_{tot} \qquad (1)$$

where U_{tot} represents the applied potential across a microfluidic device; n_{ch}, w_{ch} and l_{elec} are the number of chambers, the width of an individual chamber and length of the BPEs, respectively.

Using eq 1, ΔU_{elec} can thus be estimated to be 5 Vpp when the driving voltage is 248 Vpp (n_{ch} = 4, w_{ch} = 3.6 mm, and l_{elec} = 0.286 mm). Considering that the magnitude of ΔU_{elec} relates to the ability of the BPE to locally perturb the electric field, ΔU_{elec} can be utilized as a parameter for scaling in the open-channel design. Importantly, while such potential differences between opposing ends of a BPE can drive faradaic reactions in a DC field, the AC field

employed for DEP allows much higher potential differences without initiating unwanted electron transfer.[66]

When each BPE is bisected by an insulating wall, as is the case in the parallel-channel design, the barriers lead to a discontinuous/stepped potential profile. The time-averaged electric field (E_{rms}) and DEP force in parallel channels of width 200 µm, 100 µm, and 50 µm were evaluated by numerical simulation. In comparison with a 200 µm-wide parallel-channel device, the 100 µm and 50 µm channels required a higher field strength to achieve a similar DEP force (930 pN). The spatially and time-averaged electric field of $E_{avg,rms}$ = 13.7 kV/m required to achieve this force in the 200 µm channels increased to 17.8 kV/m (130% increase), and 26.0 kV/m (190% increase), respectively. This requirement arises from a decrease in the field gradient ($\nabla|E|$) as the channel width decreases. Consequently, $E_{avg,rms}$ has to be increased to offset the attenuation of $\nabla|E|$. These simulations were compared with experimental results for the pDEP capture of MDA-MB-231 cells in 100 µm- and 50 µm- wide parallel-channel devices. Independent from the simulations, the influence of geometrical parameters such as channel length and BPE length on the electric field were also evaluated.

Table 2.1. Scaling rules in the parallel-channel device.

Chan. Width (µm)	# Chan.	BPE length (µm)	Chan. length (µm) (# Pock.)	Vpp (appl.)	$E_{avg,rms}$ (kV/m)
200	32	2.86	2.56 (22)	248	13.7
100	**4**	**2.86**	2.56 (22)	20.2	17.8
100	4	**8.00**	2.56 (22)	20.2	17.8
100	**8**	2.86	**2.56 (22)**	40.3	17.8
100	8	2.86	**5.20 (44)**	40.3	17.8
50	4	2.86	2.56 (22)	15.0	26.0

Table 2.1 lists the geometrical and electric field parameters for six separate parallel-channel device layouts that demonstrated similar DEP force in MDA-MB-231 capture experiments. Note that for Table 2.1, parameters to be compared within a column are in bold. Further, *channel length* and *number of pockets* were scaled together and are considered as one parameter. These experimental results corroborate the conclusions of the simulations, i.e., when a potential was applied to yield the calculated value of $E_{avg,rms}$, MDA cells could be successfully trapped. Importantly, as was predicted by the simulations, a lower $E_{avg,rms}$ could be applied in a wider channel to achieve sufficient DEP capture force. In addition, the following conclusions can be made: (i) Extension of the length of the BPE under the insulating wall has no effect on the applied voltage (Vpp) required for cell capture, a result which can be ascribed to the extremely low electric resistivity of gold metal (22.14 nΩ·m at 20 °C); (ii) Extending the channel length (to add a proportional number of micropockets) also has no impact on Vpp since this extension is equivalent to adding resistors in parallel; (iii) Doubling the number of parallel channels doubles Vpp required for capturing MDA cells. This increased electric field results from the addition of the number of resistances in series. The consistency of the simulation with the experimental data demonstrates that the parallel-channel design can be optimized following straightforward scaling rules. Most importantly, the route to increased throughput is to minimize BPE length and to add more parallel channels (i and iii above). Capture efficiency is likewise easily improved by extending the channel length (ii above) and the number density of pockets.

2.4.5 Demonstration of Selective Capture of Cancer Cells

The fluorescence micrographs in **Figure 2.4** demonstrate the selective capture of model breast cancer cells from a mixture of both MDA (green) and Jurkat cells (yellow). In this

experiment, the dye-linked antibody-labeled cells were combined in DEP buffer to a final concentration of 5.0 x 10^5 MDA cells/mL and 1.0 x 10^6 Jurkat cells/mL. Considering the extremely low concentration of CTCs encountered in clinical practice, a representative sample would not clearly demonstrate the function of the present approach. For instance, only 5 CTCs would be captured in 1.0 h if the concentration of CTCs were 50 CTCs/mL, yielding ambiguous results, especially regarding the fidelity of single-cell capture. Therefore, a high concentration of CTCs was employed here with the view that the observed behavior could be extended to fewer cells. Importantly, evaluation of capture efficiency in the recovery of rare cells is forthcoming. We anticipate that the capture of CTCs at concentrations representative of what is observed in clinical practice is feasible. The challenges posed by these low concentrations are shared by all other CTC isolation schemes – namely, avoidance of cell loss during sample preparation and longer run times. In the parallel-channel design, the mixed cell sample was flowed into the device at an average linear velocity rate of 60 μm/s, and a 40 kHz AC field was applied. After allowing the MDA cells to be trapped at the BPE tips, fluorescence images for each dye (Alexa 488/green and phycoerythrin/yellow) were taken in rapid sequence and overlayed to obtain the image shown in **Figures 2.4a and 2.4b**. As shown in **Figure 2.4**, only breast cancer cells (green) were trapped and accumulated at the BPE tips, while the white blood cells (yellow) flowed past. Similar results were obtained in the open-channel device with the exception that a much lower flow rate (20 μm/s) was required to allow capture of MDA cells (**Figures 2.4c and 2.4d**). These results are significant because they demonstrate the selective capture of breast cancer cells from white blood cells in a high-throughput DEP device at an array of wireless electrodes.

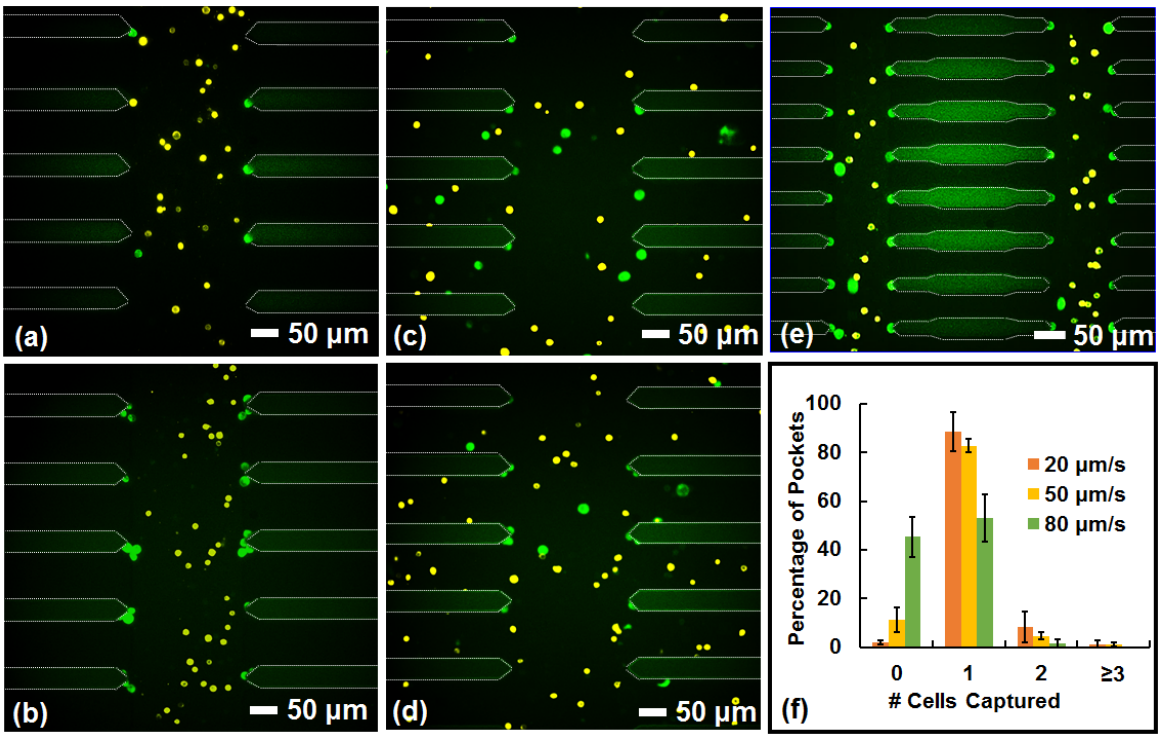

Figure 2.4. Demonstration of the capability of selective capture in both designs, and single-cell capture in a parallel-channel device with decreased pocket size. In all the fluorescent micrographs, 40 kHz AC electric field was applied to a mixture of the two cell types (MDA-MB-231 (green) and Jurkat (yellow)), in which MDA-MB-231 cells were labeled with Alexa Fluor® 488 anti-human EGFR antibody, and Jurkat cells were labeled with PE anti-human CD45 antibody. The response was recorded after the AC voltage was applied for 1 min (a), and for 3 min (b) in the parallel-channel design and for 1 min (c) and 3 min (d) in the open-channel design. (e) Fluorescent micrograph showing the capture of single MDA-MB-231 cells (green) after 3 min of AC field application in the modified parallel-channel design. (f) A plot of the single-cell capture performance at three average linear flow velocities (n = 3).

2.4.5 Demonstration of Single-Cell Capture

CTCs have shown clinic importance for determining prognosis and for guiding therapeutic decisions.[67,68] However, due to the cellular heterogeneity among CTCs from an individual patient, molecular analyses using collective cell samples can only provide averaged data, which may obscure critical information about subpopulations.[69,70] To obtain a complete picture of the genetic variability extant in tumor tissue, the development of single-cell isolation techniques becomes essential. To test the ability of the parallel-channel device to achieve

single-cell capture by geometric constraint, we decreased the pocket size from 40 μm long x 40 μm wide to 30 μm long x 25 μm wide. Pearl-chaining of cells can occur when there is insufficient drag force competing with the DEP capture force, and therefore, selective single-cell capture of MDA-MB-231 cells from Jurkat E6-1 T cells was evaluated under various flow rates. After MDA cells were captured under each flow rate for approximately 5 min, images were taken and the number of MDA cells at each pocket along 4 parallel channels was counted and averaged. According to the results shown in **Figure 2.4**, it can be concluded that: (i) The present device is robust in selectively isolating single cells under various flow rates. (ii) Over 80% of pockets obtained individual MDA cells when the flow rate was less than 50 μm/s. Increasing the flow rate beyond 50 μm/s decreased the likelihood of trapping multiple cells per chamber; (iii) Regardless of flow rate, multi-cell capture was rare (＜2%) using the current design. A key point is that the single-cell capture rate is far better than can be achieved by randomly partitioning the sample, for which Poisson statistics predicts that when 37% of pockets contain a single cell, there will also be 37% empty, 18% with double occupancy and 7% containing three or more. Further, our design leaves open the option to capture cells under a slow flow rate and to subsequently disrupt multiple occupancies by increasing the flow rate. It is worth mention that the 10 μm gap between the BPE tip and the micropocket opening plays a crucial role in capturing and stabilizing single cells. The strategy demonstrated here not only meets the challenge of high-throughput and selective CTC isolation by DEP, but also enables single-cell capture. In subsequent studies, we aim to exploit electrochemistry at individual BPEs and to adapt micropocket geometry to accomplish on-chip analysis of individual cells.

2.5 Conclusion

DEP-based techniques are advantageous for the isolation of CTCs because they do not suffer from the same bias as immunoaffinity-based techniques while being more selective than capture based on physical properties of cells alone. However, DEP devices generally suffer from low volumetric throughput, which is especially problematic for rare cells, such as CTCs. We have demonstrated that the integration of wireless electrodes allows for the creation of DEP devices that are easily scalable along the *x*- and *y*- directions. Additionally, removing the need for wire leads enables device architectures, such as branching microchannels, which further increase throughput. Using the parallel-channel design reported here, about 0.1 mL/h throughput could be achieved with a 39.6 mm^2 device footprint. If the device were scaled to 7500 mm^2, the footprint of a previously reported DEP device, a throughput of 18.9 mL/h would be anticipated.[39] Even if the device were scaled to 2.21 $x10^3$ mm^2, the footprint of the ApoStream device reported,[44] the throughput would still be over 5.5 mL/h. In this scenario, we expect that 1.0 mL of blood could be processed in approximately 11 min. In addition, assuming 1-100 CTCs/mL of whole blood, the present parallel-channel device can process the standard volume (7.5 mL) employed in the commercial CellSearch system, without exhausting the 1408 capture sites (in the 40 mm^2 device). If a buffy coat from 1.0 mL of blood suspended to 100 μL DEP buffer is utilized, a ten-fold decrease in separation time can be expected. Furthermore, due to the incorporation of micropockets into the parallel-channel design, single-cell capture was readily achieved by adjusting the size of pockets to the size of the targeted cells. The present BPE array-based designs exhibit significant advancements in DEP technology including wireless control of the AC field and enhanced design flexibility – which led to increased throughput and high-fidelity parallel single-cell capture. These advancements are

made while retaining the inherent advantages of DEP including selective and label-free isolation of cells and ease of fabrication, which provide an avenue to utilize the devices for point-of-care applications. Further evaluation of the capture efficiency and the performance of the technique in clinical samples are in progress in our laboratory.

2.6 References

1. Dong, Y.; Skelley, A. M.; Merdek, K. D.; Sprott, K. M.; Jiang, C.; Pierceall, W. E.; Lin, J.; Stocum, M.; Carney, W. P.; Smirnov, D. A. *J. Mol. Diagn.* **2013**, *15*, 149.

2. Miller, M. C.; Doyle, G. V.; Terstappen, L. W. *J. Oncol.* **2010**, *2010*, 617421.

3. Bouche, O.; Beretta, G. D.; Alfonso, P. G.; Geissler, M. *Cancer. Treat. Rev.* **2010**, *36 Suppl 1*, S1.

4. Den Toonder, J. *Lab Chip* **2011**, *11*, 375.

5. Jin, C.; McFaul, S. M.; Duffy, S. P.; Deng, X.; Tavassoli, P.; Black, P. C.; Ma, H. *Lab Chip* **2014**, *14*, 32.

6. Allard, W. J.; Matera, J.; Miller, M. C.; Repollet, M.; Connelly, M. C.; Rao, C.; Tibbe, A. G.; Uhr, J. W.; Terstappen, L. W. *Clin. Cancer. Res.* **2004**, *10*, 6897.

7. Meng, S.; Tripathy, D.; Frenkel, E. P.; Shete, S.; Naftalis, E. Z.; Huth, J. F.; Beitsch, P. D.; Leitch, M.; Hoover, S.; Euhus, D. *Clin. Cancer. Res.* **2004**, *10*, 8152.

8. Park, S.; Ang, R. R.; Duffy, S. P.; Bazov, J.; Chi, K. N.; Black, P. C.; Ma, H. *PloS. One.* **2014**, *9*, e85264.

9. Grover, P. K.; Cummins, A. G.; Price, T. J.; Roberts-Thomson, I. C.; Hardingham, J. E. *Ann. Oncol.* **2014**, *25*, 1506.

10. Dharmasiri, U.; Njoroge, S. K.; Witek, M. A.; Adebiyi, M. G.; Kamande, J. W.; Hupert, M. L.; Barany, F.; Soper, S. A. *Anal. Chem.* **2011**, *83*, 2301.

11. Stott, S. L.; Hsu, C. H.; Tsukrov, D. I.; Yu, M.; Miyamoto, D. T.; Waltman, B. A.; Rothenberg, S. M.; Shah, A. M.; Smas, M. E.; Korir, G. K.; Floyd, F. P., Jr.; Gilman, A. J.; Lord, J. B.; Winokur, D.; Springer, S.; Irimia, D.; Nagrath, S.; Sequist, L. V.; Lee, R. J.; Isselbacher, K. J.; Maheswaran, S.; Haber, D. A.; Toner, M. *Proc. Natl. Acad. Sci. USA* **2010**, *107*, 18392.

12. Johnson, E. S.; Anand, R. K.; Chiu, D. T. Anal. Chem. 2015, 87, 9389.

13. Schiro, P. G.; Zhao, M.; Kuo, J. S.; Koehler, K. M.; Sabath, D. E.; Chiu, D. T. Angew. Chem. Int. Ed. Engl. 2012, 51, 4618.

14. Mikolajczyk, S. D.; Millar, L. S.; Tsinberg, P.; Coutts, S. M.; Zomorrodi, M.; Pham, T.; Bischoff, F. Z.; Pircher, T. J. *J. Oncol.* **2011**, *2011*, 252361.

15. Yu, M.; Bardia, A.; Wittner, B. S.; Stott, S. L.; Smas, M. E.; Ting, D. T.; Isakoff, S. J.; Ciciliano, J. C.; Wells, M. N.; Shah, A. M.; Concannon, K. F.; Donaldson, M. C.; Sequist, L. V.; Brachtel, E.; Sgroi, D.; Baselga, J.; Ramaswamy, S.; Toner, M.; Haber, D. A.; Maheswaran, S. *Science* **2013**, *339*, 580.

16. Sheng, W.; Ogunwobi, O. O.; Chen, T.; Zhang, J.; George, T. J.; Liu, C.; Fan, Z. H. *Lab Chip* **2014**, *14*, 89.

17. Gerhardt, T.; Woo, S.; Ma, H. *Lab Chip* **2011**, *11*, 2731.

18. Ji, H. M.; Samper, V.; Chen, Y.; Heng, C. K.; Lim, T. M.; Yobas, L. *Biomed. Microdev.* **2008**, *10*, 251.

19. McFaul, S. M.; Lin, B. K.; Ma, H. *Lab Chip* **2012**, *12*, 2369.

20. Tan, S. J.; Lakshmi, R. L.; Chen, P.; Lim, W. T.; Yobas, L.; Lim, C. T. *Biosens. Bioelectron.* **2010**, *26*, 1701.

21. Fan, X.; Jia, C.; Yang, J.; Li, G.; Mao, H.; Jin, Q.; Zhao, J. Biosens. Bioelectron. 2015, 71, 380.

22. Zheng, S.; Lin, H. K.; Lu, B.; Williams, A.; Datar, R.; Cote, R. J.; Tai, Y. C. *Biomed. Microdev.* **2011**, *13*, 203.

23. Zheng, S.; Lin, H.; Liu, J. Q.; Balic, M.; Datar, R.; Cote, R. J.; Tai, Y. C. *J. Chromatogr. A.* **2007**, *1162*, 154.

24. Vona, G.; Sabile, A.; Louha, M.; Sitruk, V.; Romana, S.; Schutze, K.; Capron, F.; Franco, D.; Pazzagli, M.; Vekemans, M.; Lacour, B.; Brechot, C.; Paterlini-Brechot, P. *Am. J. Pathol.* **2000**, *156*, 57.

25. Kim, Y. J.; Kang, Y. T.; Cho, Y. H. Anal. Chem. 2016, 88, 7938.

26. Ma, Y. C.; Wang, L.; Yu, F. L. Technol. Cancer. Res. Treat. 2013, 12, 295.

27. Hofman, V.; Bonnetaud, C.; Ilie, M. I.; Vielh, P.; Vignaud, J. M.; Flejou, J. F.; Lantuejoul, S.; Piaton, E.; Mourad, N.; Butori, C.; Selva, E.; Poudenx, M.; Sibon, S.; Kelhef, S.; Venissac, N.; Jais, J. P.; Mouroux, J.; Molina, T. J.; Hofman, P. *Clin. Cancer. Res.* **2011**, *17*, 827.

28. De Giorgi, V.; Pinzani, P.; Salvianti, F.; Panelos, J.; Paglierani, M.; Janowska, A.; Grazzini, M.; Wechsler, J.; Orlando, C.; Santucci, M.; Lotti, T.; Pazzagli, M.; Massi, D. *J. Invest. Dermatol.* **2010**, *130*, 2440.

29. Inglis, D. W. *Appl. Phys. Lett.* **2009**, *94*, 013510.

30. Warkiani, M. E.; Khoo, B. L.; Wu, L.; Tay, A. K.; Bhagat, A. A.; Han, J.; Lim, C. T. *Nat. Protoc.* **2016**, *11*, 134.

31. Loutherback, K.; D'Silva, J.; Liu, L.; Wu, A.; Austin, R. H.; Sturm, J. C. *AIP. Adv.* **2012**, *2*, 42107.

32. Sun, J.; Li, M.; Liu, C.; Zhang, Y.; Liu, D.; Liu, W.; Hu, G.; Jiang, X. *Lab Chip* **2012**, *12*, 3952.

33. Hyun, K. A.; Kwon, K.; Han, H.; Kim, S. I.; Jung, H. I. *Biosens. Bioelectron.* **2013**, *40*, 206.

34. Moon, H. S.; Kwon, K.; Hyun, K. A.; Seok Sim, T.; Chan Park, J.; Lee, J. G.; Jung, H. I. *Biomicrofluidics* **2013**, *7*, 14105.

35. Gascoyne, P. R.; Vykoukal, J. Electrophoresis 2002, 23, 1973.

36. Gagnon, Z. R. Electrophoresis 2011, 32, 2466.

37. Pethig, R. *Biomicrofluidics* **2010**, *4*, 022811.

38. Alazzam, A.; Stiharu, I.; Bhat, R.; Meguerditchian, A. N. *Electrophoresis* **2011**, *32*, 1327.

39. Gascoyne, P. R.; Noshari, J.; Anderson, T. J.; Becker, F. F. *Electrophoresis* **2009**, *30*, 1388.

40. Henslee, E. A.; Sano, M. B.; Rojas, A. D.; Schmelz, E. M.; Davalos, R. V. *Electrophoresis* **2011**, *32*, 2523.

41. Kim, S. H.; Fujii, T. *Lab Chip* **2016**, 16, 2440.

42. Liu, Z.; Huang, F.; Du, J.; Shu, W.; Feng, H.; Xu, X.; Chen, Y. *Biomicrofluidics* **2013**, *7*, 11801.

43. Čemažar, J.; Douglas, T. A.; Schmelz, E. M.; Davalos, R. V. *Biomicrofluidics* **2016**, *10*, 014109.

44. Gupta, V.; Jafferji, I.; Garza, M.; Melnikova, V. O.; Hasegawa, D. K.; Pethig, R.; Davis, D. W. *Biomicrofluidics* **2012**, *6*, 24133.

45. Cheng, I. F.; Huang, W. L.; Chen, T. Y.; Liu, C. W.; Lin, Y. D.; Su, W. C. Lab Chip 2015, 15, 2950.

46. Moon, H. S.; Kwon, K.; Kim, S. I.; Han, H.; Sohn, J.; Lee, S.; Jung, H. I. Lab Chip 2011, 11, 1118.

47. Fabbri, F.; Carloni, S.; Zoli, W.; Ulivi, P.; Gallerani, G.; Fici, P.; Chiadini, E.; Passardi, A.; Frassineti, G. L.; Ragazzini, A.; Amadori, D. Cancer Lett 2013, 335, 225.

48. Anand, R. K.; Sheridan, E.; Knust, K. N.; Crooks, R. M. *Anal. Chem.* **2011**, *83*, 2351.

49. Anand, R. K.; Sheridan, E.; Hlushkou, D.; Tallarek, U.; Crooks, R. M. *Lab Chip* **2011**, *11*, 518.

50. Perdue, R. K.; Laws, D. R.; Hlushkou, D.; Tallarek, U.; Crooks, R. M. *Anal. Chem.* **2009**, *81*, 10149.

51. Chow, K. F.; Mavre, F.; Crooks, J. A.; Chang, B. Y.; Crooks, R. M. *J. Am. Chem. Soc.* **2009**, *131*, 8364.

52. Mavré, F. o.; Anand, R. K.; Laws, D. R.; Chow, K.-F.; Chang, B.-Y.; Crooks, J. A.; Crooks, R. M. *Anal. Chem.* **2010**, *82*, 8766.

53. Li, M.; Anand, R. K. *Analyst* **2016**, *141*, 3496.

54. Anand, R. K.; Johnson, E. S.; Chiu, D. T. *J. Am. Chem. Soc.* **2015**, *137*, 776.

55. Crooks, R. M. *Chemelectrochem* **2016**, *3*, 357.

56. Oja, S. M.; Zhang, B. *ChemElectroChem* **2016**, *3*, 457.

57. Kostiuchenko, Z. A.; Zhang, B.; Lemay, S. G. *J. Phys. Chem. C.* **2016**, *120*, 22777.

58. Essmann, V.; Barwe, S.; Masa, J.; Schuhmann, W. *Anal. Chem.* **2016**, 88, 8835.

59. Xu, W.; Fu, K.; Ma, C.; Bohn, P. W. *Analyst* **2016**, 141, 6018.

60. Velev, O. D.; Gangwal, S.; Petsev, D. N. Annu Rep Prog Chem C 2009, 105, 213.

61. Velev, O. D.; Bhatt, K. H. Soft Matter 2006, 2, 738.

62. Menachery, A.; Pethig, R. *IEE. Proc. Nanobiotechnol*. **2005**, 152, 145.

63. Voldman, *J. Annu. Rev. Biomed.* **2006**, *8*, 425.

64. Zhu, K.; Kaprelyants, A. S.; Salina, E. G.; Markx, G. H. *Biomicrofluidics* **2010**, *4*, 022809.

65. Shim, S.; Stemke-Hale, K.; Tsimberidou, A. M.; Noshari, J.; Anderson, T. E.; Gascoyne, P. R. *Biomicrofluidics* **2013**, *7*, 11807.

66. Gagnon, Z.; Chang, H. C. *Electrophoresis* **2005**, *26*, 3725.

67. Parkinson, D. R.; Dracopoli, N.; Petty, B. G.; Compton, C.; Cristofanilli, M.; Deisseroth, A.; Hayes, D. F.; Kapke, G.; Kumar, P.; Lee, J.; Liu, M. C.; McCormack, R.; Mikulski, S.; Nagahara, L.; Pantel, K.; Pearson-White, S.; Punnoose, E. A.; Roadcap, L. T.; Schade, A. E.; Scher, H. I.; Sigman, C. C.; Kelloff, G. J. *J. Transl. Med.* **2012**, *10*, 138.

68. Krebs, M. G.; Metcalf, R. L.; Carter, L.; Brady, G.; Blackhall, F. H.; Dive, C. *Nat. Rev. Clin. Oncol.* **2014**, *11*, 129.

69. Kim, J.; Cho, H.; Han, S. I.; Han, K. H. *Anal. Chem.* **2016**, *88*, 4857.

70. Armbrecht, L.; Dittrich, P. S. *Anal. Chem.* **2016**, 89, 2.

2.7 Supporting Information

2.7.1 Device Fabrication

The high-throughput microfluidic devices were fabricated using standard photolithography and etching processes. First, BPE arrays were patterned using positive photoresist (AZ P4620; MicroChemicals GmbH, Ulm, Germany) on glass slides coated with 50 Å Cr and 1000 Å Au, followed by wet-etching the Au (KI: I_2: H_2O = 4.0 g: 1.0 g: 40 mL)

and the Cr (chromium etchant; Sigma Aldrich, St. Louis, MO), respectively. Acetone was employed to dissolve the remaining photoresist. Second, channel molds were patterned using a negative photoresist (SU-8 2025; Microchem Corp., Westborough, MD) on a Si substrate. Subsequently, PDMS precursor was poured on the SU-8 mold and cured at 70 ^{o}C for 2 h. The alignment of PDMS microchannels with BPE arrays was carried out as follows. First, the slides with electrode pattern and PDMS channels were exposed to an air plasma (Plasma cleaner, Harrick Scientific, Ithaca, NY) for 90 s to activate the surfaces for permanent bonding. Second, a few drops of ethanol were applied on both surfaces to delay bonding and to facilitate the alignment. Third, the aligned device was baked at 70 ^{o}C for 2 h to completely drive off the ethanol and to encourage bonding. Finally, 3.0 μM Pluronic in 1.0 mM DEP buffer was injected into channels *via* vacuum (to remove entrapped air) and kept at room temperature overnight to coat the channel surface (to reduce non-specific adsorption of cells). After coating with Pluronic, all channels were rinsed with DEP buffer for 15 min before DEP experiments.

2.7.2 Fluorescent Labeling

MDA-MB-231 cells and Jurkat E6-1 T cells were labeled with Alexa Fluor® 488 anti-human EGFR antibody and phycoerythrin (PE) anti-human CD45 antibody (BioLegend; San Diego, CA), respectively. Briefly, 5.0 μL of the appropriate antibody solution was diluted to 100 μL in cell labeling buffer (1X PBS with 10% FBS) to label one million cells. The detailed labeling procedure was as follows. First, the antibody solution was vortexed for 1 min to disperse antibodies and to break up aggregates. 5.0 μL of this solution was subsequently diluted in cell labeling buffer (to 100 μL). Second, the mixture was centrifuged at 15,000 x g (4.0 °C, 10 min) and 5.0 μL at the bottom (containing aggregates) was discarded. The cell pellets were washed with 1X PBS buffer before suspending at 1.0 x 10^6 cells/100 μL in this labeling mixture. Third, the cells in labeling mixture were kept on a rocker at room temperature for 1 hr. Finally, the cells were washed with DEP buffer twice and resuspended at a concentration of 1.0 x 10^6 cells/mL. Pre-stained MDA cells were then spiked into Jurkat E6-1 T cells for subsequent separation experiments. To determine the mean spiking count, 5.0 μL of the mixed cell solution were pipetted on a microscope slide and manually counted in triplicate.

2.7.3 Investigation of Separation Frequency Using Quadruple Electrodes

The quadruple electrodes were designed with 500 μm width and 100 μm gap between adjacent edges. The electrodes were connected to a Tektronix AFG3011C waveform generator (Tektronix, Beaverton, OR) with copper tape as described previously.[1] After adding 100 μL of the cell suspension to the quadrupole electrodes, a glass coverslip was placed on top. 10 Vpp was applied between neighboring electrodes, and images were taken after 3 min to determine whether cells underwent a pDEP or nDEP response. Subsequently, the frequency was increased in 10 kHz increments over the range of 1 kHz to 100 kHz. Results indicated that MDA-MB-231 cells experienced strong pDEP from 40 kHz to 70 kHz, while the majority of Jurkat-E6 T cells underwent an nDEP response (a few Jurkat cells were attracted on the edges of the electrodes from 50 kHz to 70 kHz). Therefore, 40 kHz was chosen as the separation frequency to obtain a clear discrimination of the two cell types.

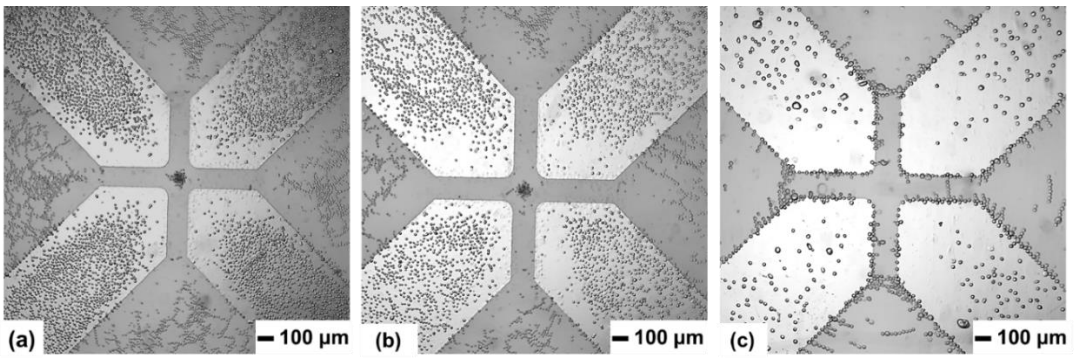

Figure 2.5. Images of DEP response of MDA-MB-231 cells and Jurkat E6-1 T cells as a function of frequency. nDEP response of Jurkat cells at (a) 50 kHz; (b) 70 kHz; pDEP response of MDA cells at (c) 70 kHz.

2.7.4 Device Optimization

To optimize BPE and channel design, COMSOL simulation software (COMSOL Multiphysics 5.2a) was employed. The dimensions used in the simulations are as follows. The channels were 100 µm wide with 60 µm (long) x 60 µm (wide) pockets separated by 120 µm (edge-to-edge distance). The tip of each of the BPEs is overlapped with the outer edge of a micropocket. The voltage difference applied between adjacent BPEs is 4 Vpp, leading to the averaged electric field of 40 kV/m.

2.7.4.1 Triangle or Square BPE

The electric field distribution resulting from two BPE shapes, i.e. triangle and square, were simulated. As shown in **Figure 2.6**. The highest electric field is located at the corner of each square BPE; while for triangle BPEs, it reaches a maximum at the electrode tips. Therefore, BPEs with triangular tips are beneficial for positioning cells at the center of each micropocket.

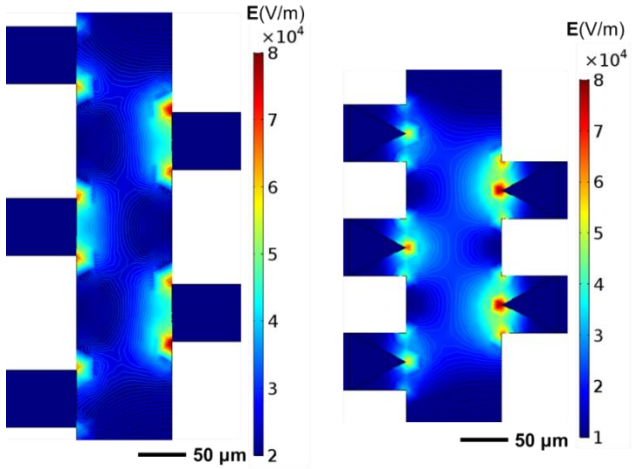

Figure 2.6. Electric field simulation in an array-based design using square BPE (left) and triangle BPE (right).

2.7.4.2 Parallel or Staggering BPE

The utilization of a staggered layout for the BPEs leads to differences in the electric field maxima among individual BPE tips as shown in **Figure 2.6**. Though this non-uniformity only impacts BPEs located near the ends of a channel (**Figure 2.7**), it may cause more cells to be trapped at one side than the other and is not favorable for single-cell capture. However, the maximum field intensity is uniform for each individual BPE if the arrangement changes to parallel. Therefore, parallel BPEs were chosen for the DEP capture experiments reported in the main text.

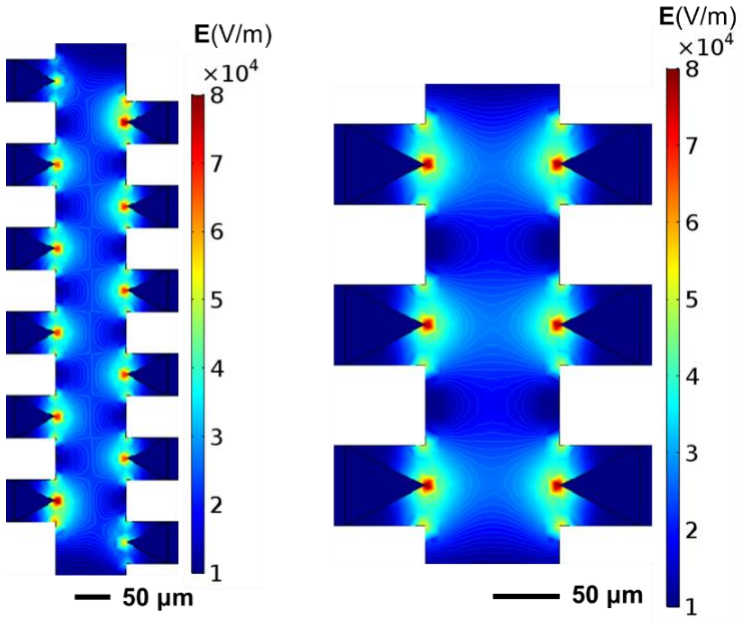

Figure 2.7. Electric field simulation in an array-based design using a large number of staggering (left) and parallel (right) BPEs with triangular tips.

2.7.4.3 BPE Tip Position

Considering that fast fluid flow may wash away the cells trapped at the electrodes, in the parallel-channel design, recessing the BPE tips into the micropockets was used as a strategy to enhance capture efficiency. We assessed the impact on the electric field of recessing the tips to two distinct distances (10 μm and 40 μm) from the micropocket opening. According to the results of the simulation, shown in **Figure 2.8**, the electric field along the channel becomes too weak to trap cells if the BPE tips are recessed to 40 μm away from the channel. Furthermore, undesirable electric field 'hot spots' appeared at the micropocket corners, which could compete with the desired capture site. However, if the recessed distance is 10 μm, which is comparable to the radius of MDA-MB-231 cells, the distribution of the electric field created a path for cells to be pulled by pDEP from the channel to the BPE tip. In this arrangement, the micropocket stabilizes the captured cell against being carried away by drag force. Based on the above considerations, a design with a 10 μm distance between the channel and BPE tip was selected.

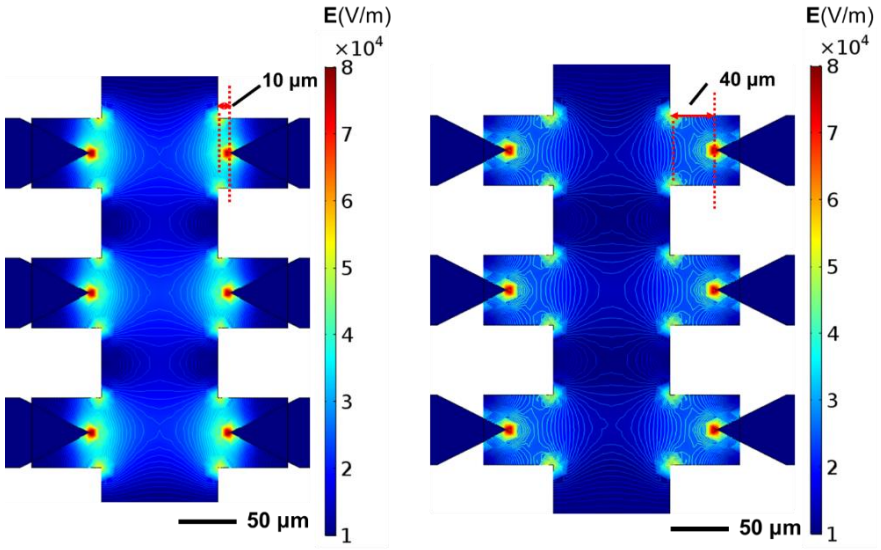

Figure 2.8. Two-dimensional numerical simulation of the electric field distribution with BPEs recessed to a distance of 10 μm (left) and 40 μm (right) away from the microchannel.

2.7.4.4 BPE Tip Sharpness

Finally, when BPEs with pointed (triangular) tips are employed, the electric field is focused at the tip, which may result in overly high local field strength and the loss of cell viability. Therefore, all the BPE tips were rounded with a radius of curvature of 5 μm (**Figure 2a**, main text). These rounded tips distribute the strongest region of the electric field over a broader area, thereby decreasing the likelihood of damage to cells. Such defocusing of the electric field decreases pDEP force at the BPE tip, and therefore, the radius of curvature must be limited to maintain good trapping performance.

2.7.5 Complete Drawing of the Two High-Throughput Designs

The microchannels are in light grey and the electrodes are in dark grey. The electrode design keep the same in both devices.

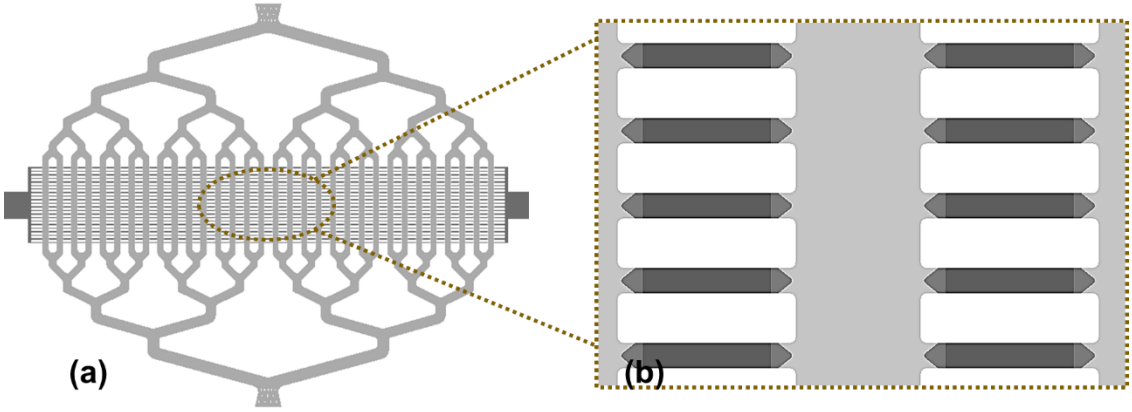

Figure 2.9. The AutoCAD drawing of the parallel-channel design. (a) zoom-out image; (b) zoom-in image.

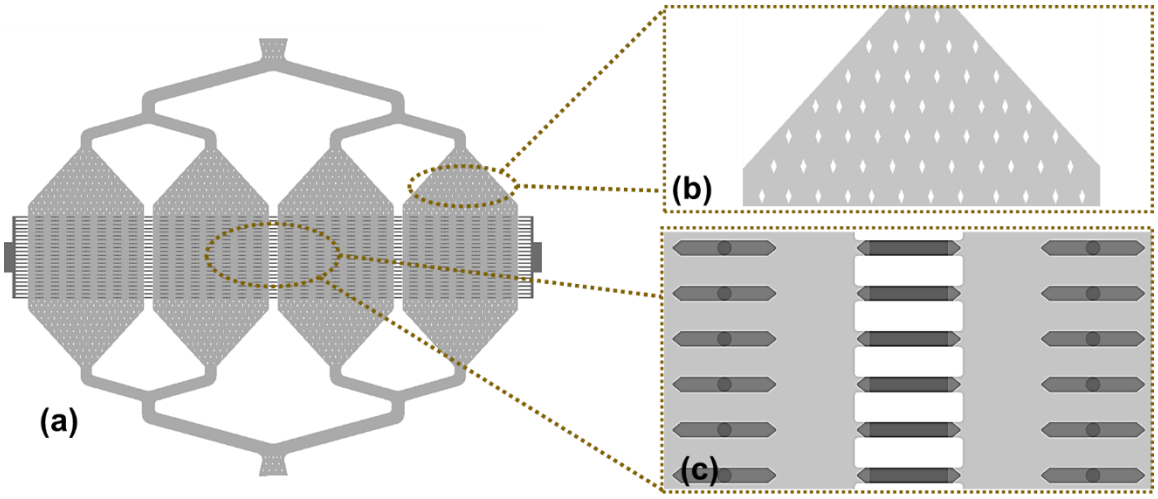

Figure 2.10. The AutoCAD drawing of the open-channel design. (a) zoom-out image; (b) zoom-in image of the diamond-shaped pillars; (c) zoom-in image of the channels near chamber junction.

2.7.6 Reference

1. Sabuncu, A. C.; Asmar, A. J.; Stacey, M. W.; Beskok, A. *Electrophoresis.* **2015**, *36*, 1499.

CHAPTER 3

CELLULAR DIELECTROPHORESIS COUPLED WITH SINGLE-CELL ANALYSIS

A paper published in Analytical and Bioanlytical Chemistry

Min Li, Robbyn K. Anand *

Department of Chemistry, Iowa State University, Ames, Iowa 50011, United States

* Corresponding Author

Abstract

In this review, recent advances that leverage dielectrophoretic (DEP) approaches to accomplish single-cell analysis (both 'on-chip' and 'off-chip') are discussed with special emphasis on eukaryotic cells. DEP as an electric field-induced force utilized for cell manipulation, can confer selectivity without labeling. Recent technical improvements have increased the volumetric throughput of the separation of cells from complex mixtures, introduced new strategies for massively-parallel single-cell confinement for subsequent on-chip analysis, enabled selective transport of individual cells off chip, and integrated pre-concentration and pre-focusing steps to enhance DEP performance. Collectively, these studies potentiate all-in-one platforms capable of taking as their input complex mixtures of cells and accomplishing single-cell analysis. Assays requiring small reaction volumes (e.g., enzymatic assays, FISH, and immunostaining) have been demonstrated. Still greater opportunities to unravel cell-to-cell variations and for point-of-care applications can be realized by enabling on-chip gene amplification, live-cell assays, and either DEP manipulation in native media, or

on-chip media exchange. We therefore conclude with a discussion of emerging capabilities in these areas.

3.1 Introduction

Single-cell analysis has had a major impact on many aspects of the life sciences, clinical diagnostics and the evaluation of pharmaceutical agents.[1] Conventional methods that analyze collective cell samples assume that average cellular response is representative of individual cells. Despite the tremendous progress that has been made using these methods, the impact of cellular heterogeneity on observed biological responses is nontrivial.[2] For instance, differences in the genetic mutations harbored by circulating tumor cells (CTCs) stemming from the same localized tumor are well documented.[3-5] Further, significant levels of phenotypic heterogeneity are commonly observed in a clonal or isogenic cell population.[6,7] A plethora of evidence has shown that this cellular heterogeneity dramatically affects cell decision-making and cell fate.[8] Moreover, a minority of cells can have far reaching implications in cancer etiology, progression, and response to therapy.[9] Consequently, the development of techniques to address the effects of cell heterogeneity is critically important.

Lab-on-a-chip (LOC) technologies have opened up many possibilities for the manipulation and analysis of single cells.[10-12] First, the dimensions (10-1000 μm) of LOC devices enable assays of biological cells on pico- to microliter scales. Structures such as microwells,[13,14] microchambers,[15,16]dams,[17,18] and functionalized surfaces [19,20] can be readily embedded for cell isolation or volume confinement. Second, the distinct laminar flow found in microfluidic systems allows local control over the chemical and physical environment – such as dosing selected cells. Furthermore, by mixing of immiscible materials, microdroplets can be formed for single-cell encapsulation, combination with reagents, and high-throughput

detection.[21-23] A wide range of applications hitherto bears testimony to the fact that LOCs are cost-effective, convenient, and robust for single-cell analysis.

Cell manipulation such as isolation of target cells from a tissue sample and direction of cells to a desired location is an inevitable step of overall analysis. Among numerous manipulation techniques, dielectrophoresis (DEP) has distinct advantages in that it is antibody-independent, non-invasive and highly selective.[24-26] Further, its high-output cell viability and label-free selectivity are crucial for further *in vivo* or *in vitro* mechanistic studies. It is reported that the viability of biological cells after DEP operation can be up to 97.1%,[27] and these cells show no difference in growth compared to DEP treatment-free cells.[27,28] Most importantly, DEP-based separation exhibits a desirable degree of selectivity when compared with size- and antibody-based approaches (which can be under- and over- selective, respectively) as it leverages a wealth of information in terms of composition and morphology, which lead to the dielectric properties of bioparticles.[29,30] As demonstrated in dielectrophoretic field-flow fractionation (DEP-FFF), over 90% efficiency was achieved when isolating three different kinds of tumor cells from a "buffy coat".[31] Henslee *et al.* also proved that MDA-MB-231 cells (late-stage cancer cells) could be successfully differentiated from a population of MCF10A and MCF7 cells (early and intermediate-stage cancer cells).[32] Due to these advantages, DEP techniques have been therefore widely applied in cell isolation, focusing and transport.

In this review, we summarize the current state of DEP approaches for single-cell manipulation and analysis with special emphasis on eukaryotic cells. A review of DEP as applied to prokaryotic cells such as bacteria can be found in prior work.[33] Considering that DEP-based methods can address several experimental steps, from processing complex mixtures of cells to single-cell analysis, various functional zones are frequently integrated into

one device. Technical improvement of any of these procedures is vital to enhance the accuracy and efficiency of overall analysis. Therefore, we will address these procedures separately to clarify the role of cellular DEP in single-cell analysis. Following a brief summary of the theory of DEP, we will discuss the application of DEP to the separation and concentration of cells and to the trapping and transport of individual cells for subsequent characterization. This final analysis step may occur either in the same device ('on-chip') or downstream ('off-chip'). These sections will be followed by a discussion of techniques employed for pre-focusing and pre-concentration of cells prior to separation. Finally, we will address current limitations and challenges to the application of DEP in single-cell analysis and identify opportunities for extension of these techniques.

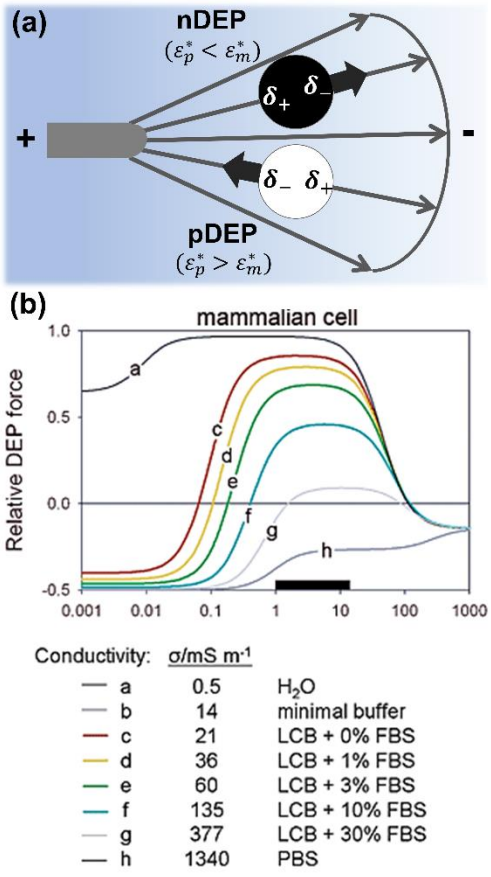

Scheme 3.1. Illustration of nDEP and pDEP mechanism (left) and the CM factor of mammalian cells in low and high conductivity (σ) solution (right, reproduced from Ref.[37].)

3.2 Technical Background

DEP [34-36] is defined as a field-induced force (F_{DEP}) exerted on particles due to the interaction of the dipole moment (***P***) of a particle and the spatial gradient of an external electric field ($\nabla \boldsymbol{E}$) (**Scheme 3.1a**). The external electric field (E) induces partial charges (δ_+ and δ_-) at the particle-medium interfaces *via* free charge and/or polarization charge to a degree dependent upon the frequency applied. When each half of the dipole is in a field of different magnitude, the case in a non-uniform electric field ($\nabla \boldsymbol{E}$), the resultant net force is non-zero leading to acceleration of the particle. For a homogeneous spherical particle placed in a linearly polarized sinusoidal field, the time-averaged DEP force is given by:

$$\overrightarrow{F_{DEP}} = 2\pi r^3 \varepsilon_m Re[K(\omega)]\vec{\nabla}\left|\vec{E}\right|^2 \quad (1)$$

where Re[$K(\omega)$] is the real part of the Clausius-Mossotti factor,

$$K(\omega) = \frac{\varepsilon_p^* - \varepsilon_m^*}{\varepsilon_p^* + 2\varepsilon_m^*} \quad (2)$$

and for which r is the particle radius; ε_m is the permittivity of the medium; and ε_p^* and ε_m^* are the frequency-dependent complex permittivitties of the particle and medium, respectively. Re[K(ω)] indicates the direction and relative strength of DEP force experienced by the particle and ranges from -0.5 to +1.0. When Re[$K(\omega)$] is positive, which indicates that the particle is relatively more polarizable than the medium, the net DEP force directs particles toward higher electric field (positive DEP, or pDEP). Accordingly, when Re[$K(\omega)$] is negative, the DEP force displaces particles toward lower electric field (negative or nDEP). Notably, the sign and magnitude of Re[$K(\omega)$] is a function of frequency and can further be tuned by medium conductivity, which impacts ε_m^*. For instance, increasing the medium conductivity leads to an increase of the crossover frequency (*cof*) at which biological cells transition from an nDEP to

a pDEP response. Under conditions of high medium conductivity, such as that encountered in 1X phosphate buffered saline (PBS) or in blood, it can be the case that nDEP occurs over the entire frequency range typically employed (**Scheme 3.1b**).[37] Thus, a low conductivity medium (near 100 mS/m) is required for cell separation. The most widely employed medium composition is 8.0% sucrose and 0.3% dextrose (to balance osmotic pressure) and 0.1% bovine serum albumin (BSA) to prevent non-specific interactions between cells and device structures. In certain cases, dilute buffer or cell culture medium is added to further support cell viability and to adjust medium conductivity.

DEP separation devices can be generally categorized into classical DEP, insulator DEP (iDEP [38]), and contactless DEP (cDEP [39]) (**Figure 3.1**). In classical DEP, metal electrodes are employed to generate a non-uniform electric field where the field density is locally high at electrode edges and significantly decreases with distance (generally, decaying over tens of microns). Examples include quadrupole electrode design,[35] nDEP microwells [13] and dielectrophoretic field-flow fractionation (DEP-FFF) [27,31,40,41] (**Figure 3.1a-3.1c**). Alternatively, in iDEP and cDEP, insulating structures (e.g., pillars or hurdles), are incorporated in microchannels to distort a uniform electric field resulting in localized trapping or deflection of cells. Since pillars are fabricated within microchannels and traverse the entire channel depth, mass fabrication of pillars and therefore high-throughput sorting can be readily achieved. Moreover, high-fidelity single-cell capture could be obtained by simply adjusting the pillar size to those of cells **(Figure 3.1d**). Considering the potential electrochemical damage of cells by direct contact with electrodes, a thin insulting membrane is incorporated between electrodes and cell suspensions in cDEP (**Figure 3.1e**). This thin membrane permits the AC field *via* capacitive charging of the membrane-solution interface. Using this approach,

up to 90% of viability was observed for trapped MOSE cells. [42] Another way of avoiding electrochemical effects is to use PDMS wall to isolate cell samples from liquid electrodes [32,43]. For instance, as depicted in **Figure 1f**, tortuous electrode channels filled with PBS were positioned alongside main channels to isolate sample solution from electrodes. When 30 Vrms was applied at a frequency of 164 kHz, MDA-MB-213 cells (early-stage cancer cells) were successfully trapped around the pillars while MCF7 and MCF10A cells (intermediate and late-stage cancer cells) flew through the main channel. This result has demonstrated the high effectiveness of cDEP as a separation approach to isolate a specific cell type from a heterogeneous population of cells. However, due to electric field losses within the PDMS insulator, high voltage is normally required to generate enough field intensity for cell trapping. For example, 60 kV/m is required for cell capture when the design shown in **Figure 1f** was utilized. Overall, factors such as cell viability, throughput and fabrication constraints need to be considered when selecting a type of DEP for a specific application.

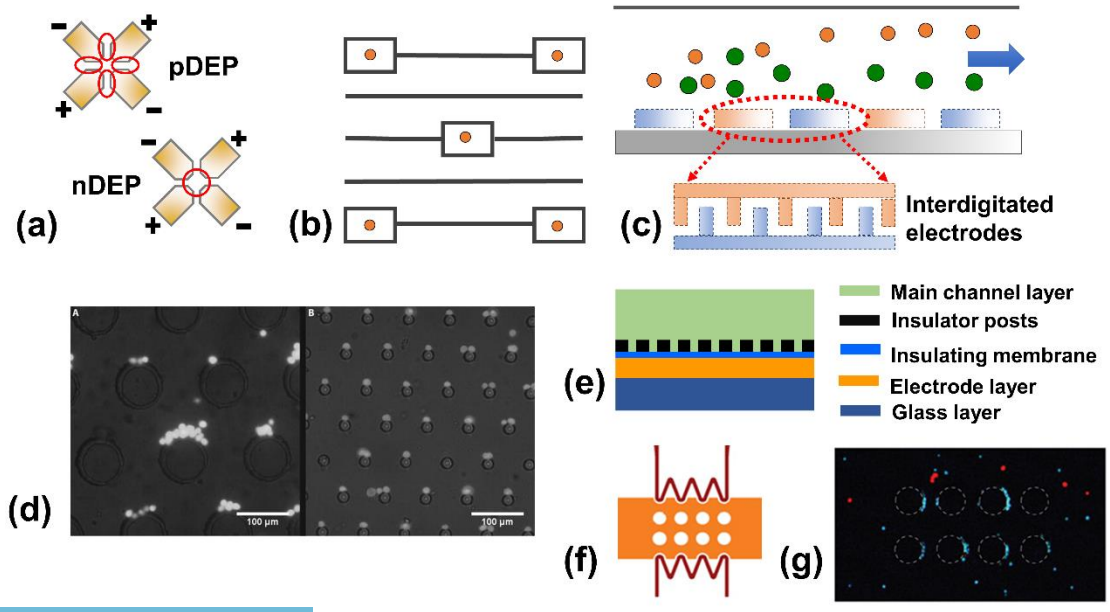

Figure 3.1. Illustration of DEP separation principles. (a) Quadrupole electrode design in which electrode edges exhibit highest electric field, while the center has lowest field strength. (b) Use of microwells to position single cells by nDEP. (c) Schematic of dielectrophoretic field-flow fractionation (DEP-FFF) in which different types of cells can be levitated to different heights by experiencing nDEP or pDEP. (d) Cell capture by using insulator pillars in AC electric field. When the pillar size decreases from 100 μm (left) to 20 μm (right), single-cell capture was achieved. (Reproduced from ref. [42]) (e) Illustration of cDEP by adding a thin PDMS insulating membrane between electrode layer and insulator posts. (f) Use of liquid electrodes in cDEP to generate electric field. (g) Result of capturing MDA-MB-231 cells (blue) in a mixture of MCF7 (red) and MCF10A (red) using electrode design of (f) (Reproduced from ref. [3]).

3.3 Advancement of DEP Strategies in Separation

The ability to discriminate between cell types is one of the most powerful features of DEP. Therefore, since the pioneering study by Pohl in 1951,[44] DEP has attracted much attention in separation applications.[45,46] The specific isolation of target cells has been a bottleneck of cellular analysis due to the wide range of cell types existing in samples derived from tissues. Separation methods including hydrodynamic chromatography, size-based filtration and immunoaffinity labeling (for sorting) or capture have been reported.[29,30] However, they often do not meet the stringent requirements for subsequent single-cell analyses, such that the cell sample must be free of labels, viable, and easily accessible after separation. For rare cell analysis, in particular, there is the additional requirement that the separation has the correct degree of selectivity and that capture efficiency (recovery rate) is high. DEP meets these requirements, making it an attractive separation approach. Further, DEP is cost-effective, due to low cost of reagents and peripheral equipment, and the devices can be disposable – both qualities that make DEP suitable for point-of-care (POC) applications. The primary challenge for DEP-based separation is low volumetric throughput (0.01 to 1.0 mL/hr), which is caused by the short range (tens of microns) over which electric field gradients extend from electrodes or insulating structures. Therefore, in this section, we discuss recent

advancements in device architecture and materials that increase volumetric throughput. The examples discussed here are all approaches targeted to cell trapping (at electrodes or pillars).

High-throughput isolation, especially when low-abundance cells are targets of interest, is essential for single-cell analysis. A recent trend in microdevices is to increase the interaction between the sample and the active device component by transitioning from an in-plane to out-of-plane architecture.[47-49] In a DEP device, instead of applying the electric field in the same plane (x, y-plane) as the separation, it is applied along the z-axis. Therefore, while the electrode separation must be small (on the order of 10-100 μm), dimensions in the separation plane are no longer constrained. J. Čemažar *et al.* developed a high-throughput contactless DEP (cDEP) array in which cell-sized pillars (20 μm) were fabricated to individually trap mouse ovarian surface epithelial (MOSE) cells.[42] In this configuration, a throughput of 2.2 mL/h was achieved. Though cDEP significantly obviates electrical damage to cells by the interposition of a thin insulating membrane, there is a concomitant increase in the voltage required to yield a sufficient DEP response (up to ~1000 Vpp).

Another strategy to exploit the z-axis is to extrude planar (2D) electrodes into 3D structures (> 1 μm thick). For example, J. Marchalot *et al.* developed a device incorporating a single pair of thick electrodes comprised of a carbon-polydimethysiloxane (C-PDMS) composite.[50] Initial simulations predicted that when the electrodes extended the full height of the channel, capture efficiency held constant (~85%) over a range of channel heights from 50 μm to 150 μm when the same average linear flow velocity was employed. Note that the volumetric throughput triples over this range. Alternatively, using coplanar electrodes the predicted efficiency peaked at ~77% in a 100 μm-tall channel (due to increased influence of wall lift force and insufficient electric field strength distant from the electrodes in shorter and

taller channels, respectively). Experimental results for capture of MDA-MB-231 cells resulted in similar trends but significantly lower capture efficiencies for matched flow rates, indicating that the numerical approach requires further refinement. While this example demonstrates the advantage of 3D electrodes, the reported device only incorporated a single pair of trapping electrodes, limiting throughput to 80 μL/min at a capture efficiency of 78%. High-throughput applications demand that the number of electrodes is also increased to provide multiple opportunities for each cell to be captured. For instance, extruding interdigitated electrodes in the *z*-direction using glass-like carbon (made *via* pyrolysis of thick photoresist films) was reported.[51-53] Using such 3D carbon electrodes, Martinez-Duarte et al. reported throughput of up to 0.6 mL/h in a device having an active area with a 0.01265 cm^2 footprint.[54]

Another route to 3D electrodes is by screen printing. A recent report incorporated printed commercial carbon paste electrodes into a device with a UV curable dielectric film as microchannels.[55] Compared to Au electrodes, the carbon electrodes exhibit greater thickness (10-15 μm vs. 50 nm). Furthermore, channel height could be controlled by the number of film layers printed. These materials may simplify the preparation of advanced DEP devices thus making them attractive for commercial products.

Despite the successful implementation of 3D electrodes in DEP technique, the throughput and complexity of accessible device architectures is limited by the requirement that all electrodes have to be connected *via* wire leads to a power supply. To address this issue, a strategy was recently reported in which separation was achieved at an array of >700 'wireless' bipolar electrodes (BPEs).[56] The BPE array functions in a way such that capacitive charging of the electrical double layer (EDL) at opposing ends of each BPE allows an AC electric field to be transmitted across the entire device. This planar thin film electrode array was either

enclosed in large chambers or integrated with a branched parallel microchannel structure, which incorporated micropockets to delimit the number of cells captured at each BPE. **Figure 3.2a and 3.2b** show a bright field optical image of a segment of a parallel-channel device and a fluorescence micrograph demonstrating the capture of individual breast cancer cells (green) against a background of leukocytes (yellow). **Figure 3.2c** illustrates the high success rate for single cell isolation over a range of flow rates employed. The authors reported throughput of 0.1 mL/h over an active area of 0.4 cm^2, which compares favorably to the commercial Apostream platform[27] when normalized to device area (0.25 mL/h/cm^2 and 0.05~0.07 mL/h/cm^2, respectively).

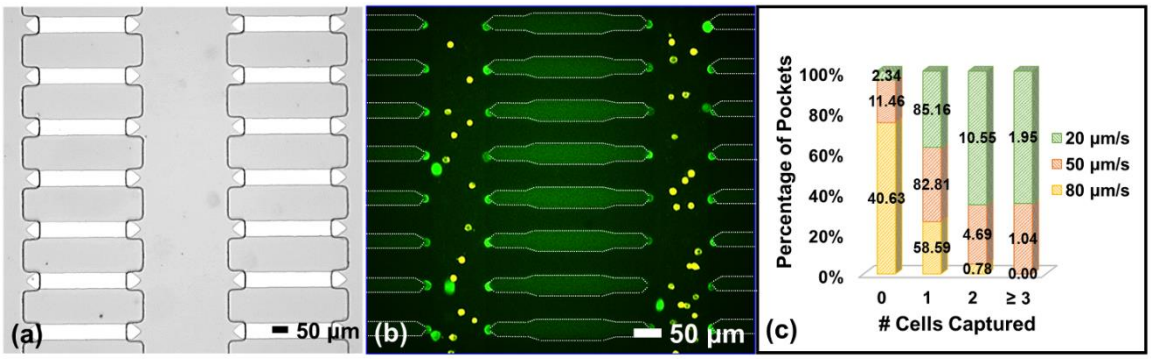

Figure 3.2. Illustration of BPEs used as wireless electrodes in DEP separation devices. (a) A bright field image of the parallel-channel design. (b) Fluorescence micrograph showing the capture of single MDA-MB-231 cells (green) from Jurkat E6-1 T cells (model white blood cells, yellow) t = 3 min after application of a 40 kHz AC trapping voltage at two outermost sets of electrodes. Pockets similar to cell dimensions (30 µm long x 25 µm wide). (c) Single-cell capture performance at three average linear flow velocities (n = 3). (Reproduced from ref.[56].)

In summary, considerable progress has been made toward increasing the throughput of DEP-based devices for separation and selective capture of biological cells as a first step in their analysis. The primary strategies reported incorporate new methods and materials (e.g., screen-printing, cPDMS, and pyrolyzed films), 3D electrode structures, and designs that increase the interaction between cells and large arrays of electrodes (interdigitated electrodes and BPEs) or

insulating structures (‘out-of-plane’ pillar array). Each of these approaches has distinct advantages in terms of ease of fabrication, throughput, cell viability and voltage requirements. It is anticipated that combinations of these concepts will lead to further improvements.

More relevant to the topic of this review is whether any of these strategies confers an advantage for integration of subsequent single-cell analysis. For optical or spectroscopic analysis, sequential analysis of cells in flow is sufficient and can be integrated with high-throughput separation if cells can be subsequently aligned to pass a detector in single file format. Strategies for cell alignment and focusing are discussed further in the final subsection of this review.

For analyses that involve reagents (e.g., enzymatic or genetic assays), cells must be fluidically isolated in a reaction volume. Therefore, of interest to the field are methods of trapping cells in compartments (such as in the BPE-based device) or in a matrix to ‘lock-in’ cell location (would could be employed, for example, for cells trapped at insulating pillars). Advancements in control over cell location and confinement are discussed in the following subsection.

Finally, a fundamental limitation of DEP is that, in most cases, to achieve separation, cells must be re-suspended in a medium with low electrical conductivity. Therefore, the incorporation of processing steps that reduce the conductivity of native media, such as blood, is highly desirable.

3.4 DEP Trapping and Transport for Single-Cell Analysis

In the previous section, we discussed advances in methods for separating cells from mixtures, and now, we turn our focus to controlling the location of cells in preparation for either on- or off-chip single-cell analysis. These two functions can be integrated, as is the case

for the BPE study described above – the cells were selectively trapped in single-cell confinements.[56] However, in this section, we will address only methods that have gone on to incorporate an analysis step. We will begin by looking at integrated *on-chip* trapping and analysis.

3.4.1 On-Chip Single-Cell Analysis

The heterogeneity of cell populations is a primary motivator of single-cell analysis, and in some cases, it is a rare subset of cells that drives normal or aberrant biological processes. Such is the case for cancer evolution, in which the process of clonal selection, under the pressure of chemotherapeutic treatment, can lead to the relapse of cancer through the expansion of a subset of cells (1:1,000 or 1:10,000) that have acquired a genetic mutation that confers resistance to the primary therapy.[3] To avoid missing these rare mutations, single-cell quantitative polymerase chain reaction (qPCR) must be carried out. The key point is that to yield meaningful information, thousands of cells must be analyzed. Therefore, carrying out analysis on-chip is desirable for massively parallel isolation of individual cells in discrete reaction volumes such as droplets or microwells.

As a further challenge, the target cells are frequently in limited supply. For example, circulating tumor cells (CTCs) are present in blood at exceedingly low concentrations (as low as 1 in 1 x 10^9 blood cells).[57] Therefore, there is a low tolerance for sample loss, which may occur if the cells are transported off of the device that is initially employed for sorting or capture. Thus, direct on-chip analysis has another compelling advantage.

Designs that incorporate microwells or microchambers for storing sufficient reaction reagents are a prerequisite for certain single-cell analyses (e.g. PCR or enzymatic assays). Accordingly, trapping and transport of single cells in predefined structures become critical.

Among the reported trapping methods, techniques based on DEP have shown superior capture efficiency compared to that of using gravity [58-60] and hydrodynamics [15,61-63] due to active capture *via* dielectric properties. In 2011, Fujii and coworkers pioneered study of electroactive microwell arrays (EMAs) [14] and and have since demonstrated its utility for many types of on-chip analysis.[64-66] The device (**Figure 3.3a**) is comprised of an interdigitated array of micropatterned ITO thin-film electrodes, over which a photoresist layer is employed to create reaction volumes (microwells) that are 25 μm in diameter and 15 μm deep.[64] Cells are delivered to this trapping array *via* an overlying PDMS fluidic structure (**Figure 3.3b**), which can be later pressed onto the array to fluidically isolate the chambers. Using this device, over 90% capture efficiency for multiple cell lines was reported.[14,64] In addition to high capture efficiency, the EMA device exhibits the following advantages: (i) A large quantity of individual cells can be simultaneously characterized in the reported arrays, which have 3600 microwells.[14] (ii) Reagent exchange is readily facilitated by the fluidic structure without dislodging the capture cells. (iii) 100% of cell lysis is achieved by applying short electric pulses to the electrode pairs. (iv) Direct imaging of cells as well as read-out *via* fluorescent changes are accessible.

In the study depicted in **Figure 3.3**, a pluripotency marker protein, Nanog, in a population of individual pluripotent stem cells (iPS cells) was monitored on the EMA chip in order to decipher their cellular heterogeneity.[64] The Nanog gene, highly associated with stem cell pluripotency, can be employed to select high-quality iPS cells. Green fluorescence protein (GFP) was employed as a gene reporter, which enabled the quantitative evaluation of the pluripotency of iPS cells *via* fluorescence imaging. As shown in **Figure 3.3d-e**, large cell-to-cell variations in the amount of GFP were observed at the single-cell level and during cell

differentiation regardless despite uniform treatment. The data obtained by EMAs was validated by comparing averaged expression levels with those obtained by qRT-PCR (**Figure 3.3f**). This result is significant because it indicates that the EMA provides quantitative read-out of gene expression.

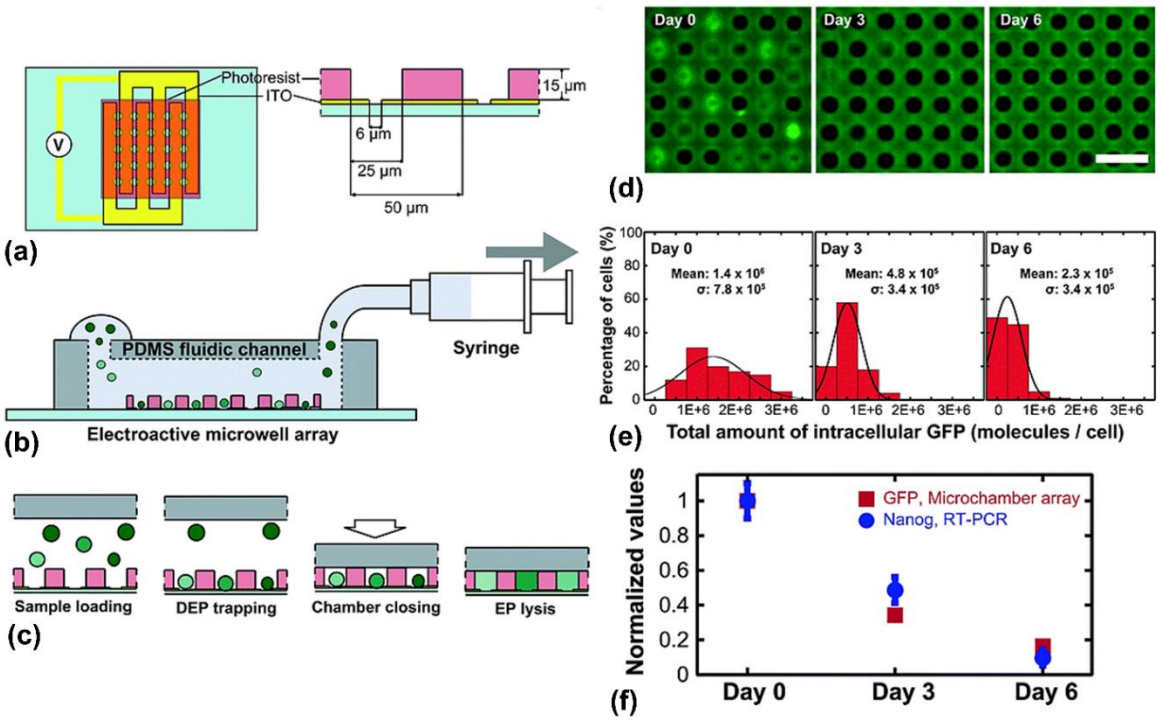

Figure 3.3. Schematic depiction of EMAs design and the results of studying Nanog expression in iPS cells. (a) Top and cross-section view of EMAs. (b) Illustration of processing of cell samples. (c) Detailed procedures for trapping and lysis of single cells. (d) Fluorescence images of lysed iPSCs after cell differentiation of 0, 3, and 6 days. The scale bar indicated 100 μm. (e) Distribution of the total amount of intracellular GFP molecules per cell in 100 randomly microchammers. (f) Comparison of the expression level of the Nanog gene using quantitative RT-PCR and EMAs device. (Reproduced from ref. [64].)

In separate studies, the EMA was employed to assess the enzymatic activity of intracellular-β-galactosidase of various cells types.[14,65] After lysis, galactosidase inside individual cells reacted with a fluorogenic substrate, fluorescein-di-β-D-galactopyranoside (FDG), resulting in hydrolysis of FDG, releasing fluorescein. The non-uniform brightness indicated the heterogeneity of β-galactosidase over the cell population. The versatility of the

EMA design was also demonstrated with the completion of other on-chip single-cell analyses including immunostaining, viability/apoptosis and fluorescent in situ hybridization (FISH) assays.[66]

It is worth noting that the dimensions of these microwells plays a crucial role in capture efficiency and subsequent on-chip reactions. On one hand, to ensure single-cell capture, the diameter of the well opening must be similar in size to the cells. On the other hand, a high-aspect ratio (wide, shallow well) leads to flow laminae that carry cells nearer to trapping electrodes, thus improving capture efficiency. A double-well array was thus developed accordingly to address these issues.[65] Specifically, instead of a single layer of SU-8 defining the microwells, a 'trap-well' layer with cell-sized openings was overlaid with a 'reaction-well' layer having a higher aspect ratio. A capture efficiency of 96 ± 3% of single PC3 cells was direct evidence that this electroactive double-layer is a superior design in such applications.

Further constraints on the 'reaction-well' dimensions are that too large of an aspect ratio can adversely impact cell retention (due to increased excursion of faster flow laminae to trapping sites) and protection during well closing (due to sagging of the PDMS into wells under external pressure). The wells reported housed a reaction volume of 56 pL, which had the advantage of preventing contamination and preventing dilution in enzymatic assays. A description of how capture efficiency scales with larger reaction volumes would be useful for extension to genetic assays at the nanoliter scale.

For certain on-chip analyses, a defined reaction volume is not required. In the following example, pDEP is leveraged to hold cells stationary during sequential dosing steps. Significantly, this is a live-cell assay, monitoring the uptake of a drug in real time by fluorescence to investigate multidrug resistance (MDR) in acute myeloid leukemia (AML).[67]

Although MDR is known to be the failure mechanism of anthracycline-based chemotherapy, studies of MDR at the single-cell level and corresponding assessment of variability among cells remain to be rare. Within this context, A. Khamenehfar *et al*. developed a DEP-based assay which permits the measurement of drug accumulation in single leukemic blast cells. cells.[67] A scheme of the layout of the DEP-based chip is shown in **Figure 3.4a**. The device is comprised of a single analysis chamber which houses a cell retention structure (a wall) partially surrounding the tips of three electrodes. DEP force near these tips was employed to retain cells during exchange of reagents, and individual cells were shuttled in and out of the detection window (red box, **Figure 3.4b**) to measure fluorescence intensity.

Leukemic blast cells were first divided into three categories – cells with MDR activity (MDR^{+}), without MDR activity (MDR^{-ve}), and W (benign WBCs) – by adding only anthracycline daunorubicin (DNR) (**Figure 3.4c-e**), which is fluorescent. The anthracycline is readily uptaken by MDR^{-ve} and W cells, but not by MDR cells. Subsequently, the effect of co-administration of MDR inhibitors, which restored uptake in MDR cells, was investigated. Pronounced heterogeneity in MDR activity among the tested leukemic blasts was observed. The study also revealed a high chance of appearance of MDR^{+} cells in patients at pre-therapy and at relapse. This DEP-based strategy provides a convenient tool to characterize the mechanistic basis for cellular heterogeneity and could be extended to other biological systems. The most impressive feature of the results is that the uptake of anthracycline was unaffected by the applied electric field, which allowed sensitive determination of the impact of cell phenotype and inhibitor dosing. The single-file nature of this approach is a serious bottleneck to obtaining a statistical description of a population of cells, which could be overcome by adopting a multi-channel or array-based approach.

The foregoing two examples, are the most recent reports of integrated DEP trapping and on-chip analysis of single cells. Interestingly, neither takes advantage of the ability of DEP to separate cells from complex mixtures. While application to CTCs is implied by cancer cell capture with the EMA device,[14] actual selective isolation from a background of blood cells is not undertaken. Several barriers exist to the integration of selection, trapping, and analysis into a single chip. Perhaps the most substantial of these is that a new requirement is placed on the analysis step to confirm the identity of the trapped cells. For example, once CTCs are isolated, they can be distinguished from leukocytes by staining the cells with a nuclear stain and a panel of dye-linked antibodies targeted to positive and negative markers. Despite this barrier, integration of selection and a means of identifying cell phenotype into such platforms is essential to drive the translation of DEP-based methods into the clinic. Further, if the cells can be identified without the addition of labels (e.g., antibodies), the identification step will not interfere with subsequent analyses, and more importantly, the advantage of DEP as a label-free technique is maintained. Characterization by Raman spectrometry is an excellent example and is described in the subsection discussing off-chip analysis below.

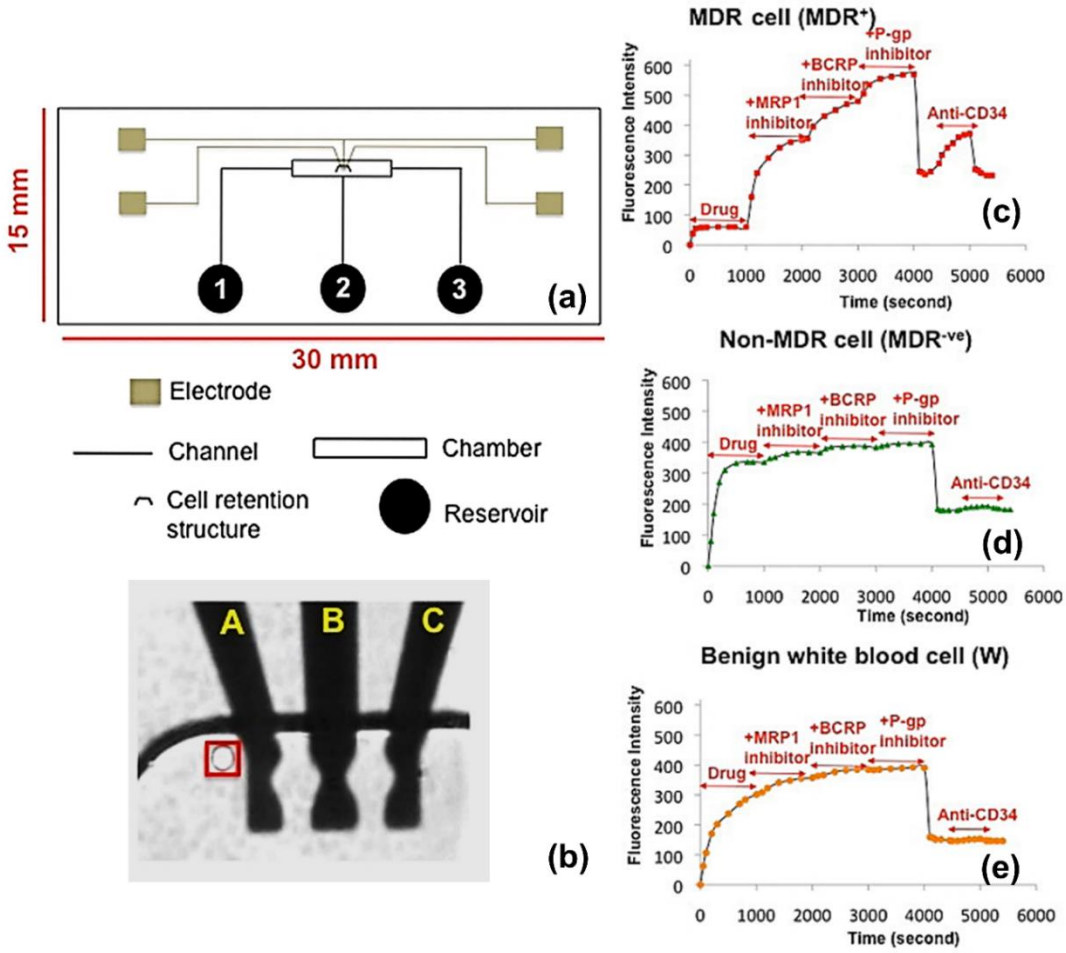

Figure 3.4. Schematic depiction and results of the DEP-based chip for MDR study. (a) Layout of the microfluidic DEP chip. (b) Image of a cell captured and retained near electrode A. The red box indicated detection window. (c) – (e) Representative results of AML cells in MDR activity. (Reproduced from ref. [67].)

Label-free analyses may assess the morphology, growth, and behavior of the target cells as their distinguishing features. The development of on-chip cell patterning, 3D tissue cultures, and migration assays have enabled an unparalleled view of how cells are stimulated by their environments. These advancements are relevant to DEP in two ways. First, DEP has had a known impact in cell patterning [35,68,69] and can contribute to the localization of cells in these devices. Second, incorporation of biomimetic environments into DEP-based devices may increase post-capture cell viability, enhance fidelity of cell response to native levels, and enable functional assays of single cells.

A recent article described a technique for DEP patterning and culturing of cells in a 3D gel matrix. Although this report does not address single-cell analysis, the results are informative for the further integration of biomimetic environments with DEP. The authors described a digital microfluidic platform (DMF) in which HEK 293 cells were first encapsulated within a 3D gelatin methacrylate (GelMA) hydrogel droplet prior to patterning and culture (**Figure 3.5a**).[70] As shown in **Figure 3.5b**, the general protocol was as follows: (i) Cell-laden GelMA hydrogel was immersed in mineral oil to prevent evaporation and dispensed onto a reservoir. (ii) The electro-wetting on dielectric (EWOD) technique was applied (175 Vpp and 1 kHz) to move the cell-hydrogel mixture towards a patterning electrode. (iii) Upon reaching the trapping electrode, nDEP was induced (10 Vpp, 20 kHz) to pattern cells, and an exposure with UV light (365 nm) crosslinked the hydrogel for immobilization of patterned cells. (iv) Cell media was immediately delivered from another reservoir to hydrate the GelMA construct and the mineral oil was removed for culturing and various cellular assessment. The number of cells patterned and the viability of cells during culture were quantitatively evaluated. The authors concluded that the number of cells patterned is proportional to cell concentration and that increasing trap diameter leads to an even more dramatic change (**Figure 3.5c**). Moreover, the trap diameter and the distance between each trap influenced cell viability (**Figure 3.5d**). Lower viabilities were obtained using smaller diameter traps due to small cell cluster size and the corresponding lack of cell-to-cell communication. The overall viability reported for this DMF device was as high as 78% after 1 day of culturing and slightly decreased to 66% after 4 days.

The results of this study provide a useful benchmark for integrating a 3D matrix into a DEP-based device. Certainly, for studies that seek to investigate live cells, factors impacting

viability, such as the electric field distribution and the sensitivity of the cells to culture density, are an important consideration. The relatively high viability of cells (78%) 1 day following immobilization indicates minimal or no lasting damage incurred by DEP. However, a control experiment detailing the viability of cells that had not undergone trapping is not reported. Further the dramatic alteration in the number of cells isolated in each nDEP well to its radius (likely due to the exponential decrease in electric field strength from electrode edges), is a promising experimental handle for investigating the impact of cell cluster size on behavior. Although the authors did not pursue single-cell isolation, it is an exciting possibility with simple alterations to the reported device, if long-term viability is not required or if low viability can be mitigated.

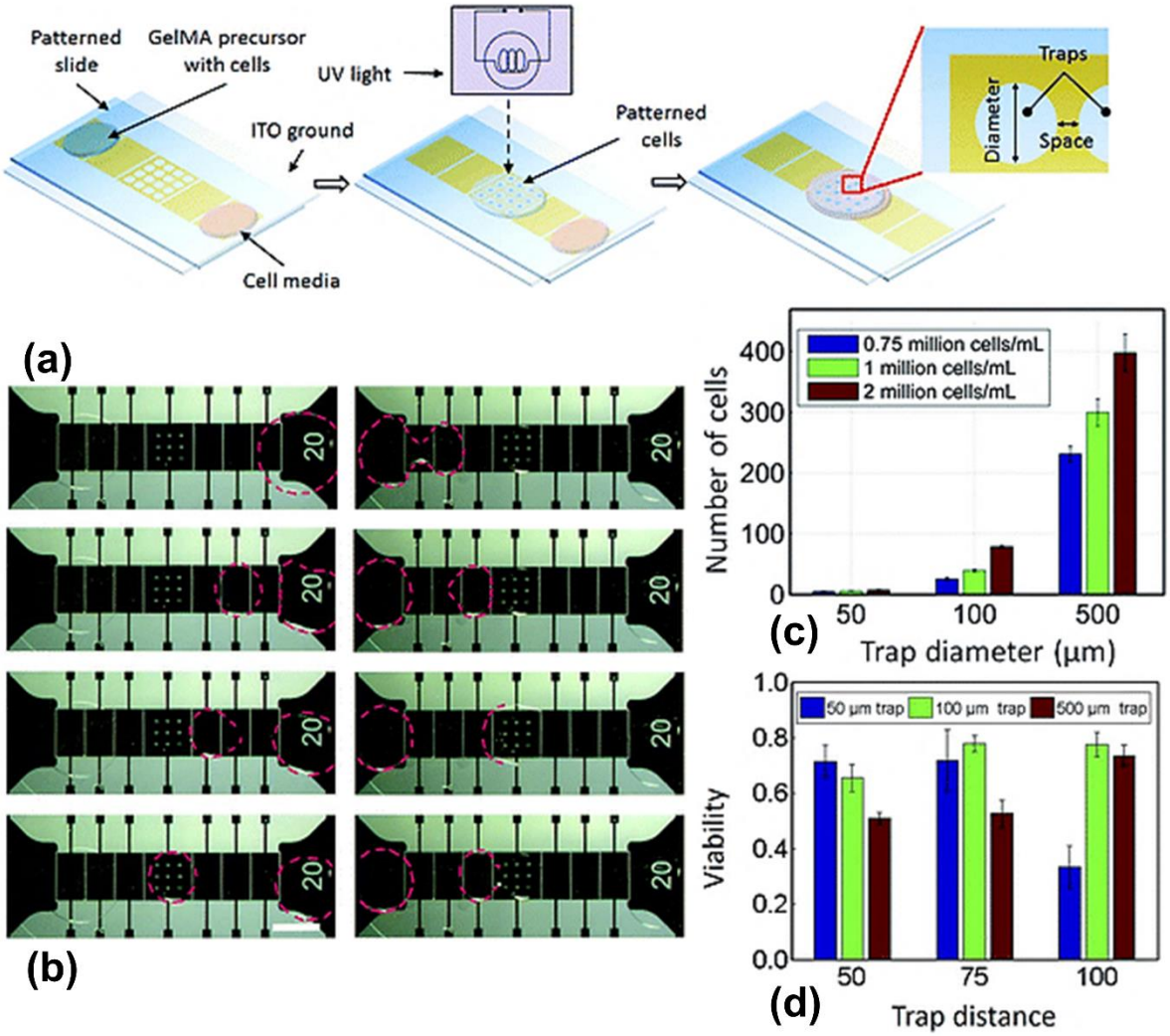

Figure 3.5. A hydrogel-based digital microfluidic platform for *in vitro* cell studies. (a) The preparation process of cell-containing hydrogel droplets. (b) Delivery of cells to the patterning electrode (left), and the subsequent transport of cell media for cell culturing (right). (c) Results of the number of cells as a function of trap diameter. (d) The effects of trap distance and trap size on cell viability. (Reproduced from ref. [70].)

3.4.2 Off-Chip Single-Cell Analysis

Although on-chip analysis offers great advantage in minimizing cell loss, it suffers from limitations to reaction volumes (e.g., only 56 pL in EMAs as limited by geometric constraints described above [65]) and additional steps are often required to prevent evaporation during on-chip reactions[71]. Off-chip cellular analysis circumvents these limitations and can thus be a complementary approach to DEP, especially for rare cells considering the low-

throughput of some of the techniques reported. For instance, K. Huang *et al*. recently integrated optoelectronic tweezers (OET) or light-induced DEP in microfluidic chips to selectively pick up individual cells and transport each out *via* a nanoliter liquid plug for off-chip cellular analysis.[16] **Figures 3.6a-e** are the schematic procedures and **Figures 3.6f-i** show the corresponding experimental results of selecting live Hela cells stained with Calcein AM. Notably, this OET-based chip only employed one single pneumatic pressure source to control cell transport to a fluidic outlet. Therefore, increased high-throughput for the transport of cells may be enabled by creating parallel independent fluidic controls. More importantly, this OET-based device incorporated a layer of transparent single-wall carbon nanotubes (SWNT) as an electrode into multilayer PDMS channels. Compared to traditional photoconductive materials such as amorphous silicon and metals, SWNT electrode are transparent, flexible, and chemically stable in aqueous environment, thus becoming a suitable material for cell manipulation in multilayer PDMS microfluidic chips. Isolated single Hela cells were analyzed off chip by RT-qPCR to detect β-actin mRNA. The measured expression levels in single cells obtained by OET and collective cell samples that underwent traditional preparation were in an expected relationship (**Figure 3.6j**). Successful molecular analysis of cells selected using this OET-based chip demonstrated its utility. Importantly, this strategy is broadly applicable to other downstream analyses or to select cells for subsequent cultivation.

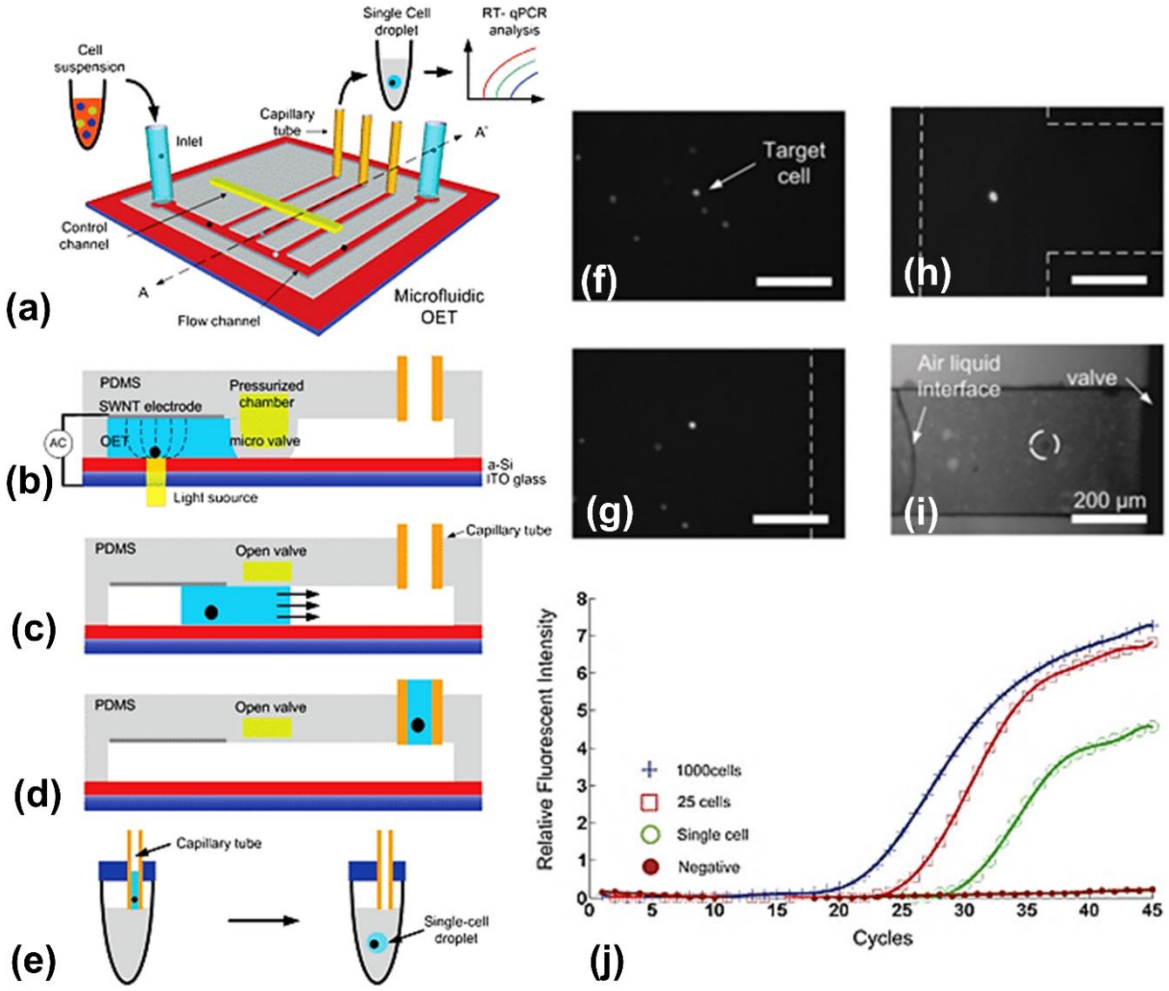

Figure 3.6. Scheme and results of the OET-based chip. (a) Overview of the preparation of single cell samples for off-chip analysis. (b) – (e) Side view and step-by-step procedures. (b) The SWNT electrode enables OET integration and manipulation of cells with multilayer PDMS microfluidics. (c) After single-cell trapping, the elastomeric valve opens, resulting in cell droplet movement towards an outlet. (d) A capillary tube is placed in the outlet to retrieve the cell in a nano-liter droplet. (e) Transport of the single-cell to a PCR tube for downstream analysis. (f) – (i) Sequential fluorescence images of the procedures. (f) Initial position of a trapped Hela cell. (g) The cell of interest in a new location as it is selected and pulled out from the population. (h) The target cell is moved to the entrance to a nearby branch channel. (i) A liquid droplet is formed after airflow is pumped to clear the liquid in the main channel. (j) Results of quantitative RT-PCR amplification of samples with different numbers of cells. (Reproduced from ref. [16].)

We end this subsection with a method that is enables both on- and off-chip analysis – the integration of pDEP with Raman-activated cell sorting (RACS).[72] Despite the label-free inherence of DEP-based separation, fluorescent tags are often required to evaluate its sorting

performance. On the other hand, although single-cell Raman spectra (SCRS) are informative of cell composition[73] in a label-free manner, the throughput has been considered as a bottleneck due to a requirement for long interrogation time and the alignment of the laser to each cell. Sequential pDEP trapping and stabilization of individual cells at the Raman laser detection spot improves throughput thus enabling practical label-free analysis. As depicted in **Figure 3.7a**, the DEP-RACS system consists of a DEP trap array aligned the Raman detection spot followed by a hydrodynamic suction region for selective removal of cells from the chip. The pDEP trap array was designed in such a way that Raman identification of single-cells could be achieved under a high flow velocity (≥ 1.0 mm/s). First, sheath flow was introduced to converge cell solutions in a single-cell stream. This pre-focusing is to precisely align cells trapped within the laser detection spot. Second, an electrode array, rather than single-pair of electrode, was fabricated to gradually drag down cells and finally trap each at the laser spot. This gentle deceleration of cells is important as high flow rate can be continuously applied to prevent cell adherence and maintain high-throughput. **Figure 3.7b-c** show 20 single cells could be precisely aligned and delivered to the laser spot by periodically turning on and off pDEP. As a proof-of-concept, carotenoid-producing and non-carotenoid-producing yeast cells were sorted using this DEP-RACS design. The characteristic peaks of carotenoid-producing yeast cells provided clear discrimination from non-carotenoid-producing yeast cells (**Figure 3.7d-e**), and 8-fold enrichment was obtained (**Figure 3.7f**). Moreover, over 577 cells were identified and sorted in 540s, which further demonstrated the high-throughput capability of this approach. The use of DEP to immobilize single cells greatly improved the throughput of this RACS system, which may eventually broaden the applications of RACS in single-cell analysis.

Meanwhile, considering the strong Raman background of ITO-glass and PDMS, this DEP-RACS chip, the sensitivity of this system could be improved if made of quartz.

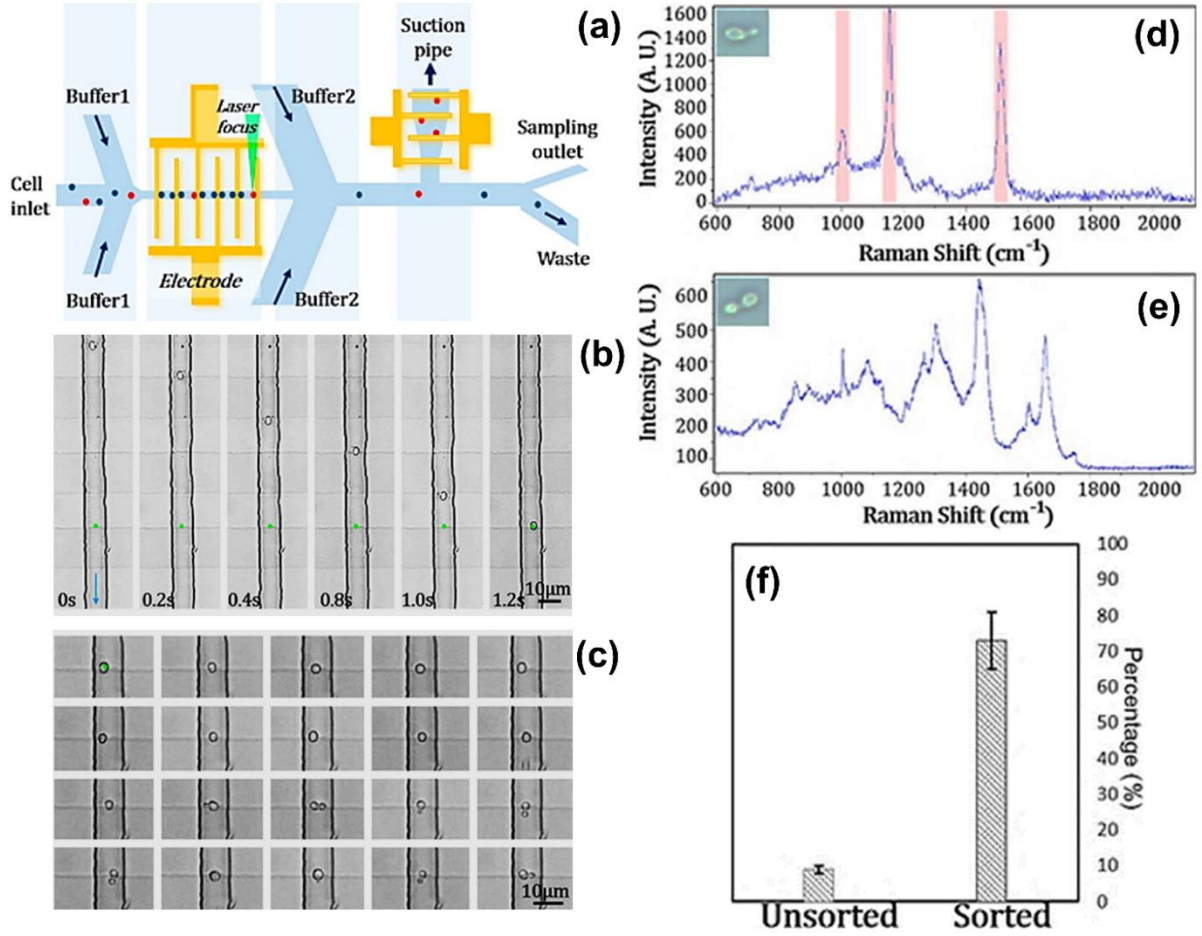

Figure 3.7. Illustration of integration of DEP with Raman-activated cell sorting (RACS). (a) Schematic layout of the RACS device showing the location of the laser spot (green). (b) Transport of a single cell to the laser detection spot using the electrode array. (c) Alignment results of 20 consecutive single cells. Raman spectra of (d) a carotenoid-producing cell and (e) a non-carotenoid-producing cell. (f) Sorting performance of the RACS chip. The percentage of carotenoid-producing cells in an unsorted and sorted population, demonstrating that sorting led to approx. 8-fold enrichment of these cells. (Reproduced from ref. [72].)

The use of fused silica as a substitute for PDMS in preparing microchannels may enhance the performance of devices that incorporate both Raman and DEP. [74] Fused silica has a dielectric breakdown of 950 V/μm resulting in a wide range of allowable voltages. More importantly, direct particle analysis using Raman spectroscopy can be exploited without

interference of PDMS signal. This enhancement is significant as DEP coupled with Raman results in label-free manipulation and identification of cells.

3.5. Integration of Pre-Enrichment and Pre-Focusing with DEP

Despite advancements in throughput and separation efficiency (selectivity), DEP-based techniques require sample pretreatment for certain applications such as the isolation of CTCs from blood. These cells are sufficiently rare that several milliliters of blood must be processed to isolate as few as one CTC. Further, if individual cell traps are employed, even a 1% rate of white blood cell (WBC) capture could result in over 98% of cell traps being occupied by WBCs due to their relative abundance (4.5 - 11 x 10^6 WBCs/mL). Such challenges motivate the integration of pre-enrichment and pre-focusing prior to DEP-based separation or trapping.

Pre-enrichment is the removal of the bulk of interfering cells prior to DEP and is frequently carried out by an orthogonal separation technique. For example, size-based pre-enrichment of cancer cells from WBCs and erythrocytes (RBCs) has been accomplished by hydrodynamic focusing. One such technique is multi-orifice flow fractionation (MOFF), in which particles are isolated and concentrated laterally as a response of their hydrodynamic inertial forces created by fluidic constrictions arranged in series. The use of MOFF is advantageous since no external force is needed and operational flow rate can be up to 300 μL/min.[75] While MOFF enables high-throughput and massive filtration of cells, the output purity is not sufficient on its own for separation of low abundance cells. A final separation step was accomplished by DEP after MOFF.[75] Using this MOFF-DEP design, the combined separation efficiencies reported were 99.24% for RBCs, and 94.23% for WBCs, respectively. MCF-7 cells were 162-fold enriched by MOFF at a flow rate of 126 μL/min (buffy coat diluted in PBS). The advantages of MOFF is its simplicity of operation and excellent enrichment

factor. Some challenges for such hydrodynamic pre-enrichment techniques are the requirement for significant dilution and size-dependent selection of target cells.[29] These relative advantages and disadvantages are shared among hydrodynamic techniques, another prominent example of which is dean flow focusing (DFF).

Pre-enrichment techniques can also lead to alignment of cell samples into a narrow stream before entering the DEP isolation zone. Such pre-focusing is pivotal for improving separation efficiency since all cells experience the same fluid velocity and start from the same lateral position. The resulting high isolation efficiency ensures collection of a representative sample of single cells which in turn is critical to unravel cell heterogeneity. Besides the use of sheath flow for pre-focusing in the DEP-RACS system (89% capture efficiency at 5.25 mm/s),[72] M. Antfolk *et al*. have also successfully demonstrated the use of acoustophoresis to enrich and separate MCF7 cells from white blood cells (WBCs) with an efficiency of 91.8 ±1.0% and 23.8 ±1.3-fold concentration at a flow rate of 100 µL/min.[76] In the acoustic field, the lateral position of particles at any time is dependent on acoustic mobility (V) which is predominantly determined by particle size (r) and proportional to r^2. This size-dependent mobility leads to greater deflection of large particles from the channel wall than that of small particles, thus allowing two cell populations to be concentrated and separated along a microchannel. Inspired by this work, Fujii and coworkers integrated acoustophoresis with the EMA single-cell trapping device chip[77,78] leading to an all-in-one microfluidic device, which integrated pre-alignment, separation, concentration enrichment, single-cell trapping and identification (**Figure 3.8**). It is worth mentioning that the flow rate needs to gear down when isolated cells enter the EMA segment of the device. This decrease in flow minimizes cell loss as DEP force is a relatively weak trapping force. Using a flow rate of 80 µL/min in the acoustic

field and 4 μL/min in the EMA segment, a 20-fold concentration enrichment and 76.2 ± 5.9% capture efficiency of cancer cells were achieved.[78] Aside from single cells, CTC clusters were observed in the EMA zone. In fact, the larger the clusters, the more readily they were deflected by the acoustic force and trapped by DEP. This result is significant because CTC clusters or microemboli have been shown to have greater metastatic potential than individual cells.

Despite the improvement of throughput using MOFF and acoustophoresis as pre-enrichment and pre-focusing tools, the fact that their separation principle is reliant on cell size can be a drawback. For example, CTCs exhibit large variation in size (4.0 - 30 μm even from a single patient [79], and therefore, these pre-enrichment and pre-focusing methods can introduce selection bias in addition to that inherent to DEP.

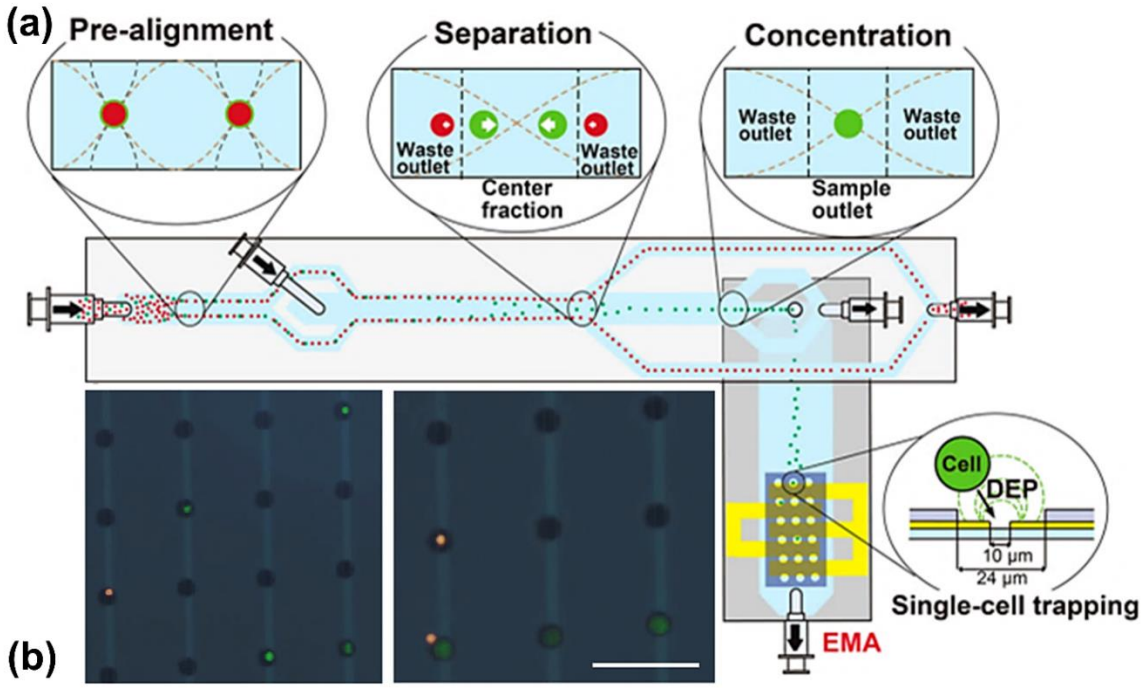

Figure 3.8. Illustration of integration of acoustophoresis with EMA for single-cell analysis. (a) Schematic illustration of the various operation zones: pre-alignment, separation, and concentration by acoustophoresis followed by DEP-based trapping of individual cells in the EMA. The majority of WBCs were diverted away from the EMA by acoustophoresis. (b) Fluorescence images demonstrating single DU145 cancer cells (green) and WBCs (orange) in the microwells. Scale bar indicates 100 μm. (Reproduced from ref. [78].)

For certain applications, only pre-focusing is required without selective enrichment. Induced charge electro-osmosis (ICEO) was recently introduced as a non-selective focusing approach prior to DEP-based continuous separation (**Figure 3.9**).[80] ICEO [81-84] refers to a surface force exerted in the electric double layer (EDL) at an electrode surface through the electric field component that lies tangential to it. When a planar electrode array is exposed to an external AC electric field, counter-ions in solution accumulate on polarized electrodes to form an EDL. The movement of the counter-ions in response to a tangential component of the electric field drags the surrounding fluid by viscous force. The resulting electroosmotic fluid flow has the following features: (i) it is frequency-dependent and peaks around 100 Hz -1 kHz when the conductivity of the medium is in the range of 1.0 – 10 x 10^{-3} S/m and quickly diminishes with increasing frequency.[82]

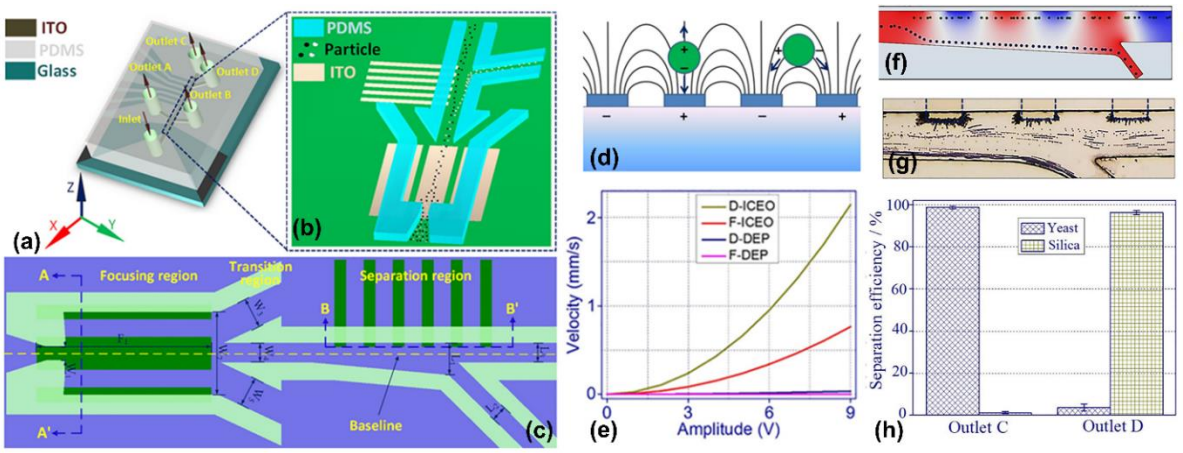

Figure 3.9. Design principle and results of ICEO-DEP device. (a) 3D view of the design. (b) Schematic illustration of the device integrating ICEO pre-focusing with DEP separation. (c) Top view of the two functional regions. (d) Scheme depicting DEP response of particles under AC electric field. (e) Simulation results of particle velocity induced by ICEO on the driving electrode (ICEO), ICEO on the floating electrode (F-ICEO), DEP on the driving electrode (DEP), and DEP on the floating electrode (F-DEP) when low frequency is applied. (f) Numerical simulation of the separation of silica and yeast when 150 V_{pp} (A2) was applied with a frequency of 1.0 MHz and flow rate of 150 μm/s. (g) Optical image of the particle separation and (h) plot showing the resulting separation efficiency using the same conditions as in (f). (Reproduced from ref. [80].)

The dominance of ICEO at low-frequencies is important because it allows the interference by DEP to be circumvented as depicted in **Figure 3.9e** (the pDEP response of biological cells often reaches a maximum well above 1 kHz). (ii) Large fluid velocities (over 500 μm/s) can be readily achieved using small voltages (~5.0 Vpp). [81] (iii) When symmetric electrodes are exposed to an AC electric field, a converging stagnation line is formed in the middle of each electrode (**Figure 3.9d**).[85,86] The integrated chips reported by X. Chen *et al*.[80] took advantage of all the aforementioned features to align both silica particles and yeast cells along the channel midline prior to DEP-based separation. The electrodes in the focusing region were designed in a way such that all particles collected at the stagnant line (**Figure 3.9b**). The focusing region was 4 cm and employed a flow rate of 150 μm/s (~26.7 s retention time). The separation efficiency of yeast cells from silica particles in the DEP region exceeded 96%. The simplicity and fast processing time of ICEO render it an attractive option for integration with DEP-based single-cell analysis.

3.6 Challenges and Emerging Needs

3.6.1 Cell Manipulation in Native Culture Media

A challenge to practical application of DEP to particle trapping and separation is the requirement for low electrical conductivity (LEC) media (on the order of mS/m), while almost all biological media feature a 100- to 1000-fold higher conductivity (1.5 S/m for whole blood). Therefore, re-suspension of cell samples in LEC solution is inevitable. The cumbersome preparation and the high risk of losing target cells during re-suspension motivate the development of methods to lower the conductivity of the native medium on chip. D'Amico *et al.* recently reported a membraneless microdialysis device (MMD) to reduce the electric conductivity of blood specimens prior to their exposure to a DEP trapping array.[87] By

connecting two MMDs in series, the conductivity of the blood sample decreased from 1.5 S/m to 15-17 mS/m with a throughput of 100 μL/min. This development is significant since it provides a means by which pDEP responses can be accessed in whole blood, enabling a wider array of trapping and separation strategies. It is also worth noting that in the MMD integrated device, the target of the study was selective pDEP trapping of bacteria from blood. Therefore, low doses of ionophores and pore-forming agents were added to the sample to facilitate ion transport outward across the blood cell membranes such that the response for only these cells changed to nDEP.

3.6.2 Pre-Enrichment and Pre-Focusing

In the previous subsection, we discussed pre-enrichment and pre-focusing by MOFF,[75] acoustophoresis,[76] and ICEO [80]. It is worth noting that these approaches enable processing of cells either with size-dependence (thus potentially introducing bias) or without offering any selectivity. The development of DEP techniques with increased throughput, using 3D carbon electrodes [52,54] and bipolar electrodes [56], opens the avenues to utilize DEP itself for high-throughput separation applications.

3.6.3 DEP Manipulation Coupled with Live-Cell Imaging

Although cellular analysis conducted using lysed cells is informative, the examination of dynamic adaptions in live cells is necessary for a complete characterization of cell function. The prerequisite of such a study is to obtain a collection of label-free and representative cell samples with high viability. Although DEP-based microfluidic systems deliver these features, they have not been coupled with live-cell analysis yet.

3.7 Conclusion

Recent advances in DEP have positioned it as a robust and efficient means of cell manipulation and analysis. The focus of these efforts has been to (1) increase throughput (using 3D electrodes and wireless electrodes); (2) leverage functional microchannel materials (e.g., fused silica) and electrode materials (e.g., screen-printed carbon); (3) incorporate fluidic structures for parallel confinement of single cells (e.g., electroactive microwell arrays); (4) employ DEP to transport cells off chip that have been selected by another means (e.g., Raman-activated cell sorting and optoelectronic tweezers); and (5) integrate pre-treatment (e.g., acoustophoresis and electroosmosis) with DEP. These advances are significant because they reduce barriers to the practical application of these DEP techniques in biological and clinical studies. However, to date, there remain relatively few studies that have demonstrated parallel (or rapid sequential) single-cell analysis in samples from culture and still fewer of clinical origin. For those that have, a wide range of analyses have been undertaken thus demonstrating the power of DEP for selection and isolation of cells. In addition to the assays demonstrated, on-chip gene amplification would be of value and could be enabled by the introduction of larger reaction volumes and additional fluidic controls.

Many of the assays that have been integrated with DEP thus far (e.g., enzymatic assays and FISH) provide a snapshot of phenotypic molecular features of cells at a single time point – immediately post capture. Given the relevance of live-cell and functional assays to understand dynamic cell response, further development of methodologies that permit such observation would be of major interest to the field. For example, DEP may be employed to pattern cells individually or in clusters in defined microenvironments that mimic conditions *in vivo* or allow interrogation of collective behavior (e.g., intercellular signaling). Subsequent

assessment of individual cells that demonstrate behaviors of interest would aid in the correlation of molecular features with specific cell response.

Further, for separation (or selective capture) the requirement to exchange native media for a low conductivity solution remains a limitation – especially in the clinical setting. While media can be exchanged prior to analysis by centrifugation, DEP response is highly sensitive to slight changes in medium conductivity and therefore, results may vary depending on the operator unless the process can be regulated by automation. In light of this need, further development of on-chip sample desalting such as by membraneless microdialysis device (MMD) would increase the viability of DEP-based methods for clinical application. In summary, recent advancements have drastically increased the versatility of DEP, yet there remain important opportunities for growth.

3.8 References

1. El-Ali, J.; Sorger, P. K.; Jensen, K. F. *Nature* **2006**, *442*, 403-411.

2. Armbrecht, L.; Dittrich, P. S. *Anal. Chem.* **2017**, *89*, 2-21.

3. Joosse, S. A.; Gorges, T. M.; Pantel, K. *EMBO. Mol. Med.* **2015**, *7*, 1-11.

4. Dong, Y.; Skelley, A. M.; Merdek, K. D.; Sprott, K. M.; Jiang, C.; Pierceall, W. E.; Lin, J.; Stocum, M.; Carney, W. P.; Smirnov, D. A. *J. Mol. Diagn.* **2013**, *15*, 149-157.

5. Pantel, K.; Brakenhoff, R. H.; Brandt, B. *Nat. Rev. Cancer.* **2008**, *8*, 329-340.

6. Kaern, M.; Elston, T. C.; Blake, W. J.; Collins, J. J. *Nat. Rev. Genet.* **2005**, *6*, 451-464.

7. Brock, A.; Chang, H.; Huang, S. *Nat. Rev. Genet.* **2009**, *10*, 336-342.

8. Perkins, T. J.; Swain, P. S. *Mol. Syst. Biol.* **2009**, *5*, 326.

9. Walling, M. A.; Shepard, J. R. *Chem. Soc. Rev.* **2011**, *40*, 4049-4076.

10. Zare, R. N.; Kim, S. *Annu. Rev. Biomed. Eng.* **2010**, *12*, 187-201.

11. Yin, H.; Marshall, D. *Curr. Opin. Biotechnol.* **2012**, *23*, 110-119.

12. Wheeler, A. R.; Throndset, W. R.; Whelan, R. J.; Leach, A. M.; Zare, R. N.; Liao, Y. H.; Farrell, K.; Manger, I. D.; Daridon, A. *Anal. Chem.* **2003**, *75*, 3581-3586.

13. Mittal, N.; Rosenthal, A.; Voldman, J. *Lab Chip.* **2007**, *7*, 1146-1153.

14. Kim, S. H.; Yamamoto, T.; Fourmy, D.; Fujii, T. *Small.* **2011**, *7*, 3239-3247.

15. Eyer, K.; Kuhn, P.; Hanke, C.; Dittrich, P. S. *Lab Chip* **2012**, *12*, 765-772.

16. Huang, K. W.; Wu, Y. C.; Lee, J. A.; Chiou, P. Y. *Lab Chip.* **2013**, *13*, 3721-3727.

17. Gerhardt, T.; Woo, S.; Ma, H. *Lab Chip.* **2011**, *11*, 2731-2737.

18. Ji, H. M.; Samper, V.; Chen, Y.; Heng, C. K.; Lim, T. M.; Yobas, L. *Biomed. Microdev.* **2008**, *10*, 251-257.

19. Cheng, S. B.; Xie, M.; Xu, J. Q.; Wang, J.; Lv, S. W.; Guo, S.; Shu, Y.; Wang, M.; Dong, W. G.; Huang, W. H. *Anal. Chem.* **2016**, *88*, 6773-6780.

20. Saliba, A. E.; Saias, L.; Psychari, E.; Minc, N.; Simon, D.; Bidard, F. C.; Mathiot, C.; Pierga, J. Y.; Fraisier, V.; Salamero, J.; Saada, V.; Farace, F.; Vielh, P.; Malaquin, L.; Viovy, J. L. *Proc. Natl. Acad. Sci. U S A.* **2010**, *107*, 14524-14529.

21. Yu, Z.; Zhou, L.; Zhang, T.; Shen, R.; Li, C.; Fang, X.; Griffiths, G.; Liu, J. *ACS. Sens.* **2017**, *2*, 626-634.

22. Schneider, T.; Kreutz, J.; Chiu, D. T. *Anal. Chem.* **2013**, *85*, 3476-3482.

23. Jimenez-Valdes, R. J.; Rodriguez-Moncayo, R.; Cedillo-Alcantar, D. F.; Garcia-Cordero, J. L. *Anal. Chem.* **2017**, *89*, 5210-5220.

24. Cetin, B.; Li, D. *Electrophoresis.* **2011**, *32*, 2410-2427.

25. Pethig, R. *Biomicrofluidics.* **2010**, *4*, 022811.

26. Gascoyne, P. R.; Shim, S. *Cancers (Basel).* **2014**, *6*, 545-579.

27. Gupta, V.; Jafferji, I.; Garza, M.; Melnikova, V. O.; Hasegawa, D. K.; Pethig, R.; Davis, D. W. *Biomicrofluidics.* **2012**, *6*, 24133.

28. Kung, Y. C.; Huang, K. W.; Chong, W.; Chiou, P. Y. *Small.* **2016**, *12*, 4343-4348.

29. Jin, C.; McFaul, S. M.; Duffy, S. P.; Deng, X.; Tavassoli, P.; Black, P. C.; Ma, H. *Lab Chip.* **2014**, *14*, 32-44.

30. Gossett, D. R.; Weaver, W. M.; Mach, A. J.; Hur, S. C.; Tse, H. T.; Lee, W.; Amini, H.; Di Carlo, D. *Anal. Bioanal. Chem.* **2010**, *397*, 3249-3267.

31. Gascoyne, P. R.; Noshari, J.; Anderson, T. J.; Becker, F. F. *Electrophoresis.* **2009**, *30*, 1388-1398.

32. Henslee, E. A.; Sano, M. B.; Rojas, A. D.; Schmelz, E. M.; Davalos, R. V. *Electrophoresis.* **2011**, *32*, 2523-2529.

33. Fernandez, R. E.; Rohani, A.; Farmehini, V.; Swami, N. S. *Ana.. Chim. Acta.* **2017**, *966*, 11-33.

34. Khoshmanesh, K.; Nahavandi, S.; Baratchi, S.; Mitchell, A.; Kalantar-zadeh, K. *Biosens. Bioelectron.* **2011**, *26*, 1800-1814.

35. Gagnon, Z. R. *Electrophoresis.* **2011**, *32*, 2466-2487.

36. Zhang, C.; Khoshmanesh, K.; Mitchell, A.; Kalantar-Zadeh, K. *Anal. Bioanal. Chem.* **2010**, *396*, 401-420.

37. Albrecht, D. R.; Underhill, G. H.; Mendelson, A.; Bhatia, S. N. *Lab Chip.* **2007**, *7*, 702-709.

38. Srivastava, S. K.; Gencoglu, A.; Minerick, A. R. *Anal. Bioanal. Chem.* **2011**, *399*, 301-321.

39. Shafiee, H.; Caldwell, J. L.; Sano, M. B.; Davalos, R. V. *Biomed. Microdev.* **2009**, *11*, 997-1006.

40. Shim, S.; Stemke-Hale, K.; Tsimberidou, A. M.; Noshari, J.; Anderson, T. E.; Gascoyne, P. R. *Biomicrofluidics.* **2013**, *7*, 11807.

41. Vykoukal, J.; Vykoukal, D. M.; Freyberg, S.; Alt, E. U.; Gascoyne, P. R. *Lab Chip.* **2008**, *8*, 1386-1393.

42. Cemazar, J.; Douglas, T. A.; Schmelz, E. M.; Davalos, R. V. *Biomicrofluidic.s* **2016**, *10*, 014109.

43. Shafiee, H.; Sano, M. B.; Henslee, E. A.; Caldwell, J. L.; Davalos, R. V. *Lab Chip.* **2010**, *10*, 438-445.

44. Pohl, H. A. *J. Appl. Phys.* **1951**, *22*, 869-871.

45. Hughes, M. P. *Electrophoresis.* **2002**, *23*, 2569-2582.

46. Gascoyne, P. R.; Vykoukal, J. *Electrophoresis.* **2002**, *23*, 1973-1983.

47. MacDonald, B. D.; Gong, M. M.; Zhang, P.; Sinton, D. *Lab Chip.* **2014**, *14*, 681-685.

48. Takei, K.; Kawashima, T.; Kawano, T.; Kaneko, H.; Sawada, K.; Ishida, M. *Biomed. Microdev.* **2009**, *11*, 539-545.

49. Guerrette, J. P.; Percival, S. J.; Zhang, B. *J. Am. Chem. Soc.* **2013**, *135*, 855-861.

50. Marchalot, J.; Chateaux, J. F.; Faivre, M.; Mertani, H. C.; Ferrigno, R.; Deman, A. L. *Biomicrofluidics.* **2015**, *9*, 054104.

51. Martinez-Duarte, R.; Renaud, P.; Madou, M. J. *Electrophoresi.s* **2011**, *32*, 2385-2392.

52. Martinez-Duarte, R.; Camacho-Alanis, F.; Renaud, P.; Ros, A. *Electrophoresis.* **2013**, *34*, 1113-1122.

53. Mernier, G.; Martinez-Duarte, R.; Lehal, R.; Radtke, F.; Renaud, P. *Micromachines.* **2012**, *3*, 574-581.

54. Islam, M.; Natu, R.; Larraga-Martinez, M. F.; Martinez-Duarte, R. *Biomicrofluidic.s* **2016**, *10*, 033107.

55. Zhu, H.; Lin, X.; Su, Y.; Dong, H.; Wu, J. *Biosens. Bioelectron.* **2015**, *63*, 371-378.

56. Li, M.; Anand, R. K. *J. Am. Chem. Soc.* **2017**, *139*, 8950-8959.

57. Miller, M. C.; Doyle, G. V.; Terstappen, L. W. *J Oncol.* **2010**, *2010*, 617421.

58. Lee, W. C.; Rigante, S.; Pisano, A. P.; Kuypers, F. A. *Lab Chip.* **2010**, *10*, 2952-2958.

59. Rettig, J. R.; Folch, A. *Anal. Chem.* **2005**, *77*, 5628-5634.

60. Figueroa, X. A.; Cooksey, G. A.; Votaw, S. V.; Horowitz, L. F.; Folch, A. *Lab Chip.* **2010**, *10*, 1120-1127.

61. Eyer, K.; Stratz, S.; Kuhn, P.; Kuster, S. K.; Dittrich, P. S. *Anal. Chem.* **2013**, *85*, 3280-3287.

62. Di Carlo, D.; Wu, L. Y.; Lee, L. P. *Lab Chip.* **2006**, *6*, 1445-1449.

63. Di Carlo, D.; Aghdam, N.; Lee, L. P. *Anal. Chem.* **2006**, *78*, 4925-4930.

64. Kim, S. H.; He, X.; Kaneda, S.; Kawada, J.; Fourmy, D.; Noji, H.; Fujii, T. *Lab Chip.* **2014**, *14*, 730-736.

65. Kim, S. H.; Fujii, T. *Lab Chip.* **2016**, *16*, 2440-2449.

66. Kobayashi, M.; Kim, S. H.; Nakamura, H.; Kaneda, S.; Fujii, T. *PLoS. One.* **2015**, *10*, e0139980.

67. Khamenehfar, A.; Gandhi, M. K.; Chen, Y.; Hogge, D. E.; Li, P. C. *Anal. Chem.* **2016**, *88*, 5680-5688.

68. Ho, C. T.; Lin, R. Z.; Chang, W. Y.; Chang, H. Y.; Liu, C. H. *Lab Chip.* **2006**, *6*, 724-734.

69. Lin, R. Z.; Ho, C. T.; Liu, C. H.; Chang, H. Y. *Biotechnol. J.* **2006**, *1*, 949-957.

70. Nestor, B. A.; Samiei, E.; Samanipour, R.; Gupta, A.; Van den Berg, A.; Derby, M. D. D.; Wang, Z.; Nejad, H. R.; Kim, K.; Hoorfar, M. *RSC Adv.* **2016**, *6*, S7409-S7416.

71. Hatch, A. C.; Fisher, J. S.; Tovar, A. R.; Hsieh, A. T.; Lin, R.; Pentoney, S. L.; Yang, D. L.; Lee, A. P. *Lab Chip.* **2011**, *11*, 3838-3845.

72. Zhang, P.; Ren, L.; Zhang, X.; Shan, Y.; Wang, Y.; Ji, Y.; Yin, H.; Huang, W. E.; Xu, J.; Ma, B. *Anal. Chem.* **2015**, *87*, 2282-2289.

73. Krafft, C.; Schie, I. W.; Meyer, T.; Schmitt, M.; Popp, *J. Chem. Soc. Rev.* **2016**, *45*, 1819-1849.

74. Hanson, C.; Vargis, E. *Sensors (Basel).* **2017**, *17*, 327.

75. Moon, H. S.; Kwon, K.; Kim, S. I.; Han, H.; Sohn, J.; Lee, S.; Jung, H. I. *Lab Chip.* **2011**, *11*, 1118-1125.

76. Antfolk, M.; Magnusson, C.; Augustsson, P.; Lilja, H.; Laurell, T. *Anal. Chem.* **2015**, *87*, 9322-9328.

77. Kim, S. H.; Antfolk, M.; Kobayashi, M.; Kaneda, S.; Laurell, T.; Fujii, T. *Lab Chip.* **2015**, *15*, 4356-4363.

78. Antfolk, M.; Kim, S. H.; Koizumi, S.; Fujii, T.; Laurell, T. *Sci. Rep.* **2017**, *7*, 46507.

79. Allard, W. J.; Matera, J.; Miller, M. C.; Repollet, M.; Connelly, M. C.; Rao, C.; Tibbe, A. G.; Uhr, J. W.; Terstappen, L. W. *Clin. Cancer. Res.* **2004**, *10*, 6897-6904.

80. Chen, X.; Ren, Y.; Liu, W.; Feng, X.; Jia, Y.; Tao, Y.; Jiang, H. *Anal. Chem.* **2017**, *89*, 9583-9592.

81. Ramos, A.; Morgan, H.; Green, N. G.; Castellanos, A. *J. Colloid. Interface. Sci.* **1999**, *217*, 420-422.

82. Green, N. G.; Ramos, A.; Gonzalez, A.; Morgan, H.; Castellanos, A. *Phys. Rev. E. Stat. Phys. Plasmas. Fluids. Relat. Interdiscip. Topics.* **2000**, *61*, 4011-4018.

83. Gonzalez, A.; Ramos, A.; Green, N. G.; Castellanos, A.; Morgan, H. *Phys. Rev. E. Stat. Phys. Plasmas. Fluids. Relat. Interdiscip. Topics.* **2000**, *61*, 4019-4028.

84. Green, N. G.; Ramos, A.; Gonzalez, A.; Morgan, H.; Castellanos, A. *Phys. Rev. E. Stat. Nonlin. Soft. Matter. Phys.* **2002**, *66*, 026305.

85. Wu, J.; Ben, Y. X.; Battigelli, D.; Chang, H. C. *Ind. Eng. Chem. Res.* **2005**, *44*, 2815-2822.

86. Wu, J.; Ben, Y. X.; Chang, H. C. *Microfluid, Nanofluid,* **2005**, *1*, 161-167.

87. D'Amico, L.; Ajami, N. J.; Adachi, J. A.; Gascoyne, P. R.; Petrosino, J. F. *Lab Chip.* **2017**, *17*, 1340-1348.

CHAPTER 4

INTEGRATION OF MARKER-FREE SELECTION OF SINGLE CELLS AT A WIRELESS ELECTRODE ARRAY WITH PARALLEL FLUIDIC ISOLATION AND ELECTRICAL LYSIS

Min Li, Robbyn K. Anand *

Department of Chemistry, Iowa State University, Ames, Iowa 50011, United States

* Corresponding author

Abstract

We present integration of selective single-cell capture at an array of wireless electrodes (bipolar electrodes, BPEs) with transfer into chambers, reagent exchange, fluidic isolation and rapid electrical lysis in a single platform, thus minimizing sample loss and manual intervention steps. The whole process is achieved simply by exchanging the solution in a single inlet reservoir and by adjusting the applied voltage at a pair of driving electrodes, thus making this approach particularly well-suited for a broad range of research and clinical applications. Further, the use of BPEs allows the array to be scalable to increase throughput. Specific innovations reported here include the incorporation of a leak channel to balance competing flow paths, the use of 'split BPEs' to create a distinct recapture and electrical lysis point within the reaction chamber, and the dual purposing of an ionic liquid as an immiscible phase to seal the chambers and as a conductive medium to permit electrical lysis at the split BPEs.

4.1 Introduction

Here we report a scalable dielectrophoretic cell array that integrates marker-free selection and sequestration of single cells with parallel lysis to prepare for analysis in one microfluidic platform. This approach is significant because (i) it addresses a need for

development of versatile devices that integrate all steps needed for single-cell analysis (selection, isolation, assays), (ii) the whole manipulation process (capture, transfer, retention, and electrical lysis) was valve-free and achieved by only adjusting the applied voltage and exchanging the fluid in a single inlet, and (iii) the use of wireless bipolar electrodes (BPEs) allows facile arraying for increased throughput.

Analysis of the composition and response of individual cells allows unique and differentiated subpopulations of cells to be delineated.[1] Understanding cell-to-cell heterogeneity, such as in the expression of a particular gene[1] or protein,[3] concentration of an ion,[4] or differences in regulatory and signaling patterns,[5] helps define their distinct roles in disease states. In pathologies that are driven by a minority of cells, broad access to such information in research and clinical settings could revolutionize medicine. For instance, in cancer biology, the interrogation of individual circulating tumor cells (CTCs) provides key information that can inform therapeutic decisions.[6] However, the enormous value of CTCs has not been completely realized because accurate cellular selection of CTCs is made challenging by their varied physical and biological characteristics and extreme rarity.[7] For such rare cell applications, a key point is that integration of selection with parallel isolation and analysis of individual cells reduces device complexity and the likelihood of cell loss.

Many microfluidic lab-on-a-chip (LOC) technologies have been developed for manipulation and sampling of cells.[8] However, they often suffer from the following issues: (i) Most methods for single-cell isolation are not selective. Cells passively settle into divots[9] or nanowells[10] or are fluidically aligned prior to encapsulation into droplets.[11] Selection must happen prior to the isolation step, and therefore, the overall process is necessarily modular. (ii) Selection methods based on immunoaffinity[12] or size[13] are either over-selective and miss

certain cell populations, thus biasing results, or are under-selective and do not result in highly pure samples. (iii) Most existing capture and detection methods are not easily interfaced with assays. After capture, cells remain trapped on pillars,[14] have been altered by molecular labels/tags,[15] or become lost during transit to a secondary device.[16] To facilitate assays in confined microstructures, embedded microvalves with a large amount of control lines are often required.[8b, 17] The engineering complexity of these microvalves hinders their application in many research and clinical settings. Further, despite there being many lysis methods reported in microfluidics, integration of cell lysis with other functions to make a complete diagnostic system remains rare.[18] Thus, development of fully integrated devices that offer simplicity in manufacturing and operation remains an important challenge.

Among cell manipulation techniques, dielectrophoresis (DEP) has distinct advantages in that it is highly selective, antibody independent and exhibits high output cell viability.[19] Recent studies have demonstrated that this selectivity stems from biophysical properties with high biological relevance.[20] Despite these advantages, most DEP sorting designs are not readily paired with single-cell assays. For instance, in dielectrophoretic field-flow fractionation (DEP-FFF),[21] high-throughput continuous sorting of rare cells is achieved, but cells are not captured individually. Additionally, DEP-based strategies that integrate selection with analysis are frequently sequential, limiting throughput, or require transport of the cells for off-chip analysis, which risks cell loss.[22] The Fujii group pioneered DEP capture in microwells for high-throughput analysis of confined cell lysates.[23] However, the geometric constraints placed on the microwells limited the reaction volumes to only 56 pL, which is insufficient for certain assays such as single-cell RT-qPCR.[24] Further, sealing microwells relies on mechanical actuation that collapses the overlying fluidic structure onto the array. An alternative DEP

design that removes these constraints would improve design flexibility and better prevent crosstalk.

We previously developed the use of DEP at a BPE array to address the need for selective and high-throughput single-cell capture.[7] In this device, BPE tips aligned to cell-sized micropockets accomplished individual capture of CTCs from a background of white blood cells (WBCs). BPEs do not require wire leads, which thereby allowed bifurcation to 32 parallel microchannels, greatly increasing throughput. However, this preliminary design did not incorporate reaction volumes for on-chip assays (e.g., for mutations, transcripts, or enzymatic activity). Separately, we recently reported insulating DEP (iDEP) capture at cell-sized constrictions and fluidic transfer of these cells into co-planar flow-through reaction chambers followed by thermal lysis and loop-mediated amplification (LAMP).[25] This design utilizes the self-digitization (SD) principle to address the need for an isolated reaction volumes – an oil phase filled the fluidic channel and sealed off the chambers. A key advantage of this design is that capture efficiency is decoupled from the geometry of the reaction chamber, and therefore, the reaction volume could be independently tuned. However, the flow-through reaction chamber and traditional electrodes employed are not readily amenable to a bifurcation scheme, thus limiting throughput. Further, the fluidic resistance of these chambers was sufficiently low that imbalances in pressure resulted in both disruption of cell capture and intrusion of oil into the chamber.

In this paper, we integrate the advantages of both the BPE and SD schemes to accomplish selection, isolation, and electrical lysis – the steps required prior to molecular analysis of the contents of individual cells – in a valve-free and robust platform with a single inlet. While the approach is conceptually similar to the electroactive microwell device

introduced by Fujii and coworkers, there are three key distinctions. First, there is only one fluidic layer, which greatly simplifies fabrication. Second, cell capture is accomplished at the reaction chamber inlet (instead of at the bottom of a reaction well), which critically provides independent control over reaction volume and capture efficiency. Third, and most importantly, the cell assay structures are readily fluidically isolated by an immiscible phase (SD principle) to prevent assay crosstalk. Beyond a simple combination of the BPE and SD schemes, a separate innovation is the incorporation of a split BPE inside the reaction chamber that allows electric field-directed cell recapture and electrical lysis. Finally, the use of ionic liquid (IL) as an electrically conductive substitute for oil allowed electrical lysis. These functions are accomplished with minimal peripheral equipment – a power supply and a microscope – thus increasing the relevance of this platform to broad application in research and clinical laboratories.

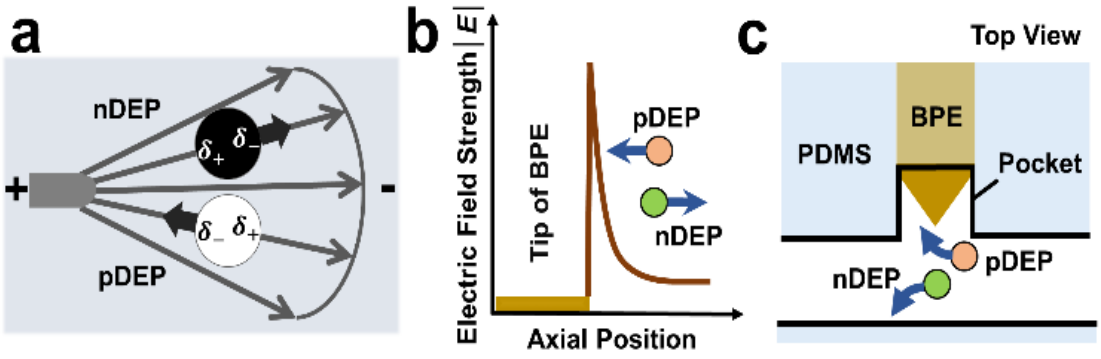

Scheme 4.1. (a) Principles of pDEP attraction and nDEP repulsion in an external electric field and (b,c) near a BPE tip.

4.2 Results and Discussion

As shown in **Scheme 4.1a**, DEP is a field-induced force exerted on a particle due to the interaction of the particle's frequency-dependent dipole moment with the spatial gradient of the electric field. **Scheme 4.1b,c** illustrate the pDEP and nDEP responses that we observed for model CTCs and WBCs, respectively, in our previously reported device.[7] We have now

advanced this design to enable analysis of the captured cells. **Scheme 4.2a** is an image of the device, which notably has only a single inlet and outlet and two electrical leads. **Scheme 4.2b-h** illustrate the steps of operation: (b) When an AC electric field is applied, cells of interest are selectively separated from the flowing sample and individually isolated in the pockets; (c,d) By turning the AC field 'off' and then 'on' again, the captured single-cells are further directed forward and retained at the center of the reaction chambers between adjacent BPE tips. (e) At this juncture, the fluid can be exchanged if warranted by the assay; (f) The microchannel is then filled with a hydrophobic IL to fluidically isolate the chambers. (g) Optionally, the AC field strength can then be increased to lyse captured cells. (h) This approach is therefore amenable to live cell assays or interrogation of cell contents.

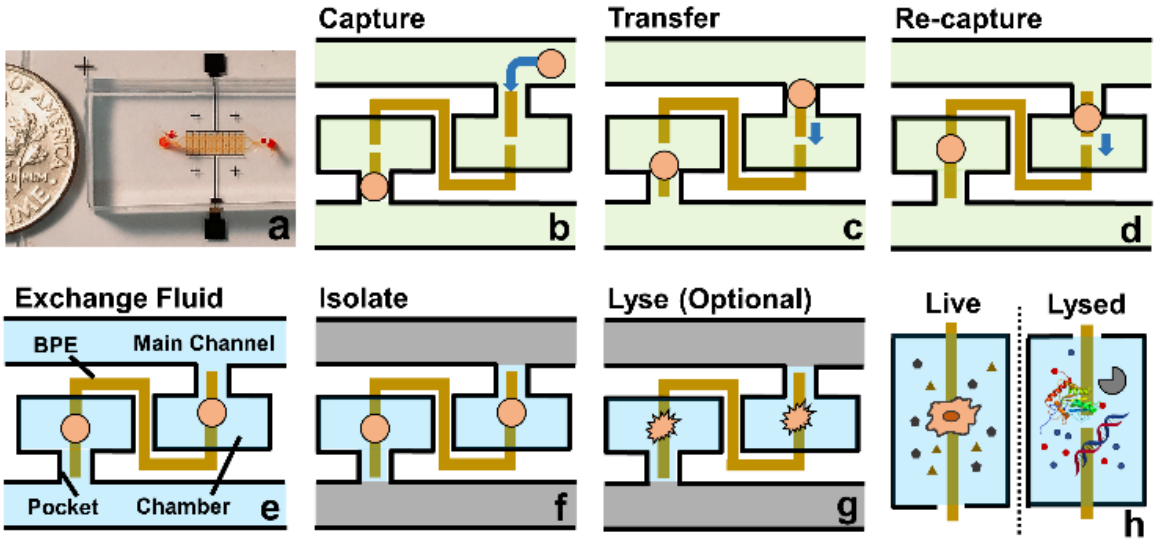

Scheme 4.2. (a) Picture of the microfluidic chip. The channels are filled up with red food dye to show detail. A coin is shown at the side for scale. (b-h) Schematic overview of the current approach.

4.2.1 Leak Channel Design

In our previous work,[7] cell-scale micropockets extruding from either side of each microchannel ensured that individual cells were captured at each electrode tip. Here,

reaction chambers are introduced adjacent to the pockets to store a sufficient amount of reagent solution (2.0 nL) for single-cell assay. Transfer of each cell from pocket to chamber must be accomplished to increase contact area between cells and reagents. However, the lift force created by fluid flow in the channel can easily pull the cell out of the pocket, once the capture voltage is turned off, and thereby impedes cell transfer into the chamber. **Figure 4.1** shows the results of cell transfer in the absence of a leak channel design. **Figure 4.1a** is a surface plot showing the total fluid flow velocity in a segment of the main channel and a micropocket that contains a cell (represented by a white circle). In the *y*-direction, the cell experiences lift force (pressure force, towards the main channel) and drag force (viscous force, towards the chamber), while in the *x*-direction, only drag force is exerted on the cell. Positive total force along the *y*-direction is required for the forward movement into reaction chambers. **Figure 4.1b** is the computed result of the total force (F_{Total}) exerted on a cell when it is located in the pocket. The *x*-axis, as depicted in **Figure 4.1a**, is the distance of the farthest edge of a cell (20.0 μm diameter) from the main channel opening. Importantly, this result was simulated for a design in which the reaction chamber has no additional fluidic connection (i.e., no leak channel). The BPE is not shown. **Figure 4.1c and 4.1d** are sequential bright field images that show the result of turning off the AC voltage after cell capture. From this result, it can be concluded that in the absence of a leak channel, the drag force along the *y*-direction is negligible, while the lift force created by fluid flow can easily pull the cell out of the pocket. Additionally, a rounded pocket corner enhances lift force, and thereby impedes cell transfer. Based on the results, sharp pocket corners are desired, and it is further apparent that an additional force is required to push cells forward into the reaction chambers. Consequently, an additional force is required to push cells forward into the reaction chambers.

We address this need by introducing a leak channel, which induces an additional drag force perpendicular to the main channel by forming a flow pathway into the micropocket and out of the leak channel (**Figure 4.2a**). To investigate the influence of leak channel width and BPE location on cell transfer, the total force exerted on captured cells was computed (**Figure 4.2b**). Based on these results, it can be concluded that F_{Drag} is very sensitive to leak channel resistance, which increases exponentially with decreasing hydraulic radius. A 7 μm width permitted cell entry into the chamber without creating excessive drag force (stronger than DEP capture force) and was therefore chosen for subsequent experiments. Additionally, a distance (*d*, **Figure 4.2a**) of 25-35 μm from the main channel to the farthest edge of the cell (20 μm diameter) prevents the cell from being washed away without compromising capture efficiency. It was found experimentally that this capture position was best achieved with a BPE tip positioned 5-15 μm inside the pocket.

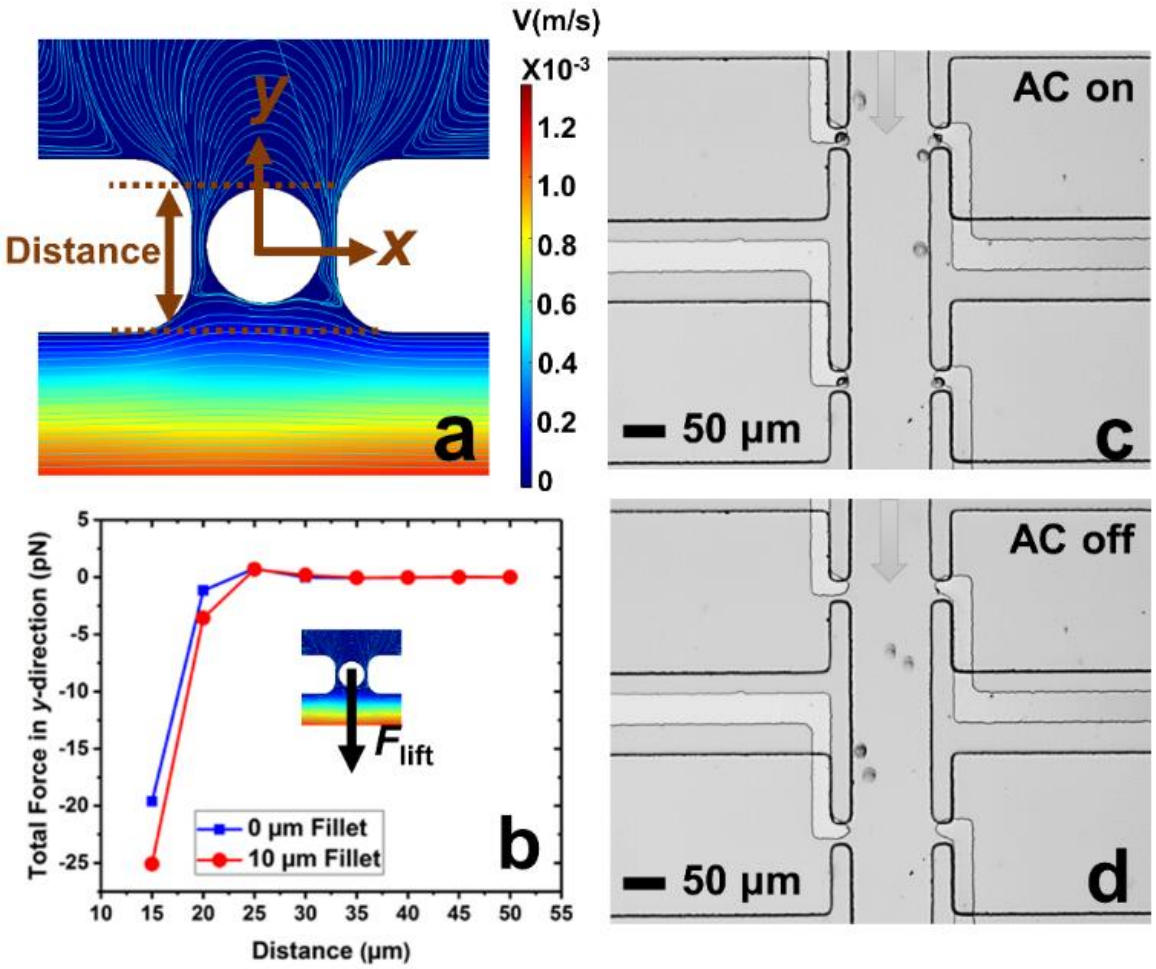

Figure 4.1. Results of the cell transfer step in the absence of a leak channel. (a) Simulated contours of the flow velocity and streamlines of the device when a cell is captured in the pocket. All pocket corners are filleted by 10 μm. (b) Numerical simulation of the total force experienced by a cell along the *y*-direction as a function of the distance of the far edge of a cell to the main channel. The inlet velocity of the main channel was set to 100 μm/s. (c-d) Brightfield images of cell captured and transfer when AC is on (c) and off (d). The grey arrows represent the flow direction.

Using this optimized design, MDA-MB-231 cells were successfully captured individually at each electrode tip when the AC capture voltage was on, and subsequently transferred into reaction chambers after turning off the AC voltage (**Figure 4.2c,d**). To obtain optimal capture and transfer performance, the effect of flow rate was evaluated. As shown in **Figure 4.2e**, increasing linear flow velocity from 80 μm/s to 120 μm/s reduced multi-cell

capture, while going further to 150 μm/s, the number of empty micropockets was significantly increased, leading to a decrease in the percentage of single-cell capture. At 120 μm/s, excellent single cell capture (81.2%) and transfer (88.0%) were achieved. Therefore, 120 μm/s was chosen for subsequent experiments. These results are significant because they demonstrate the valve-free capture and sequestration of individual breast cancer cells in a scalable DEP device at an array of wireless electrodes.

4.2.2 Split BPE Design

To prepare for on-chip molecular analysis of single cells, firm retention of isolated cells in the confined microstructures is crucial, especially if subsequent fluid exchange is required. To address such demand, we further developed a split BPE design, in which each single BPE employed previously was divided into two separate BPEs (**Figure 4.3a-f**). Due to the electric field in the split, cells transferred into reaction chambers could be attracted and firmly retained there. This approach has the following advantages: (i) only cells that experience pDEP can be re-captured, which further enhances selective trapping of target cells, (ii) rapid fluid exchange can be conducted via both convection and diffusion since cells are held in place (**Figure 4.4**), and (iii) at electric field strengths required for DEP capture, cell viability is retained (important for live cell assays), while optionally, the voltage can be increased to lyse the cells.

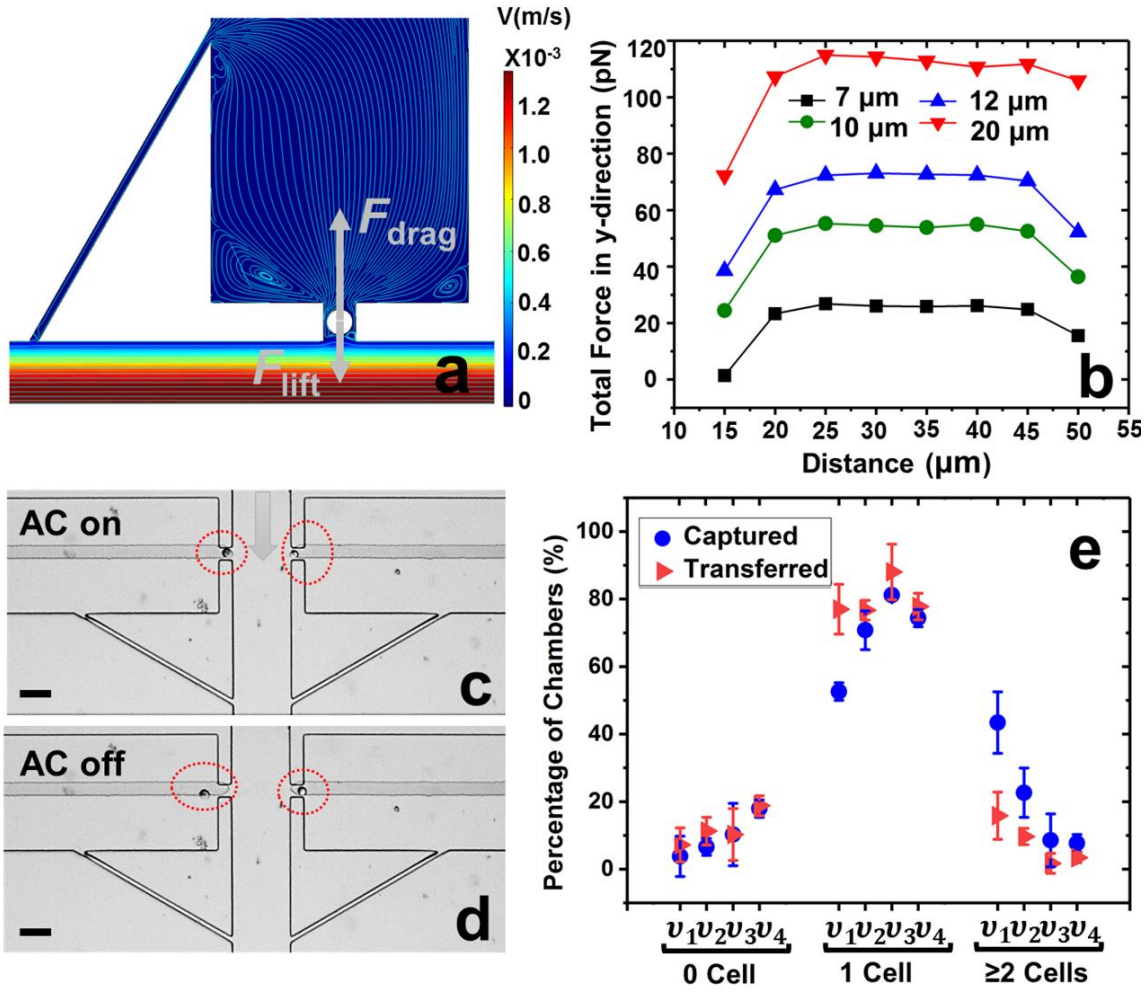

Figure 4.2. Results of the cell transfer step when a leak channel is added to each reaction chamber. (a) Simulated contours of the flow velocity and streamlines when a cell is captured in the pocket. (b) The corresponding total force experienced by a cell along the *y*-direction when varying leak channel width to 7, 10, 12, and 20 µm, respectively. The *x*-axis represents the distance of the farthest edge of a cell to the main channel. (a,b) Inlet velocity = 100 µm/s. (c,d) Brightfield micrographs of cells captured and transfer when AC voltage is (c) on and (d) subsequently, off. Applied voltage, 14 V_{pp} at 70 kHz. (e) Cell capture and transfer performance as a function of the average linear velocity in the main channel. v_1-v_4 represent average linear velocities of 80, 100, 120, and 150 µm/s, respectively. Scale bar, 50 µm.

Considering that breaking of a single BPE into two individual BPEs gives rise to an additional potential drop in the 'split', a higher voltage is necessitated to achieve cell capture. Thus, the applied voltage was increased and the optimal voltage for the split BPE device was evaluated. As shown in **Figure 4.3g**, at 18 V_{pp}, 23.3% of micropockets were empty, while this

number dropped to 5.4% after increasing the capture voltage to 22 V_{pp}. A further increase to 26 V_{pp} resulted in 100% of pockets being filled. However, at this elevated voltage, the percentage of chambers containing multiple cells dramatically increased from 10.6% to 43.1%. Based on these results, 22 V_{pp} was selected as the optimal voltage to achieve single-cell capture (84.4%) and transfer (89.4%) in the split BPE design.

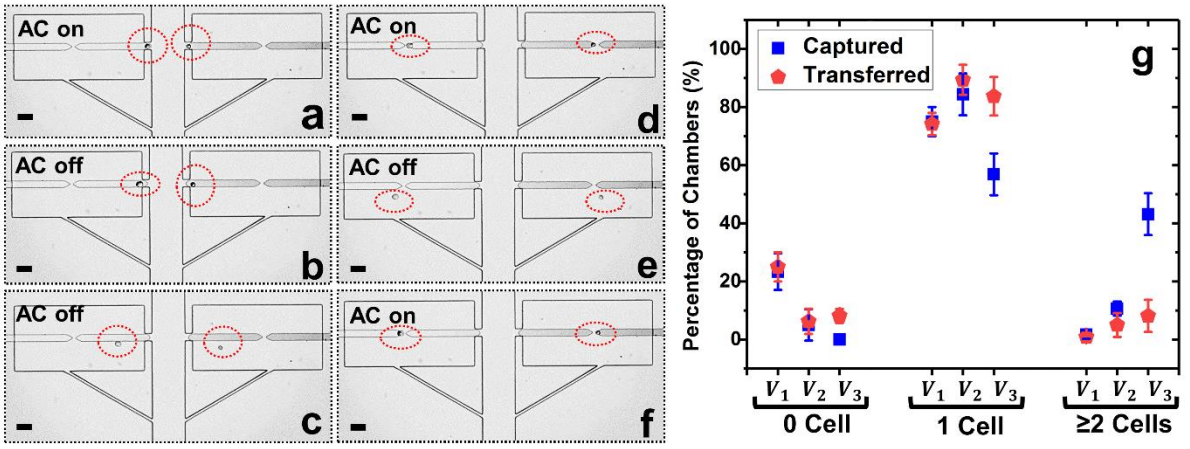

Figure 4.3. Results of the cell re-capture step using split BPEs. (a-f) Time lapse images of cell capture, transfer, and recapture accomplished by only turning the AC voltage on and off sequentially. (a) Single-cell capture (AC on). (b,c) Cell transfer (AC off) and (d) re-capture (AC on) at the tips of the split BPEs. (e) Repeated release (AC off) and (f) re-capture (AC on). Applied voltage, 22 V_{pp} at 70 kHz. Average linear flow velocity, 120 µm/s. (g) Percentage of empty, singly, and multiply occupied chambers after cell capture and transfer as a function of capture voltage 18, 22, and 26 V_{pp}. Scale bar, 50 µm.

Figure 4.3a-f depicts the cell manipulation process at 22 V_{pp}. Notably, after cell transfer is achieved with the AC field 'off', turning it 'on' again causes cells to be re-directed towards the split BPE and re-captured in the gap (**Figure 4.3e,f** and supporting information **Figure 4.10**). These results demonstrate the ability of a split BPE to recapture an individual cell inside the chamber. Such recapture allows retention of the cell during fluid exchange and positions the cell for electrical lysis.

To investigate the efficiency of fluid exchange when allowed to occur primarily by diffusion, the device without a leak channel was employed. **Figure 4.4.** shows the result obtained for the exchange of two solutions of fluorescent dye in DEP buffer. The device was first filled with green fluorescent dye at a flow rate of 0.1 μL/min by withdrawing from the outlet. Then, the solution in the inlet was exchanged for the red dye solution and fluorescence images were obtained at multiple time points (up to 1 h) after solution exchange. An important point is that the red dye is 70 kDa dextran tagged with Texas Red. Therefore, it has a diffusion coefficient that is more representative of a large biomolecule that may be incorporated into a reagent mixture for a bioassay. As a result, the exchange of the green dye (a small molecule) is much more rapid than for the red dye. As shown in supporting information **Figure 4.9c**, 78.4% of green dye was exchanged after 20 min, while red dye diffused into the chambers even after 60 min (supporting information **Figure 4.9d**). This slow rate of fluid exchange by diffusion contrasts the higher efficiency of fluid exchange by both convection and diffusion that is achieved when a leak channel is added (**Figure 4.4**). Using the device with leak channels, the green dye solution could be completely replaced within 10 min, and the red dye reached the end (furthest edge) of reaction chambers after only 5 min. Therefore, the leak channel design allows DEP buffer to be exchanged with reagent solution rapidly, which decreases potential alteration of a target molecule and increases ease of use.

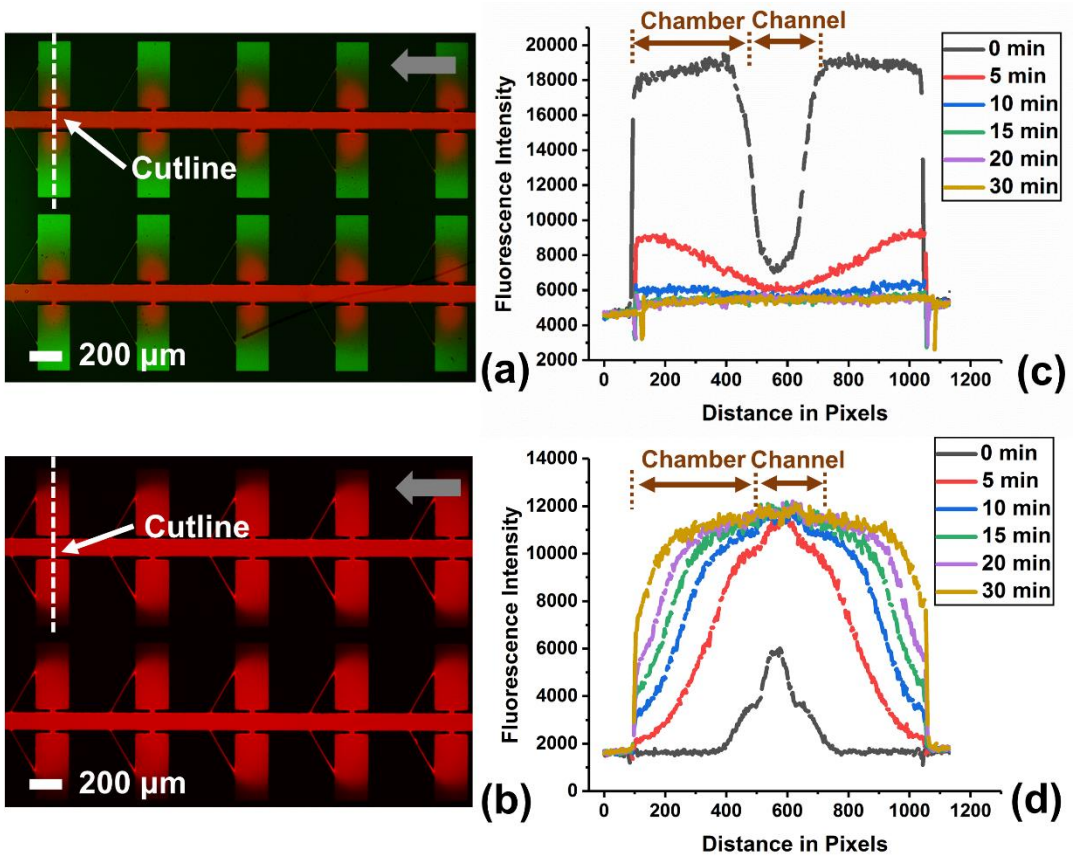

Figure 4.4. Fluorescence micrographs of the device with leak channel. The device filled with a green dye after 5 min (a), and (b) 30 min after replacement of the fluid in the channels with red dye. Time-lapse profile of fluorescence intensity for green dye (c) and red dye (d) along the cutline. Grey arrows indicate flow direction.

After cells were re-captured at the split BPEs, electric lysis was performed by stepping to a higher voltage for 5 s (**Figure 4.5**). Upon electroporation, the cell membrane was disrupted and cells expanded, which is consistent with previously reported results.[26] It was found that 100% of cells were lysed at 166 V_{pp} (supporting information **Figure 4.12**). Non-uniform lysis was observed from 112 V_{pp} to 166 V_{pp} (supporting information **Figure 4.11**) and is attributed to heterogeneous size distribution. Cells with small diameter have a higher threshold field strength for electroporation.[26] To further confirm lysis, we demonstrated release of a membrane-permeant dye Calcein from MDA-MB-231 cells. Upon electroporation, the

fluorescence intensity immediately decreased, which indicates membrane disruption and Calcein leakage (**Figure 4.5g,j**).

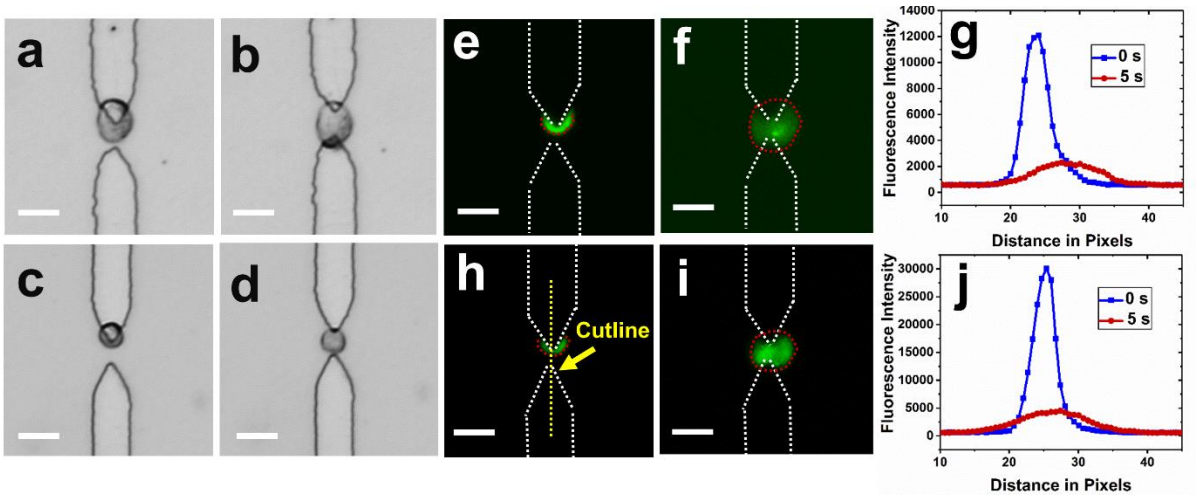

Figure 4.5. Results of electrical lysis using split BPEs. Sequential brightfield images show that the captured cells (a, c) moved to the center of split BPEs 1 s after increasing to 166 V_{pp} (b, d) to initiate lysis. Fluorescent images of capture (e,h) and lysis (f,i) of single MDA-MB-231 cells (green) after 5 s of AC field application. (g,j) Change of the fluorescence intensity before and after lysis. Scale bar, 20 μm.

4.2.3 Fluid Isolation and Electrical Lysis

Considering that cross-talk of adjacent chambers may affect the accuracy of the readout during cellular characterization, fluidic isolation of each individual reaction chamber is crucial. For live cell assays, digitization of each compartment could be conducted using a mixture of mineral oil and surfactant, as reported by the Chiu group.[27] However, to assay cellular contents in the present device, the isolation fluid must be electrically conductive to enable electrical lysis. Moreover, the fluid must be hydrophobic and exhibit modest viscosity for liquid handling. Most importantly, the phase boundary needs to be stable throughout the subsequent assay.

We addressed this need by choosing an IL as the immiscible phase considering its high hydrophobicity, low viscosity and electrical conductivity. Various flow patterns and flow rates

were evaluated to achieve optimal fluidic isolation (supporting information **Figure 4.13-4.15**). It was found that continuous flow at 0.1 μL/min allowed the fluid boundary to be maintained for at least 1 h without any propagation of IL into chambers. This result is significant because it demonstrates the potential for fluidic isolation using an IL for on-chip single-cell analysis.

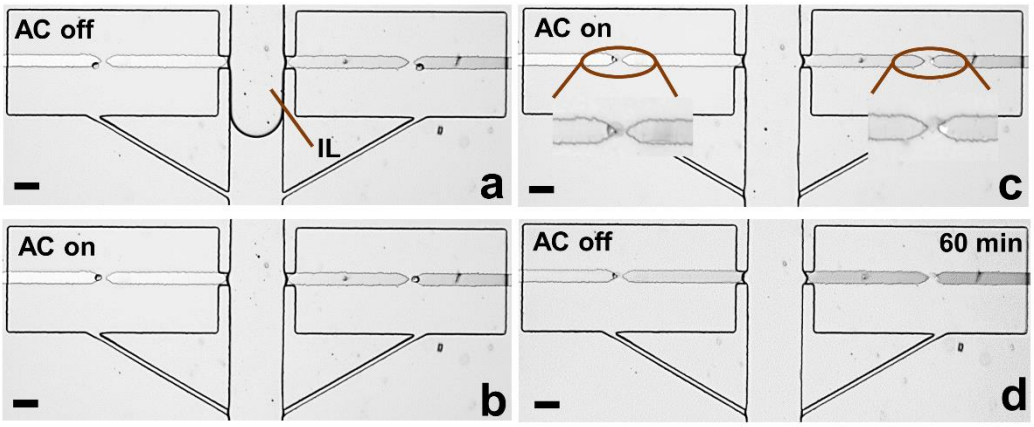

Figure 4.6. Brightfield micrographs showing the results of fluidic isolation and electrical lysis. During isolation with IL, AC was turned off (a) and back on (b) to prohibit capture of cells that had settled in the reservoir. Subsequent images show (c) lysis of the cells after isolation and (d) stable phase boundary at 1 h.

To further verify the robustness of the current technique, the entire workflow was conducted in sequence (supporting information **Figure 4.16**). Notably, after fluidic isolation using IL, 100% of captured cells were electrically lysed, and the buffer/IL boundary was maintained 1 h afterward (**Figure 4.6c,d**). These results are significant because they demonstrate the integration of all steps required prior to analysis in one microfluidic unit. Notably, in our previous report,[7] we demonstrated the selective capture of CTCs from WBCs at each micropocket. Therefore, the strategy demonstrated here not only meets the challenge of integration but also selectivity relevant to CTCs. In subsequent studies, we aim to exploit the flexibility in microchamber geometry to accomplish a variety of molecular analyses of individual cells.

4.3 Conclusions

In conclusion, we have developed a DEP-based approach for marker-free selection, isolation, and assay of single cells that is scalable and allows the reaction volume to be tuned. The process is amenable to either live cell assay or the assessment of cellular contents and is sufficiently inexpensive and easy to operate to be practical for broad application. Scalability permits sampling and analysis of larger input volumes. The current device has 2 parallel channels in a footprint of 15.6 mm^2 and 40 reaction chambers. However, we previously demonstrated bifurcation to 32 parallel channels, which with 640 chambers would approach 2.5 cm^2 and about 18 μL/h throughput, which is effective for many applications. The technology reported here is broadly applicable to individual analysis of many cell types and has a distinct advantage where cell phenotypes are distinguishable by their electrophysiological properties. In the context of CTCs, these dielectric properties are a much more specific differentiator of phenotype than size alone while not being as overly selective as a single biomarker such as EpCAM. Toner and coworkers recently demonstrated the wide range of CTC size and EpCAM expression thereby underscoring the need for alternatives to size- and antibody-based capture.[28] This study is a premier example of the cutting edge in CTC detection, and importantly, it clearly demonstrates where there is remaining need – namely, to interface cell selection with single-cell isolation and subsequent assays. We anticipate that the platform reported here would be appropriate as secondary to an inline pre-sort for nucleated cells (e.g., by lateral displacement) with or without WBC depletion[28] or to pre-enrichment by acoustophoresis.[19b] Finally, the isolation of individual cells at an array of wireless electrodes (BPEs), which are also frequently employed for sensing,[29] presents the possibility for future integration of this technology with electrochemical methods of cell analysis.[30]

4.4 References

1. a) X. Chen, J. C. Love, N. E. Navin, L. Pachter, M. J. Stubbington, V. Svensson, J. V. Sweedler, S. A. Teichmann, *Nat. Biotechnol.* **2016**, *34*, 1111-1118; b) L. Zhang, A. Vertes, *Angew. Chem. Int. Ed.* **2018**, *57*, 4466-4477.

2. C. Gawad, W. Koh, S. R. Quake, *Nat. Rev. Genet.* **2016**, *17*, 175-188.

3. S. S. Agasti, M. Liong, V. M. Peterson, H. Lee, R. Weissleder, *J. Am. Chem. Soc.* **2012**, *134*, 18499-18502.

4. L. Li, Y. Fan, Q. Li, R. Sheng, H. Si, J. Fang, L. Tong, B. Tang, *Anal. Chem.* **2017**, *89*, 4559-4565.

5. Q. Shi, L. Qin, W. Wei, F. Geng, R. Fan, Y. S. Shin, D. Guo, L. Hood, P. S. Mischel, J. R. Heath, *Proc. Natl. Acad. Sci. U S A* **2012**, *109*, 419-424.

6. S. A. Joosse, T. M. Gorges, K. Pantel, *EMBO Mol. Med.* **2015**, *7*, 1-11.

7. M. Li, R. K. Anand, *J. Am. Chem. Soc.* **2017**, *139*, 8950-8959.

8. a) B. J. Green, T. Saberi Safaei, A. Mepham, M. Labib, R. M. Mohamadi, S. O. Kelley, *Angew. Chem. Int. Ed.* **2016**, *55*, 1252-1265; b) R. N. Zare, S. Kim, *Annu Rev Biomed Eng* **2010**, *12*, 187-201.

9. D. Di Carlo, L. Y. Wu, L. P. Lee, *Lab Chip* **2006**, *6*, 1445-1449.

10. S. M. Park, D. J. Wong, C. C. Ooi, D. M. Kurtz, O. Vermesh, A. Aalipour, S. Suh, K. L. Pian, J. J. Chabon, S. H. Lee, M. Jamali, C. Say, J. N. Carter, L. P. Lee, W. G. Kuschner, E. J. Schwartz, J. B. Shrager, J. W. Neal, H. A. Wakelee, M. Diehn, V. S. Nair, S. X. Wang, S. S. Gambhir, *Proc. Natl. Acad. Sci. U S A* **2016**, *113*, E8379-E8386.

11. H. N. Joensson, H. Andersson Svahn, *Angew. Chem. Int. Ed.* **2012**, *51*, 12176-12192.

12. a) S. T. Wang, K. Liu, J. A. Liu, Z. T. F. Yu, X. W. Xu, L. B. Zhao, T. Lee, E. K. Lee, J. Reiss, Y. K. Lee, L. W. K. Chung, J. T. Huang, M. Rettig, D. Seligson, K. N. Duraiswamy, C. K. F. Shen, H. R. Tseng, *Angew. Chem. Int. Ed.* **2011**, *50*, 3084-3088; b) S. Wang, H. Wang, J. Jiao, K. J. Chen, G. E. Owens, K. Kamei, J. Sun, D. J. Sherman, C. P. Behrenbruch, H. Wu, H. R. Tseng, *Angew. Chem. Int. Ed.* **2009**, *48*, 8970-8973.

13. a) V. De Giorgi, P. Pinzani, F. Salvianti, J. Panelos, M. Paglierani, A. Janowska, M. Grazzini, J. Wechsler, C. Orlando, M. Santucci, T. Lotti, M. Pazzagli, D. Massi, *J. Invest. Dermatol.* **2010**, *130*, 2440-2447; b) X. Fan, C. Jia, J. Yang, G. Li, H. Mao, Q. Jin, J. Zhao, *Biosens. Bioelectron.* **2015**, *71*, 380-386.

14. M. G. Ahmed, M. F. Abate, Y. Song, Z. Zhu, F. Yan, Y. Xu, X. Wang, Q. Li, C. Yang, *Angew. Chem. Int. Ed.* **2017**, *129*, 10821-10825.

15. S. Hou, L. Zhao, Q. Shen, J. Yu, C. Ng, X. Kong, D. Wu, M. Song, X. Shi, X. Xu, W. H. OuYang, R. He, X. Z. Zhao, T. Lee, F. C. Brunicardi, M. A. Garcia, A. Ribas, R. S. Lo, H. R. Tseng, *Angew. Chem. Int. Ed.* **2013**, *52*, 3379-3383.

16. J. Cemazar, T. A. Douglas, E. M. Schmelz, R. V. Davalos, *Biomicrofluidics* **2016**, *10*, 014109.

17. A. K. White, K. A. Heyries, C. Doolin, M. Vaninsberghe, C. L. Hansen, *Anal. Chem.* **2013**, *85*, 7182-7190.

18. L. Nan, Z. Jiang, X. Wei, *Lab Chip* **2014**, *14*, 1060-1073.

19. a) Z. R. Gagnon, *Electrophoresis* **2011**, *32*, 2466-2487; b) M. Li, R. K. Anand, *Anal. Bioanal. Chem.* **2018**, *410*, 2499-2515.

20. A. R. Yale, J. L. Nourse, K. R. Lee, S. N. Ahmed, J. Arulmoli, A. Y. L. Jiang, L. P. McDonnell, G. A. Botten, A. P. Lee, E. S. Monuki, M. Demetriou, L. A. Flanagan, *Stem. Cell. Rep.* **2018**.

21. P. R. Gascoyne, J. Noshari, T. J. Anderson, F. F. Becker, *Electrophoresis* **2009**, *30*, 1388-1398.

22. a) K. W. Huang, Y. C. Wu, J. A. Lee, P. Y. Chiou, *Lab Chip* **2013**, *13*, 3721-3727; b) P. Zhang, L. Ren, X. Zhang, Y. Shan, Y. Wang, Y. Ji, H. Yin, W. E. Huang, J. Xu, B. Ma, *Anal. Chem.* **2015**, *87*, 2282-2289.

23. S. H. Kim, T. Fujii, *Lab Chip* **2016**, *16*, 2440-2449.

24. a) A. Ståhlberg, M. Kubista, *Expert review of molecular diagnostics* **2014**, *14*, 323-331; b) Y. Gong, A. O. Ogunniyi, J. C. Love, *Lab Chip* **2010**, *10*, 2334-2337; c) A. K. White, M. VanInsberghe, O. I. Petriv, M. Hamidi, D. Sikorski, M. A. Marra, J. Piret, S. Aparicio, C. L. Hansen, *Proc. Natl. Acad. Sci. U S A* **2011**, *108*, 13999-14004.

25. Y. Qin, L. Wu, T. Schneider, G. S. Yen, J. Wang, S. Xu, M. Li, A. L. Paguirigan, J. L. Smith, J. P. Radich, R. K. Anand, D. T. Chiu, *Angew. Chem. Int. Ed.* **2018**, *57*, 11378-11383.

26. H. Y. Wang, C. Lu, *Anal. Chem.* **2006**, *78*, 5158-5164.

27. D. E. Cohen, T. Schneider, M. Wang, D. T. Chiu, *Anal. Chem.* **2010**, *82*, 5707-5717.

28. F. Fachin, P. Spuhler, J. M. Martel-Foley, J. F. Edd, T. A. Barber, J. Walsh, M. Karabacak, V. Pai, M. Yu, K. Smith, H. Hwang, J. Yang, S. Shah, R. Yarmush, L. V. Sequist, S. L. Stott, S. Maheswaran, D. A. Haber, R. Kapur, M. Toner, *Sci. Rep.* **2017**, *7*, 10936.

29. S. E. Fosdick, K. N. Knust, K. Scida, R. M. Crooks, *Angew. Chem. Int. Ed.* **2013**, *52*, 10438.

30. T. E. Lin, S. Rapino, H. H. Girault, A. Lesch, *Chem. Sci*. **2018**, *9*, 4546.

4.5 Supporting Information

4.5.1 Chemicals

The silicone elastomer and curing agent (Sylgard 184), bovine serum albumin (BSA) (biotech grade), 0.25% Trypsin-EDTA (1X), Green dye (BODIPY™ disulfonate) and red dye (Dextran, Texas Red™, 70 kDa) were purchased from Fisher Scientific (Thermo Fisher Scientific, Inc., Waltham, MA). The DMEM/F12 cell culture medium, dextrose, sucrose, Pluronic® F-108,1.0 M Tris·HCl stock and the ionic liquid 1-Decyl-3-methylimidazolium bis(trifluoromethanesulfonyl)imide were obtained from Sigma-Aldrich, Inc. (St. Louis, MO). All dilutions were conducted with Type 1 water (18.2 MΩ·cm). DEP buffer was comprised of 8.0% sucrose, 0.3% dextrose, and 0.1% BSA in 1.0 mM Tris buffer (pH 8.1).

4.5.2 Cell Culture

MDA-MB-231 cells were obtained from ATCC and cultured in DMEM/F12 with 1% pen-strep and 10% fetal bovine serum supplementation at 37 ºC and 5% CO_2. All cells were subcultured every 2 days to maintain a cell confluence less than 80%. In preparation of DEP experiments, MDA-MB-231 cells were detached from culture flask using 0.25% Trypsin-EDTA (1X), followed by pelleting by centrifugation and resuspension in 7.0 mL DEP buffer. Pelleting and resuspension to cell concentration of $5x10^3$ cells/mL was repeated one additional time to wash cells in DEP buffer before DEP experiments

4.5.3 DEP Experiments

All the devices were designed to operate such that the MDA-MB-231 cell solutions were flowed through the main channel, from which they were attracted to and captured at BPE tips (positive DEP, pDEP). Prior to DEP experiments, all devices were treated with DEP buffer containing 3.0 μM Pluronic solution overnight, followed by rinsing with DEP buffer for 15 min. Device operation was accomplished by the application of an AC voltage at coplanar driving electrodes at each side of the BPE arrays using a Tektronix AFG3011C waveform generator (Tektro-nix, Beaverton, OR) and Trek model 2205 amplifier (Trek, Lockport, NY). The AC frequency was maintained at 70 kHz at which MDA-MB-231 cells experience strong pDEP. A Nikon Eclipse Ti inverted microscope and Nikon AZ-100 microscope (Nikon, Tokyo, Japan) were utilized to image cells to obtain fluorescence and bright field images, respectively. For experiments that were used to optimize flow rates and applied voltages, a Pluronic-treated device was rinsed with DEP buffer for 15 min. The solution in the inlet reservoir (4.0 mm

diameter) was then placed with solution, and a height differential was established between the inlet and outlet reservoirs to achieve a desired average linear flow velocity in the channels. Subsequently, an AC signal was applied at the driving electrodes to generate the desired average electric field strength for cell capture and re-capture. For experiments with fluid exchange and isolation steps, 20.0 μL of DEP buffer solution was pipetted into a 1.0 mm-diameter inlet reservoir and injected into the microchannels by using negative pressure (withdrawal from the outlet with a syringe pump (Pico Pump Elite Dual Syringe Pump, Harvard Apparatus, Holliston, MA)). The flow was then set such that the average linear velocity was 120 μm/s for cell capture, transfer and re-capture steps. Subsequently, the flow was adjusted to 0.1 μm/min for fluid exchange and isolation.

4.5.4 Device Dimensions

The dimensions for designs evaluated in the present work are described here. All designs were modified, as follows, from the parallel-channel design that was reported previously.[1] All channels, pockets and chambers are 25 μm tall. A reaction chamber (200 μm wide x 400 μm long) was extended from each micropocket (20 μm wide x 25 μm long) (**Figure 4.7**). A leak channel (0.3165 mm long) and one of several widths as described in the Results and Discussion) was affixed at a 60 ^{o}C angle to each chamber to make a fluidic connection to the main channel. For a proof-of-concept demonstration, we simplified the design from our previous 32 channels into two parallel channels. As shown in **Figure 4.8**, the resultant parallel microchannels were each 6.8 mm long × 100 μm wide × 25 μm tall and separated by 1.05 mm (center-to-center). Each side of each parallel channel featured 12 cell-assay units (micropocket, reaction chamber and leak channel), leading to 48 units in total. The electrodes extended into the pockets from under the PDMS to a distance of 5.0 μm from the channel. The two rows of electrodes at the ends (outermost channels) were interconnected and led to contacts for the waveform generator.

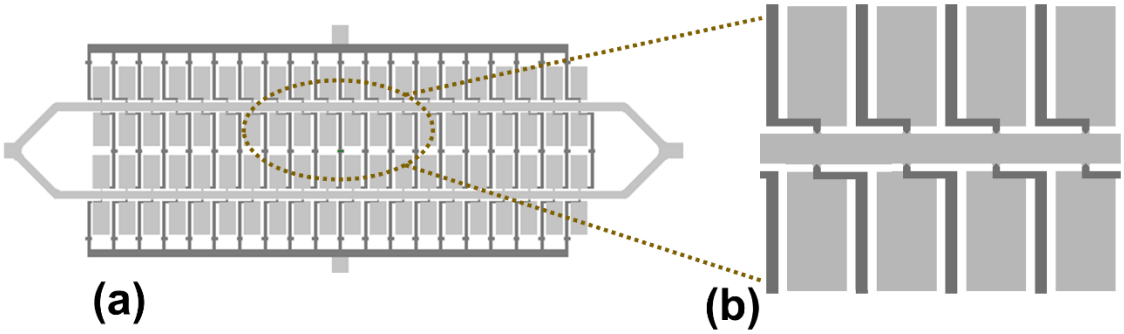

Figure 4.7. The AutoCAD drawing of the parallel-channel when no leak channel is present. (a) zoom-out image; (b) zoom-in image. The microchannels are in light grey and the electrodes are in dark grey.

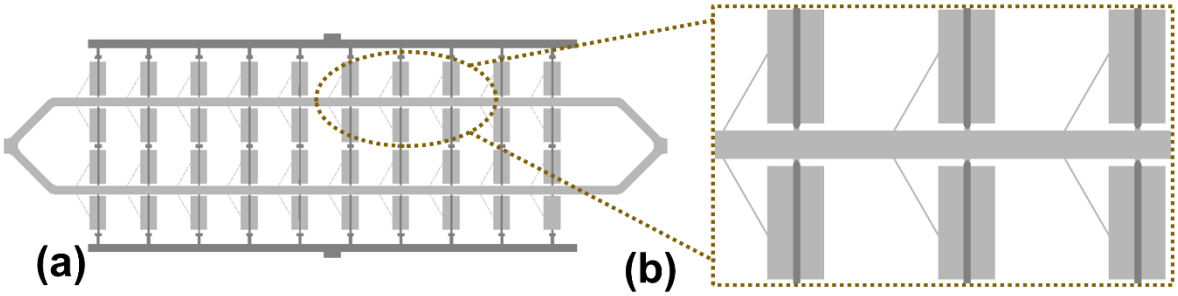

Figure 4.8. The AutoCAD drawing of the parallel-channel device with leak channel added. (a) zoomed-out image; (b) zoom-in image. The microchannels are in light grey and the electrodes are in dark grey. Split BPE design was conducted by dividing each single BPE from the middle into two separate BPEs. The tip-to-tip distance is 0 μm in AutoCAD drawing. After etching, the distance between split BPE tips is about 10 μm.

4.5.5 Fluid Exchange

Figure 4.9 shows the result obtained for the exchange of two solutions of fluorescent dye in DEP buffer in the absence of leak channel. This data was compared with the results obtained with the leak channel that are described in the main text **(Figure 4.4)**.

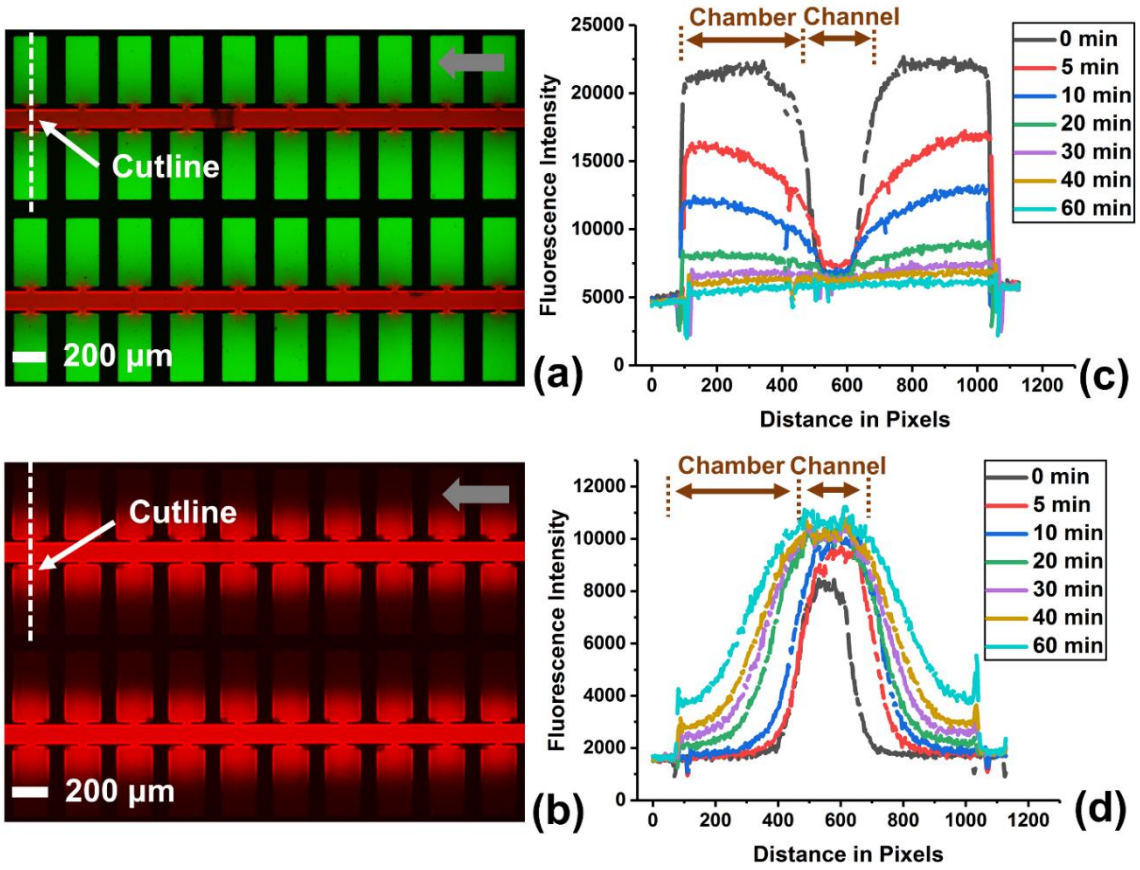

Figure 4.9. Fluorescence micrographs of the device without leak channel. The device filled with a green dye after 5 min (a), and (b) 30 min after replacement of the fluid in the channels with red dye. Time-lapse profile of fluorescence intensity for green dye (c) and red dye (d) along the cutline. To obtain such results, 10 μL of green dye solution was first pipetted in the 2.0 mm-diameter reservoir and injected into the microchannels by using negative pressure. The flow was then set to 0.1 μL/min and maintained for 30 min. Subsequently, the green dye solution in the reservoir was pipetted out and replaced with 10 μL of red dye. Grey arrows indicate flow direction.

4.5.6 Cell Recapture

The addition of a leak channel induces a flow pathway from the main channel into micropocket and out of the leak channel. Thus, two flow pathways are present and cells experience an additional drag force ($F_{Drag\text{-}y}$) created by leak flow along the *y*-direction. Consequently, when an electric field is applied, cells of interest can be selectively captured at the micropockets; and then, after turning off the AC voltage, captured single cells move along the leak flow circuit, and are transferred into chambers. To achieve the desired capture and transfer of individual cells, several parameters need to be considered: (i) *Pocket size*. Micropockets enable volumetric control of the number of cells captured and protect cells from being washed away by fluid flow. To perform single-cell capture, cell-scale pockets are required. (ii) *Leak channel width*. A large leak channel cross section leads to fast flow (strong F_{Drag}), which pushes cells into chambers even when the AC capture voltage is on and results in capture of multiple cells. Furthermore, under this condition, cells randomly circuit in and

out of chambers. On the other hand, if the leak channel width is too narrow, extremely fast flow is needed for cell transfer, and inconveniently, two distinct flow rates would be required for the capture step (slow flow) and transfer step (fast flow). Thus, the leak channel width needs to lie between these extremes. (iii) *BPE location*. Since the position of cell capture determines the relative strength of drag forces derived by the two flow pathways (along main channel and along leak channel), and thereby the direction of cell movement, the location of the BPE tip must be carefully controlled. When cells are captured within main channel streamlines, cells are readily knocked away by fluid flow. However, when BPE tips are far away from main channels, cell transfer becomes very favorable but may lead to attachment of a second cell.

Using the optimal design (20 x 25 μm pocket, 7 μm wide leak channel and BPE tip positioned 5-15 μm inside the pocket), high-fidelity capture and transfer of individual cells were achieved. During cell transport into microchambers, the flow pathway for cells with large and small diameters were investigated (**Figure 4.10**). First, transferred cells transferred only experienced drag force (proportional to cell radii, $F_{Drag} \propto r$), leading to fast movement for large cells. When cells moved further (~ 60-90 μm from the to main channel), the AC voltage was turned back on and DEP force (F_{DEP}) directed cells to move towards the split between BPE tips, while F_{Drag} pushed cells towards the leak channel. Since DEP force is more sensitive to cell diameter ($F_{DEP} \propto r^3$), the flow pathway for small cells deviated more towards leak channel than that of for large cells. To prevent cells from being dragged away, the AC voltage was increased from 22 V_{pp} to 32 V_{pp} for cell re-capture. Under such increased electric field, 100% of cells transferred were attracted and captured at split BPEs.

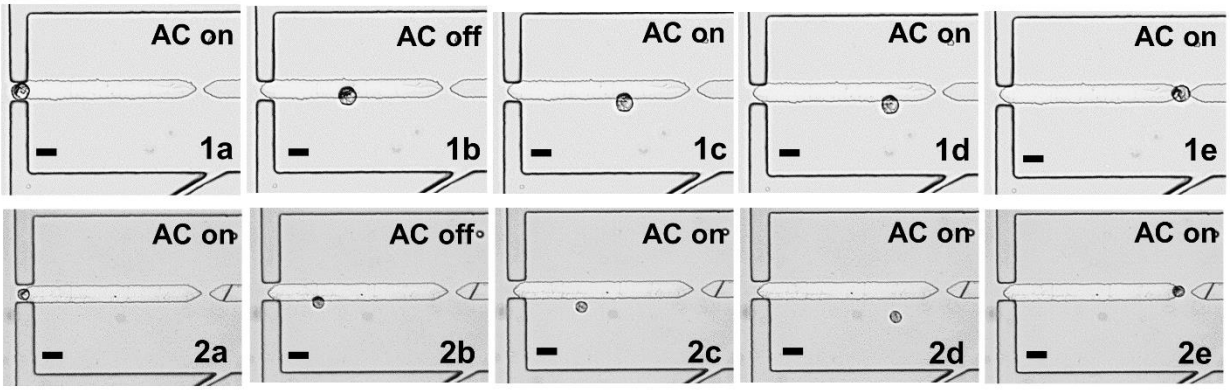

Figure 4.10. Time-lapse images of cell re-capture under the optimal conditions (linear average velocity, 120 μm/s; applied voltage, 22 V_{pp} for capture and 32 V_{pp} for re-capture). (1a-1e) Cells with large diameter moved along BPE and were re-captured at BPE tips. (2a-2e) The flow pathway of small cells deviated slightly towards leak channel (due to weak DEP force), and these smaller cells were retained mainly at one BPE tip. Scale bar: 25 μm.

4.5.7 Electrical Lysis

For assays including genomics and proteomics, of particular importance is lysis of cells to release intracellular contents. Considering the potential alteration of a target molecule's native structure and expression during lysis, the lysis approach must be both gentle and rapid. Traditional mechanical lysis such as bead beating is effective on the macroscale but not

compatible with a microfluidic device. Although sharp nanostructures have been reported for cell lysis in microchannels,[2] inclusion of such structures greatly complicates device fabrication. Sonication typically takes about 50 s for single cell lysis and the heat generated may denature proteins. Chemical lysis, often with detergents, is a potentially milder and quicker protocol, while it requires precise liquid handling (an extra fluid exchange step) and careful selection of optimal lysis media. Electrical lysis, achieved by placing cells under sufficiently high electric field for electroporation, is simple, fast (on the order of milliseconds) and efficient.[3] To avoid the formation of gas bubbles under a high electric field, AC electric field is often employed.

The split BPE design in the present work enables electrical lysis of captured individual cells without modification of channels or addition of further electrical leads. After cells were re-captured at the split BPEs, electrical lysis was performed by simply increasing the applied voltage. **Figure 4.11** shows the bright-field images of cells taken before and after the voltage was increased from 32 V_{pp} to a higher voltage in the range of 112 V_{pp} to 166 V_{pp} (as indicated in the caption) and held for 5 s. The lowest voltage for which lysis of 100% of captured cells was observed was 166 V_{pp}. **Figure 4.12** shows the successful lysis of ten different cells when the applied voltage was directly increased from 32 V_{pp} to 166 V_{pp} and maintained for 5s.

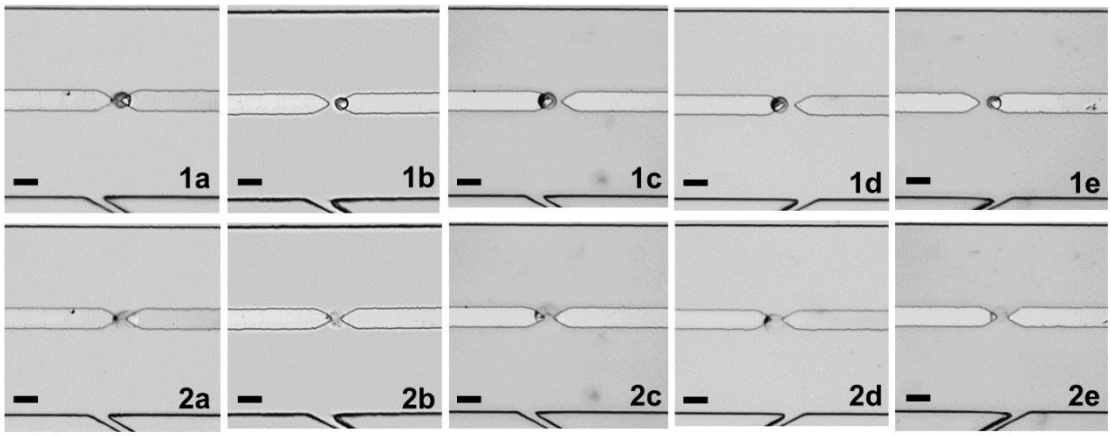

Figure 4.11. Investigation of voltage needed for electric lysis. (1a-1e) cells were re-captured at split BPEs at 32 V_{pp}. (2a-2e) The applied voltage was gradually increased to 112 V_{pp} (2a), 126 V_{pp} (2b), 140 V_{pp} (2c), 152 V_{pp} (2d), and 166 V_{pp} (2e) until electroporation was observed. Prior to cell lysis, the fluid flow in the main channels was stopped to observe the static lysis. Scale bar: 25 μm.

4.5.8 Fluid Isolation

Fluidic isolation of individual reaction chambers by an immiscible phase is crucial to circumvent cross-contamination and provide accurate readout for cell analysis, and additionally, this immiscible phase needs to be conductive to allow electrical lysis after fluid sealing. In this scenario, we selected ionic liquid (IL) to address such requirements and investigated conditions for maintaining the phase boundary. To minimize the consumption of IL, fluidic flow of IL was stopped after entering the main channels. **Figure 4.13** shows the results of such approach under various initial flow rates. It was found that IL slowly expanded into reaction chambers after flow was stopped. However, the position of the boundary was maintained at the chamber opening at early times (< 5 min) for flow rates of 1.0 μL/min and

0.5 µL/min, indicating that continuous flow lower than 1.0 µL/min may result in a stable boundary. Thus, fluidic isolation by continuous flow at rates lower than 1.0 µL/min was subsequently evaluated.

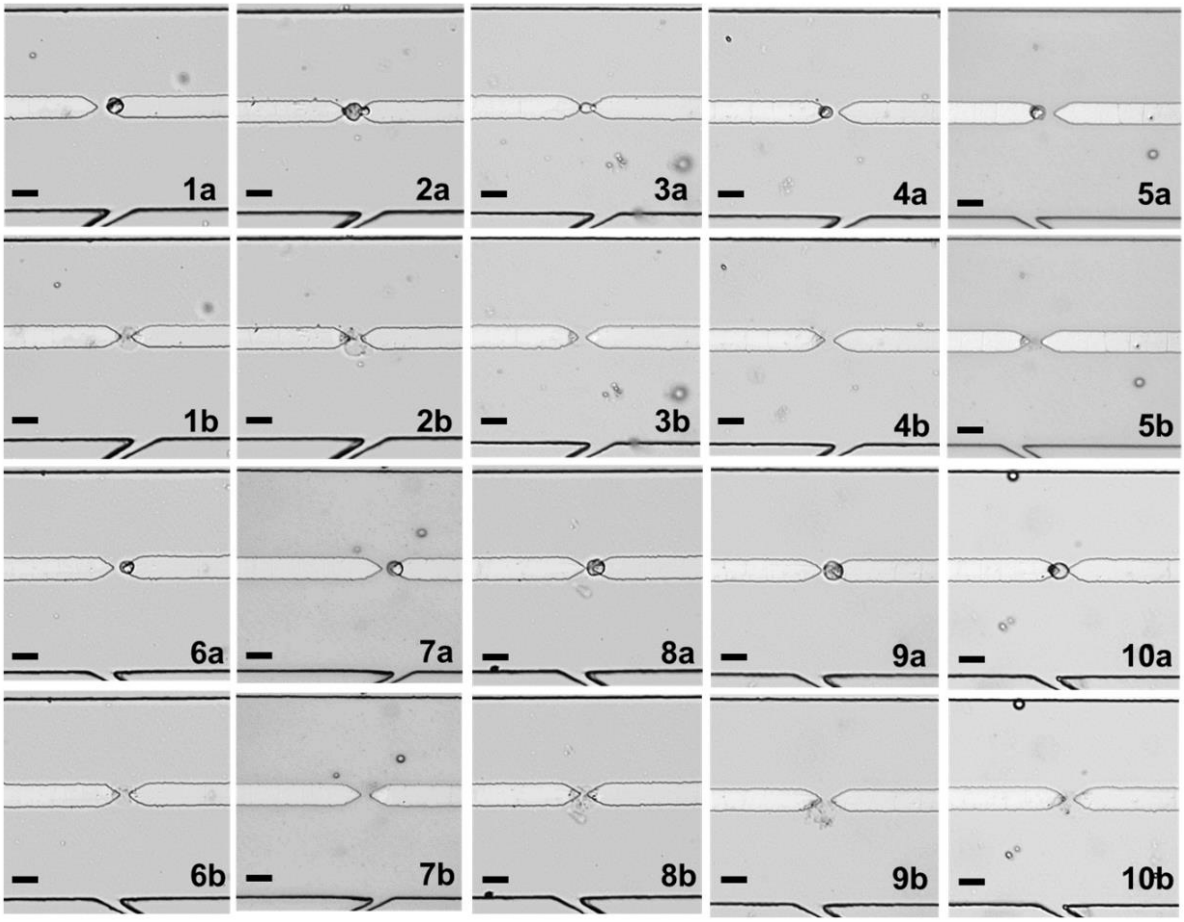

Figure 4.12. Brightfield images of cell lysis when directly increased the applied voltage from 32 V_{pp} (1a-10a) to 166 V_{pp} (1b-10b). 100% of cells were lysed under such electric field strength. Scale bar: 25 µm.

Reducing flow rate to 0.1 µL/min resulted in a stable phase boundary for at least 1 h (**Figure 4.14**), and the formation of the boundary was uniform across the entire chip (**Figure 4.15**). Using this optimized flow condition, the entire work flow was conducted (**Figure 4.16**). It is worth mentioning that fluid exchange needs to occur twice for on-chip analysis: exchange of cell solution with DEP buffer to wash away excess cells after capture and before cell transfer (**Figure 4.16b**); and exchange of DEP buffer with reagents for subsequent cellular analysis (**Figure 4.10)**. The leak channel not only facilitates cell transfer by inducing additional drag force, but also enables rapid fluid exchange in both of these instances.

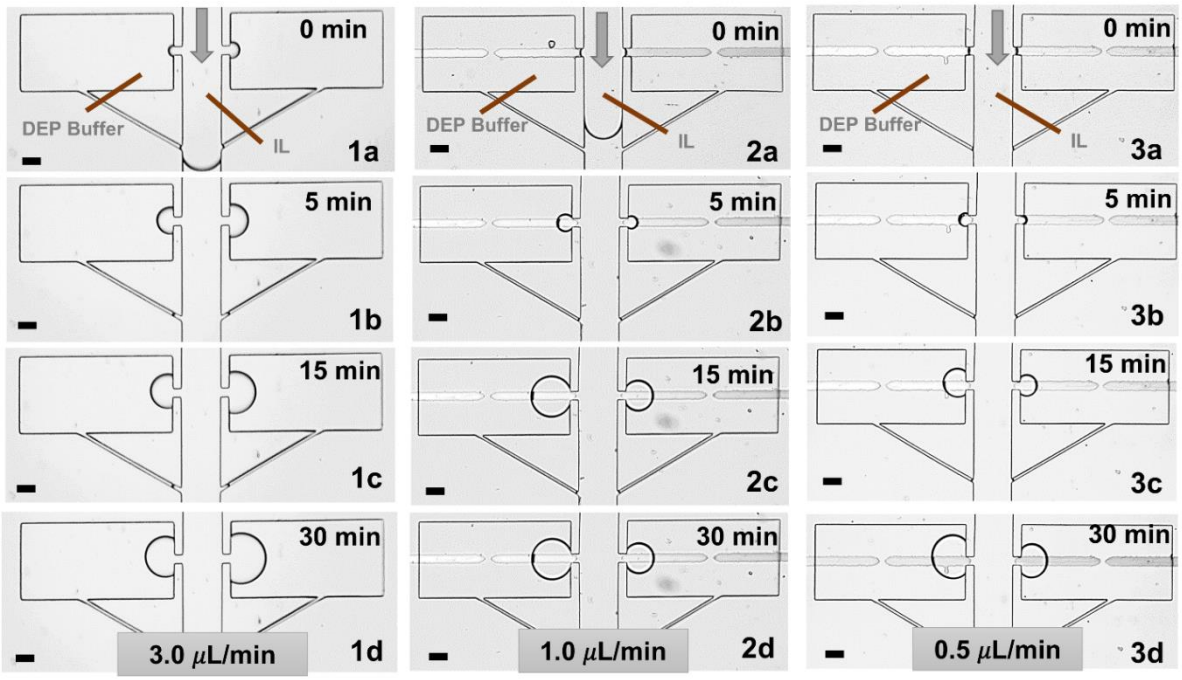

Figure 4.13. Performance of fluid isolation when initial flow rate was 3.0 μL/min (1a-1d), 1.0 μL/min (2a-2d), and 0.5 μL/min (3a-3d), respectively. To obtain such results, 20 μL of DEP buffer solution was first pipetted into the 1.0 mm-diameter reservoir and injected into the microchannels by using negative pressure. The flow was then set to 3.0, 1.0, or 0.5 μL/min and maintained for 30 min, followed by replacement of DEP buffer with 10 μL ionic liquid on the reservoir. When ionic liquid entered the main channel, the syringe pump was shut off to stop the flow. Scale bar: 50 μm. The grey arrows indicate flow direction.

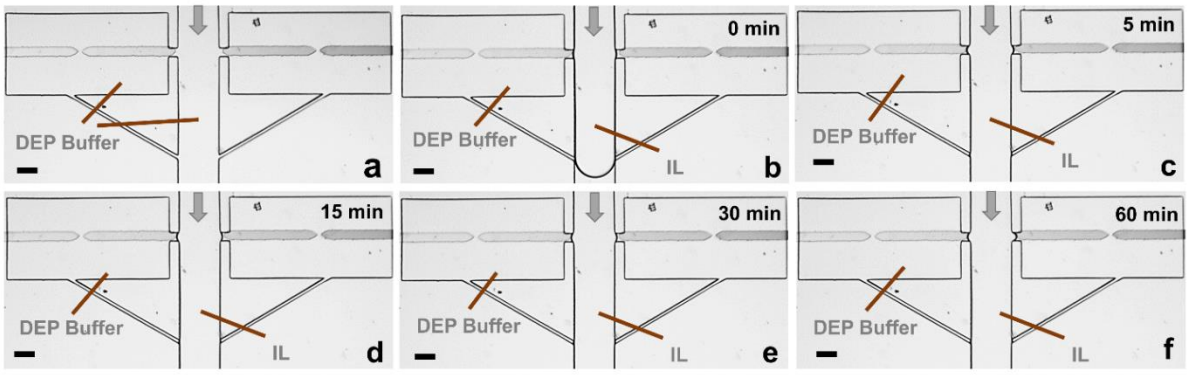

Figure 4.14. Results of fluid isolation at a flow rate of 0.1 μL/min. Scale bar: 50 μm. The grey arrows indicate the flow direction.

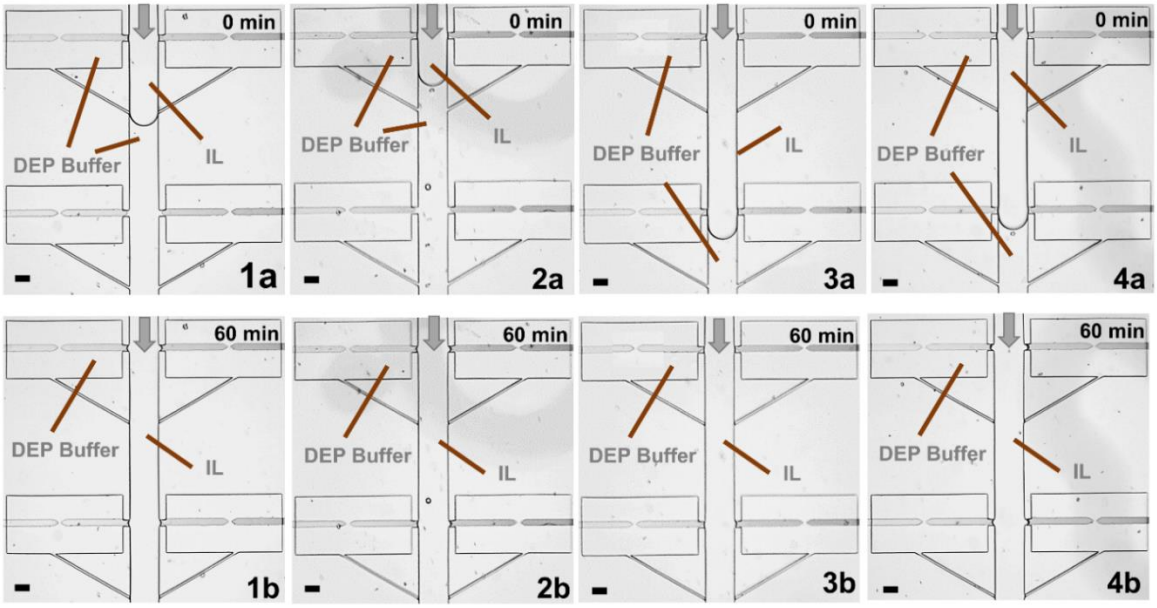

Figure 4.15. Results of fluid isolation at a flow rate of 0.1 µL/min. Chambers were selected randomly to prove the uniform formation of the stable phase boundary throughout the entire chip. Scale bar: 50 µm. The grey arrows indicate the flow direction.

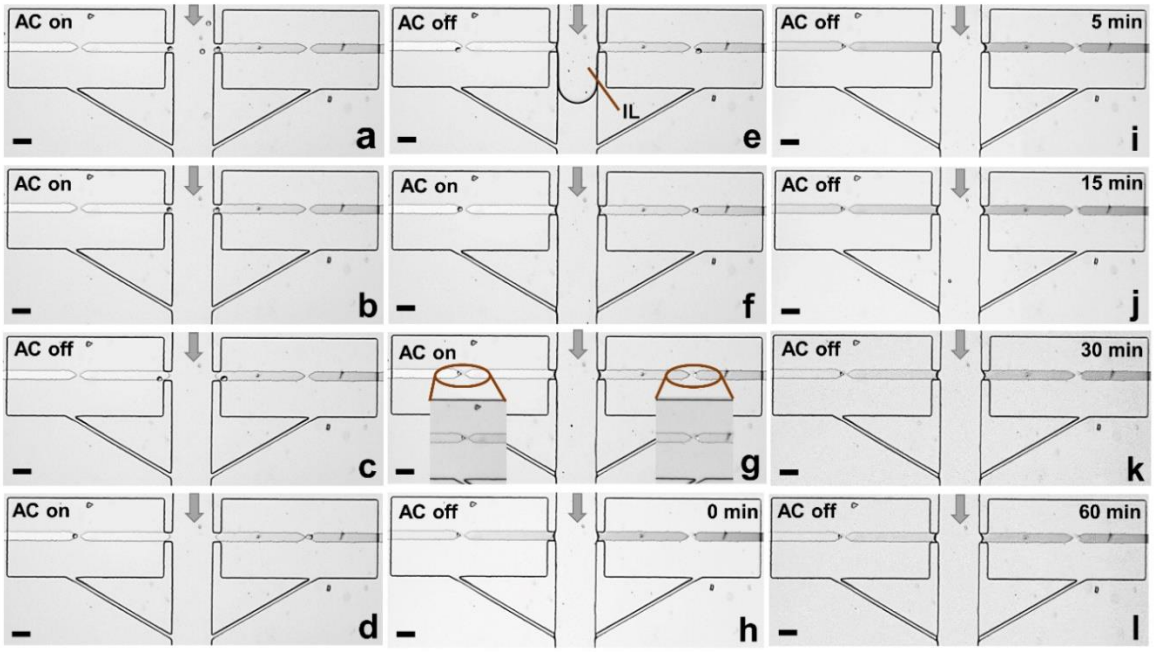

Figure 4.16. Bright-field images of the entire workflow, which includes cell capture (a), fluid exchange (b), cell transfer (c), cell re-capture (d), fluidic isolation (e-f), and electrical lysis (g). After electrical lysis, the flow of IL was maintained for 1 h to further demonstrate the stability of the boundary. The fluid exchange shown in (b) is required to wash away excess cells to ensure no further cells are captured during subsequent cell transfer. For on-chip analysis, fluid exchange after (d) needs to be added to replace buffer solution with reaction reagents. Scale bar: 50 µm. The grey arrows indicate flow direction.

4.5.9 References

1. M. Li, R. K. Anand, *J. Am. Chem. Soc.* **2017**, *139*, 8950-8959.

2. D. Di Carlo, K. H. Jeong, L. P. Lee, *Lab Chip* **2003**, *3*, 287-291.

3. S. Hosic, S. K. Murthy, A. N. Koppes, *Anal. Chem.* **2016**, *88*, 354-380.

CHAPTER 5

GNERAL CONCLUSION

The characterization of CTCs enables elucidation of the processes underlying metastasis, the leading cause of cancer mortality. The information obtained, in turn, will provide insight into the processes of cell signaling, invasion, and drug resistance, and eventually, will translate the molecular catalog into effective therapeutic strategies in the clinic. However, the isolation of CTCs, the first inevitable step of overall analysis, is incredibly difficult due to their extreme rarity and heterogeneity. Further complicating this challenge is the necessity of scoring CTCs individually since unexpected responses from a few individual CTCs may have a dramatic impact on disease progress, yet can be easily obscured at the bulk scale. In fact, due to spatial and temporal tumor variation, a subpopulation of CTCs may harbor a rare mutation that can seed relapse resistant to the primary therapy. Further, to be broadly applicable in research and clinical settings, simplicity in device manufacturing, ease in operation, and in-depth readout of assays are critical.

In this work, to address the needs encountered for understanding CTCs, a microfluidic LOC platform that integrates all steps needed for single-cell analysis (selective single-cell capture, transport, fluidic isolation and lysis) has been developed. Of particular importance, the CTC identification is based on DEP, which relates to the electrophysiological properties of cells, thus providing a much higher degree of selection than size-based approaches, while not being as over-selective as targeting biomarkers such as EpCAM. Core innovations in device design include: *(i) The employment of wireless BPEs in an AC electric field.* Without ohmic contact to the individual array elements, the capacitive charging of the electrical double layer

(EDL) at opposing ends of each BPE allows the AC electric field to be transmitted across the entire device. As a result, electrodes can be configured separately, enabling the device to be scalable along both *x*- and *y*- directions. This wireless BPE array is the key to achieving parallelization and high-throughput sampling. *(ii) The incorporation of cell-scale micropockets and microchambers*. When aligned with BPE tips, pockets extruding from either side of the microchannels render them capable of high-fidelity single-cell capture. Importantly, the pockets protect CTCs from being knocked off by fluid flow, thus allowing a high flow rate to be employed. In parallel, extension of each pocket into reaction chambers allows the storage of reagents for analysis. Notably, the volume of the microchambers can be tuned for a variety of assays by simply adjusting the dimensions. *(iii) The introduction of leak channels and split BPEs*. Once CTCs are captured, the next crucial step is to transfer into confined microstructures. The leak channel design allows valve-free transport of cells into the microchambers, while the split BPEs provide re-capture points for cell retention and electrical lysis. *(iv) The use of ionic liquid as an immiscible phase*. Prevention of cross-talk is essential for on-chip analysis, thus sealing of each individual microchambers by an immiscible phase such as oil is mandatory. In contrast, electrical lysis to release cellular contents must be conducted after fluidic isolation. Within this context, a hydrophobic ionic liquid as both immiscible and electrically conductive phase is chosen to address both needs. Overall, it is worth noting that the whole manipulation process (capture, transfer, retention, and electrical lysis) is valve-free and can be achieved by only adjusting the applied voltage and exchanging the fluid in a single inlet. Further, the elimination of microvalves for sequestration greatly simplifies the engineering complexity, which makes it a relevant approach for broad clinical operation.

The DEP approach presented here addresses the need to develop next-generation devices.[1] First, it enables *marker-free selection of CTCs*, thus avoiding the selection bias that results from targeting size alone or specific biomarkers. Second, the use of DEP maintains high viability for cell capture, while allowing the release of captured cells by simply turning off the AC electric field. The ability to *capture and release CTCs* with minimal cell alteration is crucial for *culture and expansion of CTCs*, which can be performed in the 3D microchambers. Once cell growth and division are established, it is then possible to monitor drug sensitivity and identify CTC subpopulations for the evaluation of their metastatic potential. For example, cultured cells that exhibited significant levels of drug resistance showed more aggressive migration.[2] Likewise, fluorescence readout by Calcein AM is known for the evaluation of cellular multidrug resistance (MDR) machinery.[3] This *in situ phenotypic analysis of CTCs* such as in motility is thought to be critical in cancer cell behavior, thus offering a tool to peer into the process of metastasis. Most importantly, the DEP approach isolates CTCs individually, and integrates the whole manipulation process needed for *molecular analysis of CTCs*. Thus, *the identification of CTC subpopulations* to *visualize their heterogeneity* can be exploited. Given these factors, this new DEP technique is believed to be of high value in both the scientific research and the clinic.

5.1 References

1. Green, B. J.; Saberi Safaei, T.; Mepham, A.; Labib, M.; Mohamadi, R. M.; Kelley, S. O. *Angew. Chem. Int. Ed.* **2016**, *55*, 1252-1265.

2. Zhang, Y.; Zhou, L.; Qin, L. *J. Am. Chem. Soc.* **2014**, *136*, 15257-15262.

3. Aouali, N.; Eddabra, L.; Macadre, J.; Morjani, H. *Crit. Rev. Oncol. Hematol.* **2005**, *56*, 61-70.

CHAPTER 6

FUTURE DIRECTIONS

The DEP approach developed in this document integrates all steps needed prior to single-cell analysis, thus providing a potential platform for molecular analysis of individual CTCs to peer into the machinery of metastasis. While selective capture of CTCs is demonstrated by using the cultured breast CTCs and WBCs, further evaluation using clinic samples must be performed. In particular, quantifications include capture efficiency (the percentage of captured CTCs over spiked CTCs) and purity (the percentage of target CTCs over all cells captured) are required to test the method versatility.

In an effort to obtain the desired quantitative data, device optimization needs to be considered. First, a pre-filtration step either *via* an 'on-chip' or 'off-chip' filter needs to incorporated to remove cell aggregates, thereby preventing unexpected cell clogging during sample processing. Second, it is of high importance to extend the device footprint (e.g., more parallel microchannels, taller channels) to be suitable for processing larger sample volumes (e.g., hundreds of microliters of buffy coat). Finally, considering that the extremely high background of blood cells and platelets may block CTCs from approaching the capture sites, adding a functional unit for negative depletion or pre-focusing (e.g., DLD[1] and acoustophoresis[2]) is necessary. Integration of such a pre-enrichment step will lead to improvement in both capture efficiency and purity.

Beyond quantification, specific assays need to be conducted to bridge the gap between the laboratory and the clinic. Notably, the DEP technique presented in this work allows high cell viability to be maintained during capture and release of CTCs, whereas optionally, trapped CTCs can be electrically lysed. Thus, it is possible to perform assays for live CTCs or for their

cellular contents. Live-cell imaging provides dynamic information of cell behavior, which renders it applicable for *in situ* monitoring of motility in response to the local microenvironment. Such migration data may elucidate the factors that influence the invasiveness of CTCs.

Separately, assays of cellular contents present sources for resolving the static heterogeneity of CTCs. The discrimination of distinct levels of a protein or a gene is of high value in understanding the growth and division of carcinoma cells. Enzymatic assay, such as probing the intracellular β-galactosidase activity, provides insights into cell senescence, in which proliferation of malignant cells does not occur.[3,4] Thus, intracellular β-galactosidase may be used as an indicator for testing the efficiency of chemotherapeutic agents. Likewise, single-cell PCR is powerful in identifying somatic mutations such as KRAS[5] or BRAF.[6] Consequently, customized therapies can be exploited.

While all steps needed for single-cell assays are configured in the current design, further modifications are necessary to suit customized assays. For example, picoliter microchambers are favorable for enzymatic assays,[7,8] while much larger volumes (normally, nanoliter scale[9]) are required for single-cell PCR. Additionally, although the ionic liquid used in the present work to seal microchambers permits a stable boundary for fluidic isolation, the requirement for continuous flow is not desirable, especially in the case when the chip needs to be repositioned into secondary equipment (e.g., an incubator or a thermal cycler). Consequently, strategies such as solidification of the ionic liquid *via* crosslinking or synthesis of an alternative ionic liquid are crucial. Further, the thermal cycling entailed by PCR necessitates the addition of a vapor barrier into the design to prevent solution evaporation. Overall, the proposed research is anticipated to enhance the versatility of the current platform

so that correlations between cell heterogeneity and drug response or metastatic behavior can be well-identified prior to therapy. As a result, the data obtained will enable physicians to develop efficacious treatment plans.

6.1 References

1. Fachin, F.; Spuhler, P.; Martel-Foley, J. M.; Edd, J. F.; Barber, T. A.; Walsh, J.; Karabacak, M.; Pai, V.; Yu, M.; Smith, K.; Hwang, H.; Yang, J.; Shah, S.; Yarmush, R.; Sequist, L. V.; Stott, S. L.; Maheswaran, S.; Haber, D. A.; Kapur, R.; Toner, M. *Sci. Rep.* **2017**, *7*, 10936.

2. Antfolk, M.; Kim, S. H.; Koizumi, S.; Fujii, T.; Laurell, T. *Sci. Rep.* **2017**, *7*, 46507.

3. Dimri, G. P. *Cancer. Cell.* **2005**, *7*, 505-512.

4. Cukusic, A.; Ivankovic, M.; Skrobot, N.; Ferenac, M.; Gotic, I.; Matijasic, M.; Polancec, D.; Rubelj, I. *Cell. Prolif.* **2006**, *39*, 205-216.

5. Fabbri, F.; Carloni, S.; Zoli, W.; Ulivi, P.; Gallerani, G.; Fici, P.; Chiadini, E.; Passardi, A.; Frassineti, G. L.; Ragazzini, A.; Amadori, D. *Cancer. Lett.* **2013**, *335*, 225-231.

6. Long, G. V.; Menzies, A. M.; Nagrial, A. M.; Haydu, L. E.; Hamilton, A. L.; Mann, G. J.; Hughes, T. M.; Thompson, J. F.; Scolyer, R. A.; Kefford, R. F. *J. Clin. Oncol.* **2011**, *29*, 1239-1246.

7. Schmitz, C. H.; Rowat, A. C.; Koster, S.; Weitz, D. A. *Lab Chip.* **2009**, *9*, 44-49.

8. Kim, S. H.; Fujii, T. *Lab Chip.* **2016**, *16*, 2440-2449.

9. White, A. K.; VanInsberghe, M.; Petriv, O. I.; Hamidi, M.; Sikorski, D.; Marra, M. A.; Piret, J.; Aparicio, S.; Hansen, C. L. *Proc. Natl. Acad. Sci. U S A.* **2011**, *108*, 13999-14004.

APPENDIX

RECENT ADVANCEMENTS IN ION CONCENTRATION POLARIZATION

A paper published in Analyst

Min Li, Robbyn K. Anand *

Department of Chemistry, Iowa State University, Ames, Iowa 50011, United States

* Corresponding Author

Abstract

In this minireview, we will discuss advancements in ion concentration polarization (ICP)-based preconcentration, separation, desalination, and dielectrophoresis that have been made over the past three years. ICP as a means of controlling the distribution of the ions and electric field in a microfluidic device has rapidly expanded its areas of application. Recent advancements have focused on the development of ion-permselective materials with tunable dimensions and surface chemistry, adaptation to paper microfluidics, higher-throughput device geometries, and coupling ICP with other separation (isotachophoresis and dielectrophoresis) and fluidic (valve and droplet microfluidic) strategies. These studies have made great strides toward solving real-world problems such as low-cost and rapid analysis, accessible desalination technology, and single-cell research tools.

1. Introduction

Ion concentration polarization (ICP) is an electrokinetic phenomenon brought about by selective charge transport, such as occurs in a nanofluidic channel that links two microfluidic compartments (**Scheme A1a**). This asymmetric process results in the accumulation of charged species in one compartment (ion enrichment) and ion depletion in the other. A similar effect

can be achieved via charge transfer reactions at an electrode, and therefore, a closely related technique called faradaic ICP (FICP), is also discussed in this review (**Schemes A1b and A1c**). ICP has found many areas of application owing to its unique advantage as a means of achieving sharp spatial variation in ion concentration and electric field strength. Examples include counter-flow focusing (CFF) (encompassing both concentration enrichment and separation of charged analytes), desalination, and dielectrophoresis.

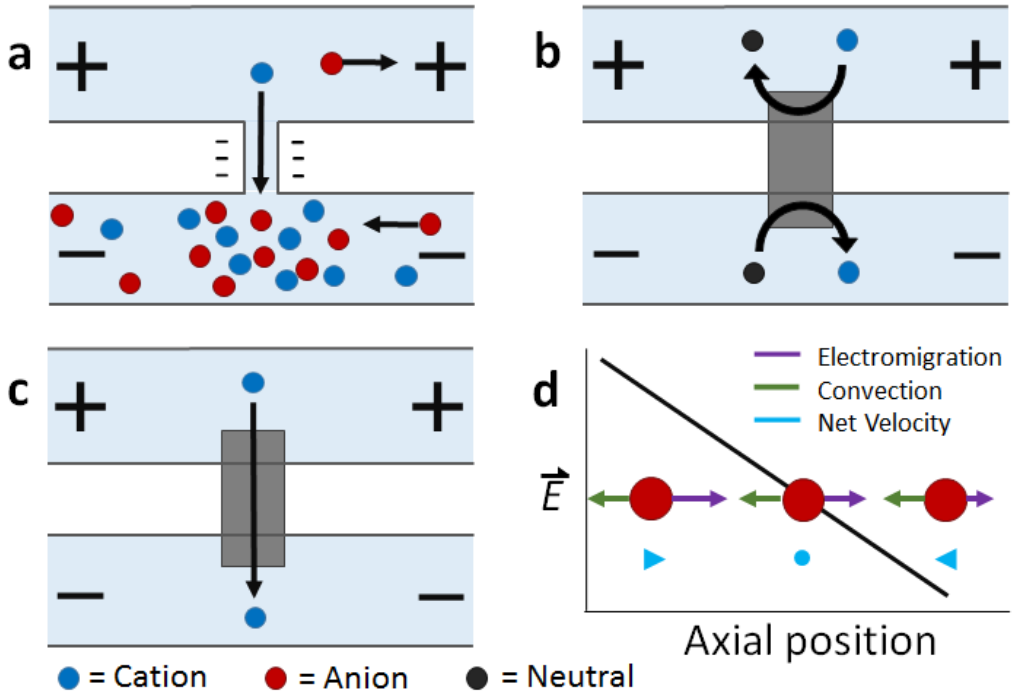

Scheme A1. Illustration of a) ICP, b-c) FICP, and d) ICP CFF mechanisms.

The foundational work preceding these ICP-based techniques described mass transport and electrokinetics in and around ion-permselective materials. Electrochemical measurements aided in quantifying these effects, such as the enrichment of counterions, mass transport, and Donnan exclusion in cation-exchange membranes1 and in individual conical nanopores.2 Highly spatially resolved fluorescence measurements later led to a clear and quantitative

description of ICP, as is exemplified by the work of Leinweber and Tallarek in packed beds of mesoporous beads in a microfluidic channel.3 The development of such hierarchical devices, which comprise both nano- and microscale components, provided a means of controlled analyte transport,4 concentration enrichment,5 and ICP.6-8 Separate reviews provide an account of the theoretical and experimental advances in ICP9 and ICP-based concentrators10 that followed.

The majority of recent advancements in this field have been driven by the needs of existing ICP-based technologies – namely, to increase their breadth of applicability and scale. For example, the cost and difficulty of device fabrication has been reduced through the expansion of ICP-based focusing of charged analytes (such as DNA) to paper microfluidic platforms.[11-13] In another area of application that benefits populations living in resource-limited settings, desalination by ICP presents an alternative to reverse osmosis and requires simpler infrastructure.[14, 15] However, the throughput of an individual desalting device is severely limited by the size of the ion depleted region that can be sustained. Therefore, new fabrication methods aim to augment selective charge transport, thus leading to a larger depletion zone and an enhanced rate of fresh water production.[16] In addition to these advancements, enhanced performance and control have been achieved by combining ICP with other techniques. For example, the recent incorporation of constrictions and valves into microfluidic ICP devices has enabled post-enrichment recovery of focused analyte plugs.[17] Further, the combination of ICP with isotachophoresis has greatly enhanced separation results.[18] Before reviewing recent advancements, we provide a technical background of ICP as a foundation for the discussion that follows it.

2. Technical Background

2.1 Ion Concentration Polarization (ICP)

This discussion will focus on ICP at micro-/nano- fluidic junctions (**Scheme A1a**). An electrical double layer (EDL) forms at the solid-liquid interface between, for example, the wall of a fluidic channel and an electrolyte solution. If the channel wall is negatively charged, the electrical potential at the wall is more negative than that in the bulk solution. Donnan exclusion occurs when two such walls are brought into close proximity causing the potential profiles of the adjacent EDLs to overlap and to exclude anions from the channel formed between them. The characteristic length scale of the EDL (the Debye length) is less than 10 nm for a 1:1 electrolyte at a concentration greater than 1 mM. Therefore, complete Donnan exclusion is limited to nanoscale channels.

If a voltage is applied across such a nanochannel, ICP results (**Scheme A1a**). The key feature of this process is that charge transport is selective – in the example depicted in Scheme 1a, only cations are able to carry charge across the pore. An ion depletion zone (IDZ) develops (upper channel, **Scheme A1a**) as cations are removed *via* the pore, and the migration of anions, away from this end of the pore is enhanced by the locally high electric field strength (due to decreased ionic conductivity). At the other end of the pore (bottom channel, **Scheme A1a**), cations accumulate and anions migrate inward, creating an ion enriched zone (IEZ). A key feature of any ICP device is the current due to selective charge transport, which is directly proportional to the rate of IDZ and IEZ growth. In general, more rapid growth is achieved when more nanochannels are present. ICP devices frequently employ nanoscale features that are too large to cause complete EDL overlap. It is important to note that ICP occurs even at larger length scales, and only partial charge selectivity is required, which is accomplished

whenever a significant proportion of the current through the pore is carried through the EDL. In fact, studies involving a related technique, faradaic ICP (FICP), demonstrated that the two microcompartments do not have to be completely separated. Both ICP and FICP have been shown to occur in a single open microfluidic channel with a nanoporous membrane or electrode located along a portion of the channel floor.[19, 20]

2.2 Faradaic Ion Concentration Polarization

Like ICP, FICP results from selective depletion and enrichment of charged species in a confined environment, such as a microfluidic channel (**Schemes A1b and A1c**).21 In this system, ion depletion is caused by neutralization of a freely diffusing ionic species via a faradaic electrochemical route. Likewise, ion enrichment results from electron transfer leading to an increase in the magnitude of charge of a chemical species. **Scheme A1b** depicts these two processes occurring at either end of a bipolar electrode (BPE), and the net result (**Scheme A1c**) closely mimics ICP. FICP has been employed to accomplish many of the same experimental goals as ICP and has the following distinct advantages: 1) ease of fabrication of electrodes versus nanofeatures, 2) different selection rules and rate for charge removal/injection, 3) possibility for ion depletion to occur in both microfluidic compartments simultaneously. FICP has been discussed in more detail elsewhere.[21, 22]

2.3 Electric Field Profile in the Ion Depletion Zone

Of the two poles of ICP, the ion depletion zone (IDZ) has, by far, produced the most compelling experimental results owing to its intense enhancement of the local electric field strength. In all ICP-based techniques, a component of the electric field is applied axially along the microchannel that contains the depletion zone. The resulting axial electric field peaks

where ion depletion is greatest and forms an extended electric field gradient as it tapers to the edge of the zone. The recent advancements in ICP-based techniques reviewed here all depend on the way by which this electric field gradient is formed, maintained, and applied to scientific problems. In the following sections, we review recent advancement of ICP-based focusing (concentration enrichment and separation), desalination, and dielectrophoresis.

3. Preconcentration of Trace Analytes

3.1 Introduction

The preceding section described how ICP occurs when a voltage bias is applied across a device feature that is capable of facilitating selective charge transport. Counter-flow focusing (CFF) can occur if opposing convective and migrational velocities of a charged analyte are balanced at an axial location along the electric field gradient at the IDZ boundary. In the example depicted in **Scheme A1d**, convection (cathodic EOF or pressure driven flow) is from right to left, and electromigration of an anion (toward the anodic end of the channel) is from left to right. The location of the balance point for a specific analyte is determined by its electrophoretic mobility. As a result, distinct analytes can be separated on the basis of differing charge-to-drag ratios. While focusing of an anionic analyte is depicted, schemes have been devised for the enrichment of cations or both cations and anions simultaneously.[23, 24]

The use of ICP CFF opens up many new possibilities in the preconcentration of analytes. First, the limit of detection of low abundance analytes can be significantly improved after preconcentration while using only a small amount of sample. Enrichment of up to one-million fold has been reported.[25] Second, this electrokinetic approach is broadly applicable to any charged species. Third, this electrically-driven system allows enrichment to be achieved rapidly – within a few minutes or even a few seconds.[26-28] Fourth, ICP CFF is robust, operating

under diverse conditions brought about by nanochannel or membrane materials (e.g., polydimethylsiloxane (PDMS), Nafion, charged hydrogel, and other modified nanopores),[10, 29-31] channel geometry,[32-34] and integration with other lab-on-chip (LOC) components (e.g. sensors[35] and droplet microfluidics[36]). Moreover, ICP CFF compares favorably to competing enrichment methods. For example, ICP does not suffer from clogging and loss of collected molecules as do morphology-based concentrators.[37] Additionally, unlike affinity-based devices, ICP can achieve high sensitivity without the need to functionalize ligands.[38] Current research in this field aims to improve performance, to increase scale, and to develop customized ICP systems for new platforms, analytes, and materials.

The main goal in sample preconcentration using ICP CFF devices is to achieve a high enrichment factor with low voltage and short residence time. Enrichment factor (EF), the ratio between the concentration of analytes before and after ICP CFF, is determined by the combined effect of sequestering and dispersive forces experienced by charged molecules. To maximize sequestering forces and minimize dispersive forces, several parameters need to be considered. For example, a steep electric field gradient yields high contrast in the electrophoretic velocity of an analyte between neighboring locations, hence narrowing a focused band. The slope of the electric field gradient, in turn, is influenced by parameters such as the buffer/electrolyte conditions, applied voltage, electrode configuration and the nanoporous materials employed. Of particular importance is the geometry of the microchannel and nanoscopic features. For example, a converging microchannel design can draw in analyte from a large area and sequester it into a more confined space. Finally, for any of these experimental parameters there is an optimum level past which ICP CFF degenerates. For a defined ICP device, increasing voltage differences between sample channels and buffer channels,[39] and extending residence

time[11, 12] are favorable for reaching high EF. However, Joule heating eventually becomes significant, which broadens the focused band.[13] Hence, extensive effort has gone into optimization of all of these factors to enhance EF.

While high EF is a key figure of merit, devices that meet more specific requirements needed in special circumstances are critical. Point-of-care (POC) applications increasingly demand customized ICP preconcentration systems. For instance, the use of POC devices in resource-limited settings requires low-power consumption, cost-effectiveness and simplified design and operation. Other applications demand simultaneous enrichment and separation of multiple targets, for which the main challenge may be resolution and not EF. Finally, some ICP devices are being designed to recover larger quantities of enriched materials for downstream analysis. For these devices, the geometry is optimized for scale.

3.2 New Approaches to Make Nano-features

The geometry, surface chemistry, and number density of nanofeatures impact the formation of an ion depletion zone. Therefore, this subsection will highlight recent advances in nanofeature fabrication.

In recent years, interest in preconcentrators having nanofeatures fabricated in PDMS has been rapidly expanding.[21, 40, 41] PDMS features convenient bonding and rapid replication, while wet etching and photolithography using silicon and glass are time-consuming.[42-44] However, with a low Young's modulus (360-870 KPa), nanochannels in PDMS substrate are prone to collapse and deformation. Hence, extensive efforts have been made to create nanochannels/nanojunctions with PDMS-based non-soft lithography methods. Examples include the nanoscale-fracturing method of oxidized PDMS,[45] the wrinkling process,[46] mechanical cutting of PDMS by razor blades[47] and the "roof-collapse" method.[48] Although all

of these reports have achieved flexible, simple and low-cost fabrication processes, the nanochannels are limited to two dimensions (2D) which greatly limits the throughput of PDMS-based microfluidic devices.

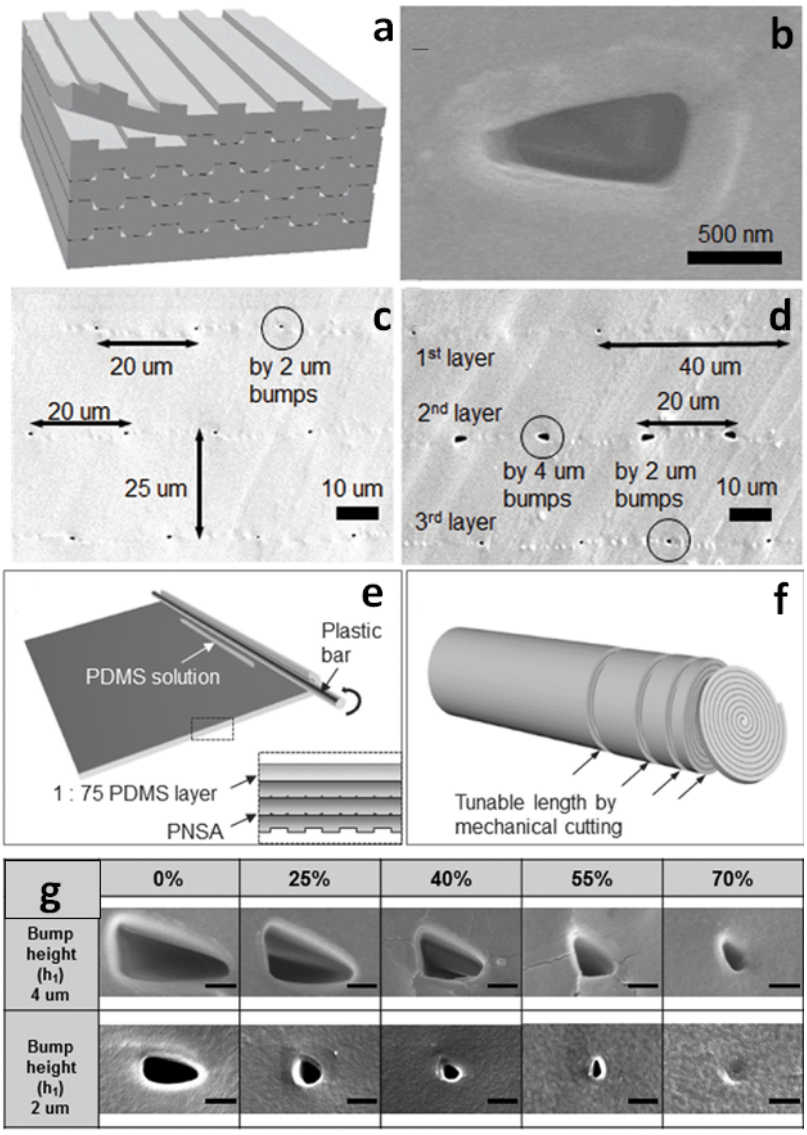

Figure A1. Fabrication and results of the 3D PNSAs. (a) Schematic of the stacking method to form a PNSA; (b) Scanning electron microscopy (SEM) image of nanochannel opening created by layer-to-layer bonding (bump height = 2 μm); (c) SEM image of PNSAs which feature a constant pitch of 20 μm, and a constant layer thickness of 25 μm; (d) SEM image of PNSAs exhibiting variable pitches and sizes at each inner layer; (e) Schematic of the rolling technique using PDMS. The magnified image is a cross-sectional view before rolling; (f) The resulting PNSAs after the rolling process; (g) Investigation of nanochannel size and shape control by various elongation rates (scale bar: 500 nm).

Recently, stacking and rolling methods have enabled the extension of topological configurations of nanochannels to three dimensions (3D).[49] For the stacking scheme, multiple PDMS layers, fabricated using traditional photolithography, were repeatedly treated with oxygen plasma and permanently bonded together to form multilayered stacks (**Figure A1a**). As shown in **Figure A1c -A1d**, the density of the 3D polymeric nanochannel stack arrays (PNSAs) is directly controlled by the master mold – bump arrays patterned onto a silicon wafer. On the other hand, the size and shape of the nanochannel arrays were controlled *via* elongation of the PDMS films (**Figure A1g**). Stretching and releasing the films created irreversible changes in nanochannel dimensions. For instance, the volume of the nanochannels shrinks irreversibly when an applied tensile force is removed. PDMS molded from a bump pattern of 2 μm or 4 μm in height were first stretched to 0%, 25%, 40%, 55% and 70% of their original volume. Depending on the degree of elongation, various shapes such as circular and elliptical nanochannels could be accessed, while the size of nanochannels continuously decreased (**Figure A1g**). Therefore, nanochannel structures with various sizes, shapes and densities could be achieved by the synergy of stacking PNSAs and elongation.

Due to the tediousness of manual stacking cycles, the authors introduced a fabrication method of simply rolling the PNSA film from its edge with a plastic bar to realize large-area integration (**Figure A1e**). The number of layers were governed by the rolling cycles, while sheets of a specified thickness could be created by cutting the PNSA cylinder (**Figure A1f**). A PNSA sheet was then sandwiched in between two PDMS layers containing two orthogonal microchannels for ICP investigation. The authors used current-voltage (*i*-*v*) measurements to demonstrate the three characteristic regions of ICP in the PNSA device. In region I (Ohmic region), the linear relationship between voltage and current indicates the constant conductance

of the nanochannels. In region II (limiting current region), the unchanged current as voltage increases suggests the formation of an IDZ. In region III (overlimiting region), the conductance increases significantly due to the formation of vortices trigged by electro-convection in the depletion zone.[50-52] These results indicate that the ICP phenomena was driven by the perm-selectivity of the PNSAs. The strategy demonstrated using stacking and rolling techniques provides an opportunity to prepare new 3D PDMS-based nanofeatures with high throughput and good control over size and shape. The ease of preparation and straightforwardness of the approach facilitate the design of nanochannels for the preconcentration of charged analytes.

The conditions under which ICP can be initiated are limited by the ratio of surface conductivity to bulk conductivity (Dukhin number, *Du*) in nanofeatures. Small channels with a high surface charge and low ionic strength electrolytes favor increasing *Du*[53, 54] due to greater overlap of the EDL. Therefore, to broaden the applicability of ICP, simple methods are required for fabrication of sub-50 nm nanofeatures with controlled surface functionalization.

Song *et al.* introduced a self-assembly process that employs colloidal silica beads to achieve size control of nanochannels, as well as selectivity *via* surface coating.[55] The strategy is based on the concept that the close-packed structure of colloidal crystals after evaporation has pores with diameters about 15% of the colloidal particle diameter.[56] Further, the authors coated the silica beads to alter their zeta potential and as a result, observed changes in their ability to initiate ICP.[55] Silica beads with diameters of 300 nm, 500 nm, and 900 nm were used to form pore sizes of ~45 nm, 75 nm and 135 nm, respectively. PSS (poly(styrenesulfonic acid)) and PAH (poly(allylamine)) were applied as coatings to study the effect of surface functionalization on charge selectivity. An array of lithographically patterned nanochannels (depth: 700 nm, width: 2 μm) were fabricated on both sides of the sample channel. These

nanochannels served to trap silica beads in the delivery channel while maintaining a connection between sample and auxiliary (buffer) channels (**Figure A2**). This self-assembly process allows for nanoscale-size control completely outside of a sealed microfluidic device. Considering the highly developed coating processes available for silica beads, the preparation of nanochannels sensitive to temperature,[57] pH,[58] and ionic strength[59] can be expected.

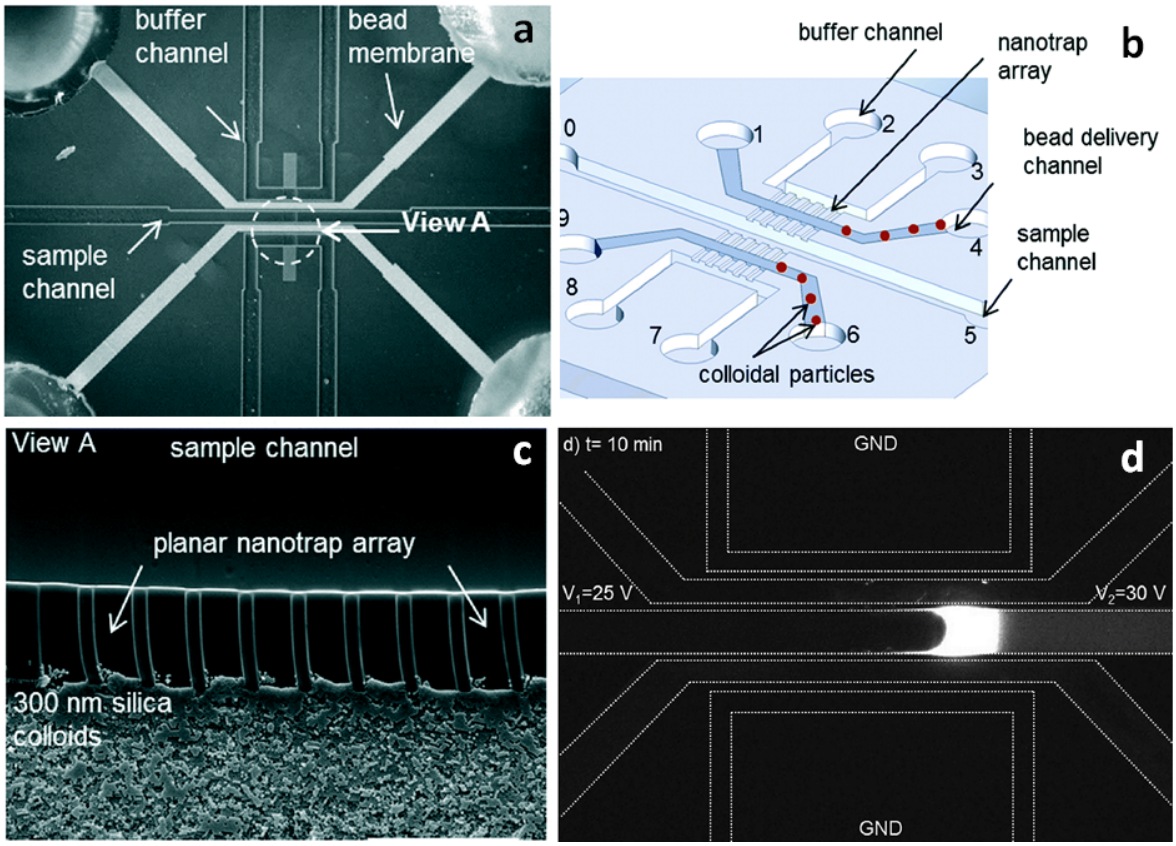

Figure A2. Schematic illustration of the microfluidic device made from self-assembled microbeads. (a) Micrograph of the device showing that the colloidal particles were assembled inside the upper and lower bead delivery channels (scale bar: 200 μm); (b) A schematic of the device design; (c) SEM image of the 300 nm silica particles trapped between the buffer and the sample channel (scale bar: 20 μm); (d) Fluorescence micrograph showing 1700-fold DNA enrichment obtained using 300 nm silica beads.

A 10 nM Cy5-tagged DNA 25-mer in 1 mM phosphate buffer solution was utilized as the target analyte for the ICP analysis. The increased zeta potential obtained through surface functionalization resulted in the initiation of ICP at low voltage (8 V – 10 V) relative to

uncoated beads (30 V). However, the high surface charge of polyelectrolyte-coated beads greatly propagated the ion depletion zone at higher voltage (e.g. 30 V), making the DNA plug unstable. This problem is often inevitable when applying a high voltage in ICP devices. However, it is possible to prevent the propagation of the depletion zone with an increase in the EOF (i.e. by channel surface modification) or by introduction of hydrodynamic flow. Fluid pumping is preferred because, running ICP in highly charged channels at high voltage may cause "bursting" of the ion depletion zone,[8] which occurs when the EOF overcomes the repulsive force of the IDZ.

Another recently developed nanoporous junction for ICP employs single-wall carbon nanotube (SWNT) films.[60] Carbon nanotubes (CNTs) are good candidates for membrane materials considering their high aspect ratio, electronic and mechanical properties.[61] Specifically, the great potential of functionalization *via* various modifications makes CNTs widely used in applications such as electrochemistry, sensing and catalysis.[62-64] With the aid of vacuum filtration and film transfer techniques, 60 nm-thick films of carboxyl-modified SWNTs were prepared and employed for ICP in a dual-channel microfluidic device. The formation of a limiting region in the *i-v* curve proved that ICP resulted from the permselectivity of the film. The 60 nm-thick SWNTs exhibited similar conductance to a 500 nm-thick Nafion membrane. The surface tunability and high conductance of SWNTs reported here suggest that this material has the potential to be a highly efficient ICP membrane.

3.3 Controlling the Location and Stability of the Concentrated Analyte Plug

Not only can flow rate be used to control ICP propagation at high voltage, it also the simplest means of achieving control over the location of the concentrated analyte plug. As a recent example, Choi *et al*. demonstrated enrichment of Alexa Fluor 488 in a Nafion-coated

straight glass channel (inner diameter = 1.1 mm) under two sets of conditions. The architecture of Nafion[65] allows the initiation of ICP *via* the overlap of EDLs. They first applied 30 µL/min flow toward the cathode with a DC voltage of 300 V, resulting in a mean fluorescence intensity of 93.[66] When flow rate was set to 40 µL/min at 400 V, the intensity increased to 243. A higher voltage shifted the concentrated plug away from the Nafion membrane, thus a higher flow rate was needed to overcome the enhanced electromigration and IDZ growth to fix the position of the concentrated plug.

Once enrichment is achieved, it is advantageous to encapsulate and store the analyte for downstream analysis. To this end, Phan *et al*. demonstrated analyte sequestration using a continuous-flow droplet ICP microfluidic device. Their results underscore the balance of applied voltage and flow rate. The authors showed that the distance between the ICP boundary and the edge of the Nafion membrane varied linearly with the applied voltage.[67] However, by increasing flow rate proportionally with voltage, the enriched band could be maintained at the droplet generator. Using this method, a maximum of 100-fold EF was obtained. The flow rate also controlled the size of the droplets formed. For instance, when the flow rate increased from 10 µL/h (30 V) to 30 µL/h (90 V), the droplet size changed from ~240 mm to ~370 mm. These results are significant because, this technique could be interfaced with a suite of microfluidic tools for droplet manipulation.

Kwak. *et al*. introduced a merged ion enrichment-depletion zone method to spatiotemporally define the preconcentrated plug in a way that is independent of ICP operating conditions.[68] The key feature of this technique is two Nafion membranes positioned 100 µm apart on the bottom of a straight microchannel. When a voltage was applied, the anions that enriched at the boundary of the IDZ formed by the right-hand Nafion membrane were

stabilized by the cations in the IEZ formed by the left-hand Nafion membrane, thus preventing expansion of the ICP boundary. A concentrated plug of a negatively charged fluorescent dye could be tuned to a specific region (100 μm × 50 μm × 10 μm) under a broad spectrum of testing conditions (voltage: 0.5 V to 100 V; ionic strength: 1 mM to 100 mM KCl; pH: 3.7 to 10.3; residence time: 0 s to 1200 s). This method addresses one of the greatest challenges encountered in ICP CFF and may render it more applicable to preconcentration in other microfluidic platforms.

Recently, another ICP concentrator driven by capillary force was introduced to eliminate the undesirable instability of the concentrated plug.69 Instead of applying a voltage to drive ions into a permselective membrane, a negatively charged hydrogel was patterned70 and employed for continuous imbibition of cations by capillary force, thus initiating the formation of an IDZ. Once the IDZ formed, anions migrated away by electrostatic repulsion and enriched at a fixed position when a counter flow (e.g., pressure-driven flow) was applied. The propagation of the IDZ was found to be dependent on the electrolyte concentration – low buffer concentration resulted in a thick EDL, which in turn led to a high propagation velocity. Compared to electrically driven ICP, the EF was relatively low (100-fold in 60 s) due to the limited absorbing capability of the hydrogel and a lack of global electromigration. However, this ICP device is significant because it operates in the absence of an electrical power source, thereby expanding the potential utilization of ICP in POC applications. In addition, the simultaneous enrichment of cations and anions by patterning functionalized charged hydrogels[71, 72] in parallel along a microchannel can be expected.

3.4 Nafion-Impregnated Paper-Based Microfluidic Devices

Several characteristics of paper-based microfluidic devices have motivated their recent surge in development: (i) They are low-cost, amenable to mass production, and easy to transport. A simple microfluidic paper-based analytical device (μPAD) is about $0.01 for the cost of the paper and patterning;[73] (ii) Typical μPAD materials, cellulose or cellulose-polymer blends, are compatible with various chemical/biochemical/medical applications;[74] (iii) The devices can be disposed of by incineration safely after use.[75] Therefore, since the pioneering study in 2007,[76] μPADs have become a versatile and scalable platform for a broad spectrum of diagnostic applications.[77-79] However, concentration enrichment in μPADs has been a challenge. The prevailing paper-wetting concentrators rely on capillary forces generated in dry portions of the paper matrix. Examples include sliding paper strips through a stationary reagent loading unit for performing enzyme-linked immunosorbent assays (ELISA),[80] adding soluble sugar to create programmable flow delays,[81] and actuating paper cantilevers to connect channels.[82] Once a paper-based assay is fully wet, these approaches based on capillary forces cannot be utilized for the concentration and transport of analytes.

The use of nanoporous membranes and ICP in μPADs opens up the avenue to develop paper-based concentrators which are independent of capillary forces. Of various nanoporous membrane materials, Nafion is most commonly used since it creates a hydrophobic barrier in paper devices while allowing selective cation transport through the hydrophilic nanopores.

Gong. *et al* have demonstrated the feasibility of concentration and transport of molecules using a Nafion membrane for ICP in a fully-wetted paper-based assay.[11] Two classes of devices were developed – an external stamp-like silicone platform comprising the driving electrodes, reservoirs, and Nafion membranes separate from the paper, and an in-paper device

patterned directly with Nafion (**Figure A3**). For the external device, two ICP regions exist, one at each of the Nafion membranes in contact with the two ends of the paper fluidic channel. Depending on the polarity of the applied voltage, an enrichment zone forms at one end of the paper and depletion at the other. An enriched analyte band formed at the boundary of the depletion zone. This configuration is not unlike that introduced by Kwak *et al*. (*vide supra*). The silicone layer containing the embedded Nafion nanoporous membranes served to prevent direct mixing of samples with buffer solutions contained in the external reservoirs. For the in-paper devices, however, the nanoporous membranes were directly patterned into the paper, which served both to separate two wetted regions and to enable ICP-based enrichment. The enrichment of fluorescein achieved with the external-device became visible at 50 s, and reached saturation at 155 s with 40-fold enrichment; while the fluorescence intensity for the in-paper device became significant at 90 s, and the maximum value was 22-fold at 510 s. The transport efficiency (percent of analyte enriched) upon reversing the polarity was investigated for two cycles in both external and in-paper devices. In both devices, the transport efficiency dropped significantly with repeated cycles. The utilization of a glass coverslip resulted in a consistent transport efficiency of ~90%, which indicated that the reduction of transport efficiency could be ascribed to evaporation.

Using the in-paper device, the authors achieved a limit of detection (LOD) for FITC-albumin of 2 pmol/mL (vs. 10 pmol/mL before concentration) and for bromocresol green dye ~10 μM (vs. 40 μM). This improvement is significant because it extends the capabilities of low-cost paper-based assays and broadens the application of ICP beyond traditional device materials.

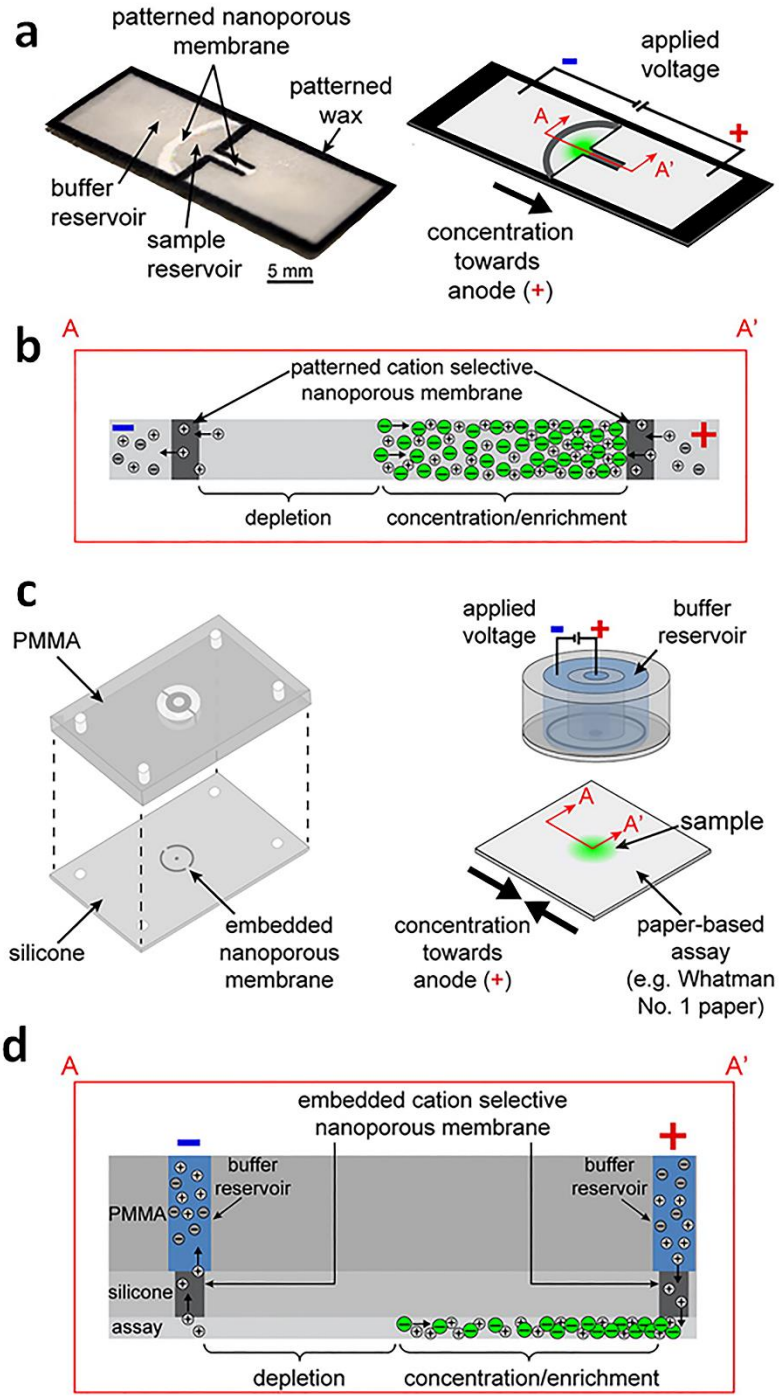

Figure A3. Design and operation of the external and in-paper devices for concentration. (a) Schematic of the in-paper transport configuration. (b) Cross-section of the in-paper devices illustrating ICP under an applied voltage. (c) Schematic of the external concentration device. (d) Cross-section of the devices and paper-based assays depicting ICP under an applied voltage. (Image reproduced from ref. [11] with permission. Copyright 2016, American Chemical Society.)

To decipher the influence of channel geometry on concentration performance, a separate study of fully-wet paper-based devices investigated convergent channels with different length and width.[12] Note that the use of convergent channels could favor the aggregation of analytes (confinement effect), while narrow channels decrease the current and the net movement of ions which is not favorable for sample enrichment (current effect). The analysis of fluorescence intensity in different convergent channels demonstrated that a trade-off existed between the two counter-effects (confinement and current), and a convergent channel with a width of 1 mm (narrowed from 2 mm) yielded the best performance in this paper-based microfluidic device.

The ICP effect of the convergent channels on paper-based devices was also investigated by measuring the *i*-*v* curve. Similar to traditional PDMS/glass devices, three characteristic regions on this paper-based microfluidic device were observed. However, for the present paper-based devices, the overlimiting current increased only slightly with the voltage. This behavior can be attributed to the intricate structure of cellulose, which tends to decrease the electro-convective effect through hydrodynamic resistance.

It is also noteworthy that the use of one straight channel in a paper-based device greatly simplifies the fabrication process compared to the traditional two-channel ICP concentrators. Phan *et al.* further simplified the fabrication process by placing a thin Nafion membrane underneath the paper strip.[83] Using such a device, an EF of 60-fold at 200 s was obtained, which was slightly higher than those obtained using manually patterned Nafion membranes (40-fold at 155 s for ref. [11], 20-fold at 130s for ref. [12]. The enhanced enrichment performance in the external Nafion device may be attributed to more uniform EOF throughout the device.

4. Simultaneous Preconcentration and Separation of Analytes

4.1 Introduction

Separation of sample components is often the starting point of chemical or biochemical analysis. Separation conducted by ICP CFF not only allows continuous separation and simultaneous enrichment, but also creates the potential for LOC integration, rendering the isolation of targets from bulk solutions rapid and convenient. Separation resolution (SR), which is defined as the ratio of peak-to-peak distance between two adjacent bands to their average width, is commonly used to evaluate performance. Separation in an electric field is based on the differences among analytes in electrophoretic mobility (μ), which is equal to the charge of a molecule (Q) over friction (ζ). A limitation of electric field based separations is therefore cases for which μ is indistinguishable for two analytes. For example, the separation of DNA is often problematic since Q and ζ are both proportional to the number of monomers in the DNA chain (M) (ie. $\mu = Q/\zeta \propto M/M$).[84] ICP CFF separation also has been limited by the difficulty of accessing enriched bands (e.g. *via* extraction or isolation). Recent advancements that are discussed in this subsection address these two limitations by integrating mobility shift strategies and a valve system with ICP CFF separation.

4.2 Paper as a Sieving Matrix in ICP Devices

Due to the indistinguishable μ of distinct DNA strands, a sieving matrix such as agarose gel is typically employed to force DNA to collide with fixed structures to a degree dependent upon strand length.[85, 86] The adaptation of ICP CFF to paper-based devices has raised the possibility that paper could serve as a suitable sieving matrix for DNA separation. It is reported that nitrocellulose papers with 0.2 μm, and 0.45 μm pore diameter correlate to 2%

and 1% agarose gels, respectively.[87] Thus, the paper-based ICP design promises to be a viable approach for the continuous separation and concentration of DNA.

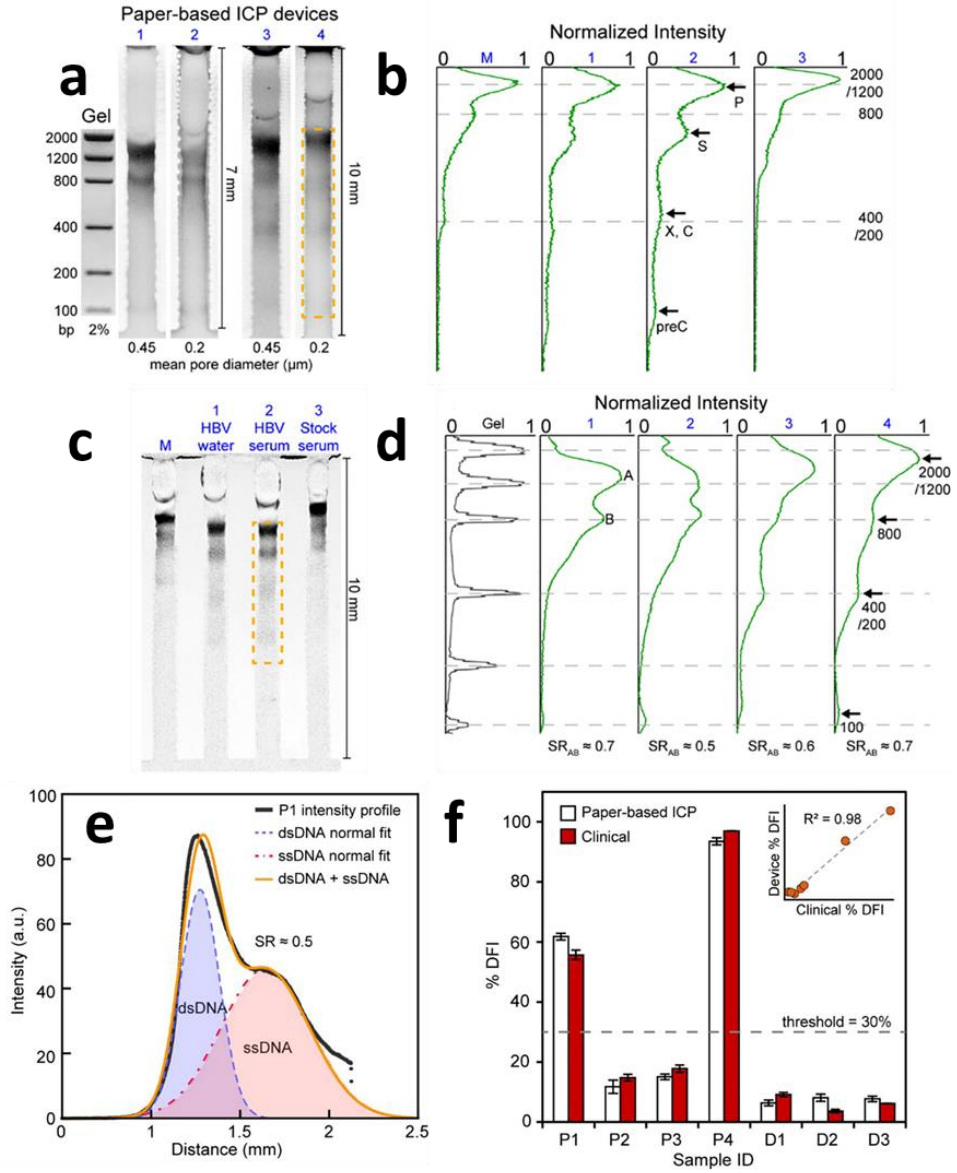

Figure A4. Results of direct DNA analysis using the paper-based ICP device. (a) Separation of a DNA standard containing six dsDNA fragments in gel and in four paper devices with varied length and pore size; (b) Comparison of the band intensities obtained by the gel and the paper-based ICP devices in (a); (c) and (d) Results obtained using the multichannel method for the analysis of (M) DNA standard, HBV fragments in (1) water and (2) serum, and (3) a stock serum sample ; (e) Intensity profile of the separation of ssDNA and dsDNA from a patient sperm sample; (f) %DFI testing results for patients and donors. 30% is used as the threshold to evaluate clinical outcome. (Image reproduced from ref. [13] with permission. Copyright 2016, American Chemical Society.)

Recently, a paper-based ICP device using Nafion was prepared and used for the direct analysis of Hepatitis B and the assessment of human sperm DNA integrity (**Figure A4**).[13] Fluorescein isothiocyanate (FITC) and calcein were utilized as anionic fluorescent tracers for a model investigation of the performance of preconcentration and separation.

A multichannel device (shown in **Figure A4c**) using the paper-based ICP design was then employed to simultaneously preconcentrate, separate and detect HBV DNA fragments (precore, core, surface, X, and polymerase). Though the device failed to distinctly identify the X and the core regions of the HBV genome, the capability to detect surface and precore regions allowed it to be used for HBV detection. Significantly, for hepatitis B testing, the low LOD (150 copies/mL) achieved without prior PCR amplification was comparable to that of commercial PCR systems (50-100 copies/mL). For the assessment of human sperm DNA integrity, the percent DNA fragmentation index (%DFI) obtained with the device strongly correlated to those detected by a flow cytometry-based sperm chromatin structure assay (SCSA) measurement (R^2 = 0.98). These results indicate that this paper-based device may provide a platform for scalable fertility testing.

Despite the capability of simultaneous preconcentration, separation and detection of DNA targets in a single operation, the low SR values achieved (0.5 - 0.7) indicate that there is still a need for data that aid in understanding the key factors impacting separation using paper-based ICP devices. One possible reason for the low SR values might be an additional dispersive mechanism (e.g. non-specific adsorption or inconsistent pore size) encountered in paper fibers. The shallow reservoirs, as defined by the paper thickness, may also hinder the supply of sample solutions from which to draw, thereby decreasing the enrichment of ions.

4.3 End-labeled Free-Solution Electrophoresis (ELFSE) Principle

To address the "free-draining" property of DNA, end-labeled free-solution electrophoresis (ELFSE), which breaks the charge-to-drag balance by labeling DNA with a large neutral molecule ("drag-tag"), is another way to achieve separation.[88] Unlike size-based separation, no sieving matrix is needed, and fast separation can be expected. Song *et al*. demonstrated the versatility of the ELFSE approach for the separation of DNA *via* ICP CFF in a Nafion-based PDMS/glass microfluidic device.[39] Two different classes of DNA (free biotinylated DNA (25 nM) and 3' streptavidin labeled DNA (5 nM)) were separated at 60 V. At 120 s, the simultaneous preconcentration and separation of the two bands became clear as the free DNA exhibited higher electrophoretic mobility than the bound DNA. A maximum enrichment of 900-fold and 500-fold was reached at 240 s for the bound, and the free DNA, respectively. Increasing the voltage difference to 80 V resulted in 1150-fold enrichment for the bound DNA and a SR of 1.85. Together with the benefits accomplished by ELFSE, the Nafion-based ICP device demonstrated fast and effective separation and preconcentration of DNA. Note that while nitrocellulose paper acted as a sieving matrix for separation, the SR value (~0.5) was much lower than that achieved by ELFSE. The introduction of the ELFSE principle in an ICP paper-based device can be anticipated to produce a fast, efficient and cost-effective separation approach.

4.4 Combination of ELFSE and FICP

FICP driven by a bipolar electrode (BPE) embedded in a microfluidic system provides another way to enrich charged analytes *via* the balance of electromigration velocity against counter flow. It has been reported for such a system that the enrichment factor for a fluorescent anionic tracer reached 1.42×10^5-fold in about 33 min (71-fold/s).[21] The ease of the fabrication

process, also makes BPEs a convenient tool for the preconcentration of analytes. In this context, Song. *et al.* have set forth the idea of integrating a BPE-based device with ELFSE for the simultaneous preconcentration and separation of DNA.[89] Compared to the aforementioned study, which employed a Nafion-based device for ELFSE, a lower enrichment factor (600-fold and 500-fold) was obtained with longer time (300 s) when the same voltage (60 V) was applied, while the SR value was similar (1.49) since the same DNA and drag-tag were utilized.

There are several possible ways to improve enrichment performance in BPE-based microfluidic devices. First, considering that a steeper electric field is favorable for enhancing enrichment process, an increase in buffer concentration can improve the EF.[90] Second, a major limitation of BPE-based device is faradaic degradation of the BPE material or electrolysis of the solution to produce gas bubbles. These problems can be alleviated by applying a non-zero voltage in the buffer (auxiliary) channel, which enables one to maintain a low voltage drop across the BPE, while increasing the voltage drop across the focusing channel. Third, increasing the surface area-to-volume ratio of the BPE, for example by the utilization of a microchannel plate (MCP), takes the BPE concentration capacity to the next level: up to 175-fold/s was obtained for an MCP exceeding rates reported for planar BPEs.[91] The authors claimed that each microcapillary tube in the MCP acted as a tiny BPE, resulting in a larger IDZ. It is worth noting that because of the reduction and oxidation reactions occurring individually at the cathodic and anodic poles (respectively), a single BPE can approximate both selective cation and anion transport thus enabling the simultaneous preconcentration and separation of cationic and anionic analytes.[24] These results, alongside those obtained through the systematic study of BPEs, such as was conducted by the Crooks group,[19, 21, 24, 40, 41, 92, 93

indicate that this “faradaic ICP” may provide an opportunity to prepare new ICP concentrators with properties not attainable by current ion-selective membranes.

4.5 ICP with Isotachophoresis to Enhance SR

In parallel with the advancement of ICP devices for DNA separation, the development of single-cell analytical approaches has been rapidly expanding due to their ability to provide an accurate picture of the heterogeneity within a population of cells. This information is of particular significance in systems for which a minority of cells has a disproportionate influence on clinical outcomes such as in drug response and disease diagnosis. Kinases, enzymes that catalyze phosphorylation, are of importance in many cell signaling pathways and are an example of a key indicator of cell behavior. Kinase activity provides information about the kinetics and state of the signal transduction network. Recently, Cheow *et al*. have developed an ICP-enhanced mobility shift assay for real-time detection of kinase activities in single-cell lysate.[18]

Their strategy leveraged the differing electrophoretic mobilities of a fluorescent substrate before and after phosphorylation. When only one kinase and its substrate were added, the reaction kinetics could be obtained by monitoring the ratio of the fluorescence intensities in enriched bands of the substrate and product with time. However, when more than one kinase was present, the small differences in electrophoretic mobility between multiple substrate/product pairs made it challenging to differentiate the bands. Moreover, there remained a need for data that could aid in evaluating the network relationship among various kinases. To improve the separation resolution, isotachophoresis (ITP)[94-96] was combined with ICP CFF, using custom synthetic peptides as spacers between each substrate. The highly concentrated spacers altered the electric field, from a smoothly sloping gradient to a stair-like

profile. Therefore, each substrate was focused on a more highly spatially confined portion of the gradient flanked by spacers bookending the substrate's mobility. With this approach, the activities of three kinases (PKA, AKt, and MK2) in a single cell were investigated.

This work provides a potential platform for *in situ* monitoring of kinase activities at a single-cell level. Multiple kinases were simultaneously detected using ICP CFF, and the separation resolution was greatly improved with the aid of ITP. Finally, this method was shown to be robust, allowing the addition of various inhibitors (off-target kinase, protease, and phosphatase) so that substrate specificity could be significantly enhanced. The authors expanded the use of ICP CFF and created a powerful tool for cell diagnosis and drug development. It has been separately reported that up to 128 samples can be analyzed in parallel in an ICP-based microfluidic chip.[97] Therefore, the integration of high-throughput single-cell analysis tools with ICP CFF is anticipated.

4.6 Continuous Preconcentration, Separation and Collection

Despite the demonstrated capabilities of ICP concentrators, the critical issue of how to achieve extraction of the concentrated plug for post-processing remains to be solved. Techniques that employ separately a two-phase droplet generator[36] and pre-binding on-site reaction[98] were reported to address this critical need. However, they each suffer from the need for additional recovery processes or cleaning steps that limit their utility for automation and commercialization. Moreover, for the extraction systems integrated in microfluidic devices, the following features are desired: (i) The concentrated plug needs to be well stabilized so that the subsequent extraction becomes possible; (ii) The undesirable dispersion of analytes should be eliminated as much as possible; (iii) Multiple targets can be selectively preconcentrated and

separated simultaneously; (iv) All targets of analytes can be collected; (v) All the processes can be continuously conducted.

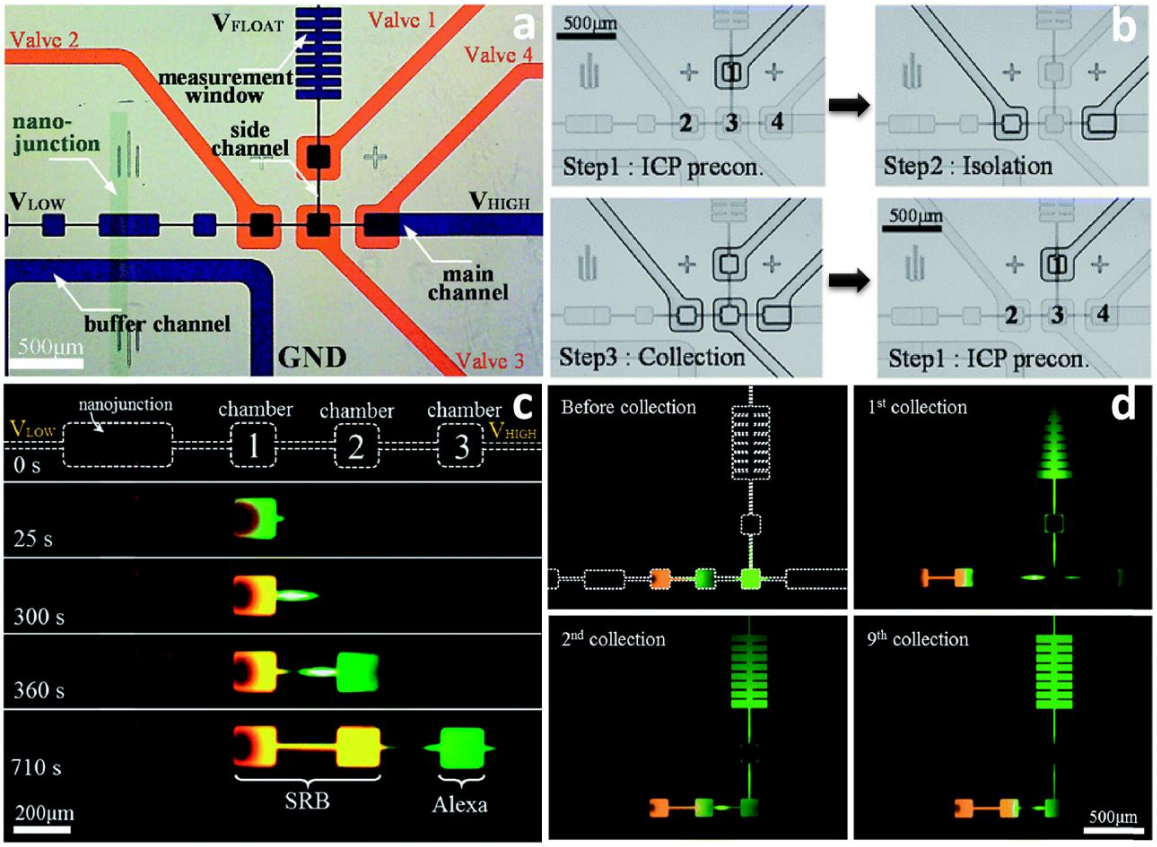

Figure A5. Schematic illustration of the mTAS using ICP and microvalves. (a) Microscopic view of the device (the microchannels in the ICP layer were indicated with blue and the microchannels in the valve layer were indicated red); (b) Depiction of the three-step microvalve control; (c) Time-lapse images of the simultaneous preconcentration and separation of SRB and Alexa; (d) Snapshots of the repeated valve operations for collecting Alexa dye.

Recently, a pioneering study of a micro Total Analysis System (mTAS) using ICP has been reported (**Figure A5**).[17] First, the implementation of microchambers restricted the expansion of vortices and strong electrokinetic flow formed in the depletion zone, thus enabling the stabilization of sample plugs and increasing the enrichment of analytes.[99, 100] Second, the connection of microvalves to microchambers rendered it applicable for the

collection of target analytes. Using this system, complete separation of two dyes (sulforhodamine B (SRB): z = -1; Alexa Fluro 488 (Alexa): z = -2) was achieved, with an SR of 1.75. Four microvalves were fabricated to collect the two dyes in individual microchambers. The authors indicate that depending on how the electric field is tuned, different dyes can be collected from the same microchamber. This study also demonstrated that continuous preconcentration, separation and collection can be achieved by sequential valve actuation. As shown in **Figure A5c**, valve 1 was closed when running the enrichment step, while the concentrated plug was isolated in the microchamber 3 when microvalve 2 and microvalve 4 were shut. Subsequently, all the four valves were closed to squeeze the isolated plug into the rib-shape measurement window. After this valve sequence was repeated 9 times, the measurement window was filled with green Alexa dye at an EF of 100-fold.

This on-line collection strategy using microchambers and microvalves has demonstrated the versatility of ICP for the selective preconcentration, separation and collection of analytes. The robustness, diversity of charged materials available, and straightforwardness of the approach will facilitate the design of new ICP-based mTAS devices for a wide range of applications.

5. Membrane-Free Seawater Desalination

Han and coworkers first recognized that the repulsion of all charged species from the IDZ could be exploited to accomplish desalination.[14] Instead of focusing charged species along the IDZ boundary, these species are continuously diverted into a side channel (termed the brine stream) for removal. Using a Nafion membrane in a PDMS/glass device, the authors demonstrated approximately 99% rejection of salts with a 50:50 fluidic split and an inlet stream

salinity approximating that of seawater (500 mM ionic strength, 45 mS cm^{-1}). The freshwater output was 10 µL/min.

More recently, Knust *et al.* demonstrated desalination by FICP at a carbon bipolar electrode (BPE) in a PDMS/glass device.[15] The IDZ formed at the BPE anode *via* the oxidation of chloride ion to chlorine. This scheme resulted in 25% rejection of salts at an exceptionally high energy efficiency of 25 mWh L^{-1}. The fresh water output was 0.04 µL/min.

The obvious drawback of these microfluidic approaches is the miniscule freshwater output of an individual desalting junction. To produce sufficient drinking water for a household, thousands of parallel microfluidic devices would be required. MacDonald *et al*. recognized that the issue of throughput could be solved by increasing the size of the IDZ, thus allowing microchannels with larger cross-sectional area.[16] The authors accomplished this goal by extruding the device design, increasing the interfacial area between the microchannel and a Nafion membrane. A cross-sectional view of the device is shown in **Figure A6**. A device with a 200 µm x 2.0 mm inlet channel is capable of a freshwater production rate of 0.5 µL/min at 13.8 Wh L^{-1} for an input salinity of 200 mM (ionic strength). Under separate conditions, the authors reported salt rejection as high as 95% and freshwater output at up to 20 µL/min for a single device.

The full potential of these desalting devices can be realized by minimizing power consumption. For example, the driving voltage is reduced when applied as close to the desalting junction as possible. Furthermore, the current across the nanofeature or BPE is linked to the degree of charge depletion and the size of the IDZ, therefore, mpacting both salt rejection and throughput. A power-optimized device will have perfectly selective charge transport.

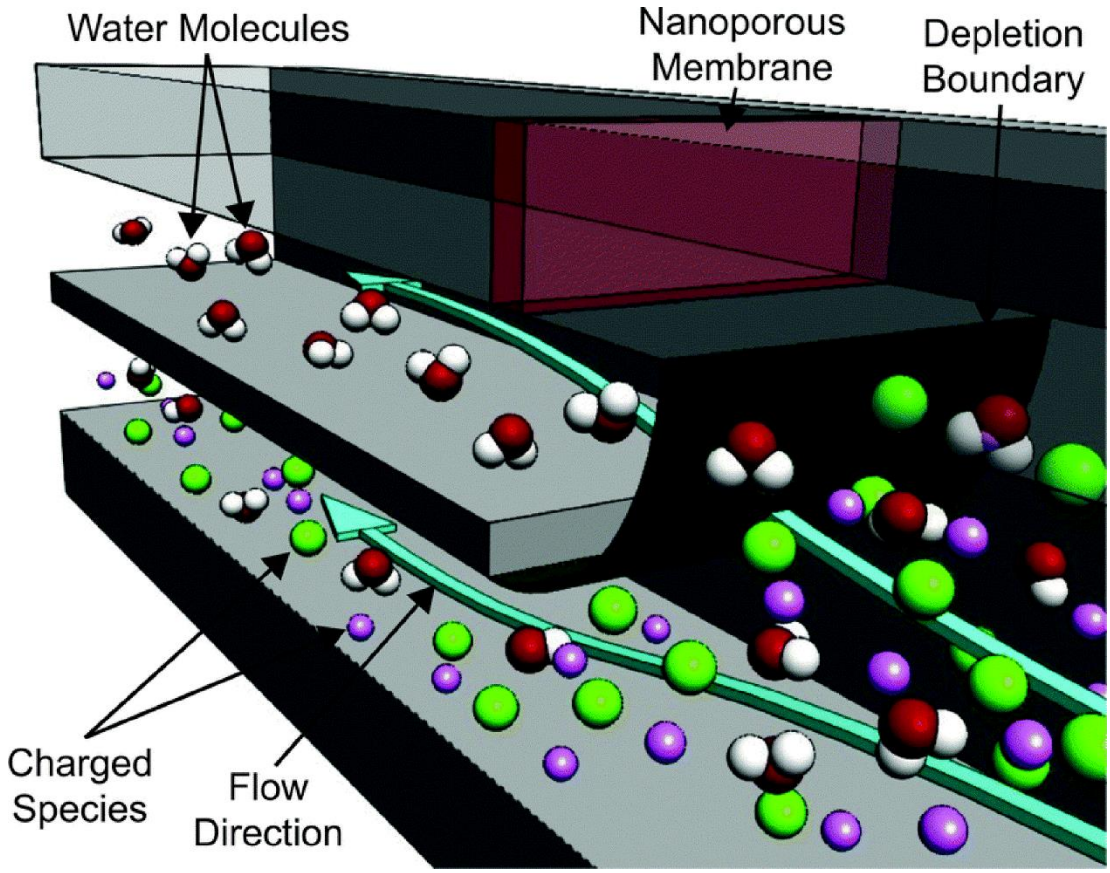

Figure A6. Depiction of the out-of-plane desalting device. The green plane indicates the boundary of the IDZ formed by the Nafion membrane at the intersection of the desalted (upper) and brine (lower) streams. By stacking these streams and the ground (auxiliary) channel vertically, the authors achieved greater functional density than can be obtained in a planar device.

6. Dielectrophoresis of Biological Cells

The non-uniform electric field presented by ICP creates an opportunity to exert dielectrophoretic force on any polarizable particle. Dielectrophoresis (DEP) has been applied to trapping, transporting, sorting, and filtering particles ranging in size from proteins to biological cells.[101] A non-uniform field exerts DEP force by simultaneously inducing a dipole in a dielectric material while exacting an electrostatic force differential on the two ends of that dipole. The dielectric properties of particles and the media in which they are suspended are

influenced by time-dependent responses of molecular dipoles and ions to an applied field, and as a result the sign and magnitude of the dielectrophoretic force vary as a function of the electric field frequency. This property of DEP imparts selectivity, allowing different particles (such as cancer cells and white blood cells) to be distinguished.[102] Therefore, DEP is often employed as an AC-field technique.

The primary shortcoming of DEP is the short distance (tens of microns) over which electric field gradients, formed near electrodes or insulating barriers, typically exist. For this reason, recent advancements in DEP technology have been brought about by the development of 3D electrodes and insulating structures.[103-106] Recently, Anand et al. utilized the extended electric field gradients generated by FICP to augment the reach of DEP.[107] The authors employed an AC electric field with a DC offset to simultaneously drive both DEP and FICP. Given a sufficiently high frequency, the AC field has a minimal impact on the rate of ion depletion and enrichment at the BPE, thus allowing independent tuning of DEP force. The AC frequency (1 kHz) and low buffer conductivity employed led to negative DEP (nDEP), which is the repulsion of cells from high electric field regions. This strategy resulted in an AC-field-strength dependent 1) repulsion of cells from an IDZ and 2) attraction to an IEZ each formed at either the BPE anode or cathode. Most importantly, DEP force was demonstrated greater than 450 μm away from the BPE, a ten-fold extension of DEP reach versus standard approaches. This initial study opens the door to many possible extensions of this combined technique in terms of particle size, DEP mode (positive or negative), and ICP/FICP device design. Intriguingly, in a recently reported device[107] intended for positive DEP (pDEP) capture of fluorescently tagged proteins in nanoconstrictions, an unusual response was observed and

attributed by the authors to a combination of pDEP and ICP in the constrictions.[108] This result implies that the combined technique is applicable over a wide range of particle sizes.

7. Conclusions

In conclusion, capabilities of ICP- and FICP-based techniques are rapidly expanding. Over the past three years, continued research has led to 1) increased throughput for enrichment, separation, and desalting schemes, 2) high resolution separation and focusing, especially through combined techniques (e.g. ICP with ITP and ELSFE), 3) extension into new materials for both the device (e.g. paper microfluidics) and the nanofeatures used for selective charge transport (e.g. silica beads and SWNTs), 4) schemes for recovering analyte bands (e.g. droplets and valves), and 5) leveraging extended electric field gradients for DEP of cells, to name a few. Although the scope of this review did not include advancements in theoretical computation, such studies are essential for progress in this field. For example, the combination of techniques such as DEP with ICP is expected to yield a complex interplay of electromigration, DEP, and both DC and AC driven fluid flow, and questions such as how an AC field impacts propogation of an IDZ remain unanswered. Further, a clearer understanding of the influence of paper fibers and their surface chemistry on EOF and analyte migration will aid in the development of higher performance paper-based ICP devices. Looking ahead, several of the remaining shortcomings of ICP-based techniques can be overcome by synthesizing ideas generated over the past three years. For example, one of the most scalable device architectures presented is that which used silica beads to achieve tunable surface chemistry. If leveraged for desalting, this scheme could lead to unprecedented fresh water output, and with highly charged bead surfaces, could do so at very low power. Further, the droplet generation scheme, if combined with droplet mass spectrometry, could produce an

exquisitely sensitive and highly selective analytical tool. Clearly, ICP-based techniques are expected to enjoy continued growth and development.

8. References

1. R. M. Penner, C. R. Martin, *J. Electrochem. Soc.*, **1985**, 132, 514-515.

2. Z. Siwy, E. Heins, C. C. Harrell, P. Kohli, C. R. Martin, *J. Am. Chem. Soc.*, **2004**, 126, 10850-10851.

3. F. C. Leinweber, U. Tallarek, *Langmuir*, **2004**, 20, 11637-11648.
T. C. Kuo, D. M. Cannon, Jr., Y. Chen, J. J. Tulock, M. A. Shannon, J. V. Sweedler, P.

4. W. Bohn, *Anal. Chem.*, **2003**, 75, 1861-1867.

5. J. Dai, T. Ito, L. Sun, R. M. Crooks, *J. Am. Chem. Soc.*, **2003**, 125, 13026-13027.

6. R. Dhopeshwarkar, R. M. Crooks, D. Hlushkou, U. Tallarek, *Anal. Chem.*, **2008**, 80, 1039-1048.

7. D. Hlushkou, R. Dhopeshwarkar, R. M. Crooks, U. Tallarek, *Lab. Chip*, **2008**, 8, 1153-1162.

8. S. J. Kim, L. D. Li, J. Han, *Langmuir*, **2009**, 25, 7759-7765.

9. T. A. Zangle, A. Mani, J. G. Santiago, *Chem. Soc. Rev.*, **2010**, 39, 1014-1035.

10. S. J. Kim, Y.-A. Song, J. Han, *Chem. Soc. Rev.*, **2010**, 39, 912-922.

11. M. M. Gong, P. Zhang, B. D. MacDonald, D. Sinton, *Anal. Chem.*, **2014**, 86, 8090-8097.

12. R.-J. Yang, H.-H. Pu and H.-L. Wang, *Biomicrofluid.*, **2015**, 9, 014122.

13. M. M. Gong, R. Nosrati, M. C. San Gabriel, A. Zini, D. Sinton, *J. Am. Chem. Soc.*, **2015**, 137, 13913-13919.

14. S. J. Kim, S. H. Ko, K. H. Kang, J. Han, *Nat. Nanotechnol.*, **2010**, 5, 297-301.

15. K. N. Knust, D. Hlushkou, R. K. Anand, U. Tallarek, R. M. Crooks, *Angew. Chem. Int. Ed.*, **2013**, 52, 8107-8110.

16. B. D. MacDonald, M. M. Gong, P. Zhang, D. Sinton, *Lab Chip*, **2014**, 14, 681-685.

17. J. Choi, K. Huh, D. J. Moon, H. Lee, S. Y. Son, K. Kim, H. C. Kim, J. H. Chae, G. Y. Sung, H. Y. Kim, J. W. Hong, S. J. Kim, *RSC Adv.*, **2015**, 5, 66178-66184.

18. L. F. Cheow, A. Sarkar, S. Kolitz, D. Lauffenburger, J. Han, *Anal. Chem.*, **2014**, 86, 7455-7462.

19. R. K. Perdue, D. R. Laws, D. Hlushkou, U. Tallarek, R. M. Crooks, *Anal. Chem.*, **2009**, 81, 10149-10155.

20. M. Kim, M. Jia, T. Kim, *Analyst*, **2013**, 138, 1370-1378.

21. R. K. Anand, E. Sheridan, K. N. Knust, R. M. Crooks, *Anal. Chem.*, **2011**, 83, 2351-2358.

22. S. E. Fosdick, K. N. Knust, K. Scida, R. M. Crooks, *Angew. Chem. Int. Ed. Engl.*, **2013**, 52, 10438-10456.

23. E. Sheridan, D. Hlushkou, K. N. Knust, U. Tallarek, R. M. Crooks, *Anal. Chem.*, **2012**, 84, 7393-7399.

24. K. N. Knust, E. Sheridan, R. K. Anand, R. M. Crooks, *Lab Chip*, **2012**, 12, 4107-4114.

25. Y. C. Wang, A. L. Stevens, J. Han, *Anal. Chem.*, **2005**, 77, 4293-4299.

26. M. Shen, H. Yang, V. Sivagnanam, M. A. Gijs, *Anal. Chem.*, **2010**, 82, 9989-9997.

27. H. Yang, M. Shen, V. Sivagnanam, M. Gijs, Solid-State Sensors, Actuators and Microsystems Conference (TRANSDUCERS), 2011 16th International, **2011**, 238-241.

28. D. W. Zhang, H. Q. Zhang, L. Tian, L. Wang, F. Fang, K. Liu, Z. Y. Wu, *Microfluid. Nanofluid.*, **2013**, 14, 69-76.

29. B. Kim, J. Heo, H. J. Kwon, S. J. Cho, J. Han, S. J. Kim, G. Lim, *ACS Nano*, **2013**, 7, 740-747.

30. J. Mai, H. Miller, A. V. Hatch, *ACS Nano*, **2012**, 6, 10206-10215.

31. L. H. Yeh, M. Zhang, S. Qian, J. P. Hsu, S. Tseng, *J. Phys. Chem. C*, **2012**, 116, 8672-8677.

32. J. H. Lee, B. D. Cosgrove, D. A. Lauffenburger, J. Han, *J. Am. Chem. Soc.*, **2009**, 131, 10340-10341.

33. L. F. Cheow, J. Han, *Anal. Chem.*, **2011**, 83, 7086-7093.
34. S. H. Ko, Y. A. Song, S. J. Kim, M. Kim, J. Han, K. H. Kang, *Lab Chip*, **2012**, 12, 4472-4482.

35. P. Dextras, K. R. Payer, T. P. Burg, W. J. Shen, Y. C. Wang, J. Y. Han, S. R. Manalis, *J. Microelectromech. S.*, **2011**, 20, 221-230.

36. C. H. Chen, A. Sarkar, Y. A. Song, M. A. Miller, S. J. Kim, L. G. Griffith, D. A. Lauffenburger, J. Han, *J. Am. Chem. Soc.*, **2011**, 133, 10368-10371.

37. S. Zheng, H. Lin, J. Q. Liu, M. Balic, R. Datar, R. J. Cote, Y. C. Tai, *J. Chromatogr. A*, **2007**, 1162, 154-161.

38. A. C. Roque, C. S. Silva, M. A. Taipa, *J. Chromatogr. A*, **2007**, 1160, 44-55.

39. H. Song, Y. Wang, C. Garson, K. Pant, *Microfluid. Nanofluid*., **2014**, 17, 693-699.

40. D. R. Laws, D. Hlushkou, R. K. Perdue, U. Tallarek, R. M. Crooks, *Anal. Chem.*, **2009**, 81, 8923-8929.

41. F. Mavré, R. K. Anand, D. R. Laws, K.-F. Chow, B.-Y. Chang, J. A. Crooks, R. M. Crooks, *Anal. Chem.*, **2010**, 82, 8766-8774.

42. P. Mao, J. Han, *Lab Chip*, **2009**, 9, 586-591.

43. A. Balducci, P. Mao, J. Y. Han, P. S. Doyle, *Macromolecules*, **2006**, 39, 6273-6281.

44. M. Yamada, P. Mao, J. Fu, J. Han, *Anal. Chem*., **2009**, 81, 7067-7074.

45. D. Huh, K. L. Mills, X. Zhu, M. A. Burns, M. D. Thouless, S. Takayama, *Nat. Mater*., **2007**, 6, 424-428.

46. S. Chung, J. H. Lee, M.-W. Moon, J. Han, R. D. Kamm, *Adv. Mater.*, **2008**, 20, 3011-3016.

47. S. J. Kim, J. Han, *Anal. Chem*., **2008**, 80, 3507-3511.

48. S. M. Park, Y. S. Huh, H. G. Craighead, D. Erickson, *Proc. Natl. Acad. Sci. USA*, **2009**, 106, 15549-15554.

49. J. Heo, H. J. Kwon, H. Jeon, B. Kim, S. J. Kim, G. Lim, *Nanoscale*, **2014**, 6, 9681-9688.

50. Z. Slouka, S. Senapati, H. C. Chang, *Annu. Rev. Anal. Chem. (Palo Alto Calif)*, **2014**, 7, 317-335.

51. H. C. Chang, G. Yossifon, E. A. Demekhin, *Annu. Rev. Fluid. Mech.*, **2012**, 44, 401-426.

52. G. Yossifon, H. C. Chang, *Phys. Rev. Lett*., **2008**, 101, 254501.

53. A. Mani, T. A. Zangle, J. G. Santiago, *Langmuir*, **2009**, 25, 3898-3908.

54. T. A. Zangle, A. Mani, J. G. Santiago, *Langmuir*, **2009**, 25, 3909-3916.

55. A. Syed, L. Mangano, P. Mao, J. Han, Y.-A. Song, *Lab Chip*, **2014**, 14, 4455-4460.

56. Y. Zeng, D. J. Harrison, *Anal. Chem*., **2007**, 79, 2289-2295.

57. O. Schepelina, I. Zharov, *Langmuir*, **2007**, 23, 12704-12709.

58. J. J. Smith, I. Zharov, *Langmuir*, **2008**, 24, 2650-2654.

59. O. Schepelina and I. Zharov, *Langmuir*, **2008**, 24, 14188-14194.

60. B. Kim, J. Heo, H. J. Kwon, I. Kim, T. An, G. Lim, Jpn. *J. Appl. Phys.*, **2015**, 54, 035102.

61. E. T. Thostenson, Z. F. Ren, T. W. Chou, *Compos. Sci. Technol.*, **2001**, 61, 1899-1912.

62. D. Vairavapandian, P. Vichchulada, M. D. Lay, *Anal. Chim. Acta*, **2008**, 626, 119-129.

63. J. J. Gooding, *Electrochimica Acta*, **2005**, 50, 3049-3060.

64. K. Gong, Y. Yan, M. Zhang, L. Su, S. Xiong, L. Mao, *Anal. Sci*., **2005**, 21, 1383-1393.

65. K. A. Mauritz, R. B. Moore, *Chem. Rev*., **2004**, 104, 4535-4585.

66. D. Choi, A. Choi, D. S. Kim, *Int. J. Precis. Eng. Man*., **2015**, 16, 1467-1471.

67. D. T. Phan, Y. Chun, N. T. Nguyen, *RSC Adv.*, **2015**, 5, 44336-44341.

68. R. Kwak, J. Y. Kang, T. S. Kim, *Anal. Chem*., **2015**, 88, 988-996.

69. Y. Oh, H. Lee, S. Y. Son, S. J. Kim, P. Kim, *Biomicrofluidics*, **2016**, 10, 014102.

70. Y. N. Xia, E. Kim, G. M. Whitesides, *Chem. Mater*., **1996**, 8, 1558-1567.

71. N. Sahiner, M. Singh, D. De Kee, V. T. John, G. L. McPherson, *Polymer*, **2006**, 47, 1124-1131.

72. J. R. Saunders, S. Abu-Salih, T. Khaleque, S. Hanula, W. Moussa, *J. Comput. Theor. Nanos*., **2008**, 5, 1942-1960.

73. A. W. Martinez, S. T. Phillips, G. M. Whitesides, E. Carrilho, *Anal. Chem*., **2010**, 82, 3-10.

74. X. Li, D. R. Ballerini, W. Shen, *Biomicrofluid.*, **2012**, 6, 011301.

75. A. K. Yetisen, M. S. Akram, C. R. Lowe, *Lab Chip*, **2013**, 13, 2210-2251.

76. A. W. Martinez, S. T. Phillips, M. J. Butte, G. M. Whitesides, *Angew. Chem. Int. Ed.*, **2007**, 46, 1318-1320.

77. A. W. Martinez, S. T. Phillips, E. Carrilho, S. W. Thomas, 3rd, H. Sindi, G. M. Whitesides, *Anal. Chem.*, **2008**, 80, 3699-3707.

78. C. Renault, M. J. Anderson and R. M. Crooks, *J. Am. Chem. Soc.*, **2014**, 136, 4616-4623.

79. D. M. Cate, J. A. Adkins, J. Mettakoonpitak and C. S. Henry, *Anal. Chem.*, **2015**, 87, 19-41.

80. X. Liu, C. Cheng, A. Martinez, K. Mirica, X. Li, S. Phillips, M. Mascarenas, G. Whitesides, Micro Electro Mechanical Systems (MEMS), 2011 IEEE 24th International Conference **2011**, 75-78.

81. B. Lutz, T. Liang, E. Fu, S. Ramachandran, P. Kauffman, P. Yager, *Lab Chip*, **2013**, 13, 2840-2847.

82. X. Li, P. Zwanenburg, X. Liu, *Lab Chip*, **2013**, 13, 2609-2614.

83. D. T. Phan, S. A. M. Shaegh, C. Yang, N. T. Nguyen, *Sensor Actuat. B-Chem.*, **2016**, 222, 735-740.

84. R. J. Meagher, J. I. Won, L. C. McCormick, S. Nedelcu, M. M. Bertrand, J. L. Bertram, G. Drouin, A. E. Barron, G. W. Slater, *Electrophoresis*, **2005**, 26, 331-350.

85. E. M. Southern, *J. Mol. Biol.*, **1975**, 98, 503-517.

86. G. F. Carle, M. V. Olson, *Nucleic. Acids. Res.*, **1984**, 12, 5647-5664.

87. J. Narayanan, J.-Y. Xiong, X.-Y. Liu, *J. Phys.: Conf. Ser.*, **2006**, 28, 83-86.

88. R. J. Meagher, J. I. Won, J. A. Coyne, J. Lin, A. E. Barron, *Anal. Chem.*, **2008**, 80, 2842-2848.

89. H. Song, Y. Wang, C. Garson, K. Pant, *Anal. Methods*, **2015**, 7, 1273-1279.

90. R. K. Anand, E. Sheridan, D. Hlushkou, U. Tallarek, R. M. Crooks, *Lab Chip*, **2011**, 11, 518-527.

91. Z. Cao, L. Yobas, *Electrophoresis*, **2013**, 34, 1991-1997.

92. I. Dumitrescu, R. K. Anand, S. E. Fosdick, R. M. Crooks, *J. Am. Chem. Soc.*, **2011**, 133, 4687-4689.

93. K. Scida, E. Sheridan, R. M. Crooks, *Lab Chip*, **2013**, 13, 2292-2299.

94. M. Bercovici, G. V. Kaigala, J. G. Santiago, *Anal. Chem*., **2010**, 82, 2134-2138.

95. T. K. Khurana, J. G. Santiago, *Anal. Chem*., **2008**, 80, 6300-6307.

96. J. Quist, K. G. Janssen, P. Vulto, T. Hankemeier, H. J. van der Linden, *Anal. Chem*., **2011**, 83, 7910-7915.

97. S. H. Ko, S. J. Kim, L. F. Cheow, L. D. Li, K. H. Kang, J. Han, *Lab Chip*, **2011**, 11, 1351-1358.

98. Y. C. Wang, J. Han, *Lab Chip*, **2008**, 8, 392-394.

99. Q. Shi, L. Qin, W. Wei, F. Geng, R. Fan, Y. S. Shin, D. Guo, L. Hood, P. S. Mischel, J. R. Heath, *Proc. Natl. Acad. Sci. USA*, **2012**, 109, 419-424.

100. K. Eyer, P. Kuhn, C. Hanke, P. S. Dittrich, *Lab Chip*, **2012**, 12, 765-772.

101. C. Qian, H. Huang, L. Chen, X. Li, Z. Ge, T. Chen, Z. Yang, L. Sun, *Int. J. Mol. Sci*., **2014**, 15, 18281-18309.

102. S. Shim, K. Stemke-Hale, J. Noshari, F. F. Becker, P. R. Gascoyne, *Biomicrofluid*., **2013**, 7, 11808.

103. R. Martinez-Duarte, *Electrophoresis*, **2012**, 33, 3110-3132.

104. R. Martinez-Duarte, P. Renaud, M. J. Madou, *Electrophoresis*, **2011**, 32, 2385-2392.

105. Y. Jia, Y. Ren, H. Jiang, *Electrophoresis*, **2015**, 36, 1744-1753.

106. S. Zeinali, B. Cetin, S. N. Oliaei, Y. Karpat, *Electrophoresis*, **2015**, 36, 1432-1442.

107. R. K. Anand, E. S. Johnson, D. T. Chiu, *J. Am. Chem. Soc*., **2015**, 137, 776-783.

108. A. Nakano, F. Camacho-Alanis, A. Ros, *Analyst*, **2015**, 140, 860-868.